



HAL
open science

Modélisation des échanges dissous entre l'estuaire de la Loire et les baies côtières adjacentes

Iman Khojasteh Pour Fard

► **To cite this version:**

Iman Khojasteh Pour Fard. Modélisation des échanges dissous entre l'estuaire de la Loire et les baies côtières adjacentes. Hydrologie. Université de Bordeaux, 2015. Français. NNT : 2015BORD0300 . tel-01316627

HAL Id: tel-01316627

<https://theses.hal.science/tel-01316627>

Submitted on 17 May 2016

HAL is a multi-disciplinary open access archive for the deposit and dissemination of scientific research documents, whether they are published or not. The documents may come from teaching and research institutions in France or abroad, or from public or private research centers.

L'archive ouverte pluridisciplinaire **HAL**, est destinée au dépôt et à la diffusion de documents scientifiques de niveau recherche, publiés ou non, émanant des établissements d'enseignement et de recherche français ou étrangers, des laboratoires publics ou privés.

THÈSE PRÉSENTÉE
POUR OBTENIR LE GRADE DE
DOCTEUR DE
L'UNIVERSITÉ DE BORDEAUX

ÉCOLE DOCTORALE DES SCIENCES ET ENVIRONNEMENTS

SPÉCIALITÉ
PHYSIQUE DE L' ENVIRONNEMENT

Par

Iman KHOJASTEH POUR FARD

**MODÉLISATION DES ÉCHANGES DISSOUS ENTRE L'ESTUAIRE DE LA LOIRE
ET LES BAIES CÔTIÈRES ADJACENTES**

Sous la direction de : Nadia SENECHAL
(co-directeur : Pierre LE HIR, Franck DUMAS)

Soutenue le 15/12/2015

Membres du jury :

| | |
|--|-----------------------|
| M. MILLET, Bertrand Professeur, Université Aix-Marseille, Rapporteur, | Président |
| M. REY Vincent, Professeur, Université de Toulon, | Rapporteur |
| M. SANCHEZ-ANGULO Martin, Maître de Conférences HDR, Université de Nantes, | Rapporteur |
| Mme SENECHAL Nadia, Maître de Conférences HDR, Université de Bordeaux, | Directrice de thèse |
| M. LE HIR Pierre, Directeur de recherche HDR, IFREMER, | Co-Directeur de thèse |
| M. DUMAS Franck, Chargé de recherche senior, IFREMER, | Co-Directeur de thèse |
| M. SOTTOLICHIO Aldo, Maître de Conférences HDR, Université de Bordeaux, | Invité |



Titre : MODÉLISATION DES ÉCHANGES DISSOUS ENTRE L'ESTUAIRE DE LA LOIRE ET LES BAIES CÔTIÈRES ADJACENTES

Résumé :

Les estuaires sont des zones à l'interface terre-mer au cœur de la question du devenir des apports continentaux drainés par les grands bassins versants. L'objet de cette étude est focalisé sur l'estuaire de la Loire et ses zones adjacentes (i.e. baie de Bourgneuf et le Mor-Bras) situés dans le nord-est du Golfe de Gascogne. C'est un environnement soumis à l'influence significative de la marée qui se propage en amont de l'embouchure à plus de 100km, de forçages météorologiques de moyennes latitudes donc hautement variables qui induisent en particulier des débits fluviaux pouvant varier d'un facteur dix. Cette variabilité est étudiée à l'aide d'un modèle numérique et des outils de description de la circulation qui permettent de mieux cerner les temps de séjours et de transits des eaux continentales dans l'estuaire et vers les baies riveraines. L'approche s'appuie sur un modèle en grille structurée mais dont la malléabilité pour décrire la complexité du domaine à simuler est donnée par le caractère non-orthogonal des mailles employées pour la discrétisation. Le choix d'un système de coordonnées optimale (covariantes ou contravariantes) est discuté puis implémenté dans le code MARS-3D. Ce nouvel outil est qualifié et validé sur des cas-test puis implémenté en conditions réelles sur un domaine à la géométrie particulièrement accidentée. Les simulations reproduisent très finement la dynamique du grand panache de la Loire et confirment sa très grande variabilité spatiale et temporelle que décrivent partiellement des observations à haute fréquence et ponctuelles ; elles permettent de décrire les chemins privilégiés des masses d'eau à travers les sections de références choisies.

Mots clés : Hydrodynamique côtière, Golfe de Gascogne, Simulations Numériques, Estuaire de la Loire, MARS-3D, Non-Orthogonal, Maillage Curviligne.

Title : MODELLING OF DISSOLVED EXCHANGES BETWEEN THE LOIRE ESTUARY AND THE ADJACENT COASTAL BAYS

Abstract :

Estuaries are key areas in between land and ocean which play a major role in the spreading of continental runoff drained by large watershed. This study focused on the Loire Estuary and its adjacent bays (i.e. Bourgneuf bay and Mor-Braz sea) all located in the north-east side of the bay of Biscay. It is influenced by the large tidal wave that propagates upstream the mouth on more than a 100 km, by highly mid-latitude meteorological forcing that may not only induced High variability in the circulation drivers but also on the river runoffs that may vary from 1 to 10 from early spring to late summer. This High variability is studied thanks to numerical simulation and tools dedicated to describe the circulation with synthetic index such as transit time and mean age of water. The approach lies on a numerical model discretized on a structure grid which constraints have been relaxed to better fit the fractal coastal line using non orthogonal grid cells. The optimal coordinate framework (co or contra-variant) have been discussed, and implemented within a pre-existing code (i.e. MARS-3D). This tools was validated with test cases and implemented on a domain with a particular complex geometry. The numerical simulations catch very accurately the dynamic of this large plume at least as it is described by available in situ observations. This numerical solution allowed to exhibit the main path of water masses through the area and from place to place and their variability according to the main forcings.

Keywords : Coastal Hydrodynamics, River Plume, Loire Estuary (France), Biscay Bay, Flushing Time, MARS-3D, Non-Orthogonal, Curvilinear grid

Unité de recherche

LABORATOIRE DE PHYSIQUE HYDRODYNAMIQUE ET SÉDIMENTAIRE
IFREMER Centre de Brest - DYNECO / PHYSED

Contents

| | |
|---|-----------|
| List of Figures | 6 |
| List of Tables | 11 |
| Remerciements | 12 |
| | |
| Introduction | 16 |
| | |
| 1 Presentation of the study area | 21 |
| 1.1 The Bay of Biscay | 22 |
| 1.1.1 Physiography and Geomorphologic characteristics of the Bay of Biscay | 22 |
| 1.1.2 Circulation forcing in the Bay of Biscay | 25 |
| 1.1.2.1 Wind forcing | 25 |
| 1.1.2.2 Atmospheric heat fluxes | 25 |
| 1.1.2.3 River inputs | 27 |
| 1.1.3 Hydrology of the Bay of Biscay | 27 |
| 1.1.3.1 Temperature | 27 |
| 1.1.3.2 Salinity variation | 29 |
| 1.1.4 Circulation in the Bay of Biscay | 30 |
| 1.1.4.1 General circulation | 31 |
| 1.1.4.2 Tides, tidal currents and tidal residual currents | 33 |
| 1.1.4.3 Density and Wind driven circulation | 35 |
| 1.2 Study area | 37 |
| 1.2.1 The Loire Estuary | 40 |
| 1.2.1.1 Physiography | 41 |
| 1.2.1.2 Loire River regime | 43 |
| 1.2.1.3 Tidal propagation and associated currents | 43 |
| 1.2.1.4 Hydrology | 45 |
| 1.2.2 Bay of Bourgneuf | 46 |
| 1.2.2.1 Physiography | 47 |
| 1.2.2.2 Geology | 48 |
| 1.2.2.3 Residual tidal circulation | 48 |
| 1.2.2.4 Water quality and turbidity | 49 |
| 1.2.3 Mor Braz (including the Bay of Vilaine, the Morbihan Gulf and the Quiberon Bay) | 50 |
| 1.2.3.1 Vilaine Bay | 51 |
| 1.2.3.2 Vilaine River regime | 52 |
| 1.2.3.3 Quiberon Bay | 52 |

| | | |
|----------|--|-----------|
| 2 | Modelling Methodology | 54 |
| 2.1 | Introduction | 54 |
| 2.2 | Classical numerical approach | 55 |
| 2.2.1 | Equations of MARS-3D in Cartesian coordinate system | 55 |
| 2.2.1.1 | Equations of internal mode | 55 |
| 2.2.1.2 | Advection-diffusion equations for heat and salinity | 57 |
| 2.2.1.3 | Equation of any passive Tracer | 58 |
| 2.2.1.4 | Equations of external mode | 58 |
| 2.2.1.5 | Boundary conditions | 59 |
| 2.2.1.6 | Turbulence closure | 62 |
| 2.2.2 | Principles of resolution | 63 |
| 2.2.3 | Time-step | 65 |
| 2.3 | Hydrodynamic modelling in curvilinear grids | 65 |
| 2.3.1 | Introduction | 65 |
| 2.3.2 | Different solutions to adjust the problematic of complex geometry | 66 |
| 2.3.3 | Different types of Coordinate Systems and Basis Vectors | 67 |
| 2.4 | Curvilinear Equations | 69 |
| 2.4.1 | Transformation relations between basis vectors | 70 |
| 2.4.2 | Metric Tensor and Scale components | 71 |
| 2.4.3 | Mapping of the Physical and computational spaces | 72 |
| 2.4.4 | contravariant and covariant vector components | 73 |
| 2.4.5 | Generalized differentiation | 76 |
| 2.4.5.1 | Absolute differential and covariant derivative | 77 |
| 2.4.6 | Differential operators | 79 |
| 2.4.7 | Choice of velocity components for complex geometry | 80 |
| 2.4.7.1 | Scale adjusting | 82 |
| 2.4.8 | Continuity equation | 83 |
| 2.4.9 | Equations of momentum conservation | 84 |
| 2.4.9.1 | Cartesian coordinate | 84 |
| 2.4.9.2 | Generalized tensor notation | 85 |
| 2.4.9.3 | Development in curvilinear coordinates | 85 |
| 2.4.10 | Passive tracer equation | 91 |
| 2.5 | Discretization of equations | 92 |
| 2.5.1 | Introduction | 92 |
| 2.5.2 | Adaptation of the ADI scheme to curvilinear coordinates, first step | 94 |
| 2.5.2.1 | Discrete equations along first ξ and second η axis | 95 |
| 2.5.3 | Principal difficulties using the ADI scheme with curvilinear coordinates | 103 |
| 2.5.3.1 | Estimate of the pressure gradient in decoupling rows (columns) of ADI curvilinear scheme | 103 |
| 2.5.3.2 | Estimation of the main Coriolis term | 106 |
| 2.6 | Preliminary tests of equations | 108 |
| 2.6.1 | Introduction | 108 |
| 2.6.2 | Tracer Advection | 109 |
| 2.6.2.1 | One-dimensional Test | 109 |
| 2.6.2.2 | Two-dimensional Test | 111 |
| 2.7 | Implementation of curvilinear terms in the general MARS-3D computing code | 112 |

3 3D modelling of hydrodynamics in South Brittany and the Loire Estuary:

| | |
|--|------------|
| implementation, configuration and validation of the model | 113 |
| 3.1 Introduction | 113 |
| 3.2 Generation of a curvilinear grid for the study area | 114 |
| 3.2.1 Choice of Lambert coordinates | 114 |
| 3.2.2 Definition of Study area boundaries | 114 |
| 3.2.3 Construction criteria of the grid | 117 |
| 3.2.4 Mesh sizes and orthogonality | 121 |
| 3.2.5 Generation of final grid | 125 |
| 3.2.6 Geometric coefficients and bathymetry interpolation | 125 |
| 3.3 Model configuration | 129 |
| 3.3.1 Vertical grid | 129 |
| 3.3.2 Forcing | 129 |
| 3.3.2.1 Tide | 129 |
| 3.3.2.2 Storm surges and other open sea conditions | 130 |
| 3.3.2.3 Wind forcing and other meteorological forcing | 131 |
| 3.3.2.4 River discharges | 132 |
| 3.3.3 Parameterization | 133 |
| 3.4 Validation | 135 |
| 3.4.1 Introduction | 135 |
| 3.4.2 Sea Surface Elevation | 136 |
| 3.4.3 Salinity | 144 |
| 3.4.3.1 Le-Pellerin | 145 |
| 3.4.3.2 Paimboeuf | 146 |
| 3.4.3.3 Le Croisic | 147 |
| 3.4.4 Temperature | 148 |
| 3.4.4.1 Le-Pellerin | 149 |
| 3.4.4.2 Paimboeuf | 150 |
| 3.4.4.3 Le Croisic | 151 |
| 3.4.4.4 Satellite images (SST) | 152 |
| 3.4.5 Velocity | 152 |
| 3.4.6 Flow patterns of the Estuary | 152 |
| 4 General circulation and Water flow patterns | 159 |
| 4.1 Overview of the forcing time series from June to December 2007 | 160 |
| 4.1.1 Tidal and Surge waves | 162 |
| 4.1.2 River discharge | 163 |
| 4.1.3 Wind Forces | 166 |
| 4.1.3.1 Wind roses | 166 |
| 4.1.4 Salinity and Temperature | 170 |
| 4.2 Tidal circulation | 171 |
| 4.2.1 Instantaneous tidal current during a spring tide | 171 |
| 4.2.2 Maximum peak currents velocity during spring tides | 174 |
| 4.2.3 Residual tidal current during a spring tide | 176 |
| 4.3 Density circulation | 177 |
| 4.3.1 Residual circulation without wind | 177 |
| 4.3.2 Wind-induced circulation | 179 |
| 4.4 Water fluxes | 181 |
| 4.4.0.1 Flux presentation | 181 |

| | | |
|----------|--|------------|
| 4.4.0.2 | Flux analyses | 182 |
| 4.4.1 | Water and Fresh-Water Fluxes at Saint-Nazaire | 183 |
| 4.4.1.1 | Water Flux (WF) and Fresh-water Flux (FWF) in Saint-Nazaire section (overall) | 185 |
| 4.4.1.2 | North/south distribution of water flux at the estuary mouth | 191 |
| 4.4.1.3 | North/south distribution of fresh water flux at the estuary mouth | 194 |
| 4.4.2 | Evolution of Water Flux in Saint-Nazaire section following the change of bathymetry after engineering works in 1984's | 199 |
| 4.5 | Water fluxes entering the bay of Bourgneuf | 205 |
| 4.5.1 | Water Flux in bourgneuf section (overall) | 208 |
| 4.5.2 | Water Flux in SW (left) and NE (right) subsections of Bourgneuf Bay | 210 |
| 4.5.3 | Fresh-Water Flux in Bourgneuf section | 213 |
| 4.6 | Water fluxes passing through the Mor-Braz region | 218 |
| 4.6.1 | Water Flux in Mor-Braz section (overall) | 221 |
| 5 | Time scales analysis (Mean Age, Flushing Time) | 228 |
| 5.1 | Age of water masses | 229 |
| 5.2 | Flushing time | 234 |
| 5.2.1 | Flushing time in the bay of Bourgneuf | 234 |
| 5.2.2 | Flushing time in the Mor-Braz region | 236 |
| | Conclusion | 238 |
| | Publications | 241 |
| | Bibliography | 243 |

List of Figures

| | | |
|------|---|----|
| 0.1 | L'estuaire de la Loire et la zone côtière adjacente. | 17 |
| 1.1 | Bathymetry of the Bay of Biscay | 21 |
| 1.2 | Schematic view of the abyssal plain, the continental slope and the Continental shelf in a coastal ocean | 22 |
| 1.3 | Map of the Bay of Biscay with isobaths | 23 |
| 1.4 | Superficial topography | 24 |
| 1.5 | 3D simulation of thermal balance (or "heat budget") for the period 1965-2004 in the 0-200 m layer | 26 |
| 1.6 | Average seasonal variations (summer and winter) of Temperature in the Bay of Biscay | 28 |
| 1.7 | Average seasonal variations (summer and winter) of Salinity (PSU) in the Bay of Biscay | 29 |
| 1.8 | Schematic representation of circulation in the Bay of Biscay | 30 |
| 1.9 | Schematic seasonal surface circulation in the Bay of Biscay | 32 |
| 1.10 | Amplitude of the M2 (a) and M4 (b) tidal components, computed with the T-UGOm 2D model | 34 |
| 1.11 | Maximum surface current in the Bay of Biscay during average spring tide | 34 |
| 1.12 | Presentation of the study area | 37 |
| 1.13 | Instantaneous tidal currents in the area of Loire-Vilaine | 38 |
| 1.14 | Maximum tidal velocity (m/s) of the depth-averaged current | 38 |
| 1.15 | Residual tidal circulation in the area of Loire-Vilaine | 39 |
| 1.16 | The Loire Estuary and river section | 41 |
| 1.17 | Evolution of the navigation channel depth | 42 |
| 1.18 | Bilho Island in the Loire Estuary | 43 |
| 1.19 | Loire river flow histogram from 1980 to 2009 | 43 |
| 1.20 | Propagation of a spring tide during low flows | 44 |
| 1.21 | The Loire Estuary average salinity ranges | 45 |
| 1.22 | Bay of Bourgneuf | 46 |
| 1.23 | Topography, bathymetry and hydrographic network of the Bay of Bourgneuf | 47 |
| 1.24 | Sedimentological map of the bay of Bourgneuf | 48 |
| 1.25 | Main features of the tidal residual circulation in the bay of Bourgneuf | 49 |
| 1.26 | Geography of the Mor-Braz area in south Brittany | 50 |
| 1.27 | Time evolution of the Vilaine river flow from 2003 to 2013 | 52 |
| 1.28 | Hydrodynamic circulation in the western part of the Mor-braz | 53 |
| 2.1 | Spatial repartition of water depths on a grid cell | 60 |
| 2.2 | Horizontal and vertical positions of variables in the Arakawa-C grid | 61 |
| 2.3 | Horizontal and vertical positions of variables in the Arakawa-C grid | 64 |

| | | |
|------|---|-----|
| 2.4 | ADI semi-implicit resolving variable with respect to the direction | 65 |
| 2.5 | Homogeneous and curvilinear coordinates, the basis vectors(covariant basis) are always tangent to coordinate lines | 68 |
| 2.6 | Definition of different basis vectors | 69 |
| 2.7 | Old coordinates system (Cartesian) presented by (x, y) with (e_1, e_2) as basis and new ones (non-orthogonal curvilinear) defined by (ξ, η) with (g_1, g_2) as new basis | 70 |
| 2.8 | Coordinate mapping, which transforms the domain into a simpler (usually rectangular) domain | 73 |
| 2.9 | contravariant and covariant components | 75 |
| 2.10 | Illustration of different type of components over a C grid | 76 |
| 2.11 | Moving from one point to another using covariant basis coordinates | 78 |
| 2.12 | Skewness variation | 81 |
| 2.13 | a) Variables positions in the Arakawa-C grid | 93 |
| 2.14 | ADI semi-implicit resolving variable with respect to the direction | 104 |
| 2.15 | Arrakawa C-grid and divergence in curvilinear coordinates. | 105 |
| 2.16 | a) Interpolation of V component of Arakawa-C grid in U position in curvilinear coordinate meshes b) Interpolation of V component of Arakawa-C grid in U position in Cartesian coordinate meshes c) Interpolation of U component of Arakawa-C grid in V position in curvilinear coordinate meshes d) Interpolation of U component of Arakawa-C grid in V position in Cartesian coordinate meshes | 106 |
| 2.17 | One-dimensional advection of a Gaussian structure for four different grids | 110 |
| 2.18 | Two-dimensional advection a Gaussian isotropic structure | 111 |
| | | |
| 3.1 | Aerial view of the whole Loire Estuary, included in the study area. | 114 |
| 3.2 | Coastline in Atlantic parts of the study area. | 115 |
| 3.3 | Streamlines at maximum tidal flood in the interest area. | 115 |
| 3.4 | Splitting of the study area into 189 sub-domains. | 116 |
| 3.5 | Bathymetry of the coastal zone Loire-Vilaine. | 118 |
| 3.6 | Part of grid superposed with isobath contours | 118 |
| 3.7 | Details of the computational grid in the Loire Estuary | 119 |
| 3.8 | Zoom of the grid at the mouth of the Loire Estuary. | 120 |
| 3.9 | Illustration of the progressive mesh size criterion to a typical cross-section of the Loire Estuary. | 120 |
| 3.10 | General view of the grid with depth contours and coastline | 121 |
| 3.11 | General view of the non-orthogonal curvilinear grid: deviation from orthogonality | 123 |
| 3.12 | General view of the grid with depth contours and coastline. | 124 |
| 3.13 | Study area in transformed computational grid. | 125 |
| 3.14 | Example of grid splitting around an island | 126 |
| 3.15 | General view of the grid after projection on the bathymetry | 127 |
| 3.16 | Different references of bathymetry | 128 |
| 3.17 | View of the grid in the area of the Loire mouth | 128 |
| 3.18 | Transformation into sigma coordinates | 129 |
| 3.19 | Reconstitution of the total See Surface elevation | 131 |
| 3.20 | Surge considered at the open boundary | 132 |
| 3.21 | Loire and Vilaine discharges | 133 |
| 3.22 | Distribution of the bottom roughness length in different reaches of the Loire estuary | 134 |
| 3.23 | Geometric relationship between the correlation, standard deviation and RMSE | 136 |
| 3.24 | Tide gauges positions | 137 |

| | | |
|------|--|-----|
| 3.25 | Validation of the simulated surface elevation, during the whole period | 138 |
| 3.26 | Wind forcing during neap tide from 14 Sep 2007 to 28 Sep 2007 | 139 |
| 3.27 | Wind forcing during spring tide from 20 Sep 2007 to 4 Oct 2007 | 139 |
| 3.28 | Validation of the simulated surface elevation, during a severe neap tide period . | 140 |
| 3.29 | Validation of the simulated surface elevation, during a severe spring tide period . | 141 |
| 3.30 | Wind forcing from 3 to 19 Dec 2007 | 142 |
| 3.31 | Wind forcing from 5 to 25 Jun 2007 | 143 |
| 3.32 | Le-Pellerin, Paimboeuf and Le Croisic stations | 144 |
| 3.33 | Wind forces from 11/08 to 28/12 | 145 |
| 3.34 | Observed and predicted salinity at Le-Pellerin station | 145 |
| 3.35 | Observed and predicted salinity at the Paimboeuf station | 146 |
| 3.36 | Wind forces from 27/11 to 20/12 | 147 |
| 3.37 | Observed (ADCP) and predicted Salinity at Le Croisic | 148 |
| 3.38 | Observed and predicted temperature at Le-Pellerin station | 149 |
| 3.39 | Observed and predicted temperature at Paimboeuf station | 150 |
| 3.40 | Observed and predicted temperature at Le Croisic station | 151 |
| 3.41 | Comparison between a Sea Surface Temperature (SST) satellite (NOAA) image and surface results of the MARS-3D model on 10-12/12/2007 2h | 152 |
| 3.42 | Flow pattern at the mouth of the Loire Estuary | 153 |
| 3.43 | Comparison between measured and simulated current magnitude at Le Croisic station | 154 |
| 3.44 | Wind vectors from 22 Nov to 22 Dec 2007 | 154 |
| 3.45 | Comparison between measured and simulated current direction at Le Croisic station | 155 |
| 3.46 | Imaginary particle trajectories | 157 |
| 3.47 | Time-integrated wind hodograph from 8 to 12 December 2007 | 158 |
| 3.48 | Change the direction of the plume of the Loire, between 10 and 12 December . . | 158 |
| | | |
| 4.1 | Forcing time series from June to December 2007 | 161 |
| 4.2 | Mars2D model for current and storm surge levels | 162 |
| 4.3 | Computed storm surges level in the study area | 163 |
| 4.4 | Relative frequency histogram of the Loire and Vilaine River discharges | 164 |
| 4.5 | Chronology of the Loire and Vilaine River discharges | 165 |
| 4.6 | Schematic wind forces used for realistic modeling comparing the measured wind during past years | 167 |
| 4.7 | Time-integrated wind hodograph | 168 |
| 4.8 | Wind rose in time-evolution divided in four interval (next to Le-Croisic) | 169 |
| 4.9 | Surface tidal current during a spring tide on 14/08/2007 in a simulation without wind and river discharge | 172 |
| 4.10 | Surface tidal current during a spring tide on 14/08/2007 in a simulation without wind and river discharge | 173 |
| 4.11 | Maximum instantaneous currents between 13 to 16/08 | 174 |
| 4.12 | Surface residual tidal current during a whole neap/spring tidal cycle, from 08/08 to 14/08/2007 | 176 |
| 4.13 | Mean salinity and residual current during spring tide (16/08) and neap tide (22/08) by considering real river discharge and without wind forces | 177 |
| 4.14 | Residual salinity and current during spring tide (18/02) with a constant mean-flow | 178 |
| 4.15 | Mean salinity and residual current during spring tide (16/08) and neap tide (22/08) by considering real river-flow and wind forces | 180 |

| | | |
|------|---|-----|
| 4.16 | Vilaine, Saint-Nazaire and Bourgneuf sections | 181 |
| 4.17 | Saint-Nazaire cross-sections | 184 |
| 4.18 | Schematic view of the cross-section; (Fresh) Water Flux is calculated over the first 1m below the surface in St-Nazaire | 184 |
| 4.19 | Schematic view of the cross-section; (Fresh) Water Flux is calculated over the first 1m above the bottom in St-Nazaire | 184 |
| 4.20 | Water exchange in the St-Nazaire cross-section | 186 |
| 4.21 | Averaged residual current | 187 |
| 4.22 | Time-evolution of wind speed from 01/Jun until 28/Dec nearby Le-Croisic according to the ARPEGE meteorological model. | 188 |
| 4.23 | Depth-averaged Residual Salinity and Current | 188 |
| 4.24 | Fresh-Water exchange in the St-Nazaire cross-section | 189 |
| 4.25 | Representative vertical profiles of hydrological characteristics across the Saint-Nazaire section | 190 |
| 4.26 | Water exchange in the St-Nazaire north-section (deep) | 192 |
| 4.27 | Water exchange in the St-Nazaire south-section (shallow) | 193 |
| 4.28 | Fresh-Water exchange in the St-Nazaire north-section (deep) | 195 |
| 4.29 | Fresh-Water exchange in the St-Nazaire south-section (shallow) | 196 |
| 4.30 | Water and freshwater exchanges in the St-Nazaire cross-section for 10 scenarios . | 197 |
| 4.31 | Bathymetry before and after engineering works in 1984. | 200 |
| 4.32 | Fresh Water exchange in the Saint-Nazaire cross-section before and after 1984. . | 201 |
| 4.33 | Fresh-Water exchange in the St-Nazaire north-section (deep) before and after 1984. | 203 |
| 4.34 | Fresh-Water exchange in the St-Nazaire south-section (shallow) before and after 1984 | 204 |
| 4.35 | Bourgneuf section | 205 |
| 4.36 | Schematic view of the cross-section; (Fresh) Water Flux is calculated over the first 1m below the surface in Bourgneuf | 205 |
| 4.37 | Schematic view of the cross-section; (Fresh) Water Flux calculated over the first 1m above the bottom in Bourgneuf | 205 |
| 4.38 | Representative vertical profiles of hydrological characteristics across the Bourgneuf section | 207 |
| 4.39 | Water exchange in the Bourgneuf section (overall). | 209 |
| 4.40 | Water exchange in the Bourgneuf SW sub-section. | 211 |
| 4.41 | Water exchange in the Bourgneuf NE sub-section. | 212 |
| 4.42 | Fresh-Water exchange in the Bourgneuf section (overall). | 215 |
| 4.43 | Water and Fresh Water exchange in the Bourgneuf section for 10 scenarios . . . | 216 |
| 4.44 | Mor-Braz section | 218 |
| 4.45 | Schematic view of the cross-section; (Fresh) Water Flux is calculated over the first 1m below the surface in Mor-Braz | 218 |
| 4.46 | Schematic view of the cross-section; (Fresh) Water Flux is calculated over the first 1m above the bottom in Mor-Braz | 218 |
| 4.47 | Representative vertical profiles of hydrological characteristics across the Mor-Braz section | 220 |
| 4.48 | Water exchange in the Vilaine section (overall). | 222 |
| 4.49 | Water exchange in the Vilaine left sub-section. | 224 |
| 4.50 | Water exchange in the Vilaine eastern subsection (right). | 225 |
| 4.51 | Water and Fresh Water exchanges in the Mor-Braz subsection for 10 scenarios . | 227 |
| 5.1 | Areas of interest for water age and Flushing-time | 228 |

| | | |
|-----|--|-----|
| 5.2 | Time evolution of mean age of fresh water provided by the Loire River | 230 |
| 5.3 | Spatial distribution of mean age of freshwater from the Loire River on neap tide (LW), simulation without wind. | 232 |
| 5.4 | Spatial distribution of mean age of freshwater from the Loire River on neap tide (LW), simulation with realistic wind | 233 |
| 5.5 | Spatial distribution of vertically averaged flushing time of the bay of Bourgneuf. | 235 |
| 5.6 | Spatial distribution of vertically averaged flushing time of the Mor-Braz. | 236 |

List of Tables

| | | |
|-----|---|-----|
| 1.1 | Annual mean runoff of major rivers. | 27 |
| 1.2 | Surface level for average tides (in m) | 44 |
| 2.1 | Choice of velocity components | 82 |
| 3.1 | Sizes of meshes used in different sectors of computational grid | 122 |
| 3.2 | Statistical errors of surface elevation at different stations of tidal gauges | 139 |
| 3.3 | The best and the worst surface elevation RMSE computed in different stations . | 142 |
| 4.1 | (Fresh) Water Flux in Bourgneuf during 01/Jun-28/Dec. | 214 |

Remerciements

Ce projet a bénéficié du soutien de l'IFREMER et des fonds européens FEDER du Plan Loire via le GIP Loire-Estuaire.

Je souhaite remercier toutes les personnes qui ont contribué à sa réalisation, concrètement ou indirectement.

J'exprime tout d'abord mes remerciements aux membres du jury et en particulier à mes rapporteurs, surtout au directeur de l'école doctorale sciences et environnements Frédéric GARABETIAN, pour leur enthousiasme vis-à-vis de ce travail et leur compréhension des retards successifs du manuscrit.

Je remercie Nadia SENECHAL d'avoir accepté la direction de cette thèse, et pour l'intérêt qu'elle a porté à ce travail, pour son soutien et ses précieux conseils.

Je remercie chaleureusement et énormément Pierre LE HIR pour son accompagnement tout au long de cette thèse, pour ses nombreux conseils, ses relectures critiques du manuscrit, mais aussi pour son exemple pédagogique et parfois difficile à respecter. J'ai appris beaucoup grâce à toi et je suis reconnaissant de tes efforts qui m'ont permis de finir cette thèse avec toutes les difficultés auxquelles j'ai été confronté pendant ces dernières années.

Je tiens à remercier particulièrement Franck DUMAS, qui m'a non seulement initié à la conception de la modélisation, mais qui a aussi suivi et orienté mon travail dans ce domaine avec toujours autant d'enthousiasme et de nombreux encouragements. Merci pour tes nombreuses relectures. Je suis aussi grandement reconnaissant envers Jérôme GOURRION qui a été l'initiateur de ce projet si riche d'expériences.

Je souhaite remercier Monsieur PAGES qui a contribué à la préparation et à la réalisation des maillages curvilinéaires que j'ai utilisés. Il nous a suivi avec patience et a accepté nos multiples demandes visant à modifier et à construire un maillage curvilinéaire très précis. Ce travail n'aurait pas pu être réalisé sans les efforts de l'IFREMER pour financer une année de plus les développements techniques et m'accueillir au sein de l'équipe de DYNECO-PHYSED.

Je tiens aussi à remercier particulièrement Albert MOREAU, chef d'équipe de la sécurité de l'IFREMER Brest.

Au cours de ma thèse, j'ai eu la chance de rencontrer et de travailler avec beaucoup d'autres

personnes, je les remercie pour leur aide et leur fais part de toute ma sympathie : merci à Valérie GARNIER pour son aide sur le modèle MARS-3D et également à Sébastien THEETTEN pour leurs aides ponctuelles en début de thèse.

Je tiens à remercier Pierre GARREAU pour sa patience, ses réactions calmes même quand je faisais des bêtises :D !

A Fabrice ARDHUIN pour sa formation au logiciel WW3, que je n'ai malheureusement pas pu utiliser dans mon modèle.

Merci aussi à Pascal LAZURE pour son humour, ainsi que ses remarques critiques et constructives de mes résultats.

Merci à Guillaume CHARRIA, pour son partage du savoir en Matlab (l'analyse des données, les statistiques ...) , pour sa gentillesse et son soutien quotidien.

Merci à Romaric VERNEY pour m'avoir aidé à récupérer les données ADCP qui m'ont aidées ainsi que pour sa gentillesse et son soutien quotidien.

Merci à Frédéric VANDERMEIRSCH pour son initiation au modèle MARS, ses coups de pouce réguliers depuis mon arrivé au labo et son chaleureux soutien personnel. Tous mes collègues ont été sympas, mais d'avoir un ami parmi eux, ça m'a fait beaucoup de bien...

Merci à nouveau à Hervé JESTIN pour tout ce qu'il m'a appris sur les calibrations au cours de quelques mouillages en mer et merci aussi pour sa bonne humeur quotidienne.

Merci à Philippe CANN (sa place nous a manqué énormément) pour ses contributions et son enseignement aux techniques du labo, mais aussi pour le partage du bureau pendant un an et pour sa grande sympathie.

Merci à Youen KERVELLA et François BATIFOULIER, Florian GANTHY, pour les discussions sympathiques et leurs conseils qui m'ont bien aidés.

Merci aux super informaticiens, Jean-Francois LE ROUX et Mathieu CAILLAUD, pour leurs dépannages réguliers et leur disponibilité.

Merci à Pascale pour ses services et sa gentillesse. Enfin, je termine en remerciant toutes les autres personnes qui m'ont entouré au cours de la thèse.

Un grand merci aux gens avec qui j'ai partagé mon bureau! Matthieu JOUAN, Imene KAROUI, Emmanuel RENAULT, Charaf ASSASSI, pour la bonne ambiance assurée au quotidien et pour leurs encouragements tout au long de ma thèse.

Je tiens a remercier mes amis qui m'ont beaucoup encouragés pendant ces années quelques fois très difficiles! à Marielle CALVEZ (une vrai amie), Neda (la meilleure) et Hoda SAYYADI (encourageante), Armand BOLOORCHI et Sepehr NAMDAR (pour les moments détente)...

Je tiens a remercier ma famille (Asghar, Azadeh, Reza et Elmira) et surtout ma mère Parvine <3.

Abstract

Estuaries are key areas in between land and ocean which play a major role in the spreading of continental runoff drained by large watershed. This study focused on the Loire Estuary and its adjacent bays (*i.e.* Bourgneuf bay and Mor-Braz sea) all located in the north-east side of the bay of Biscay. It is influenced by the large tidal wave that propagates upstream the mouth on more than a 100 km, by highly mid-latitude meteorological forcing that may not only induced High variability in the circulation drivers but also on the river runoffs that may vary from 1 to 10 from early spring to late summer. This High variability is studied thanks to numerical simulation and tools dedicated to describe the circulation with synthetic index such as transit time and mean age of water. The approach lies on a numerical model discretized on a structure grid which constraints have been relaxed to better fit the fractal coastal line using non orthogonal grid cells. The optimal coordinate framework (covariant or contravariant) have been discussed, and implemented within a pre-existing code (*i.e.* MARS-3D). This tool was validated with test cases and implemented on a domain with a particular complex geometry. The numerical simulations catch very accurately the dynamic of this large plume at least as it is described by available in situ observations. This numerical solution allowed to exhibit the main path of water masses through the area and from place to place and their variability according to the main forcing.

Key-words: Coastal Hydrodynamics, River Plume, Loire Estuary (France), Flushing Time, MARS-3D, Non-Orthogonal, Curvilinear grid.

Résumé

Les estuaires sont des zones à l'interface terre-mer au cœur de la question du devenir des apports continentaux drainés par les grands bassins versants. L'objet de cette étude est focalisé sur l'estuaire de la Loire et ses zones adjacentes (*i.e.* baie de Bourgneuf et le Mor-Bras) situés dans le nord-est du Golfe de Gascogne. C'est un environnement soumis à l'influence significative de la marée qui se propage en amont de l'embouchure à plus de 100km, de forçages météorologiques de moyennes latitudes donc hautement variables qui induisent en particulier des débits fluviaux pouvant varier d'un facteur dix. Cette variabilité est étudiée à l'aide d'un modèle numérique et des outils de description de la circulation qui permettent de mieux cerner les temps de séjours et de transits des eaux continentales dans l'estuaire et vers les baies riveraines. L'approche s'appuie sur un modèle en grille structurée mais dont la malléabilité pour décrire la complexité du domaine à simuler est donnée par le caractère non-orthogonal des mailles employées pour la discrétisation. Le choix d'un système de coordonnées optimale (covariantes ou contravariantes) est discuté puis implémenté dans le code MARS-3D. Ce nouvel outil est qualifié et validé sur des cas-test puis implémenté en conditions réelles sur un domaine à la géométrie particulièrement accidentée. Les simulations reproduisent très finement la dynamique du grand panache de la Loire et confirment sa très grande variabilité spatiale et temporelle que décrivent partiellement des observations à haute fréquence et ponctuelles ; elles permettent de décrire les chemins privilégiés des masses d'eau à travers les sections de références choisies.

Mots clés : Golfe de Gascogne, Simulations Numériques, Estuaire de la Loire, MARS-3D, Non-Orthogonal, Maillage Curviligne.

Introduction

Il est commun de rappeler l'importance des estuaires, zones de transition entre milieux continentaux et océaniques, entre eaux fluviales et eaux marines, qui remplissent de nombreux services écosystémiques (Costanza et al., 1997), offrent une diversité de paysages originaux, mais qui sont aussi soumis à de multiples pressions anthropiques : ils sont le réceptacle de rejets agricoles, industriels et urbains, ont souvent été transformés pour faciliter la navigation de bateaux de plus en plus grands vers des ports intérieurs, et surtout sont soumis à une pression d'urbanisation très forte, car ils offrent les atouts recherchés de la zone côtière et la proximité des réseaux de transport souvent liés aux infrastructures portuaires. Ces mêmes raisons concourent aussi à susciter des implantations industrielles, nécessitant souvent un accès sur le domaine maritime, accroissant encore la pression foncière sur le milieu naturel. Le cas de l'estuaire de la Loire est tout fait représentatif en France de ces enjeux et difficultés, et a fait naturellement l'objet de nombreuses études et modélisations (CSEEL, 1984, Migniot and Le Hir, 1997).

Très souvent l'estuaire a été considéré comme un objet d'investigation en soi, l'embouchure en constituant une frontière. Il est alors difficile de préciser les entrées et sorties, et la méconnaissance des conditions à cette limite arbitraire empêche la fermeture de bilans intra-estuariens, qu'il s'agisse d'éléments dissous ou particuliers. L'estuaire débouche sur un secteur côtier constitué de baies plus ou moins ouvertes au sein desquelles nous cherchons à connaître l'influence des eaux issues du fleuve amont (la Loire en l'occurrence) ainsi que leur temps de séjour. S'agissant de l'estuaire de la Loire, la question du bilan sédimentaire reste aujourd'hui posée avec beaucoup d'acuité pour des questions de gestion et d'aménagements (gestion des dragages notamment), et il est très difficile d'y répondre, car on se heurte à la méconnaissance totale du flux particulaire à l'embouchure. On ne sait même pas dans quel sens ce flux est dirigé (vers l'amont, ou vers l'aval), ni ses fluctuations dans le temps ni les facteurs qui influencent cette variabilité.

Par ailleurs, se pose la question du devenir des eaux de la Loire. Elle concerne à la fois les éléments dissous et les éléments particuliers (matières en suspension). En ce qui concerne les éléments dissous, s'il est clair qu'en moyenne l'eau s'écoule vers l'aval (débit fluvial à évacuer), des épisodes de vent peuvent inverser temporairement cet écoulement. Surtout,

les stratifications et inversions de circulation résiduelle (*i.e.* après avoir filtré la marée) entre la surface et le fond à l'embouchure sont susceptibles de faire entrer des eaux marines, en particulier à proximité du fond. Ces mêmes mécanismes peuvent prolonger les temps de résidence de certaines masses d'eau dans l'estuaire, tout en accélérant le transit des eaux fluviales, plus douces, qui restent en surface et s'évacuent vers la mer.

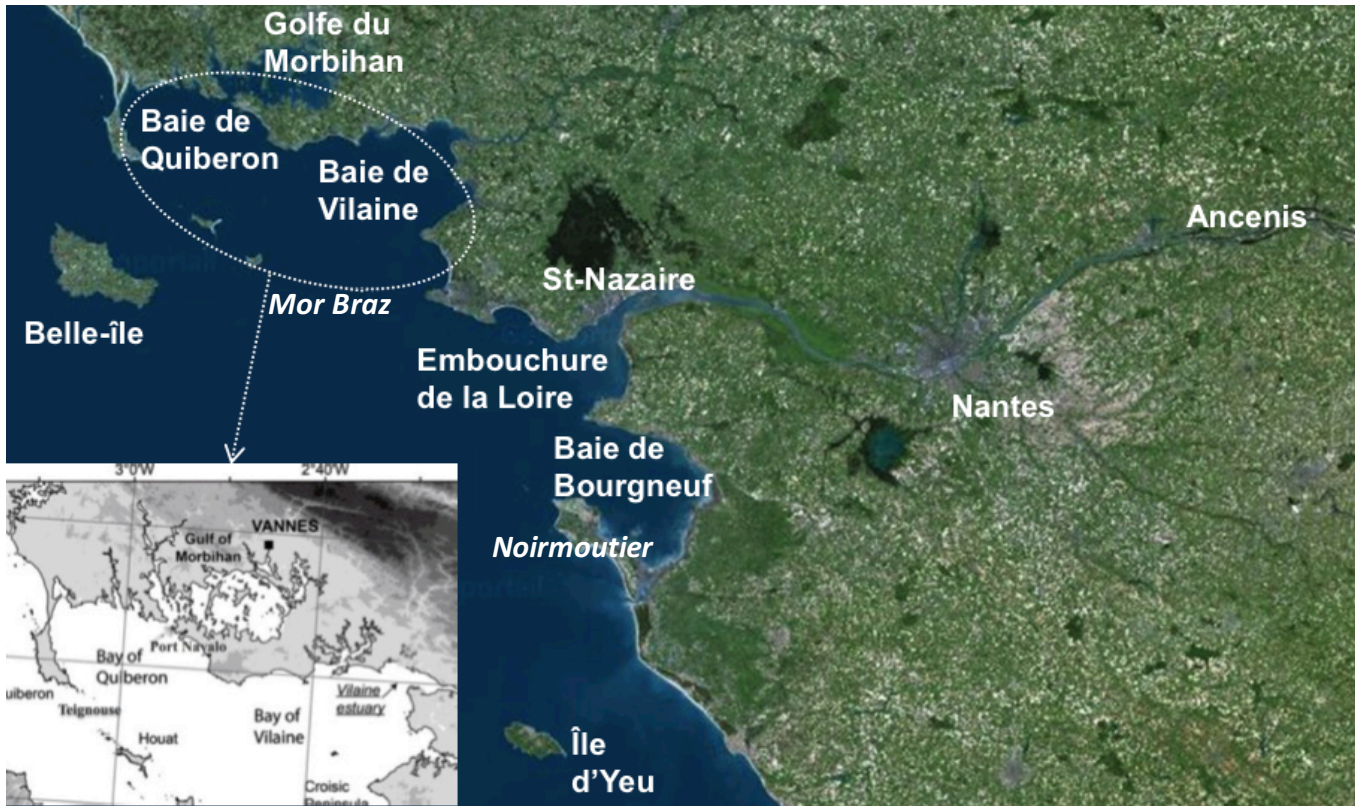


Figure 0.1: L'estuaire de la Loire et la zone côtière adjacente. Le Mor-Braz est représenté par le secteur en pointillés.

Parallèlement, la zone côtière à proximité de l'estuaire de la Loire (Fig. 0.1) a fait l'objet de nombreuses attentions depuis quelques années, motivées par des questions liées à l'exploitation conchylicole (en baie de Bourgneuf et en baie de Quiberon notamment), aux extractions de granulats en mer (*e.g.* secteur du Pilier au Nord de Noirmoutier), aux rejets de dragages (du Grand Port Maritime de Nantes/St-Nazaire, GPMNSN), aux implantations d'éoliennes offshore et aux installations pour les énergies marines renouvelables. Des études relatives à la qualité de l'eau (en particulier en baie de Vilaine où les eaux de fond connaissent des épisodes d'hypoxie, voire d'anoxie), aux nurseries de poissons (soles...), ou encore aux développements de macroalgues ont été menées récemment.

Une majorité de ces études ignore le fonctionnement estuarien, et considèrent les apports de la Loire à travers la connaissance disponible sur les apports fluviaux ou urbains, mais sans tenir compte des transformations intra-estuariennes, ou de façon très schématique. En particulier,

beaucoup de modèles côtiers restituant les circulations côtières (*e.g.* Tessier, 2006) sont restés très grossiers dans le domaine estuarien.

L'ambition de cette thèse est de caractériser les échanges entre l'estuaire de la Loire et la zone côtière limitrophe et de mettre en place une modélisation unique englobant à la fois l'estuaire et les mers côtières adjacentes afin de mieux prendre en compte l'estuaire et ses processus internes dans les études côtières, de façon à interpréter les flux obtenus aux frontières de ces baies. Inversement, il s'agit de mieux définir la condition limite lors des investigations spécifiques à l'estuaire. Le modèle doit aussi pouvoir simuler les variations saisonnières (voir annuelles) et en même temps être suffisamment précis en particulier dans l'estuaire et le fond des baies. La caractérisation des échanges entre l'estuaire et les zones adjacentes s'est focalisée sur la baie de Bourgneuf d'une part et la baie de Vilaine d'autre part. Enfin, la configuration spécifique du Mor-Braz (Fig. 0.1) qui englobe la baie de Quiberon à l'ouest et la baie de Vilaine à l'est, qui échange un volume tidal considérable avec le golfe du Morbihan au nord, et s'appuie sur une chaussée rocheuse naturelle au sud (Quiberon, Houat, Hoëdic et presqu'île du Croisic) suscite beaucoup d'interrogations sur les quantités d'eau échangées avec la zone côtière plus au large : en particulier les travaux de Tessier (2006) indiquaient une forte sensibilité de ces échanges à la direction du vent. Le présent travail de thèse est l'opportunité de caractériser tous ces échanges et leur variabilité selon l'ensemble des forçages, principalement la marée, la surcote/décote météorologique, le débit des fleuves et le vent. La variation du vent fait l'objet d'une attention plus particulière. Le système côtier "Loire-Bretagne" est aussi le réceptacle du fleuve Vilaine, ce qui nous a conduit à évaluer en second lieu l'influence de la Loire et de La Vilaine dans la baie du Mor-Braz. Nous avons cherché à prendre en compte l'influence des autres fleuves (*e.g.* la Gironde), en considérant les variations de la salinité et de la température au large, ainsi que la circulation générale. L'objet premier de ce travail est d'examiner la variabilité des échanges en fonction de la variabilité des forçages et d'évaluer les influences respectives de ces derniers. Une contribution essentielle de la thèse est le développement d'un modèle qui concilie une bonne résolution horizontale dans l'estuaire pour traduire le rôle spécifique des chenaux et des secteurs rivulaires moins profonds, une bonne restitution de la bathymétrie dans les baies adjacentes, incluant le golfe du Morbihan, une extension du domaine d'étude suffisamment large pour que l'imprécision des conditions aux limites n'influence pas trop les résultats annoncés, et enfin une rapidité de calcul autorisant des simulations assez longues (typiquement de l'ordre de l'année) pour explorer la variabilité des échanges, et pour permettre ultérieurement une modélisation des processus sédimentaires et écologiques. La solution retenue est basée sur le code MARS-3D de l'Ifremer largement utilisé et validé, en particulier sur les façades métropolitaines françaises, mais comprend un développement très ambitieux. Elle

consiste à modéliser les processus hydrodynamiques selon une grille de calcul composée de mailles de dimensions variables : pour y parvenir, le principe d'un maillage curviligne non orthogonal est retenu, et une grande partie du travail de thèse a porté sur la transformation du code MARS-3D pour permettre une résolution des équations de l'hydrodynamique sur un maillage curviligne. L'absence de contrainte sur l'orthogonalité, qui rend beaucoup plus souple la mise en place de la grille de calcul dans une configuration géographique quelconque, nécessite la prise en compte de nombreux termes additionnels dans les équations, et une refonte complète du code.

Le présent mémoire est organisé en cinq parties. Le premier chapitre décrit la région où l'étude a été réalisée ainsi que les travaux de référence qui ont été conduits précédemment. La discussion porte sur le golfe de Gascogne et plus particulièrement le secteur d'étude qui va de la presqu'île de Quiberon au nord-ouest à l'île d'Yeu au sud. Cette entité régionale englobe l'estuaire de la Loire (de Saint Nazaire en aval jusqu'à Ancenis en amont), la baie de Bourgneuf, le Mor-Braz (incluant la baie de Vilaine et la baie de Quiberon), et le golfe du Morbihan qui lui est rattaché, ainsi que cinq îles principales : Belle-île , île de Houat, île d'Yeu, île de Hoëdic et île de Noirmoutier.

Le second chapitre présente la méthodologie de modélisation et surtout les importants développements réalisés durant la thèse afin que la formulation des équations régissant la dynamique des écoulements à surface libre et leur résolution soient compatibles avec un maillage non orthogonal, mais toujours structuré. La discrétisation des équations utilisées dans le code est ensuite décrite. A la fin de cette partie, nous présentons des cas-tests uni et bidimensionnels comme étape obligée de validation des méthodes utilisées.

Le troisième chapitre décrit l'implémentation et la configuration du maillage curviligne dans l'estuaire de la Loire et la zone côtière adjacente. La validation du code de calcul y est également présentée en comparant les résultats issus du modèle à des mesures réalisées durant l'année 2007; elle inclut les observations des marégraphes répartis en cinq stations le long de l'estuaire : Saint Gildas, Saint Nazaire, Donges, Cordemais, le Pellerin et Nantes. Les mesures d'un ADCP et d'une sonde mouillés près du Croisic comprenant les courants, la température et la salinité durant neuf mois sont également exploitées pour la validation du modèle.

Le chapitre 4 analyse la circulation générale, la distribution des panaches de la Loire et de la Vilaine ainsi que les échanges de masses d'eau douce au niveau de différentes sections clés:

- séparant les estuaires interne et externe de la Loire,
- délimitant l'entrée de la baie de Bourgneuf,
- délimitant le Mor-Braz.

En particulier sont examinées la structuration surface/fond et la variabilité de l'intensité des échanges en fonction de la variabilité des forçages.

Le chapitre 5 est consacré à la caractérisation des échelles de temps de séjour ou d'échanges des masses d'eau, et en particulier de l'eau douce originaire de la Loire. Cette partie utilise deux concepts pour conduire l'analyse : le temps de résidence ou de renouvellement d'un secteur donné, et l'âge moyen d'une masse d'eau issue d'une source spécifique. L'étude se focalise notamment sur la baie de Bourgneuf et le Mor-Braz.

Nous concluons les résultats principaux dans une synthèse-conclusion pour finir avec quelques perspectives pouvant donner lieu à de futures études.

Chapter 1

Presentation of the study area

Introduction

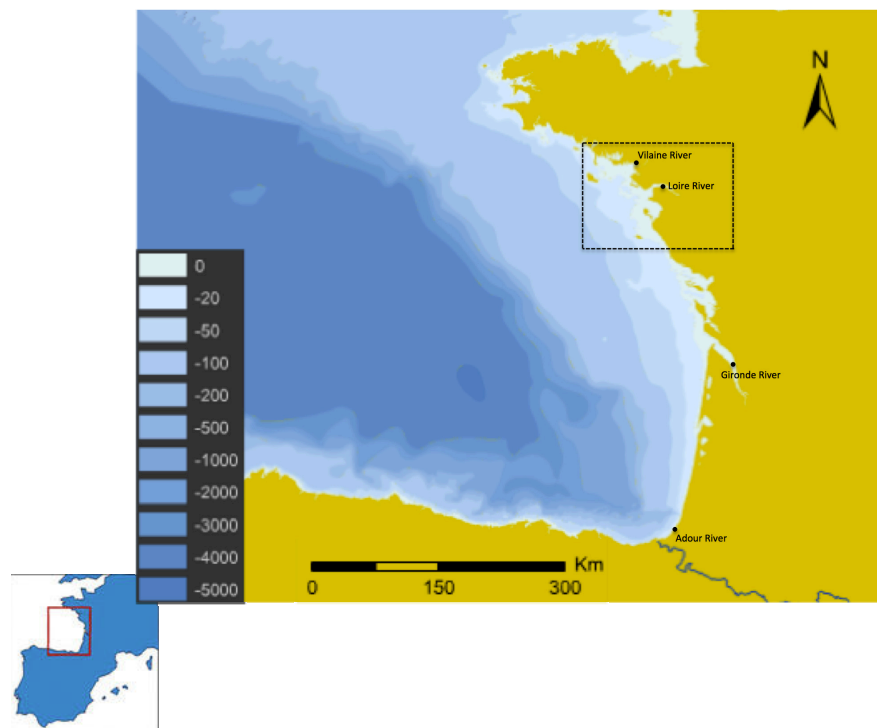


Figure 1.1: Bathymetry of the Bay of Biscay (ESRI, 2002), the dashed rectangle shows the study area and the points present the main sources of fresh water.

This work focuses on the river plume and the transport properties of dissolved substances among the Loire Estuary, the Bourgneuf and Vilaine Bays, located on the Atlantic coast of France (Bay of Biscay). These regions are characterized by an irregular coastline and bathymetry (Fig. 1.1). In this chapter the geographic location and basic characteristics of these places are presented as well as river discharges, hydrology, residual and tidal circulation, in order to provide a brief background on where the study has taken place. All these features

are first considered at the scale of the Bay of Biscay, and then described with more details for the different geographical entities of our study area.

1.1 The Bay of Biscay

The Bay of Biscay (Fig. 1.1) is opened to the Eastern part of the North Atlantic Ocean, bounded by the West coast of France and the North coast of Spain, forming a roughly triangular body with an area of about 223000 km². The Bay of Biscay is a complex oceanic domain divided into two parts, the continental shelf and the abyssal plain, which are distinguished by the difference in their depth orders of magnitude.

1.1.1 Physiography and Geomorphologic characteristics of the Bay of Biscay

According to Fig. 1.2, the principal features of the Bay of Biscay can be described by following three main regions characterized by different topographic conditions : the abyssal plain, the continental slope, the continental shelf.

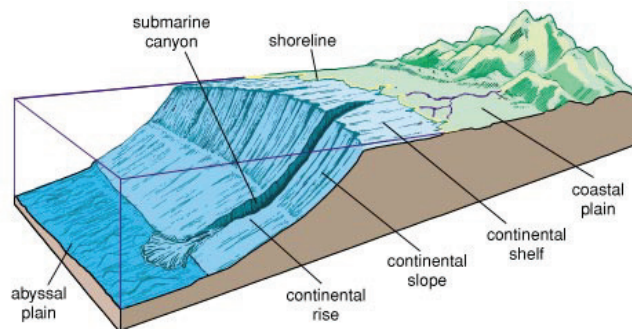


Figure 1.2: Schematic view of the abyssal plain, the continental slope and the Continental shelf in a coastal ocean (Britannica, 2011).

Abyssal plain

The Abyssal plain located in the central part of the Bay of Biscay is the deepest part with depths up to 5000 m, and is affected by the north Atlantic ocean circulation (see further in Fig. 1.8). The average circulation inside the Bay of Biscay remains weak ($1 \sim 2$ cm/s) following anticyclonic eddies (Pollard and Pu, 1985).

Continental slope and shelf

The continental shelf in the Bay of Biscay is commonly divided into two sections, the Armorican shelf and the Aquitaine shelf. The study area is connected to the Armorican shelf which extends from the English Channel entrance (north) to the Plateau de Rochebonne (south) (Lazure et al., 2008) (see Fig. 1.3).

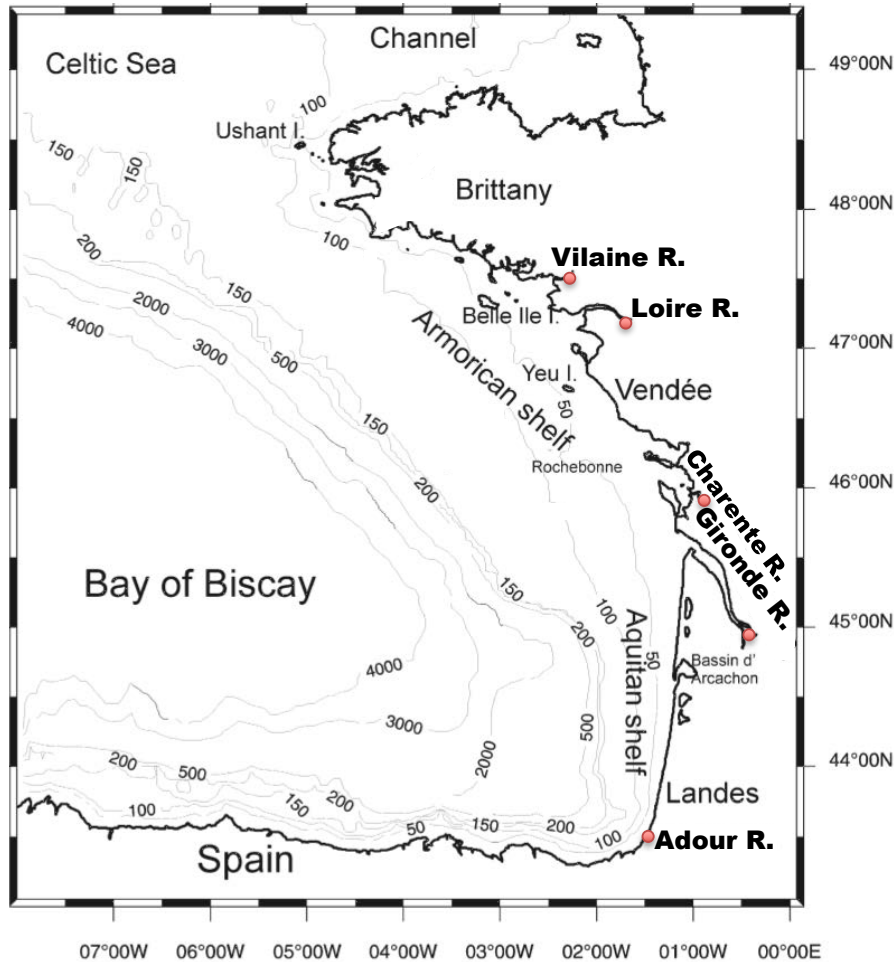


Figure 1.3: Map of the Bay of Biscay with bathymetric contour lines (isobaths) and main rivers (Lazure et al., 2008).

Here, we focus on the characteristics of water circulation over the Armorican shelf. The depth of the continental shelf varies from 10 to 200 m. The shelf is 150 – 180 km wide off the coast of Brittany with a gentle slope (OSPAR, 2010), while it narrows to 50 km in the southern region (Aquitaine Shelf). The shelf break begins at depths around 200 m, beyond which the bottom slope is steep and incised by canyons.

Bottom sediment

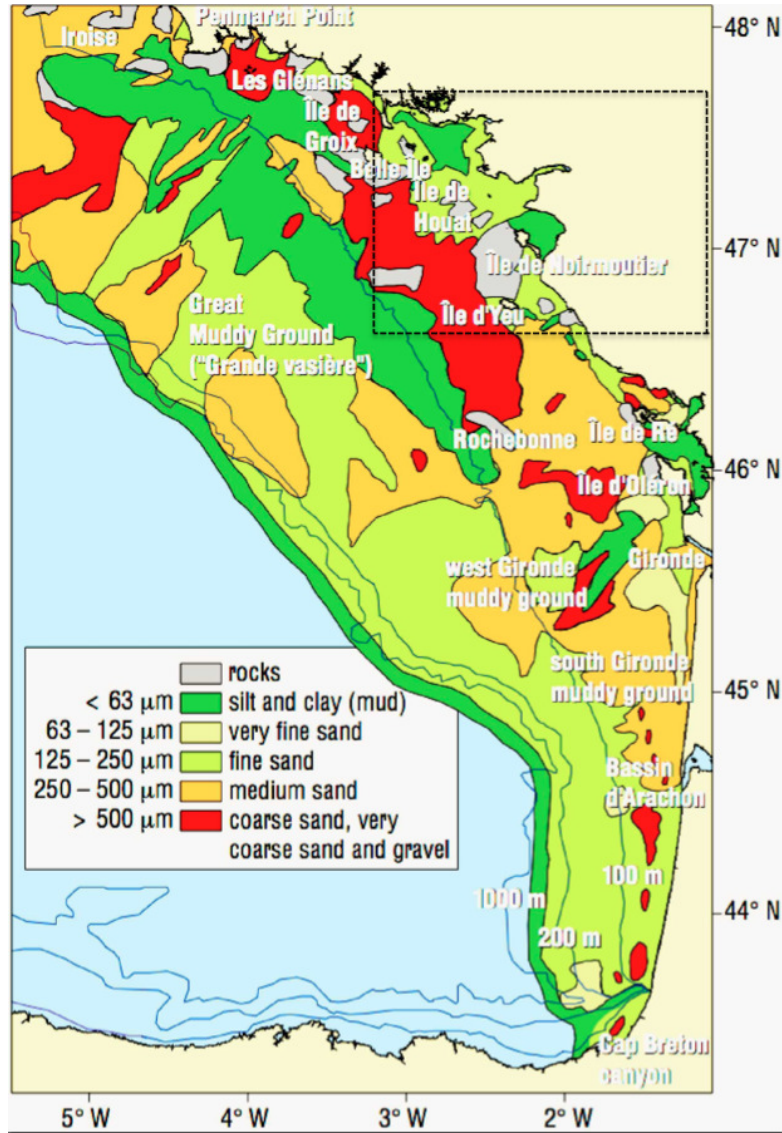


Figure 1.4: Bottom sediments on the continental shelf, French coast of the Bay of Biscay (Allen and Castaing, 1977), the study area of the present research is indicated by the dashed rectangle.

The bottom topography is an important means for identifying current and sediment dynamics (*i.e.* areas of sedimentation and erosion, and the routes by which sediments are transported) (OSPAR, 2010). The maritime area of the French Coast in the Bay of Biscay has a complex geomorphology, which is associated with a wide variety of sediment cover (see Fig. 1.4). According to Vanney (1977), the shape of the continental shelf and the configuration of deposits in the Bay of Biscay are issued from the succession of tectonic deformations and climate changes, with alternating transgressions and regressions of the sea level. The main sediment facies of the superficial layer are shown in Fig 1.4 (Allen and Castaing, 1977). The following descriptions are mainly from the explanatory note of this map and Vanney's

book (Vanney, 1977). The area is mainly covered by sandy and muddy sediments, 70% and 25%, respectively (Castaing and Jouanneau, 1987). In our study area, the bed of the deepest part is composed of coarse sand ($> 500 \mu\text{m}$), gravel and rocks. The main part, including the Loire Estuary and the Vilaine Bay is mostly covered by fine sandy sediments ($125 - 250 \mu\text{m}$). However, large muddy ($< 63 \mu\text{m}$), can be found in sheltered zones near the coast, in particular on each side of the Loire mouth.

However, there are two large areas with sandy-muddy sediments ($< 63 \mu\text{m}$), one on SE and the other on NW sides of the Loire Estuary.

1.1.2 Circulation forcing in the Bay of Biscay

1.1.2.1 Wind forcing

Wind forcing plays a major role on circulations over the continental shelf of the Bay of Biscay, particularly when river run-off is low and tidal forcing is weak (Lazure and Jégou, 1998). According to recent researches (Puillat et al., 2006, Lazure et al., 2008, Ferrer et al., 2009), the wind variability is very important over the shelf part of the Bay of Biscay and shows a significant seasonal variation (stronger winds in winter, weaker winds in summer). The above-mentioned researches also propose that short-term variations (meso-scales) can outweigh any seasonal trend. In addition, comparing average patterns with those of specific years reveals great inter-annual variability in the direction and magnitude of the winds for the same season reference (Charria et al., 2013). Northwesterly (NW) winds are prevailing from spring to late summer which pushes the plume southwards (Summer configuration). Winds forcing turns over to Westerly (W), South Westerly (SW) from autumn to late winter, which causes the river plume to accumulate at the coast (Winter configuration) and for a higher winter run-off a geostrophically balanced density current is associated with the high winter run-off (Le Cann and Pingree, 1995, Lazure and Jégou, 1998, Lazure et al., 2008).

In addition the drift induced by the wind in South-Brittany plays an important role on the dispersal direction of the Loire & Gironde River plumes (Lazure and Jégou, 1998).

1.1.2.2 Atmospheric heat fluxes

The Bay of Biscay is known as a region of weak net heat flux from the atmosphere to the sea (0.1 W/m^2 averaged between 1965 and 2004) (Large and Yeager, 2004), with a zero isoline usually lying around 45° N in the Eastern Atlantic (south of our study area), depending on the flux dataset. According to Michel et al. (2009a), the annual mean value of the heat flux is positive (heat gain to the ocean) close to the coasts in the western and southwestern part, particularly along the Iberian coast (up to 40 W/m^2), where cold upwelled water is warmed

at the surface. The flux is negative (heat loss from the ocean) over the Armorican Shelf and offshore the Aquitaine and Cantabrian slopes (down to -10 W/m^2) (Michel et al., 2009a).

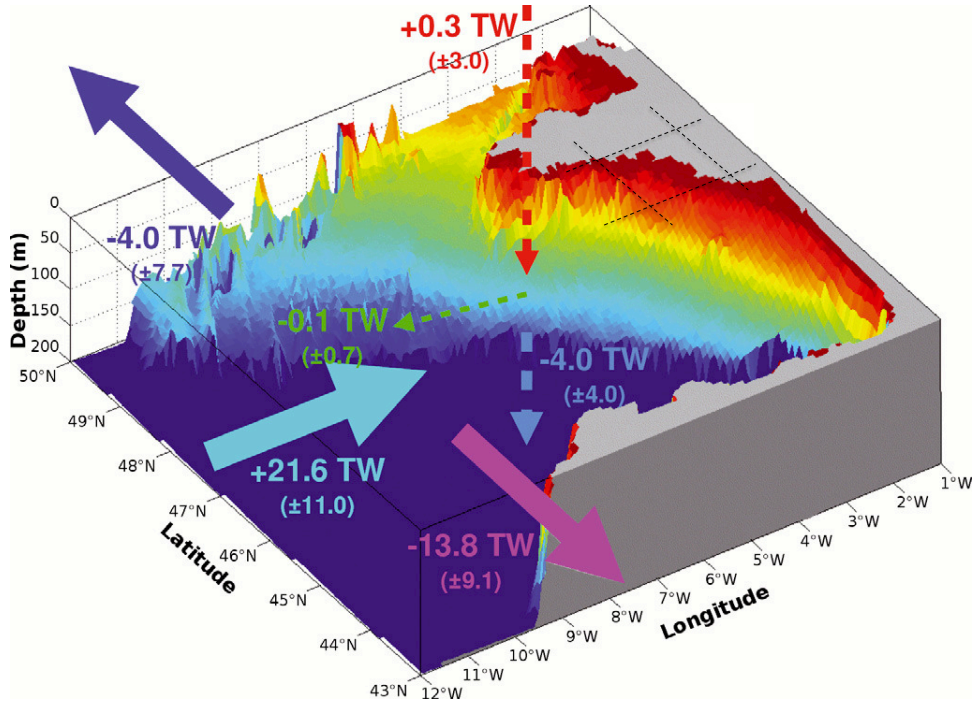


Figure 1.5: 3D simulation of thermal balance (or "heat budget") for the period 1965-2004 in the 0-200 m layer. Coloured 3D surface: bathymetry in the 0-200 m range. Arrows: heat inputs/outputs in terawatt (TW, 10^{12} watt) with standard deviations in brackets, dashed lines represent the study area in this research (Michel et al., 2009b).

The flux variability is also high over the Armorican Shelf and along the Cantabrian coast, where SST is essentially controlled by upwelling conditions. The variability of the sea-surface temperature is primarily controlled by air-sea fluxes (std. dev. = ± 3.0 TW). Over the Armorican and Celtic shelves, at the sea surface, the warming and inter-annual anomalies are stronger. When considering the whole depth of continental shelf the oceanic processes largely contribute to such variations. According to Michel et al. (2009b), during the 1965-2004 period, a huge quantity of heat is conveyed into the Bay of Biscay by the North Atlantic Drift (mean = $+22$ TW). Although most of this heat is evacuated by currents toward the south and north (mean = -14 and -4 TW respectively), a substantial part remains in the Bay of Biscay (mean = $+4$ TW). Almost all this excess heat is then conveyed downwards by vertical currents, heating deeper layers of the Bay of Biscay (see Fig. 1.5) (Michel et al., 2009b). The important point is that the details of the thermal balance depend on the location of the selected lateral boundaries of the domain; however, its qualitative features remain unchanged when shifting the limits (Michel et al., 2009a).

1.1.2.3 River inputs

Among a set of 23 rivers supplying freshwater in the Bay of Biscay, main rivers are the Loire and the Gironde, and secondarily the Vilaine, Charente and Adour rivers. The four rivers of Loire, Gironde, Vilaine and Adour represent 93% of freshwater inputs. These freshwater inputs from the main rivers (Loire, Gironde, Vilaine, Adour, Charente, plus Odet and Nive) have a total mean annual flow of $\sim 2500 \text{ m}^3/\text{s}$. The two major rivers (*i.e.* Loire and Gironde) account for 75% of freshwater inputs to the Bay of Biscay (Lazure et al., 2009). The annual mean outflow of the Loire and Gironde (see Fig. 1.3) is about $900 \text{ m}^3/\text{s}$ for each of them. Flow rates are maximum (Lazure and Jégou, 1998) in late winter and minimum in summer. In winter or spring the Loire and Gironde peak runoff may reach $5000 \text{ m}^3/\text{s}$ (e.g. in 2007 or 2009) and their minimum in summer is about $150 \text{ m}^3/\text{s}$ (eaufrance, 2007). The influence of other rivers such as Vilaine (mean outflow $70 \text{ m}^3/\text{s}$, exceeding $200 \text{ m}^3/\text{s}$ during floods) and Adour is less but still significant, particularly in their surroundings. Thus, all these river discharges can induce significant density currents (Lazure et al., 2009).

The two main rivers supplying the study area with freshwater are Loire and Vilaine. However, freshwater and inputs coming from the Gironde (in the South of the study area) also have significant influence in the study area and therefore should be taken into account. An overview of the main freshwater inputs is given in Table. 1.1.

| Name of river or group of rivers | Annual mean runoff in cubic metres per second |
|----------------------------------|---|
| Vilaine | 70 |
| Loire | 850 |
| Gironde | 885 |
| Adour | 315 |
| Northern Brittany | 35 |
| Southern Brittany | 360 |
| Basque rivers | 45 |

Table 1.1: Annual mean runoff of major rivers (Lazure et al., 2009).

1.1.3 Hydrology of the Bay of Biscay

1.1.3.1 Temperature

Water temperature over the continental shelf is homogeneous from the surface to the bottom during winter, although river contributions induce local heterogeneities, within depths

shallower than 80m, as shown in Fig. 1.6a & b, by results from the BOBYCLIM climatology produced by IFREMER (Vandermeirsch et al., 2010).

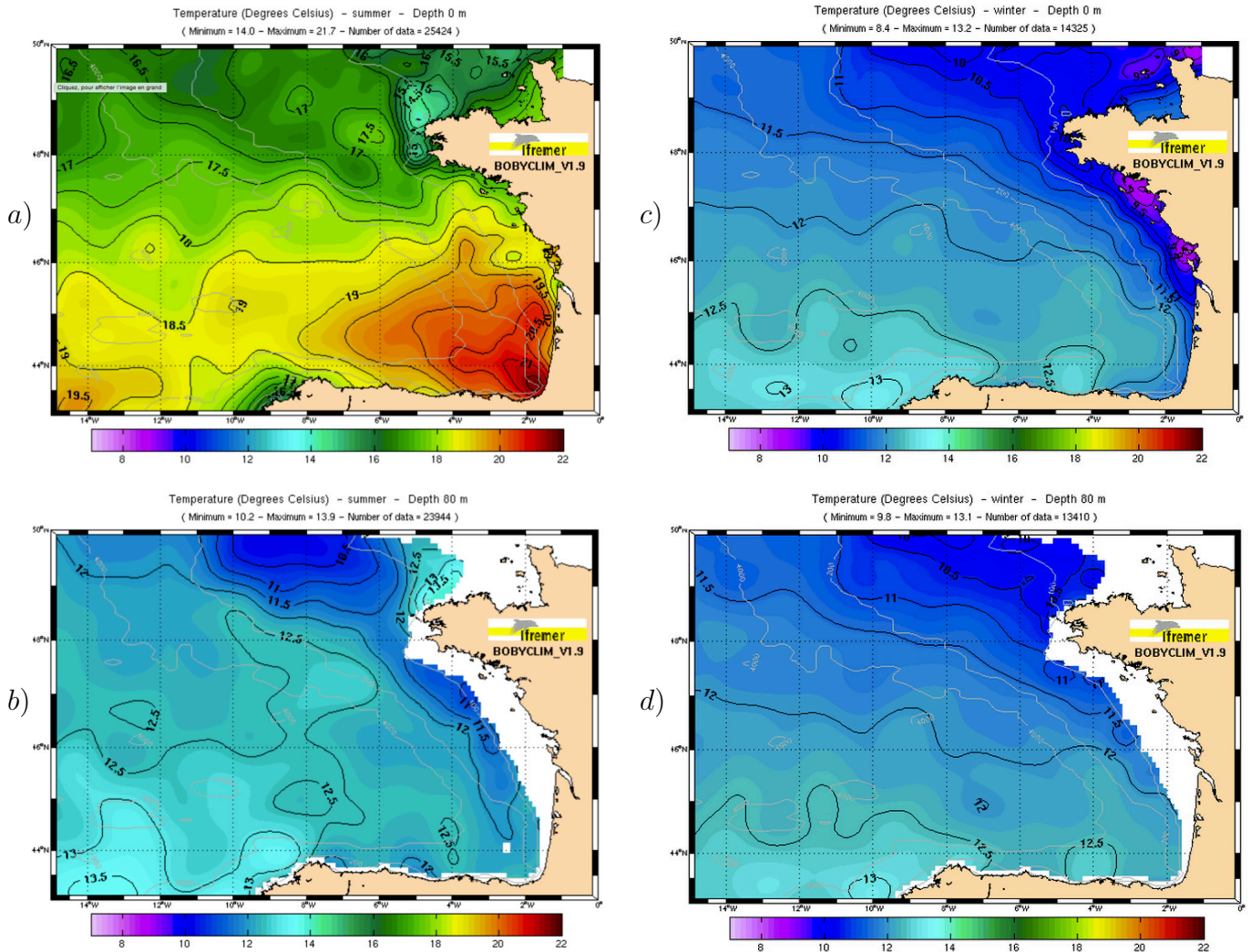


Figure 1.6: Average seasonal variations (summer and winter) of Temperature ($^{\circ}\text{C}$) in the Bay of Biscay (Vandermeirsch et al., 2010); a) surface water (summer), b) At 80m below the surface (summer), c) surface water (winter), d) At 80m below the surface (winter); data are taken from BoByClim climatology.

According to Fig. 1.6, it appears that water temperature over the continental shelf is no more homogeneous during summer and differences between the surface layer and the one 80 m below the surface can exceed 8 degrees, in relation with a strong rising of the surface water temperature from spring to late summer together with a low mixing of the water column in these areas. These stratifications are more significant in the south part of the Bay of Biscay.

In winter, the surface temperature over the continental shelf of Biscay Bay varies, on average, between 10 and 15 $^{\circ}\text{C}$ from North to South, with a minimum situated over the continental shelf, while in summer this interval becomes 11 to 22 $^{\circ}\text{C}$. According to Puillat (2004), the seasonal trend in temperature can be described in three stages (Puillat et al., 2004). First, a thermal stratification occurs between May and mid-September in a layer up to 80 m thick (see

Fig 1.6a & b), then a second period corresponds to the progressive destruction of the thermocline, this period occurring in the interval of mid-September to December. The third period is from January to the beginning of April when the water column remains homogeneous (see Fig 1.6c & d).

.5cm

1.1.3.2 Salinity variation

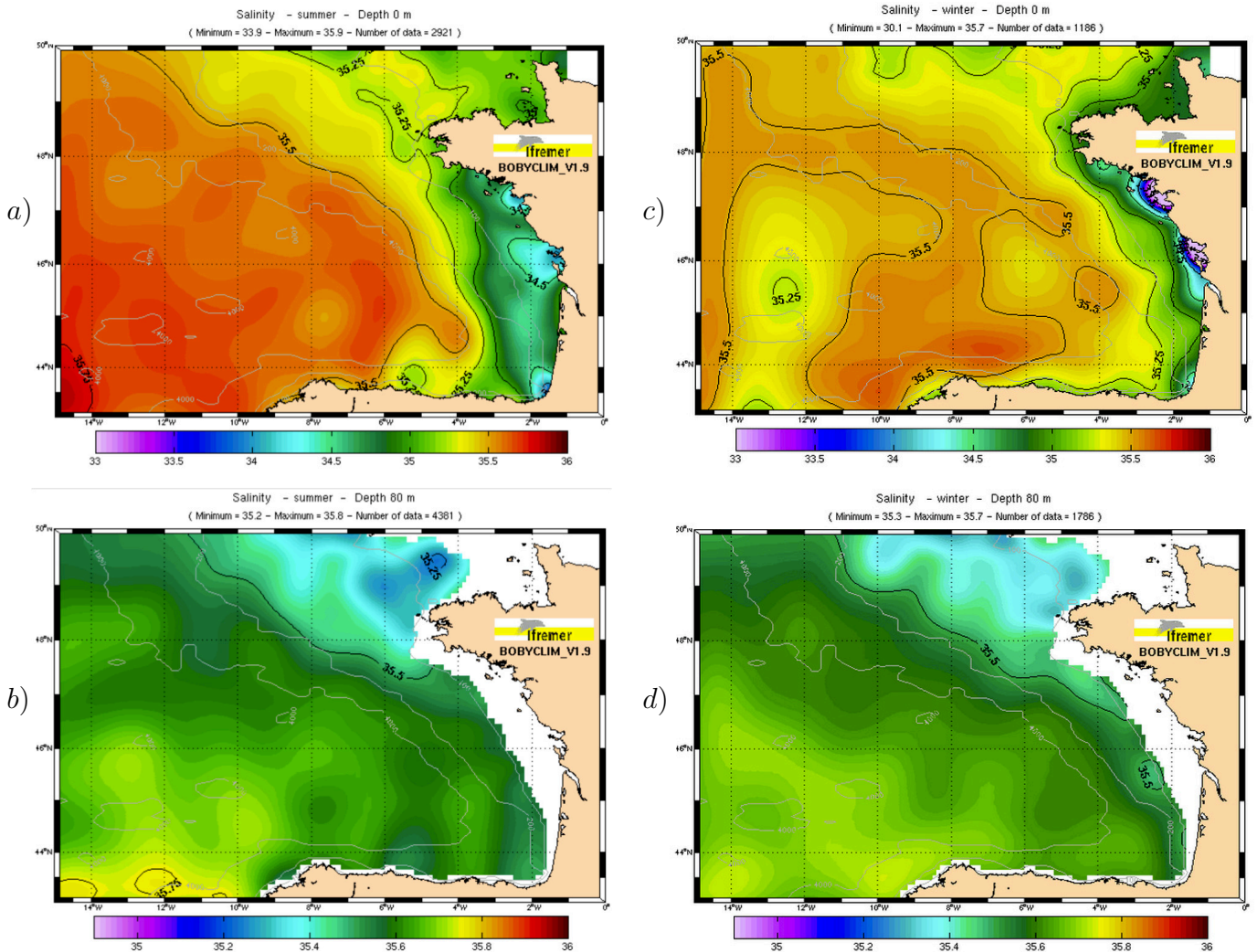


Figure 1.7: Average seasonal variations (summer and winter) of Salinity (PSU) in the Bay of Biscay (Vandermeirsch et al., 2010); a) surface water (summer), b) at 80m below the surface (summer), c) surface water (winter), d) at 80m below the surface (winter); data are taken from BoByClim climatology.

During winter, unlike temperature, salinity distributions are not the same throughout the water column (see Fig. 1.7c & d). In winter, a significant increase of river flows, generates an extension of low salinity plumes near the surface. Puillat et al.(2004) categorized the salinity distribution in two main seasonal patterns. During late winter and spring, the haline stratification is strong and waters of the southern French continental shelf often have a low surface

salinity for depths less than 100m because of high river run-off, especially from Loire and Gironde, and low vertical mixing.

Near the surface, low salinity waters usually extend further across the shelf, often reaching the shelf break (Castaing et al., 1999, Reverdin et al., 2013). Puillat et al.(2004) analyzed observations according to different spatial and temporal scales (inter-annual, seasonal and meso-scale), and conclude to an interdependence of processes at those scales to explain the salinity variations. The importance of meso-scale variability on the continental shelf hydrology has been highlighted by these observations. Winds' direction intensely influences the salinity gradients, particularly when it is upwelling favorable. In contrast stratifications are low during late summer and autumn, in response to low river discharge and wind-induced vertical mixing. Nevertheless, this seasonal signal could be biased by the high inter-annual variability (Puillat et al., 2004).

1.1.4 Circulation in the Bay of Biscay

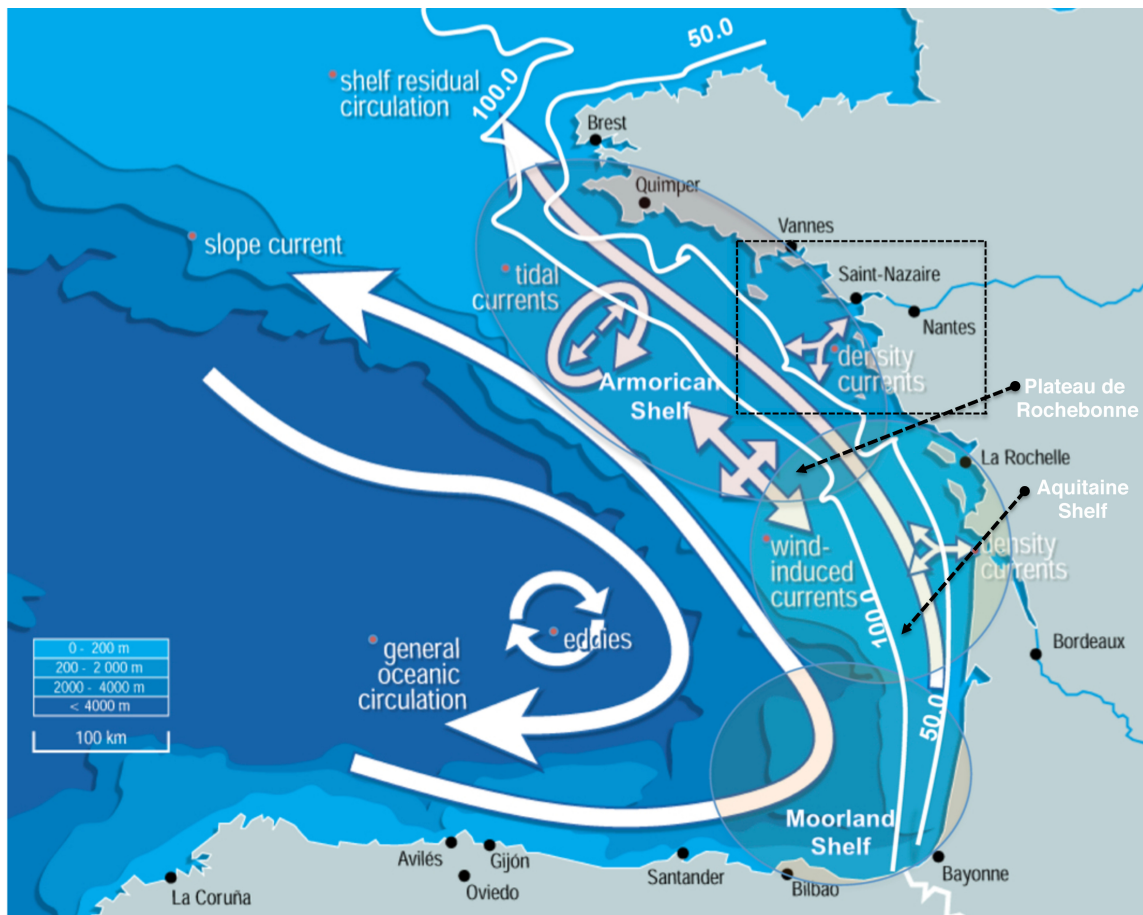


Figure 1.8: Schematic representation of circulation in the Bay of Biscay : general oceanic circulation, eddies, slope current, shelf residual circulation, tidal currents, wind-driven currents and density currents (modified from (Koutsikopoulos and Le Cann, 1996, OSPAR, 2010)); the rectangle with dashed line presents the study area

1.1.4.1 General circulation

Off the continental shelf, the mean oceanic circulation in the Bay of Biscay is characterized by a weak (1 – 2 cm/s) and variable anticyclonic circulation (Pingree and Le Cann, 1989, Koutsikopoulos and Le Cann, 1996)(Fig. 1.8). Van Aken’s work (van Aken, 2002) based on results provided by drifting buoys, has highlighted the seasonality of mean currents in the Bay of Biscay. In summer, the surface circulation in the deep zone is oriented South-SouthEast (average speed ~ 1.7 cm/s). In winter, the average flux is oriented mostly to the east (speed ~ 1.5 cm/s).

Fig. 1.9, highlights the different patterns of the surface currents in the Bay of Biscay and their main seasonal variation (Charria et al., 2013).

During autumn (October–November–December, see Fig. 1.9a), we notice a cyclonic dominant main circulation over the domain. Currents are flowing eastward south of the Bay of Biscay along the narrow Moorland Shelf. Averaged velocities observed are around 5-10 cm/s. On the Landes plateau, the current is transported northward, eventually derived from the northern Spanish slope area. In front of the Arcachon Bay and Loire Estuary, velocities (~ 3 cm/s) and associated errors are smaller (~ 2 cm/s) compared to the values over the abyssal plain and along the Spanish coast. Farther to the north, from the Rochebonne plateau to the South-West of Brittany, a North-Westward increasing current is observed, with speeds up to ~ 16 cm/s. According to Charria et al. (2013), this increase is associated with the inner branch of a cyclonic cell centered around 47° N, 5° W. The outer shelf branch of this cell is the South-Eastward current seen near 47.3° N. However, over the abyssal plain, the residual circulation remains South-Eastward. Over the continental slope, the mean current seems weak (~ 1 -3 cm/s). This might be an artifact as, for this time period in their dataset, trajectories are dominated by eddies in this region, hiding the residual circulation which then remains difficult to evaluate.

In winter (January–February–March), the overall circulation stays cyclonic with a poleward slope current better established along the Aquitaine and Armorican shelves (Fig. 1.9b). Velocities over the slope range from 3.5 to 7 cm/s, in agreement with previous observations (Pingree and Le Cann, 1989). Over the Aquitaine shelf, an intense mean poleward current (13 cm/s) is highlighted by drifter trajectories (Charria et al., 2013). Over the Armorican shelf, the cyclonic cell is still noticeable, weaker than in autumn. Close to the coast, greater uncertainties are due to the influence of a smaller scale dynamics (e.g. eddies generated by river plumes, tidal current variability, local bathymetry, local atmospheric forcing).

Within spring (April–May–June), the general surface circulation (Fig. 1.9c) is almost reversed with weak equatorward currents along the slope and over the Celtic and Armorican

shelves. Outside the continental shelf, the overall surface circulation in spring is mainly South-Eastward (south of 45.5° N) and closed with a return westward current following the Moorland shelf. Over the continental shelf, we can observe the signature of a South-Eastward current in the Celtic sea entering the Armorican shelf with a mean speed around 6 cm/s . Along the Aquitaine Coast, in the southern part of the Bay of Biscay, we perceive northward currents which are slightly oriented toward the coast. Indeed, the cross-shore component of the velocity is onshore (Fig. 1.9).

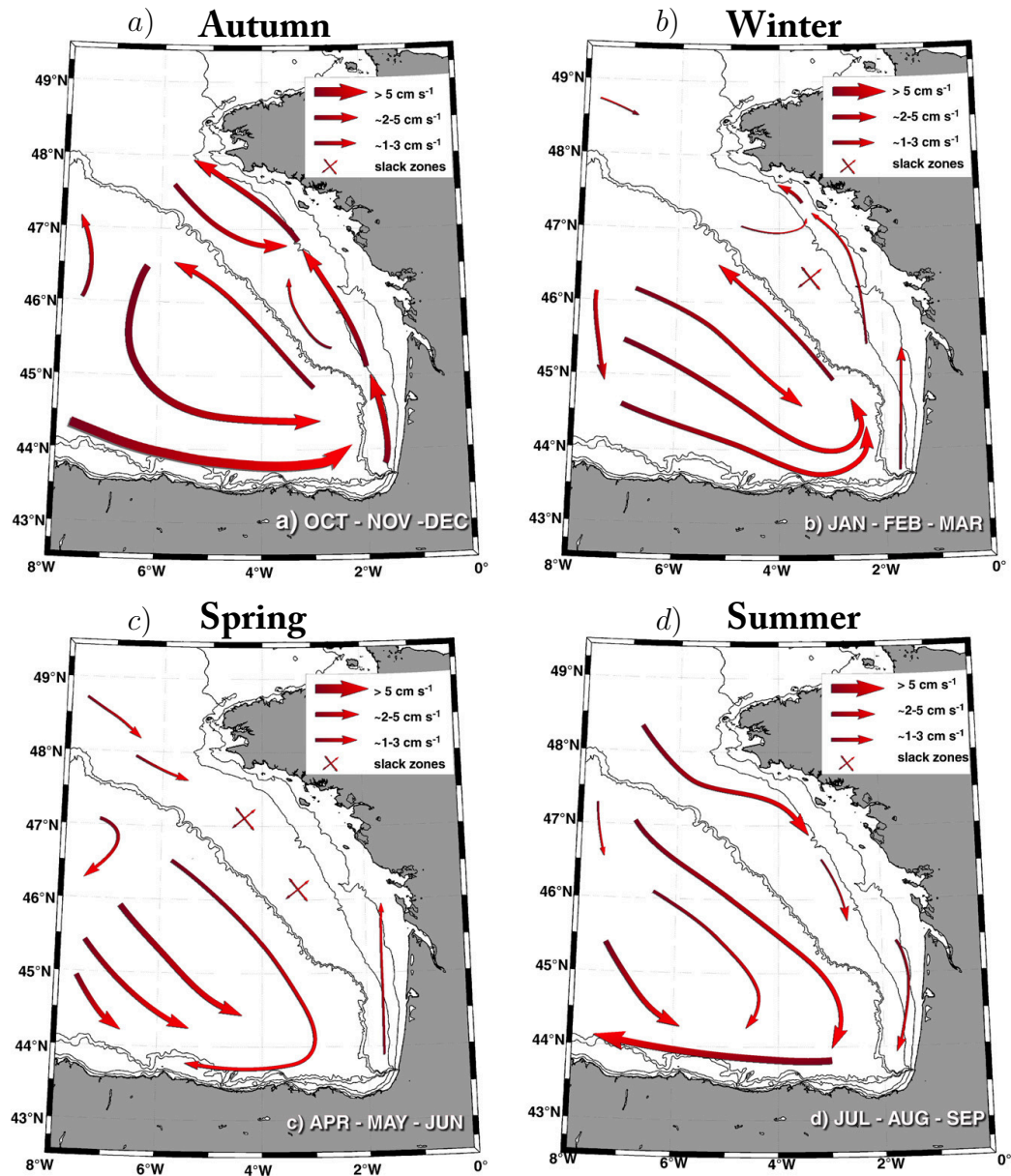


Figure 1.9: Seasonal climatology of the surface circulation in the Bay of Biscay: (a) Autumn from October to December, (b) Winter from January to March, (c) Spring from April to June, and (d) Summer from July to September. Black lines are representing 500 m, 200 m, 100 m and 50 m isobaths. Red thick vectors are used for current velocities larger than 5 cm/s . For lower current velocities $\sim 2 - 5$ and $\sim 1 - 3$, vectors are thinner (Charria et al., 2013).

Finally in summer (July–August–September), the general circulation on the abyssal plain remains anticyclonic with a dominant South-Eastward flow and a now established westward return current along the North Spanish slope, average speeds between 4 and 14 cm/s (see Fig. 1.9d). The main characteristic of summer circulation is the occurrence and extension of the South-Eastward current observed in spring on the Armorican shelf. Indeed, this branch is propagating into the Bay of Biscay to 47° N. South of this latitude, on the continental shelf, currents remain south-eastward and weak, less than 2.5 cm/s becoming important except in one region where drifters are quickly reaching the coast around 46° N (with speeds around 5 cm/s).

As stated by Koutsikopoulos and Le Cann (1996), the circulation over the shelf is mainly controlled by the wind and water density gradients, the role of tides becoming important in the northern part of the Bay. In general, we notice for different seasons the classical difference between weak current on the continental shelf and a more intense dynamics in the deep ocean. On the continental shelf at lower frequency than the semi-diurnal tidally driven circulation, residual currents are moving toward the Northwest on the Armorican shelf (Charria et al., 2013, Pingree and Le Cann, 1989).

1.1.4.2 Tides, tidal currents and tidal residual currents

The tidal wave enters the Bay of Biscay from the open Atlantic, crosses the shelf break perpendicularly and then is largely amplified over the shelf (Pairaud et al., 2008a, Pairaud et al., 2010). In the Bay of Biscay, tides are mainly semi-diurnal (M2) but the non-linear quarter diurnal wave (M4) component should not be neglected, and in certain zones, it is necessary to account for a hundred of wave components to obtain a precise tide forecast (Le Cann, 1990, Pairaud et al., 2008b). The tidal range is typically 2.5m off the shelf, and increases towards the coast, reaching about 4-5 meters on the North Biscay shelf (Tessier, 2006).

Maximum ranges occur in narrow passages (*e.g.* La Rochelle and the Loire Estuary) where they may reach 6m (OSPAR, 2010). Tidal currents are relatively weak on the abyssal plain but intensify while arriving on the continental shelf. Over steep slopes and around sharp shelf-breaks tidal oscillations may dominate the current dynamics. There can be also a contribution of internal tides.

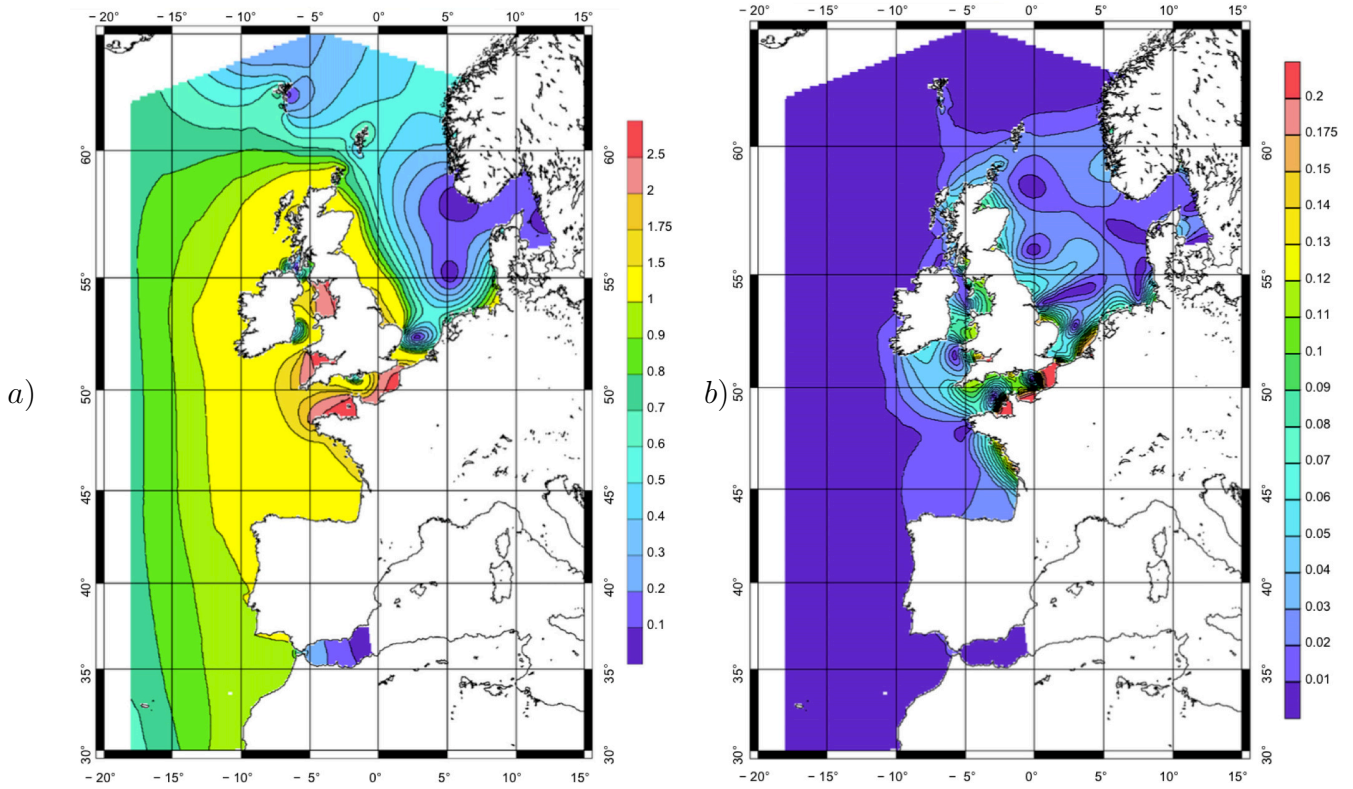


Figure 1.10: Amplitude of the M2 (a) and M4 (b) tidal components, computed with the T-UGOm 2D model (Pairaud et al., 2008b): (a) Amplitude of the M2 tide (b) Amplitude of the M4 tide.

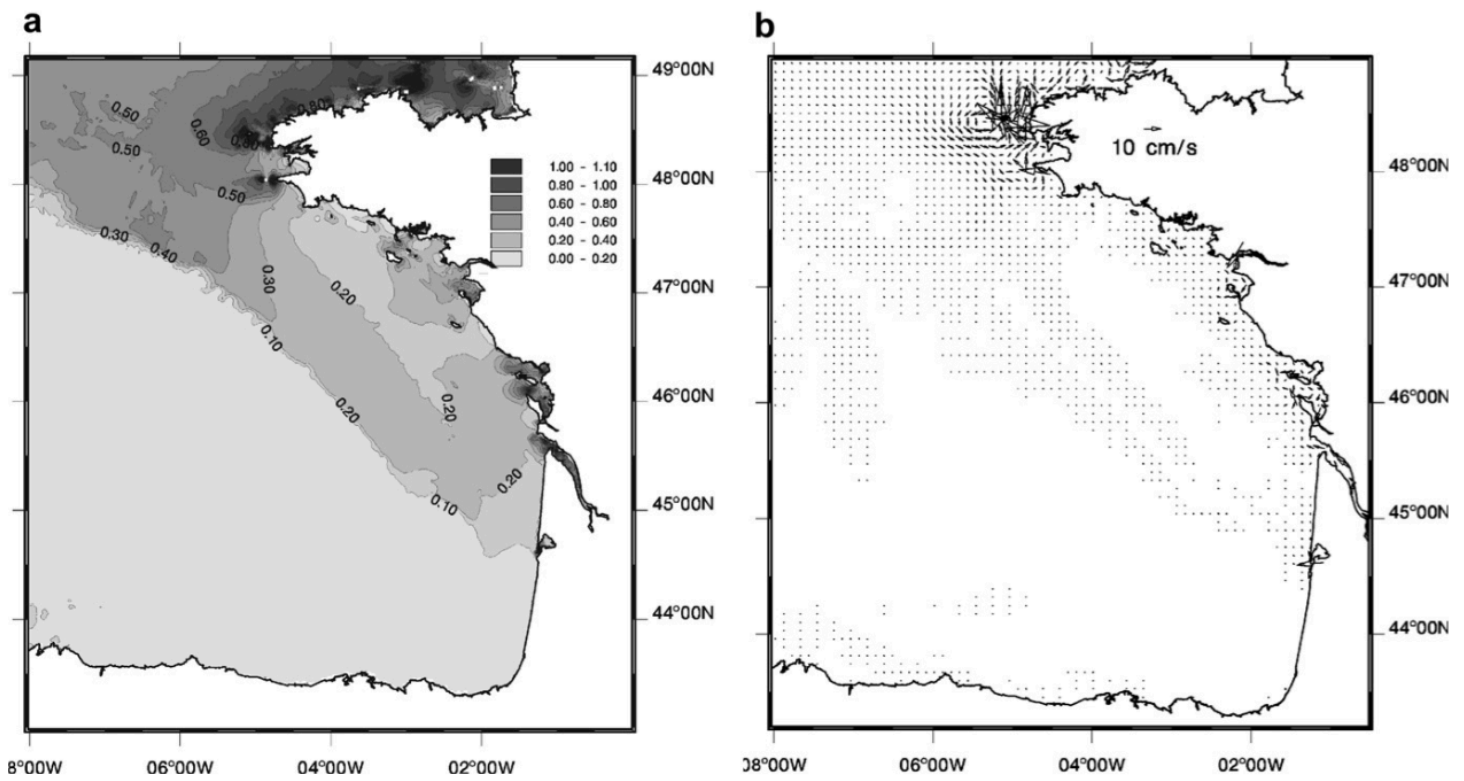


Figure 1.11: a) Maximum velocity during average spring tide. b) Tidal Eulerian residual current (Lazure and Dumas, 2008)

Tidal currents over the French shelf play a major role in water mixing and are likely to create thermal fronts between offshore stratified areas and alongshore vertically mixed areas where tidal currents are intensified (Le Boyer et al., 2009). This is the case in the Northern part of the Bay of Biscay (with a maximum at the Brittany head) (Salomon and Breton, 1993). However, in the southern part of the bay (south of $\sim 45^{\circ}\text{N}$) these currents are quite weak, less than ~ 15 cm/s (Le Cann, 1990). Tides interact with the topography and tidal currents are significantly amplified over the continental slope (Fig. 1.11a) during their propagation towards the shore (Jézéquel et al., 1998). The semi-diurnal component is higher over the north-west Armorican Shelf (~ 30 cm/s) (Puillat et al., 2004).

1.1.4.3 Density and Wind driven circulation

Dynamics over the continental shelf is much more variable than the one observed in the abyssal plain. On the continental shelf, the circulation is highly dependent on the combined effects of river discharges, tide and wind. In general, density gradients are generated by differences in both temperature and salinity. Density currents over the Continental Shelf are in the order of 2 to 10 cm/s and play an essential role on the water mass circulation where tidal residual currents are very weak (Pingree and Le Cann, 1989, Puillat et al., 2004, Puillat et al., 2006). According to the literature, significant density currents are often observed in the vicinity of estuaries, as rivers discharge freshwater into the surface layers (Wiseman and Garvine, 1995). The characteristic current structure is sea-ward near surface and land-ward near bottom mostly during the run-off period. Besides the density currents induced by river discharges are often modified by the wind-induced circulation. The highest salinity gradients in the Bay of Biscay are due to freshwater discharges from large rivers (Loire and Gironde) (Wiseman and Garvine, 1995). However, the temperature horizontal gradients can be sharper in the area of thermal fronts due to tidal vertical mixing on one side, or when upwelling is occurring, more often during spring and summer (Lazure and Jégou, 1998, Puillat et al., 2004). Generally speaking, the density gradients related to the freshwater discharge from rivers drive a poleward circulation in surface layers (about 10 cm/s) modulated by the wind forcing (Lazure et al., 2006).

This northward flow of both principal rivers (Loire and Gironde) alongside the coast is related to the influence of the Coriolis force : the form and spatial expansion of river plumes associated with density currents are under the influence of geostrophic forces (Jégou and Lazure, 1995, Puillat et al., 2004). Other rivers such as the Adour and Vilaine have less influence on the density currents. Mesoscale variability near the coast is mostly induced by the influence of wind forces on the river plume (Froidefond et al., 1996).

For instance, under specific conditions of winds (North-West or Westerly wind) river plumes can propagate towards the South-West (Charria et al., 2013). According to Lazure, in some

regions (deeper than 30 m), density gradients can also affect the sub-tidal (subsurface) transport by creating a baroclinic coastal current (Lazure and Jégou, 1998). On the other hand, the thermocline depth varies from 25 to 50 m. Some local thermal fronts appear during spring and summer. Conversely, a cold coastal strip appears in winter and early spring. This cold water is correlated with small depths and salinity patterns (Puillat et al., 2004).

In winter, the combination of high river discharges and dominant SW winds promotes a northward drift of plumes close to the coast, together with a decrease of their vertical stratification. When the river outflow slumps and the prevailing winds blow from the NW, the northward spread of plumes may be stopped and driven offshore or southwards; this occurs usually in spring (Puillat et al., 2004). The analysis of the wind-driven current on the Armorican and Celtic shelves shows a relatively rapid response of shelf waters to wind stresses (Puillat et al., 2004); among them the NW winds produce the largest wind-driven current (Pingree and Le Cann, 1989).

Upwelling and downwelling

According to Jégou and Lazure (1995), the south Brittany coasts are sensitive areas for upwelling. In spring, river discharge begins to decrease and dominant winds for upwelling (NW winds) produce strong vertical movement when tidal currents are weak until late summer (Puillat et al., 2006). On each side of the Loire Estuary and in agreement with Ekman's theory, upwelling events are not generated by the same wind directions because of different coastline orientations; NW to N winds induce upwelling in the south part of the Loire Estuary where the coastline is oriented N-S, while W to NW winds generate upwelling on the northern side of the Loire Estuary as the coastline is oriented NW-SE (Lazure and Jégou, 1998). Along these coasts upwelling and downwelling play an important role in the expansion of thermal and haline fronts.

Generally, during winter the winds often blow from the SW (downwelling favorable) and coincide with high river run-off, which plumes spread northwards and alongshore. On the opposite, during spring and summer, river discharges reduce and prevailing winds blow from the NW, constituting upwelling-favorable conditions. This is particularly the case along the Landes coastline and occasionally along the Southern region of Brittany coast) (Lazure et al., 2008). Then the northward spread of plumes may stop and shift southwards and mostly offshore (Puillat et al., 2004).

1.2 Study area

The study area is located in the north-east part of the **Bay of Biscay** (46.6 – 47.6 N, 2 – 3 W). The offshore part extends over a 120 km long strip of French Coastline from the Quiberon Peninsula to Yeu Island, located in front of the north coast of the Vendée region. The width of the study area is about 80 km off Saint-Nazaire harbor (Fig. 1.12). The continental shelf has a width of 160-180 km in the sector of our study. This region surrounds many different parts such as : the Loire Estuary, the bay of Bourgneuf, Noirmoutier and Yeu Island and the Mor-Braz area, which encloses the bay of Vilaine, the Morbihan Gulf and the bay of Quiberon, and is surrounded by Houat and Hoedic Island and the Quiberon peninsula.

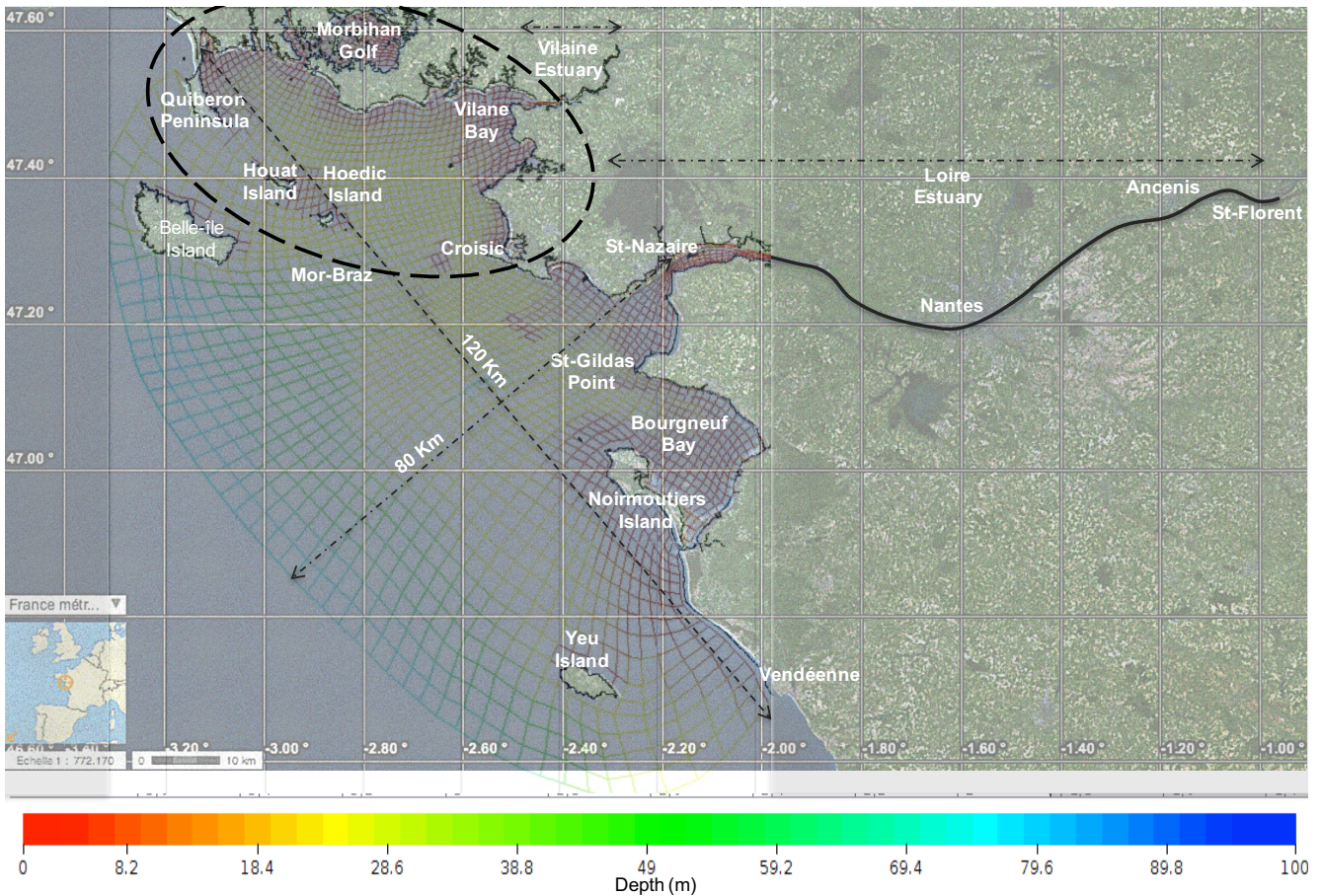


Figure 1.12: Presentation of the study area : Bay of Bourgneuf, Bay and Estuary of Vilaine, Morbihan Gulf, Quiberon Peninsula, Houat, Hoedic, Belle-Ile & Yeu Islands and the Loire Estuary from St-Nazaire to St-Florent.

Tidal currents are low (Fig. 1.13), less than 25 cm/s for the instantaneous currents in most part of the study area.

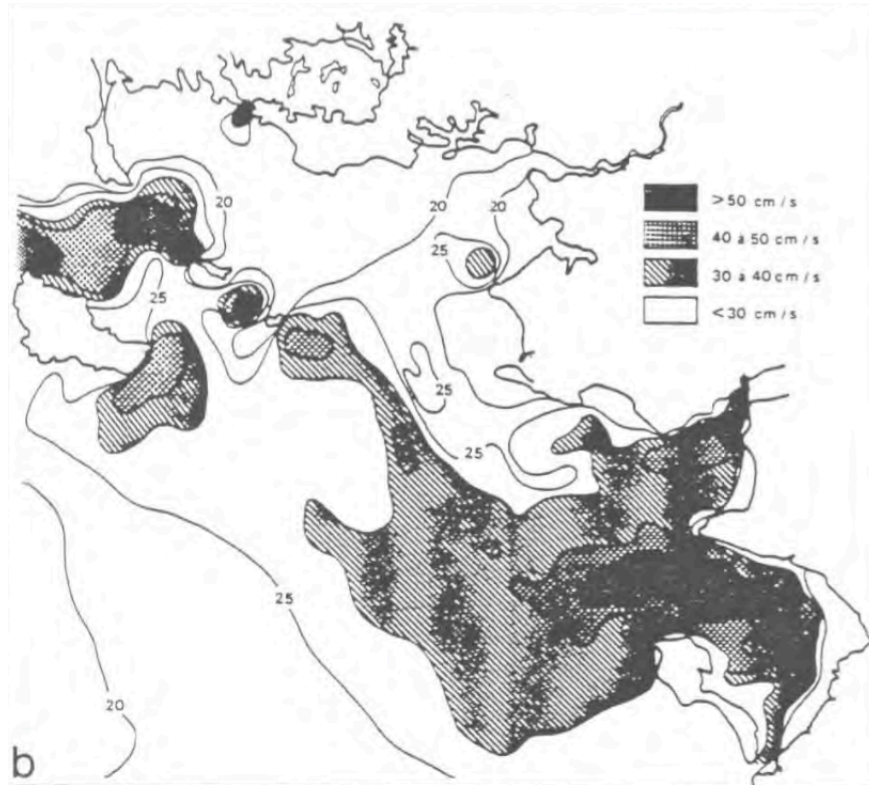


Figure 1.13: Instantaneous tidal currents in the area of Loire-Vilaine (Lazure and Salomon, 1991a).

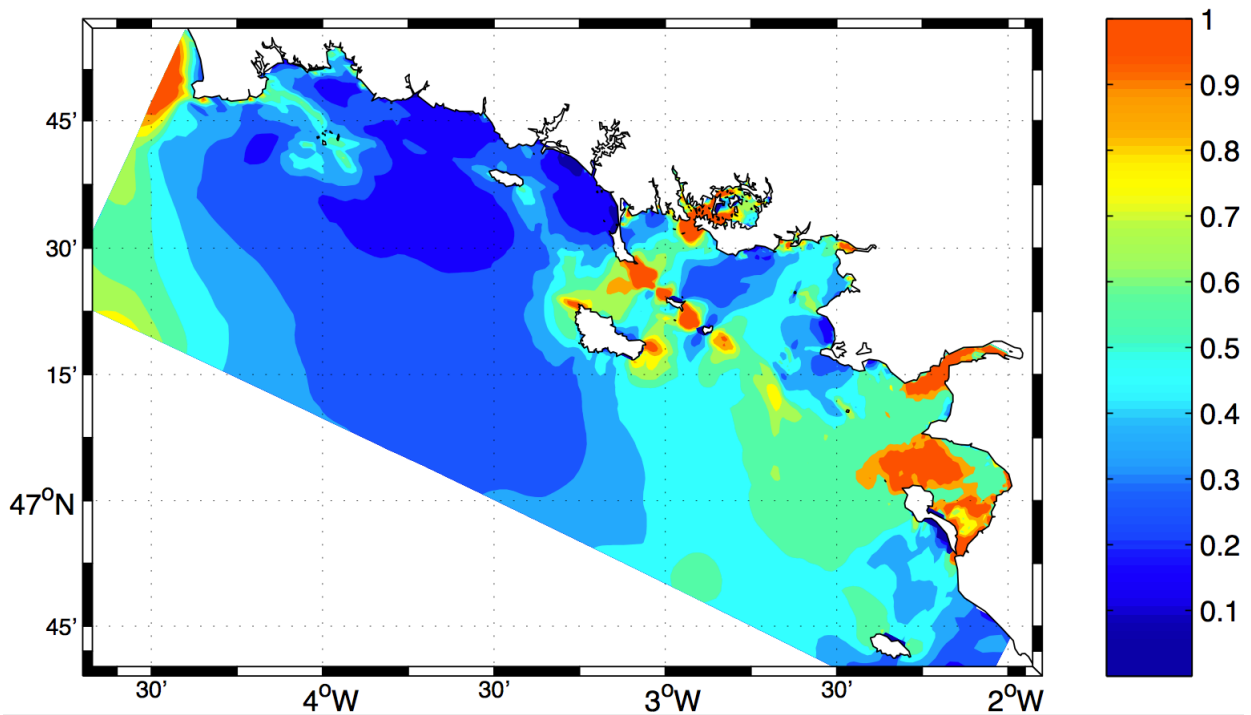


Figure 1.14: Maximum tidal velocity (m/s) of the depth-averaged current, for a mean spring tide (Tessier, 2006).

Along the south-Brittany coast and further southwards, maximum tidal currents can exceed

1.4 m/s locally, in the vicinity of the Loire Estuary, and around some islands (*e.g.* in La-Teignouse Strait between the Quiberon Peninsula and Houat Island); they even reach 4 m/s in narrow straits, like in the mouth of Morbihan Gulf (Le Cann, 1990).

Residual tidal current

During a tidal period, the advective effects of alternating tidal currents are likely to be cancelled, and tidally-averaged currents, also designated as residual currents, may inform on residual effects. The tide-induced residual component tends to be less than 1 cm/s over most part of the shelf, although locally it may be up to one order of magnitude higher. This is the case near the islands of Noirmoutier, Oléron and Ré, where it may reach 10 cm/s, then playing a major role in long-term transport (Lazure and Jégou, 1998).

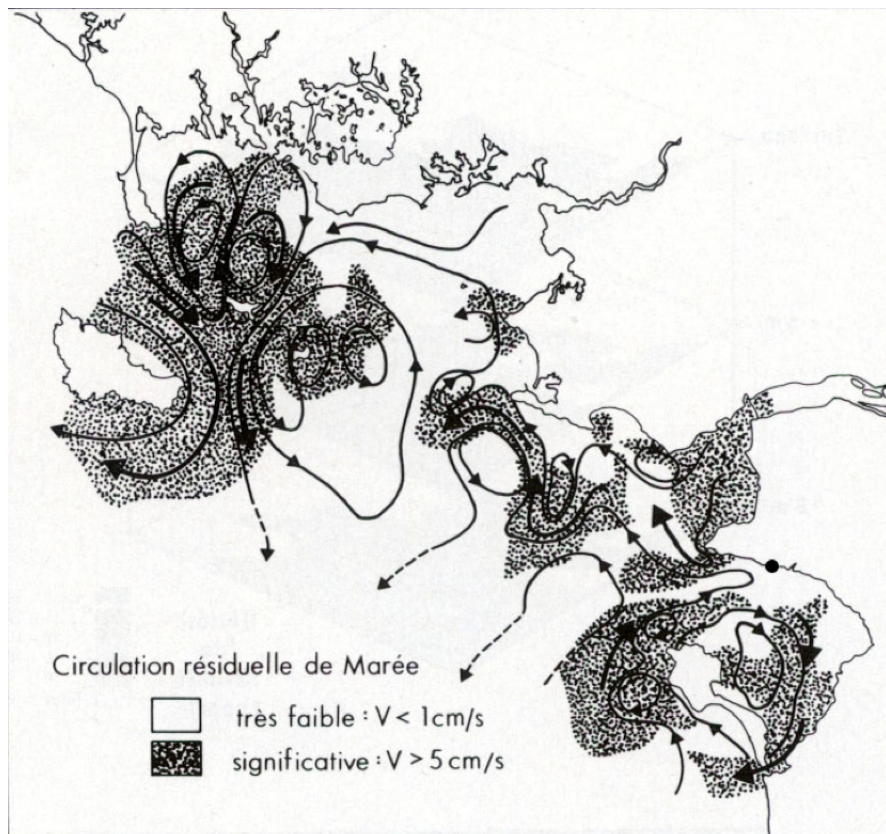


Figure 1.15: Residual tidal circulation in the area of Loire-Vilaine (Lazure and Salomon, 1991a)

In our study area, residual tidal currents are also weak, but can be significant in the vicinity of main islands such as Noirmoutier, Belle-Ile, Houat, Hoedic Islands and next to the entrances of the Loire Estuary and the Morbihan gulf (Fig. 1.15). As a result of these generally weak tidal residual currents, mean and long term, or large scale, water circulation is principally governed by wind-induced and density currents.

1.2.1 The Loire Estuary

The Loire Estuary is one of the largest French Estuaries. Its mean latitude and longitude are respectively $47^{\circ} 17'$ N and $2^{\circ} 7'$ W. The Loire Estuary is macrotidal. The river flow and tides induce large seasonal, fortnightly and diurnal salinity variations, a rather long flushing time and a developed turbidity maximum. Variations of these features are often cyclic and their magnitude depends on climatic conditions (rainfall, wind) (Figueres et al., 1985, Marchand, 1993).

The upstream source of the Loire Estuary is the Loire River, which is known as the last wild river in western Europe because there is no large dam to control the semi-natural condition of the river especially in the upper reaches. The Loire Estuary is known for sandy fluvial sediment import, but during the second half of the XX^{th} century large quantities of sand have been extracted from the river bed upstream the estuary, so that the net sediment input became mainly very fine.

During periods of average run-off, the suspended particulate load in the estuary varies from $0.05 e^6t$ on neap tides to $1 e^6t$ on spring tides, forming a turbidity maximum ; the difference can be explained by temporary deposits of fluid mud (1 to 3 m thick) on neap. At low run-off, this turbidity maximum extends over the estuary about 40 km; its upper limit is 80 km from the river mouth. Under flood conditions, these sediments are partly (30%) expelled from the estuary and the upper limit of the turbid maximum zone is only about 20 km from the river mouth (OSPAR, 2010). Sedimentation in the estuary has been influenced by various engineering works that have reduced the area of intertidal flats between Saint-Nazaire and Nantes by almost 30% between 1957 and 1990s (Migniot and Le Hir, 1997).

1.2.1.1 Physiography

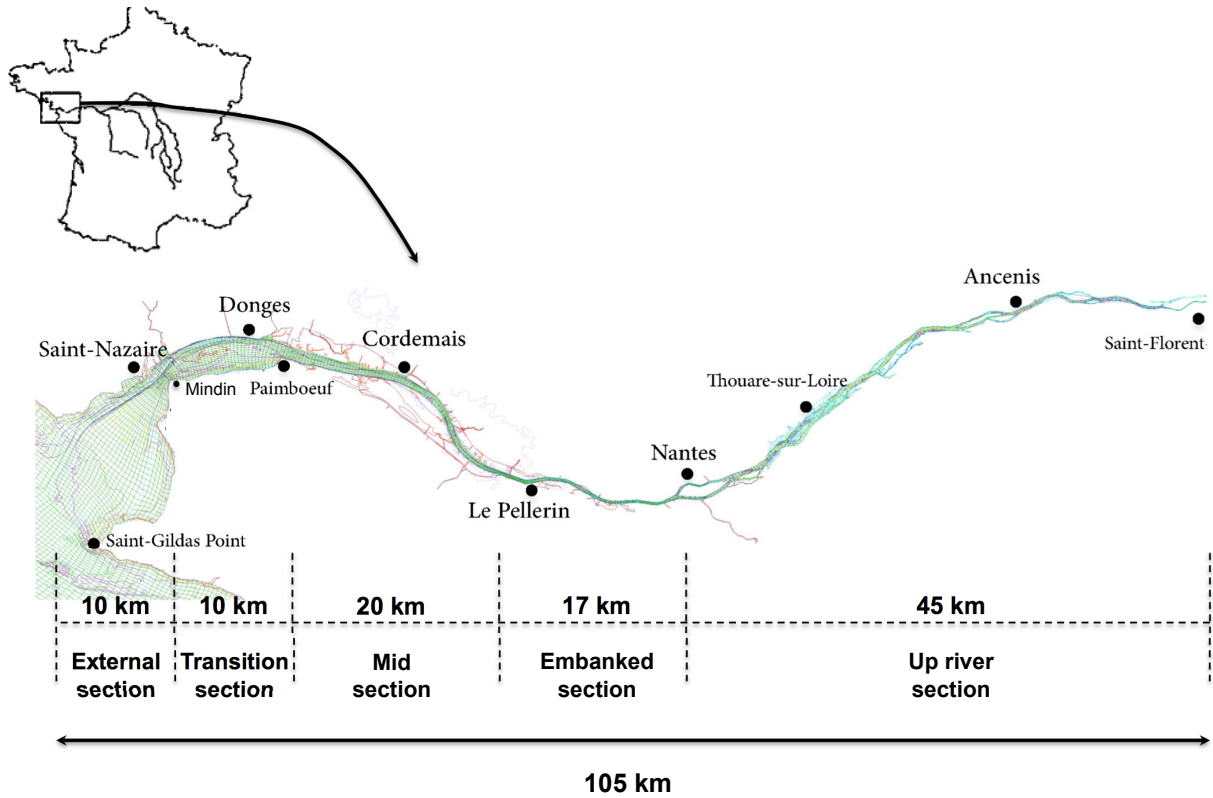


Figure 1.16: Study area : the Loire Estuary up to saint-Florent (tidal wave limit).

The whole area of the Loire Estuary is illustrated in Fig. 1.16, where St-Florent is the upper limit of the tidal wave. The length of the estuary exceeds 100 km from the outside limit of St-Gildas Point. Several harbors and cities are situated along both river banks. Most important ones are located on the northern bank such as Saint-Nazaire, Donges, Nantes and Ancenis (see Fig. 1.16). The width of the estuary is between 2 and 3 kilometres downstream, and gradually decreases (*e.g.* 300 m at le Pellerin). The estuary is navigable up to Nantes thanks to maintained channel.

The Loire River drains an area of 117054 km² (Rincé et al., 1985), which represents more than a fifth of France's land area. At the mouth, the tidal prism is estimated about 250 million m³ on spring tides.

Water circulation in the inner estuary is mainly through the channel. The penetration of tidal wave has progressed about 30 km upwards during the last 100 years because of dredging operations, either for deepening the navigation channel downstream of Nantes (Fig. 1.17) or for extracting sand materials upstream, where cross sections have increased fourfold (CSEEL, 1984).

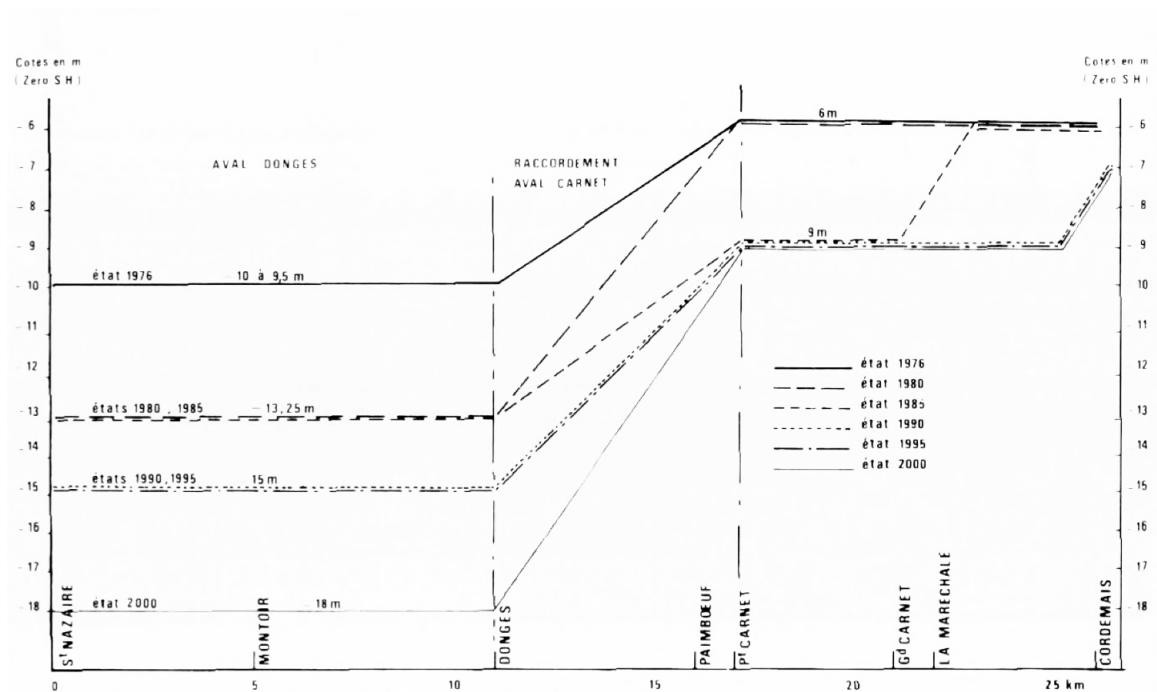


Figure 1.17: Evolution of the navigation channel depth in the last quarter of XXth century (by the time of the graphic drawing, the state "2000" was only "planned") (CSEEL, 1984).

In the lower reaches, downstream of Donges Harbor, the navigation channel is maintained below -13.25 m (with lower tide elevation at St-Nazaire as datum) while in the middle and the upstream part, the bottom depth becomes -6 m (Fig. 1.17), up to Nantes. On the north bank, between Donges and Cordemais, mudflats are present and experience a progressive infilling.

On the south bank, low levels mudflats extend from Paimboeuf to Mindin (Rincé et al., 1985). Between St-Nazaire and Donges harbors, the artificial Bilho Island extends over 3 km x 1 km (see Fig. 1.18). This island has been implemented for economical objectives (from navigation channel dredging). Water depths are contrasted on each bank of the Bilho Island.

This is not a permanent island, as it can be submerged during spring tide periods. Due to its large influence over current velocity and thus sedimentation processes in the Loire Estuary, this island have to be taken into account in our study.



Figure 1.18: Bilho Island in the Loire Estuary

1.2.1.2 Loire River regime

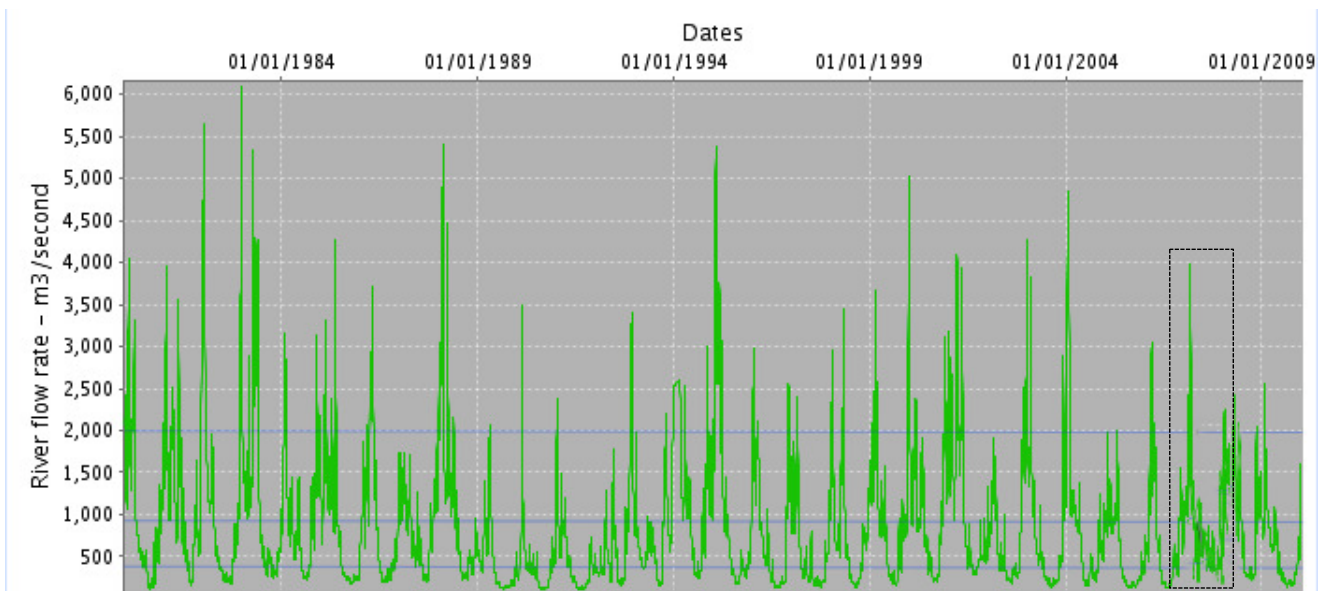


Figure 1.19: Loire river flow from 1980 to 2009 (data from measurements provided by the French freshwater office database), the selected period of this study (chapters 3 and 4) is shown by a rectangle.

The flow rate of the Loire River can vary between $100 \text{ m}^3/\text{s}$ at low regime to $5500 \text{ m}^3/\text{s}$ (see Fig. 1.19). For example, the recent flood of January 2004 peaked at $4900 \text{ m}^3/\text{s}$, while the river discharge reached $4000 \text{ m}^3/\text{s}$ in 2007 (simulated period of our study).

1.2.1.3 Tidal propagation and associated currents

Tidal forcing is the main hydrodynamic forcing in the Loire estuary. The tidal wave is semi-diurnal with a slight diurnal inequality (Figueres et al., 1985); tidal amplitude varies from

6 m in Saint-Nazaire to 7m in Nantes, and then decreases to 0.8m near Ancenis (Fig. 1.16), which ranks the Loire estuary among macro-tidal estuaries. According to Robin (1991), tidal currents in the main channel of the Loire Estuary can exceed 2 m/s.

Table 1.2 provides indications of low and high water levels for averaged spring and averaged neap tides, above a reference level selected as the lowest sea level at St-Nazaire. During the propagation upwards, the tidal curve deforms and becomes more asymmetrical, the duration of the flood being shorter and the duration of ebb longer (Fig. 1.20). This phenomenon is even more sensitive when the amplitude of the tide is greater and the average depth of the estuary is low, since the propagation speed depends on the water depth, inducing a faster propagation around High water level than around low water. Then the rising time is shorter than the falling one.

| Gauges Stations | HWs | | | LWs | |
|-----------------|--------------|------------|---------------|--------------|------------|
| | Spring tides | Neap tides | Average level | Spring tides | Neap tides |
| St-Nazaire | 5.5 | 4.2 | 3.15 | 1.9 | 0.6 |
| Paimboeuf | 5.6 | 4.3 | 3.15 | 1.8 | 0.9 |
| Le Pellerin | 5.8 | 4.5 | 3.15 | 1.8 | 1.5 |
| Nantes | 5.8 | 4.6 | 3.15 | 1.9 | 1.5 |

Table 1.2: Surface level for average tides (in m) (CSEEL, 1984).

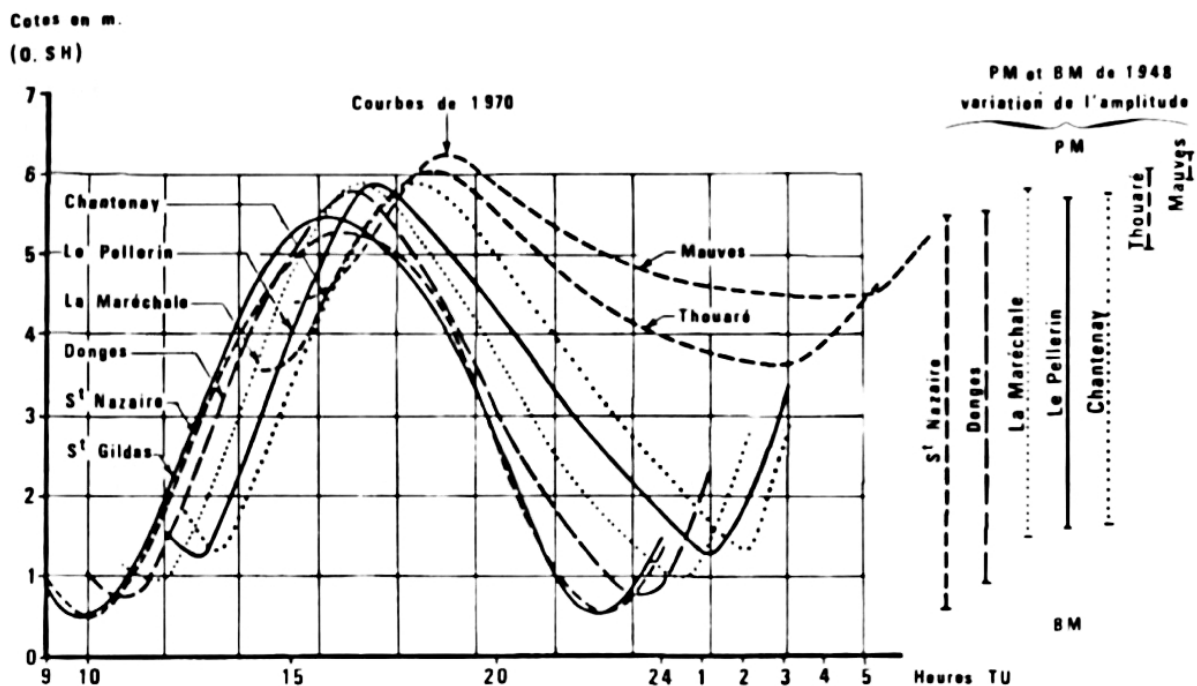


Figure 1.20: Propagation of a spring tide during low flows (CSEEL, 1984)

The tidal regime has a direct influence on the currents that can exceed 2 m/s during low water spring tide and reach even 3.7 m/s in exceptional flood (CSEEL, 1984).

1.2.1.4 Hydrology

The river flow is an important forcing that controls hydrodynamics, suspended matter load, dissolved nutrients concentration and oxygenation. The annual hydrological cycle is composed of two periods.

When the river discharge is low, the turbidity maximum shifts upstream and becomes longer, with higher suspended matter concentrations and depletion of dissolved oxygen in summer. In high river flow, the turbidity maximum shifts downwards and is less concentrated as cross-sections are larger, and concentration of dissolved oxygen is restored (Rincé et al., 1985).

The salinity distribution in the estuary depends on the river flow and the tidal amplitude, leading to a limit of salt intrusion not far from Nantes. Based on mean river flow conditions, the estuary can be divided into four major areas with different haline characteristics (Fig. 1.21). During the XXth century, changes in the tidal propagation induced a shift of the salinity front (0.05 PSU) up to Nantes. It is clear that the main cause of the shift of salinity front is the increased volume of the tidal basin upstream and probably downstream of Nantes (*e.g.* (Migniot and Le Hir, 1997)). In comparison, it seems that downstream engineering works carried out in 1984 (channel deepening to -13,25 m downstream of Donges (Fig. 1.17)) did not alter so much the tide propagation, and weakly affected the the salt-water intrusion (CSEEL, 1984).

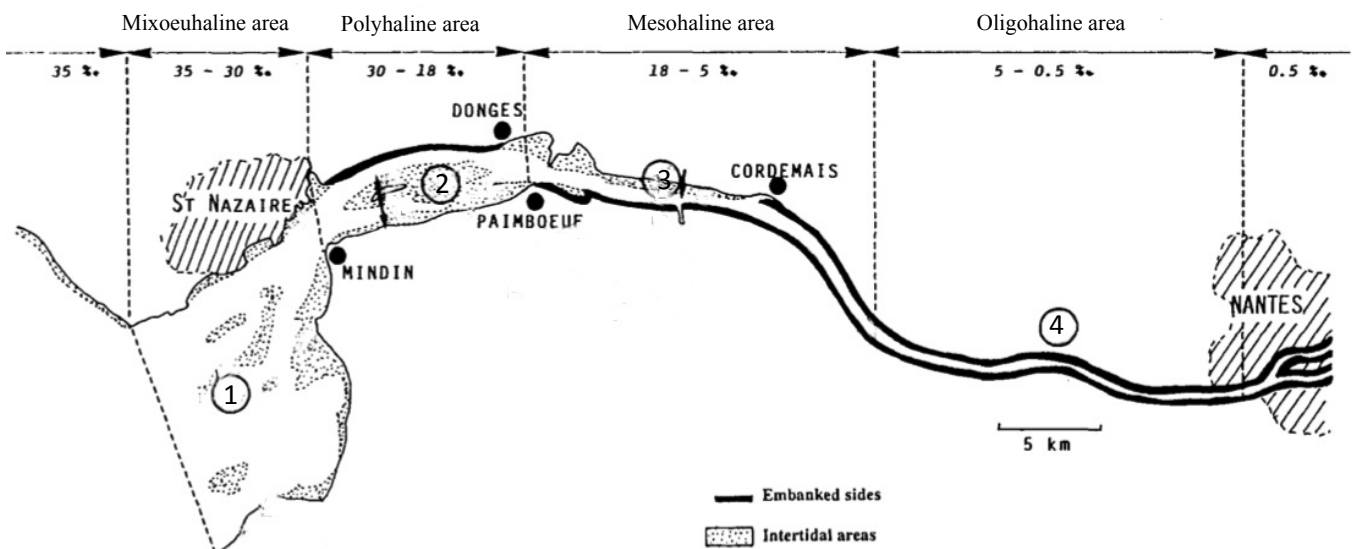


Figure 1.21: Map of the Loire estuary with averaged limits of haline areas (from Robin, 1991)

Near the estuary mouth, freshwater tends to flow in the surface layer while waters are saltier

near the bottom; the salinity (haline) stratification is maximum during large river discharge and neap tide. Due to density gradients, tide-averaged currents are directed downwards at the surface and upwards near the bottom. Out of the mouth, the Coriolis force is likely to induce a preferential expansion of the brackish water plume on the right hand side (*i.e.* to the north).

The residence time of fresh water (and associated dissolved pollutants) in the estuaries, is closely linked to the river discharge and varies from 0.5 days in high river regime (5000 m³/s) to almost 20 days during low river regime (70 m³/s) (CSEEL, 1984).

1.2.2 Bay of Bourgneuf

The bay of Bourgneuf is located south of the Loire Estuary mouth on the coastline of the "Pays de Loire" region. It extends between the Saint Gildas Head and L'Herbaudière Head on the Noirmoutier Island (Fig. 1.22) with latitude and longitude coordinates respectively in the range 46° 53' - 47° 6' N, 1° 58' - 2° 15' W.

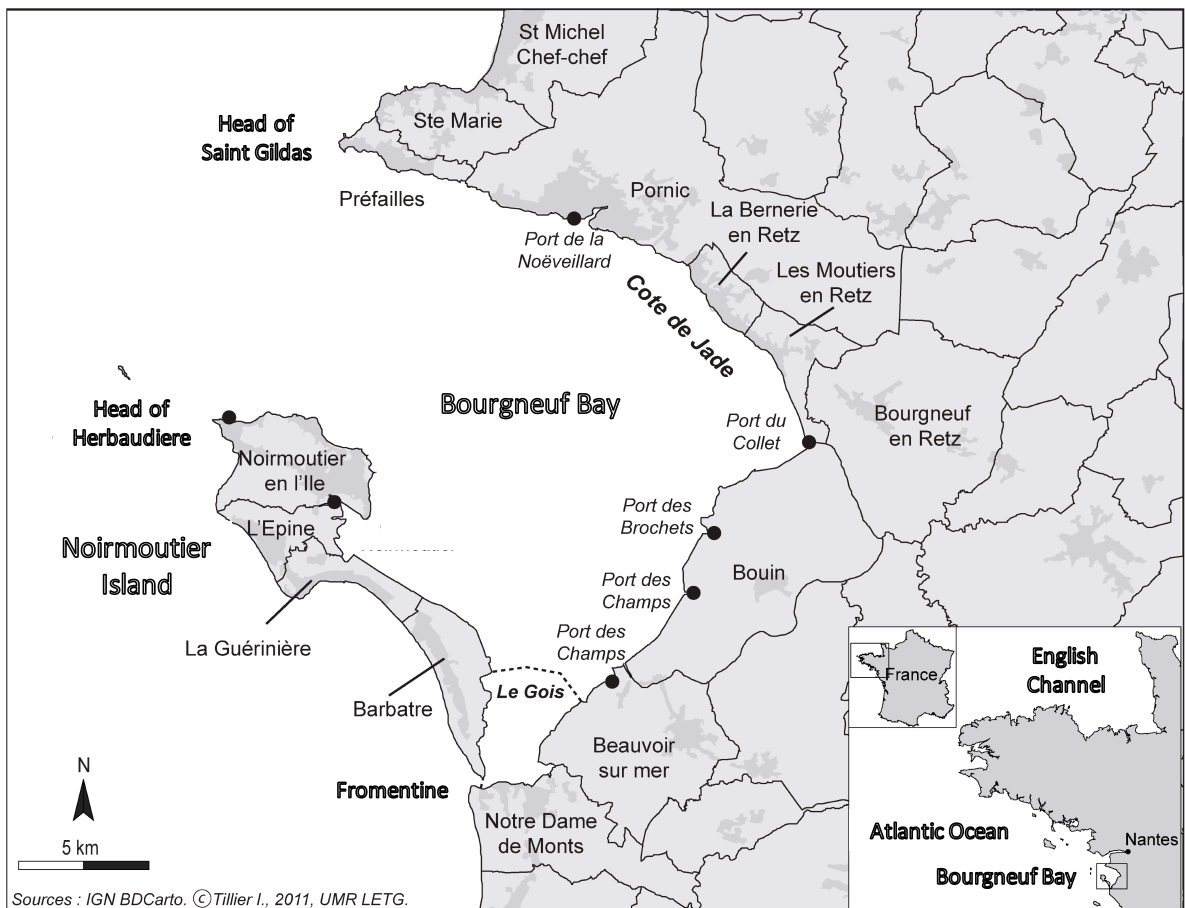


Figure 1.22: Bay of Bourgneuf (Robin, 2011).

1.2.2.1 Physiography

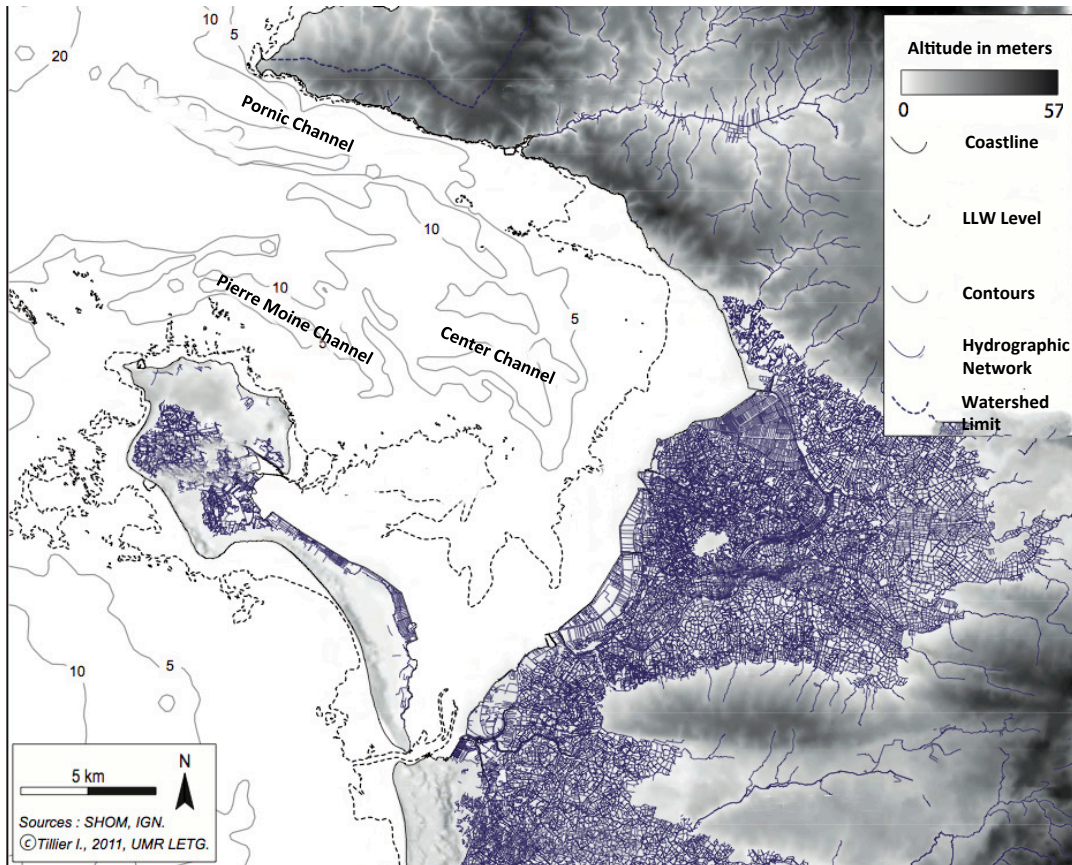


Figure 1.23: Topography, bathymetry and hydrographic network of the Bay of Bourgneuf (Robin, 2011).

The bay of Bourgneuf covers an area of approximately 340 km². It has a main oceanic opening on the North-west which allows important water mass exchange with the Atlantic Ocean. A secondary opening located in the south-west, is characterized by a width of 800 meters, the so-called Strait of Fromentine (Robin, 2011). The Bay is divided into two areas bounded by a rocky barrier-oriented from East to West (Fig. 1.24). Generally the North part is deeper, with a depth in the order of 15 to 20 meters near the entrance, while the southern part is characterized by shallow depths. The catchment area has low topographic amplitudes (the highest point is 57m NGF) (Fig. 1.23).

Direct freshwater inputs are low in the bay of Bourgneuf (Haure and Baud, 1995). The main tributaries are Falleron and Sallertaine Rivers that provide a daily average volume of water estimated about 85000 m³ (Lazure, 1992, Robin, 2011) and a dense network of creeks drain the lower part of the catchment area, as shown on Fig. 1.23.

1.2.2.2 Geology

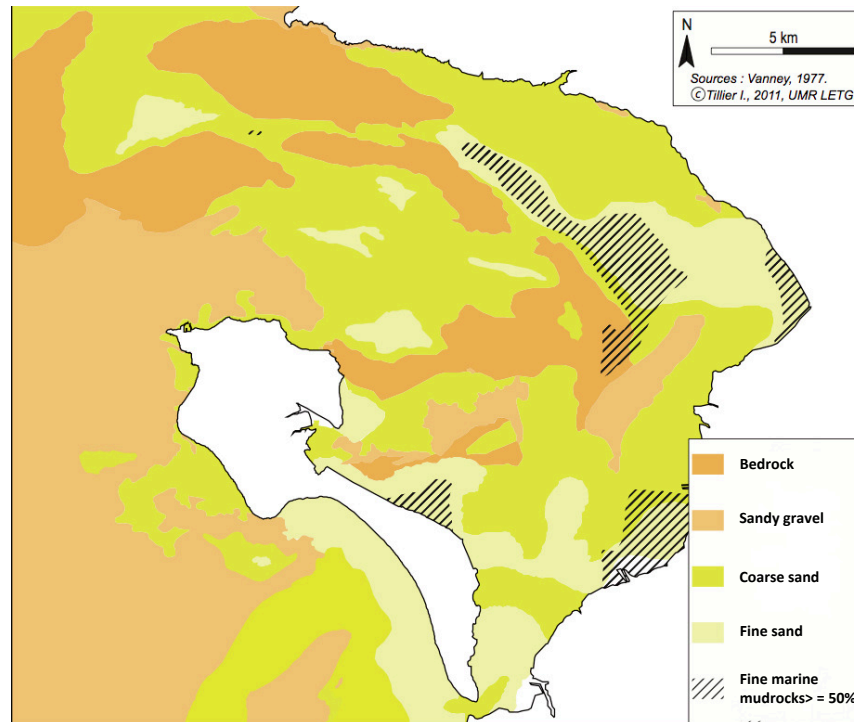


Figure 1.24: Sedimentological map of the bay of Bourgneuf (Vanney, 1977).

From a sedimentological point of view, the bay of Bourgneuf is mainly an accumulation field (Vanney, 1977). Apart from some rock sills, the nature of its bed is dominated by sediments ranging from coarse sand to mudflats (Fig. 1.24).

The sediment mobility due to various sea conditions and seasonal changes makes recognition of fine sediment fraction difficult in this bay (Dussauze et al., 2009, Ifremer, 2010b).

1.2.2.3 Residual tidal circulation

The Bay of Bourgneuf is macrotidal with a maximum tidal amplitude of 6 m during spring tides (Mélédér et al., 2007). Lazure (1992) has presented, a hydrodynamic scheme of the bay of Bourgneuf in which the residual tidal currents are categorized in 7 zones (Fig. 1.25). In the one labelled "1", S-W of Noirmoutier Island, residual currents are weak, and their directions are determined by meteorological conditions. The second zone, N-W of Noirmoutier, experiences a very short flushing time (3 to 5 days) which feeds (inward) the bay, except when the winds blow in the opposite direction. The residence time in the area "3" is estimated two weeks. This sector appears independent of the littoral area (east coast of the bay exhibited by dashed line) if weather conditions are calm, and water masses are well mixed despite the depths. Zone "4" presents the fastest renewal of the bay since water mass passes through this sector in 2 to 4 days depending on the tidal amplitude (Haure and Baud, 1995).

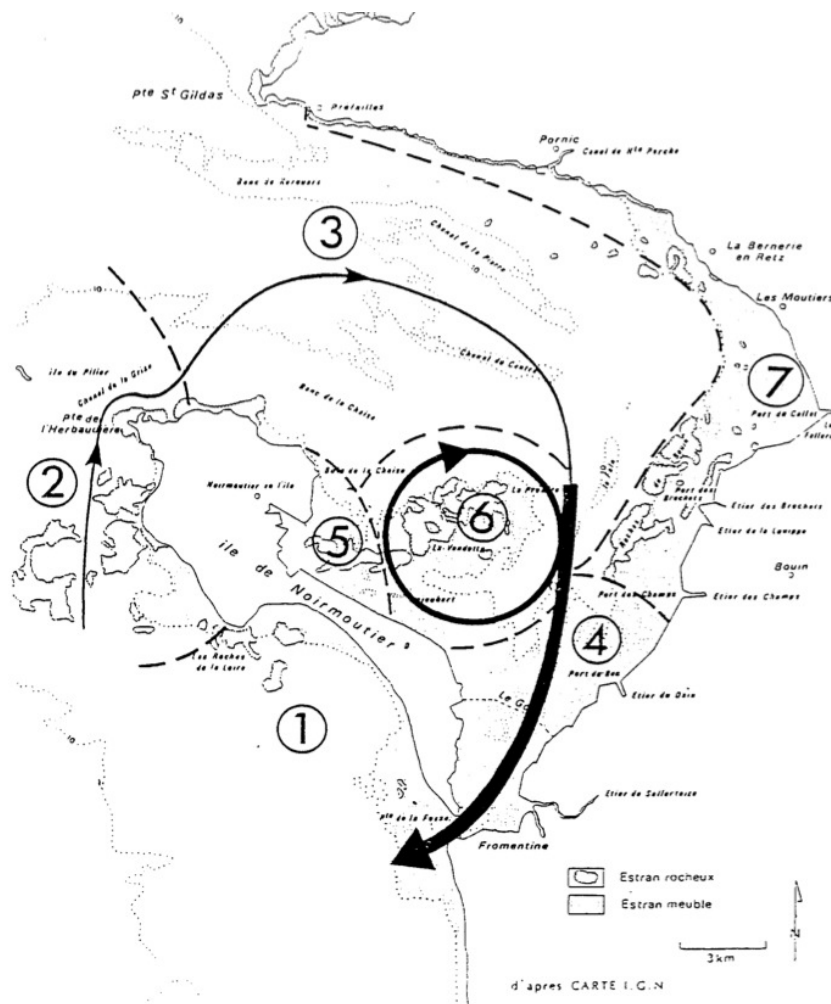


Figure 1.25: Main features of the tidal residual circulation in the bay of Bourgneuf (Lazure, 1992).

The fifth area called Noirmoutier Bay, in which residence time is longer in comparison with other parts of the bay, is more sensitive to pollutant discharges into the front part of Noirmoutier. The sixth one is a very homogeneous area whose water mass renewal is longer than other parts. Water comes from offshore and spread southward more or less quickly, depending on the amplitude and direction of the wind. The seventh zone includes intertidal areas of the east coast of the bay. Residence time is rather larger here and makes this sector very sensitive to freshwater input from Haute Perche and Falleron channels during calm weather (Lazure, 1992).

1.2.2.4 Water quality and turbidity

The effect of tidal wave on water quality in the bay of Bourgneuf is characterized by turbidity ranging from low to high levels: 4 to 415 mg/l as daily average values, reaching a maximum of 1000 mg/l during spring tides, because of strong tidal currents (Haure et al., 1996). Haure and Baud (1995), have shown that the annual depth-averaged concentrations of suspended particle are higher in the northern part of the bay (154 mg/l) than in the southern part (34

mg/l).

The northern sectors are characterized by high variability of particulate inorganic and organic matter. In contrast, the southern sites would be significantly different and characterized by stable environmental parameters and low particulate matter concentration during the year (Haure and Baud, 1995). The water quality in the bay of Bourgneuf is strongly related to the contributions of the Loire River discharge (Sanchez et al., 2008), especially next to saint-Gildas head at the southern outer of Loire Estuary.

1.2.3 Mor Braz (including the Bay of Vilaine, the Morbihan Gulf and the Quiberon Bay)

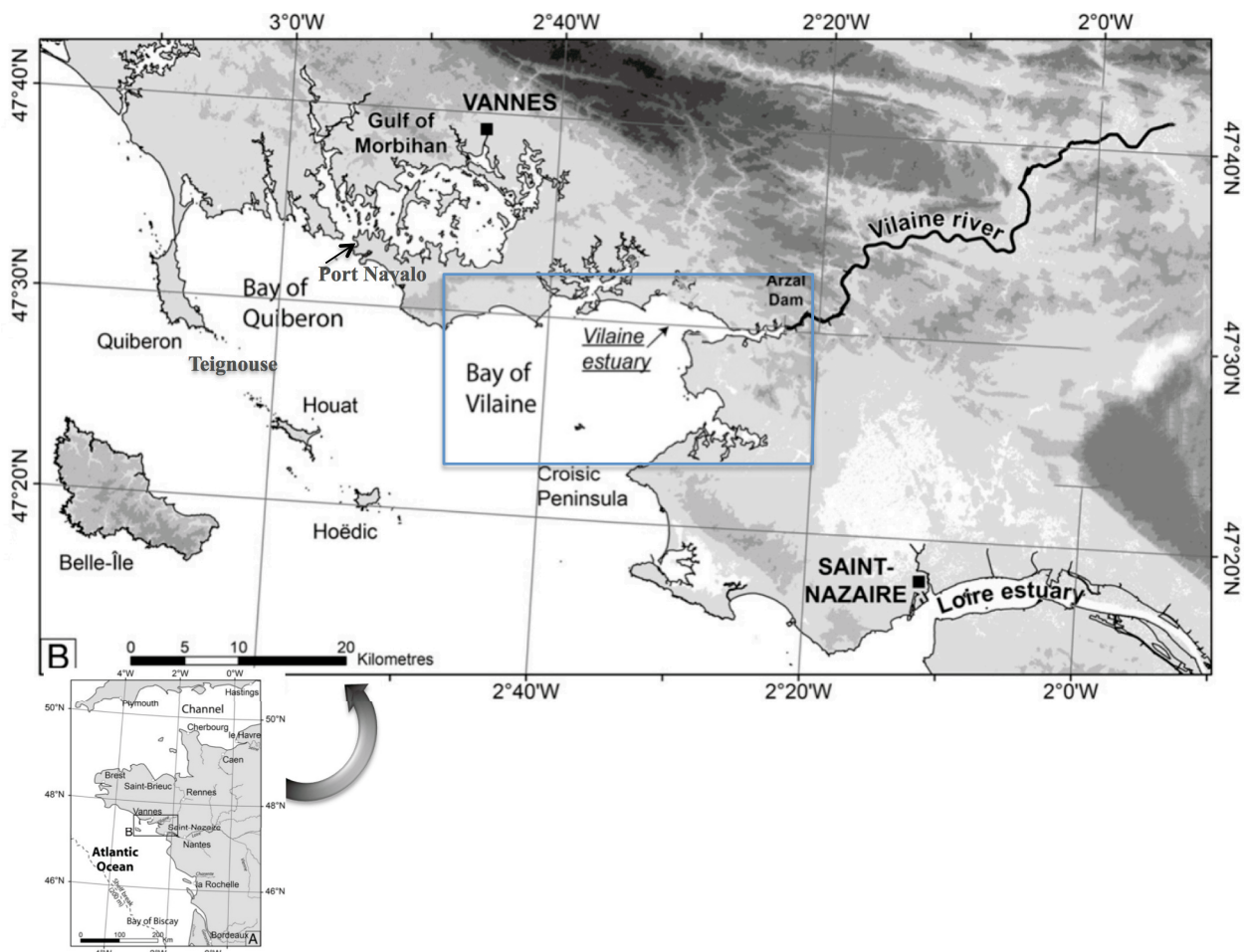


Figure 1.26: Geography of the Mor-Braz area in south Brittany, the Vilaine Estuary, Quiberon Bay and adjacent Islands: Belle-Ile, Houat, Hoëdic (from Traini et al., 2011).

The Mor-Braz is a region situated in the northern part of our study area bounded by the eastern side of the Quiberon peninsula, Houat and Hoëdic Islands, and a line that joins the coast at Le Croisic peninsula. It includes the Vilaine bay and estuary, the Gulf of Morbihan

and the bay of Quiberon (Fig. 1.26). The Mor-Braz is protected from the offshore waves by the Quiberon Peninsula, the Belle-ile island and a long rocky threshold including, *inter alia*, Houat and Hoedic Islands (Lemoine, 1989).

1.2.3.1 Vilaine Bay

The Vilaine Estuary is located in South Brittany with mean latitude and longitude coordinates $46^{\circ} 24' - 47^{\circ} 34' \text{ N}$, $2^{\circ} 50' - 2^{\circ} 20' \text{ W}$, respectively. The Vilaine River enters the Bay of Biscay in the Bay of Vilaine which is the most sheltered estuary of the French Atlantic coast. The semi-diurnal tidal range varies between 2.5 to 5 m at neap and spring, respectively. In the Vilaine estuary, tidal currents can reach 1.5 m/s, both during floods and ebbs (S.H.O.M., 1997).

In this region, currents show a seasonal character largely due to the magnitude and direction of dominant winds. These currents are oriented towards the North-West in winter and towards the South-East in summer (Sorrel et al., 2010). The strongest swells are assorted with westerly storms, favoring the resuspension and the transport of fine sediments towards the Vilaine Estuary. The mean significant wave height lies between 1 and 2 m for a mean period of 2–5 s (Tessier, 2006).

Approximately 10 km upstream of the river mouth, the Arzal weir blocks the tide. Since the Arzal Weir was completed in 1970, the length of the estuary has reduced by 80%, the tidal prism by 40% (Gouleau et al., 1981), the saline layer has increased and the sediment load upstream input has greatly reduced (Le Hir et al., 1986). According to literature, the inner part of the Vilaine Bay is influenced by the freshwater inflow and a moderate mixed energy controlled by wave and tides, while the outer part is under marine influence (Dorel et al., 1991, Sorrel et al., 2010). The Vilaine Bay has undergone eutrophication over decades mainly due to the high nutrient inputs of the Vilaine River, the low residual circulation in the bay and strong stratification. This results in chronicle appearance of colored waters (dark grey) followed by oxygen depletion of bottom waters (on summer) which threaten the marine organisms health and impact fishery resources (Chapelle, 1990).

1.2.3.2 Vilaine River regime

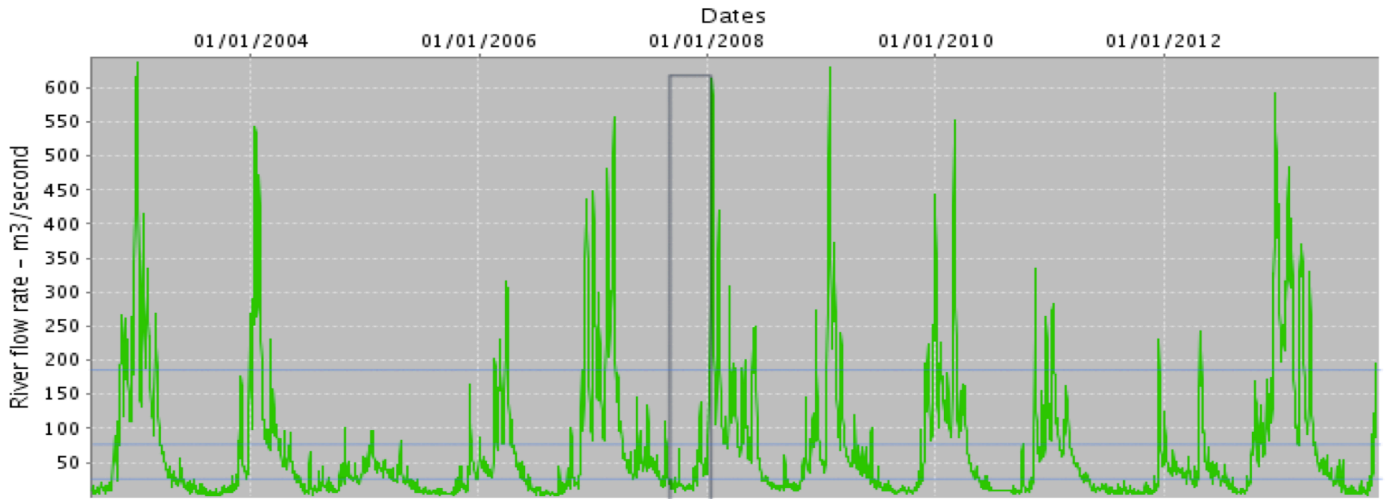


Figure 1.27: Time evolution of the Vilaine river flow from 2003 to 2013 (data from measurements provided by the French freshwater office database), the period of this study is shown by a rectangle.

The Vilaine River is the largest river of Brittany. It is 227 km long and its catchment drains one third of the Brittany area (10530 km²) (Traini et al., 2013). The Vilaine river outflow experiences a significant variation (Fig. 1.27) due to the strong variability of rainfall, either seasonal or inter-annual (Le Pape et al., 2003). The typical daily averages of low and high river discharge is about 30 and 360 m³/s, respectively. The yearly average discharge is 70 m³/s (Vested et al., 2013).

1.2.3.3 Quiberon Bay

The bay of Quiberon is part of the western end of Mor-Braz, east of the Quiberon Peninsula (Fig. 1.26). According to the literature classification, the Quiberon Bay belongs to the 'ventilated' type because of entering currents which prevent the water masses to be stagnant (Lemoine, 1989). These currents depend on the local bathymetry, with maxima in channels, and are related to the phase delay between local tide and the offshore tidal waves. For this reason, the hydraulic inertia of the Bay of Quiberon is also dependent on the Morbihan Gulf filling up and emptying, which communicates with the Mor-Braz, just east of the Quiberon Bay, through the narrow strait of Port-Navalo. Within the Bay of Quiberon, S-SW to N-NW winds predominate on an annual basis, while between late winter and spring, the wind blowing from the NE or S becomes dominant.

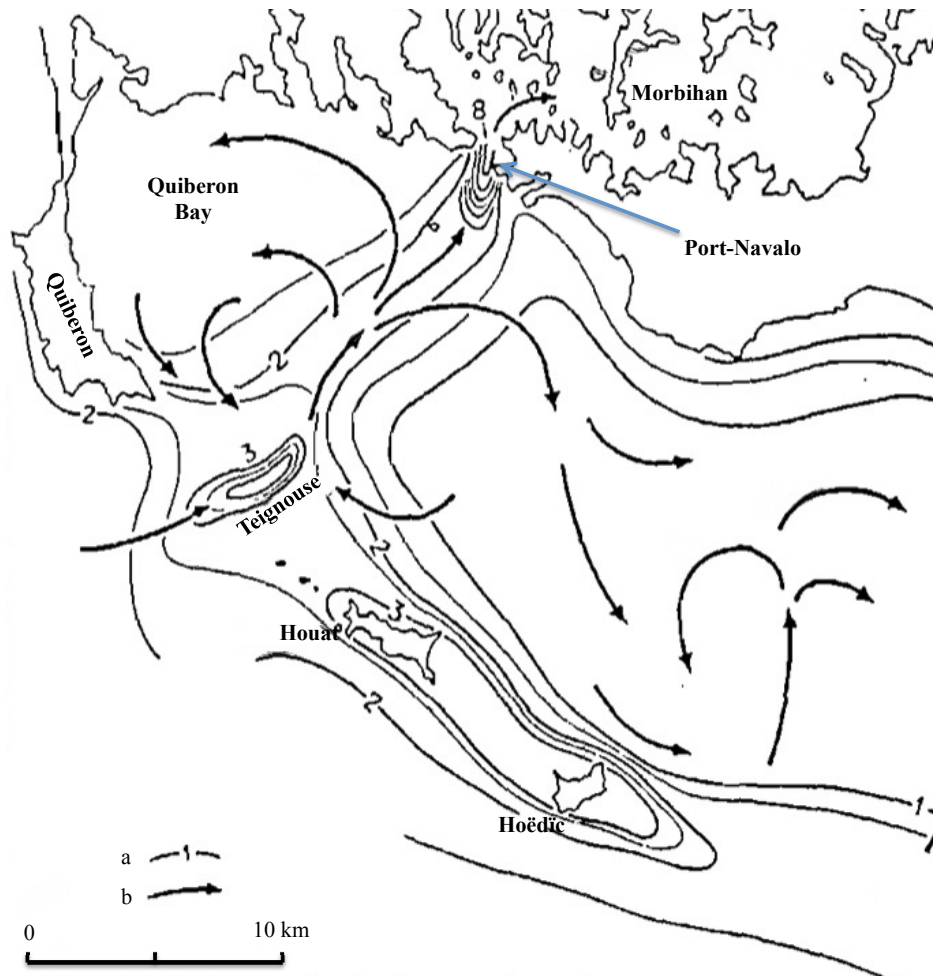


Figure 1.28: Hydrodynamic circulation in the western part of the Mor-braz; a) isocontours of velocity, digit present the speed in knots, as measured by SHOM; b) arrows represent the direction of tidal currents, considering the maximum values in spring tides (from (Lemoine, 1989)).

Tidal currents separate the Mor-Braz into two cells having independent circulation on each side of a line between Port Navalo and La-Teignouse strait (Fig. 1.15 & 1.28). This essential feature explains the hydraulic independence of bay of Quiberon, from the Vilaine Bay and the Loire Estuary. According to Fig. 1.28, tidal currents can reach 2 m/s in La-Teignouse passageway and up to 4 m/s at the entrance of the Morbihan Gulf during a spring tide. Hence, the resulting privileged orientation of flow (along an axis NNE-SSW) induces limited transversal exchanges between the Quiberon and Vilaine Bays (Lemoine, 1989).

The Gulf of Morbihan (Fig. 1.26 & 1.28) is similar to a 115 km² inland sea. It contains 40 islands and extremely large intertidal areas. It has a negligible drainage basin and communicates with the ocean via a narrow inlet (Port-Navalo strait). The area is eventually under pressure from tourism and dispersed urbanisation.

Chapter 2

Modelling Methodology

2.1 Introduction

As explained in the introduction, one goal of the present work is to set up a numerical model of the Loire estuary and the adjacent coastal areas; able to simulate estuarine inner processes and circulation patterns in the complex coastal zone with precision, and simultaneously not too much dependent on the boundary conditions.

Using a finite difference model on structured grids, it becomes possible to locally refine the horizontal resolution and to follow bathymetric contours as well as main streamlines by adapting the model to curvilinear grids, non necessarily orthogonal. This is the aim of the present chapter 2.

The basis of our development is the numerical code named MARS-3D. It is a coastal hydrodynamical model, developed by IFREMER (**French Research Institute for the Exploitation of the Sea**), which allows calculating the hydrodynamic, hydrology and transport of dissolved and particulate elements in a defined area.

The hydrodynamic applications of this model are numerous, in a large range of time and spatial scales, from the local one (beaches, estuaries) to the regional one (bays, continental shelf from the open sea to the coastline and from tides to seasonal and pluriannual periods for the time-scales (Douillet et al., 2001, Andre et al., 2005, Pous, 2005, Tessier, 2006, Lazure and Dumas, 2008, Lazure et al., 2009, Ouillon et al., 2010, Bailly Du Bois et al., 2012, Dufois et al., 2014).

2.2 Classical numerical approach

The model solves Reynolds averaged Navier-Stokes equations for geophysical fluid mechanics. The assumptions under which these equations (so called primitive equations) are obtained are classic approximations:

- Boussinesq: the fluid density slightly deviates from a reference density called ρ_0 and therefore can be replaced by a reference density everywhere except in the internal pressure term,

$$\rho = \rho_0 + \rho'(x, y, \sigma, t) \quad \text{with} \quad \rho_0 \gg \rho'(x, y, \sigma, t)$$

- The hydrostatic approximation resulting from scaling the equations: the scale considered for horizontal movements is assumed to be an order of magnitude larger than the vertical one. Under such approximation the vertical accelerations can be neglected.

2.2.1 Equations of MARS-3D in Cartesian coordinate system

The equations of the MARS-3D model are written in spherical coordinates, in order to take into account the sphericity of the earth. However, for a better readability, the equations presented here are those obtained in the standard framework of Cartesian horizontal (x, y) coordinates (Lazure and Dumas, 2008). The MARS-3D model uses the system of reduced vertical coordinates named **sigma**, which has the advantage of following the bottom topography in order to better represent the bottom circulation; in addition it allows a constant number of calculation points on the water column whatever the water depth and the free surface elevation.

2.2.1.1 Equations of internal mode

MARS-3D model takes into account all forcing present in coastal areas (tidal forcing, wind, density gradient, heat flux, and river discharges) to reflect the best of the various observable phenomena (river plumes, tidal current, up-welling, inter-tidal drying flats, seasonal cycle of thermodynamic properties of the ocean). MARS-3D model is based on the mode splitting method. It implies a separation of internal (movements and structure of internal densities) and external (propagation of the barotropic tidal wave) modes (Blumberg and Mellor, 1987). The MARS-3D model solves the Navier-Stokes equations (mass and momentum conservation) with the Boussinesq approximation and the hypothesis of hydrostatic equilibrium (Eq. 2.1 to 2.4). It is important to note that the Boussinesq approximation does not imply whether the water density is steady nor uniform. The density variations can still occur in this model due to salinity and temperature variations.

After transformation of Cartesian vertical coordinates in sigma coordinates, the Navier-Stokes equations can be written as follows:

$$\frac{\partial \zeta}{\partial t} + \frac{\partial Du}{\partial x} + \frac{\partial Dv}{\partial y} + \frac{\partial D\omega^*}{\partial \sigma} = 0 \quad (2.1)$$

$$\underbrace{\frac{\partial u}{\partial t}}_1 + \underbrace{u \frac{\partial u}{\partial x} + v \frac{\partial u}{\partial y} + \omega^* \frac{\partial u}{\partial \sigma}}_2 - \underbrace{fv}_3 = \underbrace{-g \frac{\partial \zeta}{\partial x}}_4 - \underbrace{\frac{1}{\rho_0} \frac{\partial P_\alpha}{\partial x}}_5 + \underbrace{\pi_x}_6 + \underbrace{\frac{1}{D} \frac{\partial}{\partial \sigma} \left(\frac{N_z}{D} \frac{\partial u}{\partial \sigma} \right)}_7 + \underbrace{F_x}_8 \quad (2.2)$$

$$\underbrace{\frac{\partial v}{\partial t}}_1 + \underbrace{u \frac{\partial v}{\partial x} + v \frac{\partial v}{\partial y} + \omega^* \frac{\partial v}{\partial \sigma}}_2 + \underbrace{fu}_3 = \underbrace{-g \frac{\partial \zeta}{\partial y}}_4 - \underbrace{\frac{1}{\rho_0} \frac{\partial P_\alpha}{\partial y}}_5 + \underbrace{\pi_y}_6 + \underbrace{\frac{1}{D} \frac{\partial}{\partial \sigma} \left(\frac{N_z}{D} \frac{\partial v}{\partial \sigma} \right)}_7 + \underbrace{F_y}_8 \quad (2.3)$$

$$\frac{1}{D} \frac{\partial p'}{\partial \sigma} = \rho b \quad (2.4)$$

with ω^* as the vertical velocity in the σ coordinate framework when ω is the vertical velocity in the physical framework (z); Both are related according to:

$$\omega^* = \frac{1}{D} \left(\omega - \sigma \frac{\partial \xi}{\partial t} - u \left(\sigma \frac{\partial \xi}{\partial x} + (\sigma - 1) \frac{\partial H}{\partial x} \right) - v \left(\sigma \frac{\partial \xi}{\partial y} + (\sigma - 1) \frac{\partial H}{\partial y} \right) \right) \quad (2.5)$$

The different terms of momentum equations (Eq. 2.2 & 2.3) correspond to:

- (1) Acceleration
- (2) Advective and convective acceleration
- (3) Effect of earth rotation (Coriolis force)
- (4) Pressure gradient induced by the sea surface slope
- (5) Atmospheric pressure gradient
- (6) Buoyancy $b = -g(\rho - \rho_0)/\rho_0$ within a sigma coordinate framework, zonal and meridian components of internal pressure gradient, which are mentioned above as (π_x, π_y) ,

$$\pi_x = \frac{\partial}{\partial x} \left[D \int_\sigma^0 b \, d\sigma \right] + b \left(\sigma \frac{\partial D}{\partial x} - \frac{\partial H}{\partial x} \right) \quad \pi_y = \frac{\partial}{\partial y} \left[D \int_\sigma^0 b \, d\sigma \right] + b \left(\sigma \frac{\partial D}{\partial y} - \frac{\partial H}{\partial y} \right)$$

(7) Vertical turbulent diffusion

(8) Horizontal turbulent diffusion, which is expressed in simplified manner as follows:

$$F_x = \frac{\partial}{\partial x} \left(\nu_x \frac{\partial u}{\partial x} \right) + \frac{\partial}{\partial y} \left(\nu_y \frac{\partial u}{\partial y} \right) \quad F_y = \frac{\partial}{\partial x} \left(\nu_y \frac{\partial v}{\partial x} \right) + \frac{\partial}{\partial y} \left(\nu_x \frac{\partial v}{\partial y} \right)$$

The horizontal turbulent diffusion operators are not written in a fully developed form, but they are simplified according to Mellor (Mellor and Blumberg, 1985). This approximation is relatively acceptable, as long as the discretized vertical layers cross the isopycnal contours

smoothly, *i.e.* in the case of a smooth bathymetry gradient(Lazure and Dumas, 2008).

Previous equations involve the following notations:

u, v, ω^* are the three components of the velocity in the three dimensions of space (x, y, σ) ,

$D = H + \zeta$ height of the water column,

S, T, p pressure,

P_a atmospheric pressure,

g acceleration of gravity,

$f = 2\Omega \sin\phi$ Coriolis parameter, ϕ is (latitude) geographic coordinate in decimal degrees

$\Omega = 2\pi/86164 \text{ rad.s}^{-1}$ earth's rotation frequency

$\rho = \rho(S, T, p)$ seawater density

ρ_0 reference density,

$p' = -\rho_0 \int_{-1}^0 b \, d\sigma$ pressure anomaly,

N_z vertical eddy viscosity coefficient,

ν_x, ν_y horizontal eddy viscosity coefficient, estimated in each mesh and at each time-step, depending on the mesh size of the velocity deformation tensor.

Density is computed by the following linear approximation proposed by Mellor et al. (1991):

$$\rho = \rho_0[1 + \alpha(T - T_0) + \beta(S - S_0)] \quad (2.6)$$

α thermal expansion

β saline contraction

S, T, p salinity, temperature and pressure,

2.2.1.2 Advection-diffusion equations for heat and salinity

The principle of internal energy conservation leads to determinate the temperature of seawater in the model by the following heat equation:

$$\frac{\partial DT}{\partial t} + \frac{\partial D(uT - K_x \frac{\partial T}{\partial x})}{\partial x} + \frac{\partial D(vT - K_y \frac{\partial T}{\partial y})}{\partial y} + \frac{\partial D(\omega^*T - \frac{K_z}{D^2} \frac{\partial T}{\partial \sigma})}{\partial \sigma} = \frac{1}{\rho_0 C_p} \times Q_T \quad (2.7)$$

Q_T is the heat source term evaluated in each layer of the model, using incident radiative flux which enter in the water column. Losses are integrated in the boundary condition on the surface. The horizontal eddy diffusivity coefficients are chosen constant ($K_x = K_y$). K_z is the vertical eddy diffusivity.

For this study, in order to avoid unrealistic summer warming in shallow water areas where the residence time is long, and following Lazure et al.(2009), the heat flux not absorbed in the

water column and reaching the bottom is considered as lost. This assumption was used by Holt and James (1999) in the North Sea for the same reasons.

Taking into account the salt conservation, the salinity equation solved in the MARS-3D model is as follows:

$$\frac{\partial DS}{\partial t} + \frac{\partial D(uS - K_x \frac{\partial S}{\partial x})}{\partial x} + \frac{\partial D(vS - K_y \frac{\partial S}{\partial y})}{\partial y} + \frac{\partial D(\omega^* S - \frac{K_z}{D^2} \frac{\partial S}{\partial \sigma})}{\partial \sigma} = 0 \quad (2.8)$$

2.2.1.3 Equation of any passive Tracer

The transport of any dissolved matter is resolved by the advection-dispersion equation:

$$\frac{\partial DC}{\partial t} + \frac{\partial D(uC - K_x \frac{\partial C}{\partial x})}{\partial x} + \frac{\partial D(vC - K_y \frac{\partial C}{\partial y})}{\partial y} + \frac{\partial D(\omega^* C - \frac{K_z}{D^2} \frac{\partial C}{\partial \sigma})}{\partial \sigma} = S_o - S_i \quad (2.9)$$

where C stands for any dissolved tracers, S_o s and S_i s are the sources and sinks of tracer C , respectively.

2.2.1.4 Equations of external mode

As developed by Lazure and Dumas (2008), the MARS-3D code uses the splitting mode which leads to build a specific barotropic model by integrating Eq. 2.1, 2.2 & 2.3 over the vertical axis from bottom ($\sigma = -1$) to top ($\sigma = 0$) and considering kinematic boundary conditions. It gives the following set of equations:

$$\frac{\partial \zeta}{\partial t} + \frac{\partial D\bar{u}}{\partial x} + \frac{\partial D\bar{v}}{\partial y} = 0 \quad (2.10)$$

$$\frac{\partial \bar{u}}{\partial t} - f\bar{v} = -g \frac{\partial \zeta}{\partial x} - \frac{1}{\rho_0} \frac{\partial P_a}{\partial x} + \frac{1}{\rho_0 D} (\tau_{surf}^x - \tau_{fond}^x) + \int_{-1}^0 [-L(u) + \pi_x + F_x] d\sigma \quad (2.11)$$

$$\frac{\partial \bar{v}}{\partial t} - f\bar{u} = -g \frac{\partial \zeta}{\partial y} - \frac{1}{\rho_0} \frac{\partial P_a}{\partial y} + \frac{1}{\rho_0 D} (\tau_{surf}^y - \tau_{fond}^y) + \int_{-1}^0 [-L(v) + \pi_y + F_y] d\sigma \quad (2.12)$$

where the mean current over depth and the function L are defined as:

$$\left\| \left\| \begin{aligned} (\bar{u}, \bar{v}) &= \int_{-1}^0 (u, v) d\sigma \\ L(A = (u, v)) &= u \frac{\partial A}{\partial x} + v \frac{\partial A}{\partial y} + \omega^* \frac{\partial A}{\partial \sigma} \end{aligned} \right\| \right\|$$

2.2.1.5 Boundary conditions

Boundary conditions involve kinematic conditions and fluxes at the upper ($\sigma = 0$) and lower ($\sigma = -1$) boundaries of the domain. Fluxes concern heat transfer and wind-induced friction. The following sets of equations is obtained:

| Boundary condition at the surface $\sigma = 0$ | Boundary condition at the bottom $\sigma = -1$ |
|---|---|
| $\frac{N_z}{D} \frac{\partial u}{\partial \sigma} = \tau_{surf}^x / \rho_0$ | $\frac{N_z}{D} \frac{\partial u}{\partial \sigma} = \tau_{bottom}^x / \rho_0$ |
| $\frac{N_z}{D} \frac{\partial v}{\partial \sigma} = \tau_{surf}^y / \rho_0$ | $\frac{N_z}{D} \frac{\partial v}{\partial \sigma} = \tau_{bottom}^y / \rho_0$ |
| $\frac{K_z}{D} \frac{\partial T}{\partial \sigma} = \frac{Q_T}{\rho_0 C_p}$ | $K_z \frac{\partial T}{\partial \sigma} = 0$ |
| $K_z \frac{\partial S}{\partial \sigma} = 0$ | $K_z \frac{\partial S}{\partial \sigma} = 0$ |
| $\omega^* = 0$ | $\omega^* = 0$ |

where:

Q_T is the heat flux at the air/sea interface,

$(\tau_{surf}^x, \tau_{surf}^y) = \rho_a C d_S \|\vec{W}\| (W_x, W_y)$ are the wind-induced surface stress components,

$\rho_a = 1.25 \text{ kg} \cdot \text{m}^{-3}$ is the air density.

$C d_S = 0.016$ is the surface drag coefficient,

(W_x, W_y) is the wind velocity vector at 10 m above the sea surface,

$(\tau_{bottom}^x, \tau_{bottom}^y) = \rho_0 C d_B \|\vec{u}\| (u, v)$ are the bottom stress components, where $C d_B$ results

from equation:

$C d_B = \left(\frac{\kappa}{\ln\left(\frac{Z+z_0}{z_0}\right)} \right)^2$ where $\kappa = 0.4$ refers to the *von Karman* constant, Z the elevation above bottom where u, v are expressed and z_0 the bed roughness.

Lateral boundary conditions in MARS-3D model may be required for the sea surface level, velocity components and tracers concentrations (salinity, temperature, sediment), depending on the selected configuration.

Open boundary conditions

Numerical models of limited coastal regions inevitably involve the treatment of open boundaries where the numerical grid ends. Ideal open boundaries are "transparent" to motions which are generated within the computational domain and which are "felt" at the open boundaries.

There is no numerical treatment of open boundaries which achieves this ideal. A large number of open boundary conditions have been proposed in the past (Palma and Matano, 1998). Due to the essentially hyperbolic nature of the incompressible, hydrostatic primitive equations, external data are required for only inward boundary fluxes. The outward fluxes may be treated with an algorithm for two-dimensional radiation. In the MARS-3D model the prescription of the Open Boundary Conditions (OBCs) is based on the method of characteristics.

Moving Boundaries

In shallow coastal areas, some of them may dry up at low water level, which means that we have moving boundaries. The definition of these boundaries appears to be rather straightforward: the instantaneous water depth $D = 0$ (this parameter is also defined by h , Eq. 2.13). Several techniques have been developed to track the moving boundaries, but may be difficult to apply in operational numerical models. In the MARS-3D model, the wetting and drying processes have been simplified by introducing a water depth on each side of a grid cell, thanks to the use of an Arakawa-C grid (Fig. 2.1).

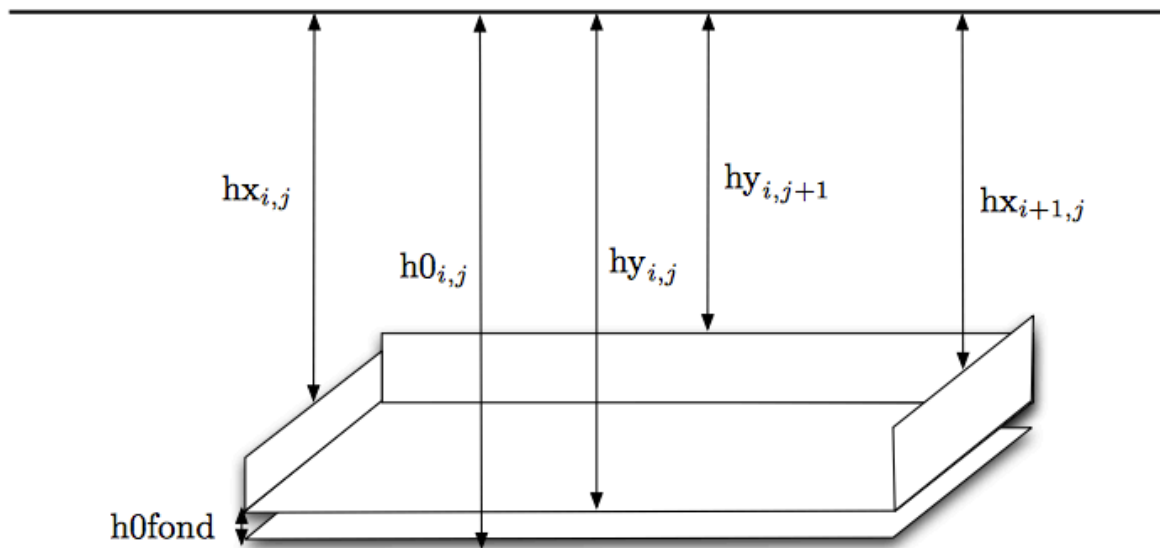


Figure 2.1: Spatial repartition of water depths on a grid cell (Issues from "user manual Mars-3D V.9.06").

In the MARS-3D model, the wetting and drying processes have been cleared up by introducing a water depth on each side of a grid cell, thanks to the use of an Arakawa-C grid (see further).

$$D \text{ or } h(x,y,t) = H(x,y) + \zeta(x,y,t) \quad (2.13)$$

A central depth is introduced:

$$H_{i,j} = \max(hx_{i,j}, hx_{i+1,j}, hy_{i,j}, hy_{i,j+1}) + h0fond \quad (2.14)$$

$h0fond$ is a minimum depth. The instantaneous depths $hx + \zeta$, $hy + \zeta$ are used to solve momentum equations while the global advection-diffusion equation is solved by introducing the central depth $H + \zeta$.

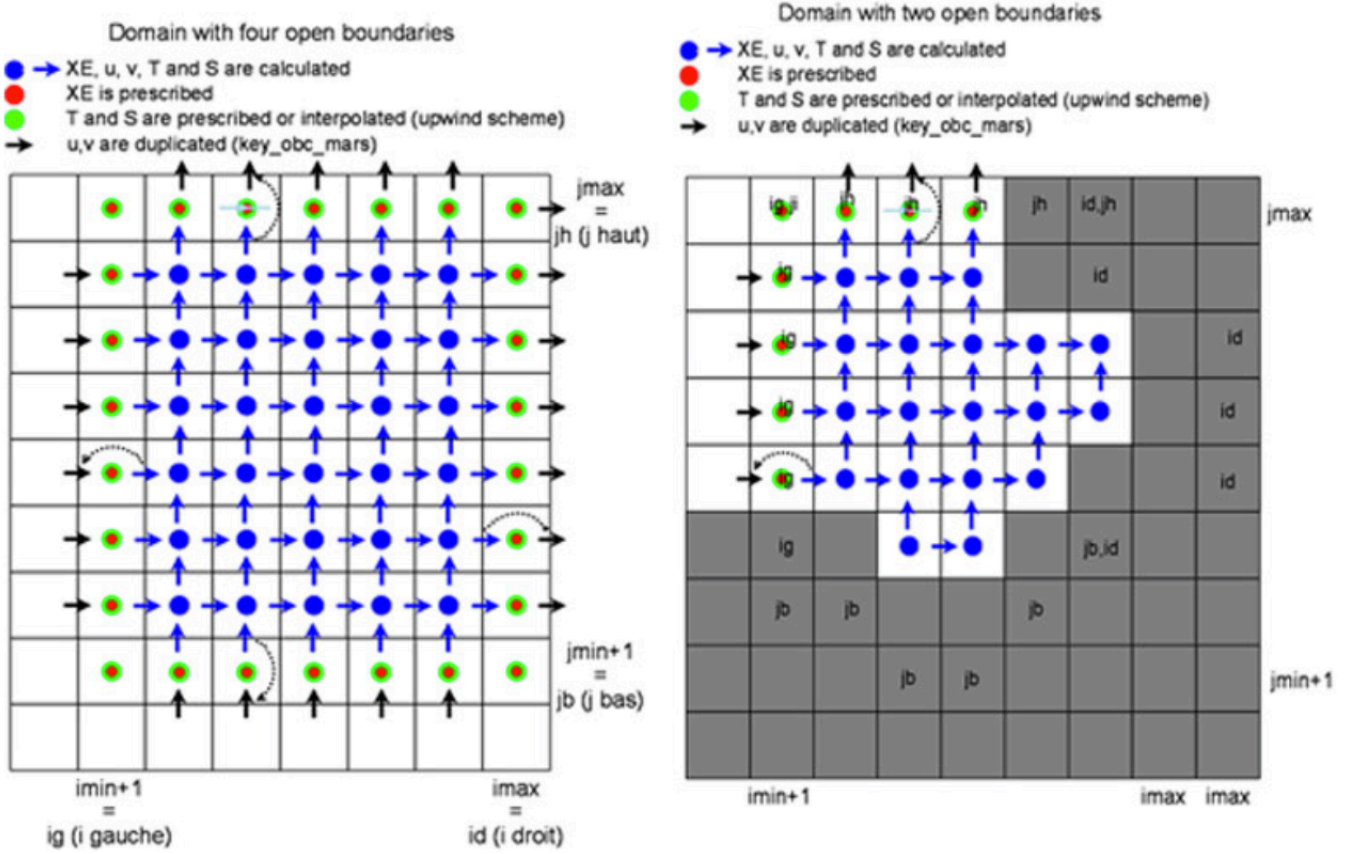


Figure 2.2: Horizontal positions of variables in the Arakawa-C grid.

The boundary conditions for velocities at the coast is written by imposing a zero flux across the coastline.

The MARS-3D model is considered as a nesting model with sub-model operating inside a larger one, for which boundary conditions are interpolated among the available measurements. For the water level, current velocity, temperature and density gradient, the model uses the results of a larger model for the same period but not necessarily with a same time step: by applying a series of interpolation, it provides the adequate values at the boundary meshes.

2.2.1.6 Turbulence closure

Small-scale vertical exchange processes that cannot be resolved by the model because they occur within meshes are parameterized by the turbulence closure. There are different models of turbulence closure with different ranges of complexity, but the most often used closure scheme in coastal ocean models are the two-equation closure model that follows the $k - kl$ theory assumptions (Mellor and Yamada, 1982) and the k -epsilon one. The present research uses the turbulent closure scheme from Gaspar (Gaspar et al., 1990). Horizontal turbulent diffusion is computed according to the formulation of Smagorinsky (Smagorinsky, 1963). This latter model uses a prognostic equation (2.15) for the turbulent kinetic energy k and the definition of the dissipation rate ε (Luyten et al., 1996) which is expressed as follows:

$$\frac{\partial k}{\partial t} + u \frac{\partial k}{\partial x} + v \frac{\partial k}{\partial y} + \omega^* \frac{\partial k}{\partial \sigma} = \frac{1}{D} \frac{\partial}{\partial \sigma} \left(\frac{N_z}{s_k D} \frac{\partial k}{\partial \sigma} \right) + Prod + Dest - \varepsilon \quad (2.15)$$

where s_k stands for the turbulence Schmidt number for k (Lazure and Dumas, 2008); $Prod$ and $Dest$ are respectively the production by velocity shear and the destruction by buoyancy, and are defined as:

$$Prod = \frac{N_z}{D^2} \left[\left(\frac{\partial u}{\partial \sigma} \right)^2 + \left(\frac{\partial v}{\partial \sigma} \right)^2 \right] \quad \text{and} \quad Dest = -\frac{K_z}{D} \frac{\partial b}{\partial \sigma}$$

ε is the dissipation term of turbulent kinetic energy, which is expressed as a function of the mixing length l_m :

$$\varepsilon = \frac{C^{4/3} k^{3/2}}{l_m} \quad \text{with} \quad C = 0.09 \quad (2.16)$$

Viscosity N_z and turbulent vertical diffusion K_z in this case are related to the turbulent kinetic energy by the following relationship:

$$N_z = c_k l_k k^{\frac{1}{2}} \quad (2.17)$$

$$K_z = N_z / Prt \quad (2.18)$$

with $c_k = 0.1$ as a constant. The mixing scale l_k and the mixing length (dissipation) l_m are evaluated at each layer from the following relations which involve the distance l_u (resp. l_d) which is the distance upwards (resp. downwards), along which a moving fluid particle converts

its turbulent kinetic energy into potential energy (Gaspar et al., 1990):

$$l_m = (l_u l_d)^{\frac{1}{2}} \quad (2.19)$$

$$l_k = \min(l_u, l_d) \quad (2.20)$$

Distances l_u and l_d are assessed at each depth using the following formulations that involves the profiles of k and b (buoyancy).

$$\int_z^{z+l_u(z)} (b(z') - b(z)) dz' = k(z) \quad (2.21)$$

$$\int_{z-l_d(z)}^z (b(z) - b(z')) dz' = k(z) \quad (2.22)$$

Gaspar considers $Prt = 1$ but in this study, we adjusted the Prandtl's number during the validation process of tracers (Salinity and Temperature) which will be explained in more details in the next chapter.

2.2.2 Principles of resolution

The spatial discretization is done using a staggered grid resulting in a finite-volume type formulation.

Using the same time step for the resolution of both modes is a specificity of the MARS-3D model, which is achieved by an iterative method that controls the convergence. To simulate free surface elevations and currents fields (2D & 3D), MARS-3D model uses an alternate direction implicit (**ADI**) scheme (Leendertse and Gritton, 1971). This feature helps an implicit calculation of some terms (pressure gradients and bottom friction in momentum equation, fluxes divergence in continuity equation). The turbulence closure scheme is based on the equation of evolution of the turbulent kinetic energy and mixing length formulation from Gaspar (Gaspar et al., 1990). Vertical eddy viscosity and diffusivity are deduced from the turbulent kinetic energy. Horizontal turbulent diffusion is computed according to Smagorinsky (1963). To compute the advection of active tracers like salinity, the ULTIMATE QUICKEST MACHO multidimensional scheme with "universal limiter" (Leonard et al., 1995, Leonard, 1996) is implemented using the same time-step as hydrodynamics. This scheme provides the third-order accuracy in time and space (Duhaut et al., 2008).

As mentioned in Sec. 2.2.1, the MARS-3D model uses the system of σ coordinates named sigma, which has the advantage of following the bottom topography in order to better represent the bottom circulation; in addition it allows a constant number of calculation points on the water column.

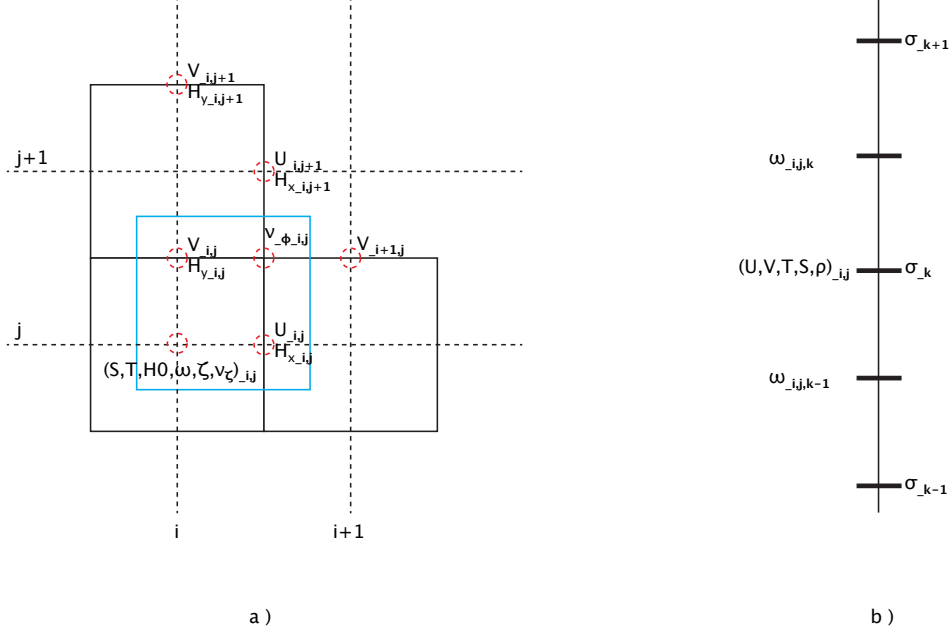


Figure 2.3: a) Horizontal positions of variables in the Arakawa-C grid. b) Positions of variables on the vertical axis.

All differential equations in the MARS-3D model are solved by using the finite difference technique. The discretization of the Navier-Stokes equations is operated on a staggered Arakawa-C grid (Arakawa and Lamb, 1977). In this type of grid, the computations of the free surface elevation, concentrations of tracers, and variation of buoyancy are expressed in the center of the cells, while the current components (u, v) are at their edges (Fig. 2.3a). Along the vertical axis, horizontal velocities and concentrations are calculated in selected sigma level (Fig. 2.3b), while vertical velocities (ω) are considered at intermediate levels. In this study, we chose 10 sigma levels regularly distributed on the vertical axis ($\sigma_1 = -0.95, \sigma_2 = -0.85, \dots, \sigma_{kmax} = -0.05$).

The external mode calculates the free surface elevation ζ and the vertical velocities ω , whereas the internal mode operates a full resolution of the currents field (u_z, v_z) and tracers considered in three dimensions.

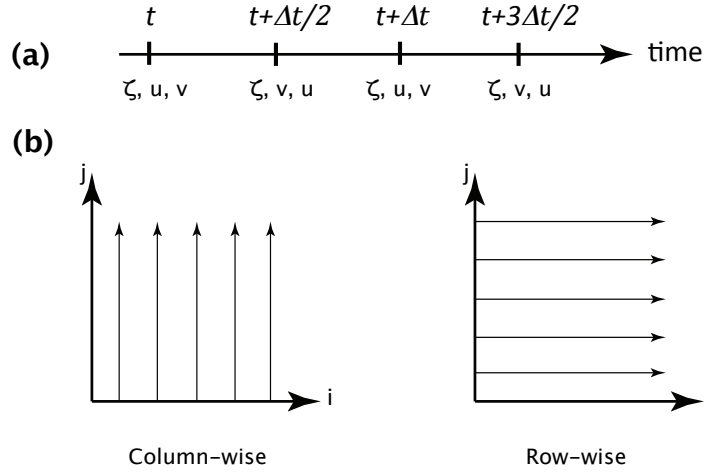


Figure 2.4: ADI semi-implicit resolving variable with respect to the direction. (a) time evolution (b) Computation of u , v and ζ are performed in a row-wise manner during the first half time step whereas v , u and ζ computations are performed in column-wise during the second half time step.

The equations of motion for the two horizontal components are decoupled by the **ADI** (Alternating Direction Implicit) method (Leendertse and Gritton, 1971); in each half time step, both velocity components are solved (Fig. 2.4a), one time along the axis Ox (row-wise, Fig. 2.4b) one time along the axis Oy (column-wise, Fig. 2.4b). The curvilinear version of MARS-3D (developed during this study) also uses similar finite differences techniques, as described further in this chapter.

2.2.3 Time-step

The time step is variable. It is adjusted according to the maximum horizontal velocity observed during a defined period, for having a maximum time step fully respecting the **CFL** (Courant-Friedrich-Lewy) stability criteria, constrained by the explicit horizontal advection scheme:

$$\Delta t < 0.6 \frac{\Delta x}{\max(u, v)} \quad (2.23)$$

2.3 Hydrodynamic modelling in curvilinear grids

2.3.1 Introduction

In practice, the grids used in many CFD (computational Fluid Dynamics) applications are not Cartesian. To handle complex geometries, curvilinear, boundary-fitted grids are used. These grids are also referred to as structured grids, because they have a regular topological structure, as opposed to unstructured grids as used in FEM (Finite Element Methods).

In fluid mechanics, using curvilinear coordinates aims of following topography and generally main current fields, therefore helps having more realistic hydrodynamic structures. In addition, having freedom to refine meshes in areas of interest and use larger meshes elsewhere is another advantage of using non-orthogonal curvilinear coordinates without increasing the computational cost in terms of time and required memory, in comparison with a rectangular uniform grid having the required resolution.

The idea of using preferred directions is common in the field of solid mechanics. In solid mechanics modelling, stress is expressed as a function of the strain tensor and material properties. These properties are likely to be **anisotropic**, as it is the case in a composite matrix where the fibbers direction should be privileged. Non-orthogonal curvilinear grids become useful when those directions are not necessarily orthogonal.

2.3.2 Different solutions to adjust the problematic of complex geometry

Technology advancements and development of powerful computers have provided researchers with more accurate tools and methods for 3D circulation and transport process in coastal regions, lakes and estuaries. However, modelling the complex specifications of these regions often encounters difficulties despite all the efforts. To adopt a precise modelling method for the region under study, different methods can be taken into consideration. The efforts to guarantee high precision come from the complex topography and bathymetry that are frequently encountered in the shallow water areas.

Here, we present some different suggested methods:

- Uniform refinement of the Cartesian grid, keeping rectangular or square meshes: using this type of meshes is a traditional method (LeVeque and Calhoun, 2001). All points beyond the computational region are flagged "inactive" and do not participate in computation processes, although they stay present in computer memory. The modelled area is bounded by a "stair-step" shoreline which approximates the actual shoreline. This method does not require any change in Navier-Stokes governing equations. However, it significantly increases the computational cost. Apart from the huge cost involved, Brand et al (Brand et al., 1991), reports that the grid orientation effects do not vanish with the grid refinement when large mobility rates are considered. They state that the solution is always contaminated with numerical diffusion and grid orientation effects.
- Flexible Cartesian grids: rectangular meshes have a varying grid size in order to have better accuracy where the strongest gradients are expected. Telescoping grid in which

rectangular grid lines are pushed in or out is a simple way to do this (Sturman and Zawar-Reza, 2002). The main problem with this method is the very limited flexibility. Another problem is that it normally involves an adjustment of finite-difference formulas to account for uneven grid sizes surrounding a particular grid point, except if the variation of mesh sizes is quite progressive (Cugier and Le Hir, 2002).

- Finite element method (FEM): provides high flexibility in modelling complicated geometries. The drawback of this method is its expensive computation, in particular when long-term simulations are planned. There is a large possibility that advancement of super calculators can overcome the expenses caused by this method in the future, and therefore lead to a further use of the method.
- Finite-difference method using curvilinear grids: curvilinear grids allow complex domains to be represented with smooth grids that can be aligned with the boundaries (boundary-fitted). There are two types of curvilinear grids: orthogonal curvilinear grids which are used when geometry is simple (Blumberg et al., 1987); non-orthogonal curvilinear (boundary-fitted) grids are more suitable for most of estuaries and coastal regions. The use of non-orthogonal grids is particularly attractive for problems where the solution is sensitive to any grid induced numerical artifacts (Cheshire and Henshaw, 1990). Here, the grid is structured in such manner that any mesh can be identified by two indices (i, j) covering the two dimensions of the horizontal space, so that any differential form can be expressed as finite differences between values easily locatable. This method has great advantages for programming as the differential equations will have the same structure as in the rectangular grid and the number of neighboring points can be referenced by subscripts (i, j) in just the same way. The advantages of this method are (i) an increase in accuracy for modelling borderline conditions of the coastal region (Sheng, 1990, Sheng et al., 2010), (ii) a decrease in numerical error by aligning meshes with main flow directions and (iii) an optimization of the "Courant number" in direction of the main flow. However, the complex formulation is among the drawbacks of this method.

The finite-difference method using **non-orthogonal curvilinear grids** is used in the present research.

2.3.3 Different types of Coordinate Systems and Basis Vectors

The coordinate system is an arrangement of coordinate lines which are used to identify the location of points in space. Considering a set of points and their coordinates, if only one coordinate varies, with the other ones staying constant, then the set of points is known

as coordinate line. In elementary geometry, the basis vectors are defined as the unit vectors tangential to the coordinate grids.

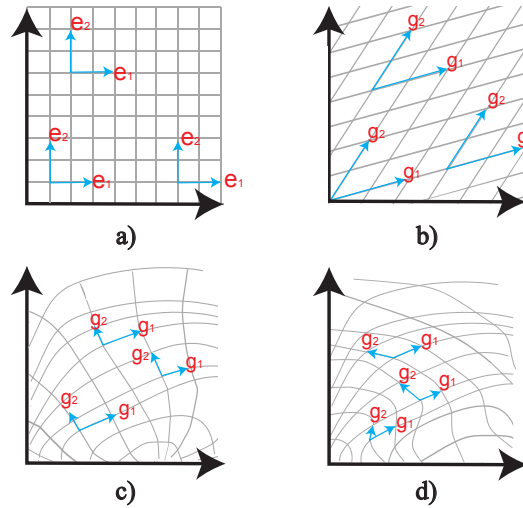


Figure 2.5: Homogeneous and curvilinear coordinates, the basis vectors are always tangential to coordinate lines, a) Orthogonal coordinates. b) Non-orthogonal coordinates. c) Orthogonal curvilinear. d) Non-orthogonal curvilinear.

Coordinate systems are called homogeneous or global if the basis vectors defined as tangential unit vectors to the coordinate axes do not change from point to point; these kind of coordinate could be orthogonal (Fig. 2.5a) or non-orthogonal (Fig. 2.5b). If the coordinate grid contains curved lines, the coordinate system is called **curvilinear**, as shown in Fig. 2.5c & d. In Fig. 2.5c, the coordinate system has basis vectors that are orthogonal everywhere. Therefore the coordinate system is simultaneously curvilinear and orthogonal. The general form of curvilinear coordinate is shown in Fig. 2.5d. In order to keep more flexibility for the grid generation, we chose a non-orthogonal curvilinear coordinates system.

In mathematics literature, the curvilinear coordinates are considered as related to an affine space ¹ in which two sets of basis vectors can be defined. The first set of basis vectors, known as **covariant basis** vectors (g_1, g_2) , consists of vectors locally tangential to coordinate lines. The second set, known as **contravariant basis** vectors (g^1, g^2) , consists of vectors locally normal to grid lines (See Fig. 2.6). Both sets of basis vectors do not necessarily have a unit length (Thompson et al., 1985). According to the definition of basis vectors, covariant and contravariant basis vectors are coincide in Cartesian coordinate system, therefore they are just referred to as basis vectors.

¹As described by Papin ((Denis-Papin and Kaufman, 1966), p43), when the axes used to define a coordinate do not have the same physical dimensions, and when there is no possibility of comparing the units of one axis against the units of another axis, we say that these coordinates belong to an **affine** or **non-metric** space. In affine geometries, we are only interested in properties that remain invariant under arbitrary scale and angle changes of the axes. On the contrary, when the coordinates admit any common measure, we can define a length and angle, we say that the coordinate system belongs to a **metric** space.

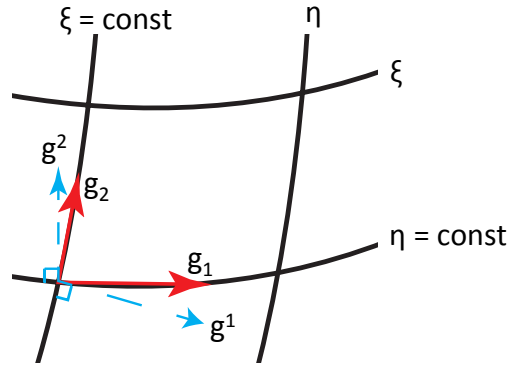


Figure 2.6: Definition of covariant g_i and contravariant g^i basis vectors over a non-orthogonal curvilinear coordinates system (ξ, η) .

2.4 Curvilinear Equations

Before writing the curvilinear equations, we need to explain how the components of a given physical vector quantity are likely to change. Then, the modified Navier-Stokes equations in generalized curvilinear coordinates will be presented. The following sections describe a few concepts related to the domain of differential geometry and tensor analysis (coordinate system, vector, tensor, covariant and contravariant components). These concepts are required to describe changes in governing Navier-Stokes equations.

Scalars, vectors and Tensors

Scalars are invariant quantities that do not depend on the coordinate system and are specified by a single real number, for example this is the case of density and temperature. There are other quantities associated with a point that not only have a magnitude but also a direction. They are named vectors. A vector itself has an invariant character which is independent of the coordinate references. However, each vector in given coordinate systems can be defined by its components according to a chosen basis vectors. Then the components of a vector depend on the basis coordinate but the sum of components times base vectors should be invariant, so we have to distinguish between the vector as an entity and its components which allow us to reconstruct it in a particular coordinate system. For transforming a vector from one coordinate to another we just need to know how the base vectors of the new system can be expressed in terms of the old ones.

For instance, a same vector \vec{V} can be written in two different basis coordinates \mathbf{g}_k and \mathbf{g}'_k :

$$\vec{V} = \sum_k v^k \mathbf{g}_k = \sum_k v'^k \mathbf{g}'_k$$

These concepts can be generalized in term of tensor. A tensor of order m is a set of n^m numbers, in n dimensions of space. The feature of tensor invariance is really important when it provides a powerful techniques to describe affine space in general and particularly in curvilinear coordinate systems. However, its components are dependent on the basis vectors with respect to any chosen coordinate system. In this context, a scalar is a tensor of order zero, a vector is a tensor of order one and a deformation matrix is considered as a tensor of order two.

2.4.1 Transformation relations between basis vectors

As mentioned previously, a non-orthogonal curvilinear coordinates system is chosen for this study. In order to work with vector and tensor components in the new coordinates system and respecting their invariant characteristic (Douglas Downing, 2009), we have to define a basis transformation. Let \mathbf{e}_i be the "old" tangential basis vectors (Cartesian coordinates considered as the old coordinate, see Fig. 2.7). Let \mathbf{g}_i be the "new" tangential basis vectors (Curvilinear coordinates considered as the new coordinates). Here, the curvilinear coordinates are used in horizontal plane. Hereinafter, we will use two notations; the tensorial one, ξ^i , useful for contracted expressions using the Einstein summation, and the developed one, (ξ, η) more readable in expanded equations and common in literature. The correspondence writes $\xi^1 \leftrightarrow \xi$ and $\xi^2 \leftrightarrow \eta$. The two Cartesian coordinates (x, y) are represented by x^i . Then the new basis vectors are defined as:

$$\mathbf{g}_1 = \frac{\partial x}{\partial \xi} \mathbf{e}_1 + \frac{\partial y}{\partial \xi} \mathbf{e}_2$$

$$\mathbf{g}_2 = \frac{\partial x}{\partial \eta} \mathbf{e}_1 + \frac{\partial y}{\partial \eta} \mathbf{e}_2$$

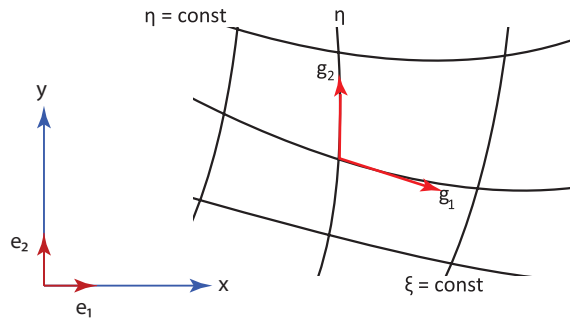


Figure 2.7: Old coordinates system (Cartesian) presented by (x, y) with (e_1, e_2) as basis and new ones (non-orthogonal curvilinear) defined by (ξ, η) with (g_1, g_2) as new basis.

One can also write with the tensor notation:

$$\mathbf{g}_i = \sum_{\delta=1,2} A_i^\delta \mathbf{e}_\delta = A_i^\delta \mathbf{e}_\delta \quad \text{using Einstein summation, where} \quad A_i^\delta = \frac{\partial x^\delta}{\partial \xi^i} \quad (2.24)$$

$$\mathbf{e}_\alpha = \sum_{k=1,2} B_\alpha^k \mathbf{g}_k = B_\alpha^k \mathbf{g}_k \quad \text{using Einstein summation, where} \quad B_\alpha^k = \frac{\partial \xi^k}{\partial x^\alpha} \quad (2.25)$$

2.4.2 Metric Tensor and Scale components

After defining the physical and computational space, our goal is to express all terms of the governing hydrodynamic equations such that the independent variables are (ξ, η, σ, t) . To achieve this goal, we use the Jacobian matrix $[J]$ of transformation that is given by:

$$[J] = \begin{bmatrix} \frac{\partial x}{\partial \xi} & \frac{\partial x}{\partial \eta} \\ \frac{\partial y}{\partial \xi} & \frac{\partial y}{\partial \eta} \end{bmatrix}$$

Covariant metric components are associated with the covariant base vectors, which are often used to represent differential increments (Thompson et al., 1985) of length, surface area, and volume. This tensor ensures that the distance between two points should be independent of the coordinate system. Here we present the components of the covariant 2×2 symmetric metric tensor (because we have curvilinear coordinate in horizontal plane ($2D$)). The metric tensor is also called fundamental tensor (Spain, 2003) and it can be determined with²:

$$g_{ij} = \frac{\partial x^i}{\partial \xi^i} \frac{\partial x^j}{\partial \xi^j} = \mathbf{g}_i \cdot \mathbf{g}_j \quad i, j = 1, 2 \quad (2.26)$$

The components of this tensor are:

$$g_{11} = \mathbf{g}_1 \cdot \mathbf{g}_1 = x_\xi^2 + y_\xi^2 \quad g_{12} = g_{21} = \mathbf{g}_1 \cdot \mathbf{g}_2 = \mathbf{g}_2 \cdot \mathbf{g}_1 = x_\xi x_\eta + y_\xi y_\eta \quad g_{22} = \mathbf{g}_2 \cdot \mathbf{g}_2 = x_\eta^2 + y_\eta^2$$

The determinant of matrix g_{ij} is indicated by g (in order to avoid the confusion with gravity (g_0) we defined gravity symbol as g).

then we can write:

$$\sqrt{g} = \sqrt{\|g_{ij}\|} = \|J\| \quad (2.27)$$

²Any index that is repeated twice in a tensor term indicates the Einstein summation convention

which can be written in a more familiar manner (Fletcher, 1988) as:

$$\sqrt{g} \equiv \frac{\partial(x, y)}{\partial(\xi, \eta)} = \begin{vmatrix} \frac{\partial x}{\partial \xi} & \frac{\partial x}{\partial \eta} \\ \frac{\partial y}{\partial \xi} & \frac{\partial y}{\partial \eta} \end{vmatrix}$$

The general arc length increment can be written as:

$$(ds)^2 = \sum_{i=1}^2 \sum_{j=1}^2 g_{ij} d\xi^i d\xi^j \quad (2.28)$$

The new basis ($\mathbf{g}_1, \mathbf{g}_2$) may be not normalized, hence $\sqrt{g_{ii}}$ can be used to find components with respect to normalized unit vectors, thus an increment of arc length (Thompson, 1982) on a coordinate line along which ξ^i varies is given by:

$$ds^i = \|\mathbf{g}_i\| d\xi^i = \sqrt{g_{ii}} d\xi^i$$

Also the differential surface element dS^i on a coordinate surface of constant ξ^i is given by:

$$dS^i = \sqrt{g_{jj}g_{kk} - g_{jk}^2} d\xi^j d\xi^k = \sqrt{g^{ii}g} d\xi^j d\xi^k \quad i = 1, 2, 3 \quad (2.29)$$

The differential volume element is given by:

$$dV = \sqrt{g} d\xi^1 d\xi^2 d\xi^3 \quad (2.30)$$

2.4.3 Mapping of the Physical and computational spaces

The method used for this study of SWE (Shallow water Equations), is often used by the researchers working with the curvilinear boundary-fitted coordinates (Thompson, 1982, Sheng and Hirsh, 1984, Sheng et al., 2010). While the use of non-orthogonal curvilinear grids allows for a large variety of geometries, numerical procedures are much more difficult in curved grids. This is the reason why in CFD flow solvers, the curvilinear grid in the physical domain (physical space) is often internally mapped to a Cartesian grid in a new domain (computational space). Many calculations are performed much more efficiently in the simple Cartesian grid in computational space (Sadarjoen et al., 1994, Fletcher, 1988). Consequently, it is extremely convenient to perform all computations in the transformed space where the grid mesh is uniform and Cartesian. This simplicity does not come without a price, it is important to know how to create the transformation metrics (metric tensor), which relate two counterpart domains. The mapping of the physical region onto the transformed region must be one-to-one, so that

every point in the physical field corresponds to one, and only one point in the transformed field (Fig. 2.8). The fact that differential equations in curvilinear grid have the same structure as in the rectangular grid, is to the advantage of coding. The number of adjacent points is known and presented by subscripts i, j in the same way. All computations will be done in the computational region in which we have a simple rectangular grid with space step $\Delta\xi = 1, \Delta\eta = 1$. The drawback in application of this method is that equations are more complicated.

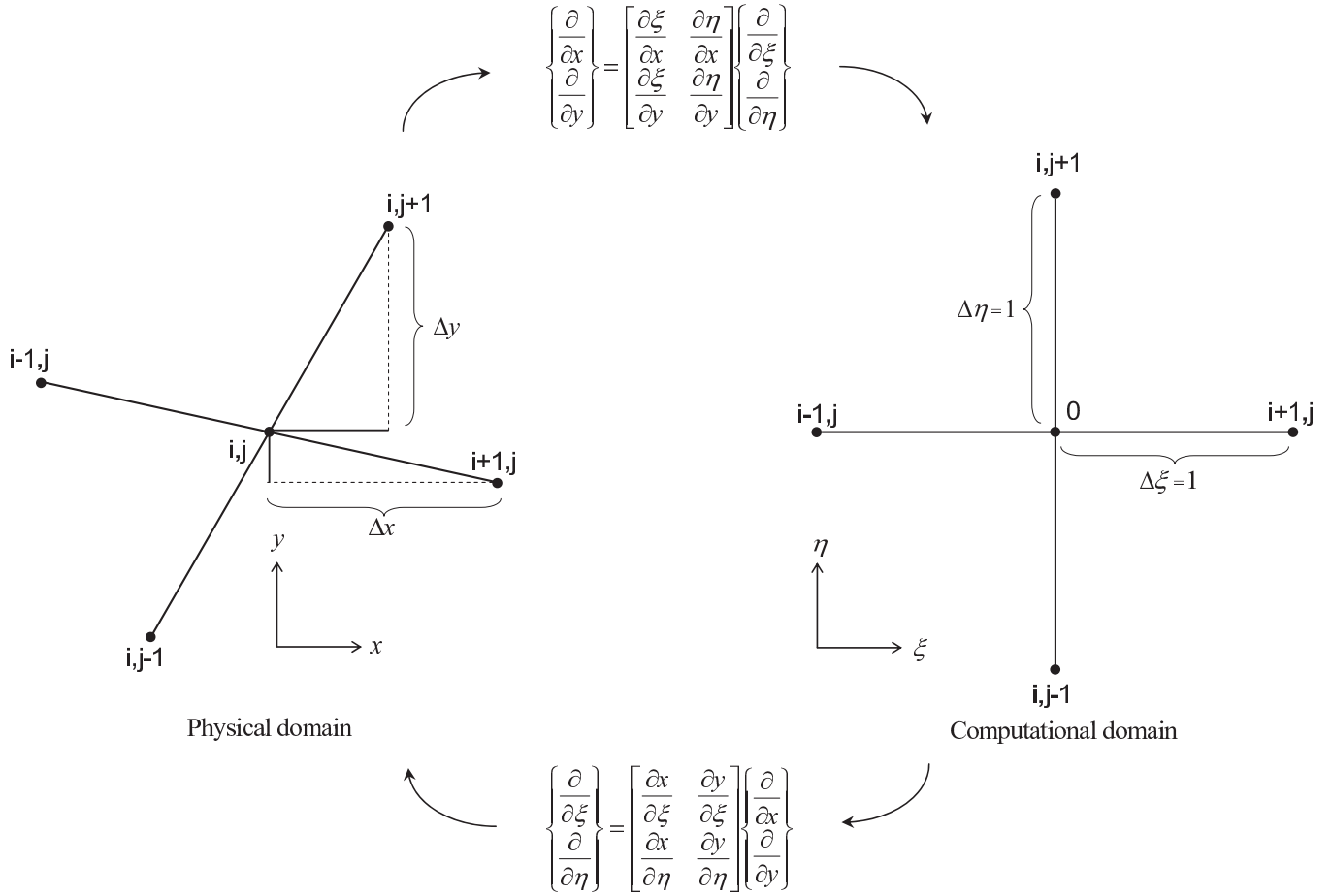


Figure 2.8: Coordinate mapping, which transforms the domain into a simpler (usually rectangular) domain.

2.4.4 contravariant and covariant vector components

A physical vector quantity \vec{V} can be expressed with two different types of components, **covariant** and **contravariant**.

$$\vec{V} = v^i \mathbf{g}_i \quad (\text{contravariant components of } \vec{V}) \quad (2.31)$$

$$\vec{V} = v_i \mathbf{g}^i \quad (\text{covariant components of } \vec{V}) \quad (2.32)$$

In the case of **contravariant** components, the numerical values of the components of these quantities in a "new" coordinate system can be calculated, given the components of the same vector in an "old" coordinate system, by using a linear transformation which is **inverse** of the linear transformation used to calculate the components of new tangential basis vectors in terms of the old tangential basis vectors (Agrawal, 2002): this is the reason why these components are called "contravariant". The details of these transformations have been discussed in Sec. 2.4.1. They are represented by superscripted indices in tensor notations or in Einstein convention such as velocity vectors $v^i = (v^1, v^2)$. The components of contravariant vectors are taken with respect to tangential basis vectors (ordinary basis that we call the covariant basis vectors) which are represented with subscripts like $\mathbf{g}_1, \mathbf{g}_2$. Hence vector \vec{V} writes:

$$\vec{V} = v^1 \mathbf{g}_1 + v^2 \mathbf{g}_2$$

In addition, some physical vectors are preferred to be defined by covariant components regarding to the contravariant basis vectors. The reason why they are called **covariant** is that the numerical values of the components of these quantities in a "new" coordinate system can be calculated from the components of the same vector in an "old" coordinate system using a linear transformation which is the **same** as the linear transformation used to calculate the components of new tangential basis vectors in terms of the old tangential basis vectors. In tensor notations or in Einstein convention, such components are represented with subscripts, $v_i = (v_1, v_2)$. The components of covariant vectors are taken with respect to perpendicular basis vectors (the contravariant basis vectors) which are represented with superscripts like $\mathbf{g}^1, \mathbf{g}^2$. Hence we can also write the vector \vec{V} :

$$\vec{V} = v_1 \mathbf{g}^1 + v_2 \mathbf{g}^2$$

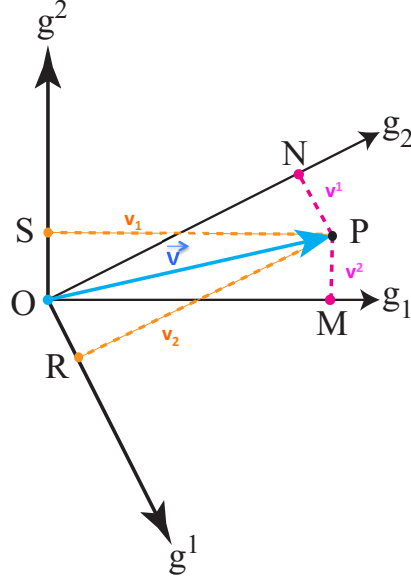


Figure 2.9: The contravariant components (red dotted lines) of the vector \vec{OP} are \vec{PN} and \vec{PM} , the covariant components (orange dotted lines) are \vec{PS} and \vec{PR} .

To clarify these definitions, an example in two dimensions space is provided here. Fig. 2.9 indicates that the first contravariant component of the vector \vec{OP} is a perpendicular projection of \vec{OP} on g^1 , \vec{OR} . The second contravariant components of \vec{OP} is \vec{OS} on g^2 . Besides, the first covariant component of the vector \vec{OP} is a perpendicular projection of \vec{OP} on g_1 , \vec{OM} . The second covariant components is \vec{ON} on g_2 .

Considering the two systems of basis vectors (Sec. 2.4.4), it should be noted that they form a bi-orthogonal system:

$$\mathbf{g}^i \cdot \mathbf{g}_j = \delta_j^i$$

where δ_j^i is named Kronecker symbol ($\delta_j^i = 1$ if $i = j$, $\delta_j^i = 0$ otherwise)

Then the contravariant and covariant components of a vector \vec{V} can be expressed as:

$$\vec{V} = \mathbf{e}_i \cdot v^i \quad i = 1, 2 \quad \text{where in Cartesian } (v^1, v^2) = (u, v) \quad (2.33a)$$

$$\vec{V} = (\mathbf{g}^i \cdot \vec{V}) \mathbf{g}_i \quad i = 1, 2 \quad (2.33b)$$

$$\vec{V} = (\mathbf{g}_i \cdot \vec{V}) \mathbf{g}^i \quad i = 1, 2 \quad (2.33c)$$

where $v^i = \mathbf{g}^i \cdot \vec{V}$ is the **contravariant component** and $v_i = \mathbf{g}_i \cdot \vec{V}$ is the **covariant component** of the vector \vec{V} (See Fig. 2.10).

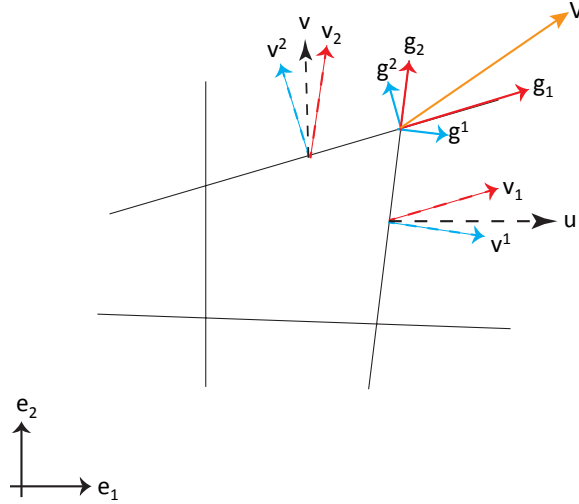


Figure 2.10: Illustration of Cartesian components (u, v) (black), covariant v_i (red) and contravariant v^i (blue) components of \vec{V} vector (orange) over a staggered grid.

Transformation of components between different basis

According to Sec. 2.4.4, one can define the two principal transformation rules of vector components regarding their basis. General transformation rules between two coordinate systems that can be introduced by, $\{\tilde{x}^i\}_{i=1,2,\dots,n}$ and $\{x^j\}_{j=1,2,\dots,n}$, as a way of assigning n real numbers for each point. The first transformation rule can be generalized to a set of vectors that we call contravariant vector components (Smirnov, 2004):

$$\tilde{v}^i = \frac{\partial \tilde{x}^i}{\partial x^j} v^j \quad (2.34)$$

The second one can be generalized to a set of vectors that we call covariant vector components:

$$\tilde{v}_i = \frac{\partial x^j}{\partial \tilde{x}^i} v_j \quad (2.35)$$

2.4.5 Generalized differentiation

In order to resolve the Navier-Stokes and transport equation, we need to use some differential operators, particularly gradient and Laplacian. Therefore, we have to redefine these basic operations in general form account for that when changing the coordinate basis. Most of the variables involved in Navier-Stokes and transport equations are in form of tensor.

Note that a tensor is linked to a given point and given coordinates. When we want to perform the differential operations on a tensor, these operations should refer to the same point

and at the same reference. However, a partial derivative of a tensor of the order one (vector) is not generally an **invariant** under coordinate transformations of type Eq. 2.34 and Eq. 2.35. In the general case of a non-orthogonal curvilinear coordinate system we should use more complex differentiation rules to preserve the invariance of the derivative related to the direction change of basis vectors in different points. In the following, we will use the contravariant components via the covariant basis. Thus, we need to be familiar with the different operators in covariant form. This choice gives us a very simple form of divergence; later, we will talk more about the reasons for which we have taken this decision (Sec. 2.4.7).

2.4.5.1 Absolute differential and covariant derivative

In this part, we discuss some differential operations for the E_2 (2D space with covariant basis vectors, see in Fig. 2.6), in the general system of coordinate. These rules are called the rules of covariant differentiation and they guarantee that the derivative itself is a tensor. According to these rules the derivatives for covariant and contravariant components are slightly different. They are expressed as follows in vector case (Smirnov, 2004). If $\vec{\mathbf{a}}$ is an arbitrary vector of E_2 with contravariant components $a^i(\xi, \eta)$ in the basis coordinates \mathbf{g}_i :

$$\mathbf{a} = a^i \mathbf{g}_i$$

By moving from point $P(\xi, \eta)$ to the point $P'(\xi' = \xi + d\xi, \eta' = \eta + d\eta)$, the basis coordinate also changes from \mathbf{g}_i to $\mathbf{g}_i + d\mathbf{g}_i$ (see in Fig. 2.11). We need an **affine connexion** when we try to find a relation between these two basis coordinate ($\mathbf{g}_i \rightarrow \mathbf{g}_i + d\mathbf{g}_i$). The $\vec{\mathbf{a}}$ vector becomes $\vec{\mathbf{a}} + d\vec{\mathbf{a}}$ with

$$d\vec{\mathbf{a}} = da^i \mathbf{g}_i + a^i d\mathbf{g}_i \quad (2.36)$$

$$d\mathbf{g}_i = \Gamma_{ki}^j d\xi^k \mathbf{g}_j \quad i, j, k = 1, 2 \quad (2.37)$$

$$d\vec{\mathbf{a}} = \nabla a^i \mathbf{g}_i \quad (2.38)$$

with

$$\nabla a^i = da^i + \Gamma_{kl}^j a^l d\xi^k \quad (2.39)$$

and,

$$da^i = \frac{\partial a^i}{\partial \xi^k} d\xi^k$$

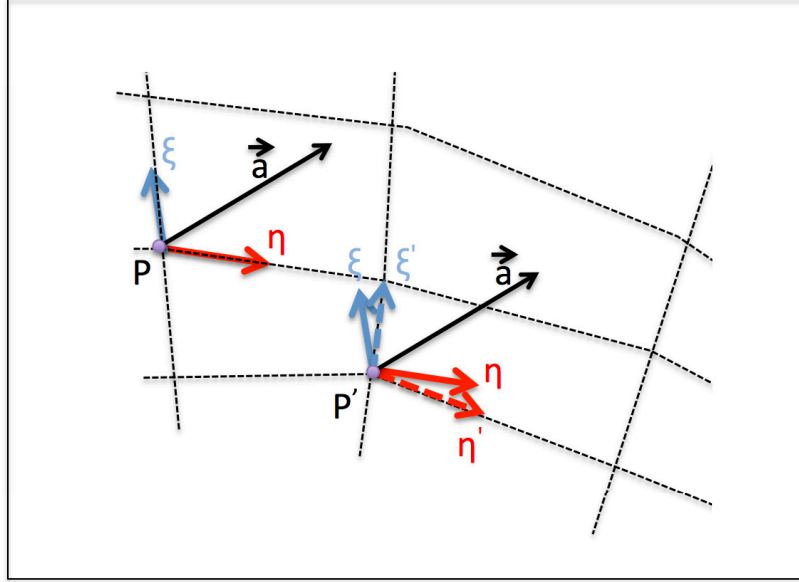


Figure 2.11: Moving from point $P(\xi, \eta)$ to the point $P'(\xi + d\xi, \eta + d\eta)$ by using covariant basis coordinates.

The expression ∇a^j is the absolute differential of the contravariant component a^j of \vec{a} and is finally defined as:

$$\nabla a^i = \left(\frac{\partial a^i}{\partial \xi^k} + \Gamma_{kl}^j a^l \right) d\xi^k = \nabla_k a^i \cdot d\xi^k \quad (2.40a)$$

$$\nabla_k a^i = \frac{\partial a^i}{\partial \xi^k} + \Gamma_{kl}^j a^l \quad (2.40b)$$

where the mixed tensor $\nabla_k a^j$ (k covariant and j contravariant) is the covariant derivative of the contravariant component a^j of vector \vec{a} relative to the ξ^k coordinate. It constitutes the generalization to curvilinear coordinates of the notion of partial derivative $\frac{\partial a^j}{\partial y^k}$ relative to a fixed reference.

The Γ_{ki}^j is defined as:

$$\Gamma_{kl}^j = \frac{\partial \xi^j}{\partial x^p} \frac{\partial^2 x^p}{\partial \xi^l \partial \xi^k} = \frac{1}{2} g^{jp} \left(\frac{\partial g_{pl}}{\partial \xi^k} + \frac{\partial g_{pk}}{\partial \xi^l} - \frac{\partial g_{lk}}{\partial \xi^p} \right) \quad (2.41)$$

and is also known in tensor calculus as Christoffel symbol of the second order³. The methods to obtain functions Γ_{kl}^j are not explained in details here (Denis-Papin and Kaufman, 1966), p107-108). It can be shown that all Γ_{kl}^j are zero if the coordinate system \mathbf{e}_j is fixed. Indeed, in this case, $d\mathbf{g}_j \equiv 0$, which implies that all Γ_{ki}^j are zero.

³In general in mathematics:

Γ_{ijk} : Christoffel symbol of the first order.

Γ_{ik}^j : Christoffel symbol of the second order.

The differentiation of a general n-covariant, m-contravariant tensor can be written:

$$\begin{aligned} \nabla A_{i_1 \dots i_n, p}^{j_1 \dots j_m} = & \frac{\partial}{\partial x^p} A_{i_1 \dots i_n, k}^{j_1 \dots j_m} + \Gamma_{qp}^{j_1} A_{i_1 \dots i_n}^{qj_2 \dots j_m} + \dots + \Gamma_{qp}^{j_m} A_{i_1 \dots i_n}^{j_1 \dots j_{m-1}q} \\ & - \Gamma_{i_1 p}^q A_{qi_2 \dots i_n}^{j_1 \dots j_m} - \dots - \Gamma_{i_n p}^q A_{i_1 \dots i_{n-1}q}^{j_1 \dots j_m} \end{aligned} \quad (2.42)$$

Despite their seeming complexity, the relations of covariant differentiation can be easily implemented algorithmically (Smirnov, 2004) and used in numerical solutions on arbitrary curved grids.

2.4.6 Differential operators

This section explains how to define the classic operators typically encountered in geophysical fluid dynamics such as gradient, divergence and Laplacian in curvilinear coordinate system.

Gradient of a scalar

Consider a scalar function $\Phi(\xi^1, \xi^2, \dots, \xi^n)$ (contravariant components in covariant basis) and its differential:

$$d\Phi = \frac{\partial \Phi}{\partial \xi^i} d\xi^i$$

The n functions $\frac{\partial \Phi}{\partial \xi^i}$ constitute the covariant components of a tensor named *gradient vector*:

$$\text{Grad}_k \Phi = \frac{\partial \Phi}{\partial \xi^k} \quad (2.43)$$

In this method, we get the derivative of the contravariants components of the same gradient vector by taking advantage of metric tensor.

$$\text{Grad}^j \Phi = g^{jk} \text{Grad}_k \Phi = g^{jk} \frac{\partial \Phi}{\partial \xi^k}$$

Divergence of a contravariant vector

Consider the vector $\vec{A}(\xi^1, \xi^2, \dots, \xi^n)$ defined by its contravariant components. We define the *divergence of vector* \vec{A} with the following expression

$$\text{Div} \vec{A} = \delta_k^i \nabla_i A^k = \nabla_k A^k$$

$$\delta_k^i$$

is the Kronecker symbol defined as:

$$\delta_k^i = \begin{cases} 0 & \text{if } (i \neq j), \\ 1 & \text{if } (i = j). \end{cases}$$

Using the previous results on the covariant derivative of a contravariant vector, we obtain:

$$\text{Div} \vec{A} = \frac{\partial A^k}{\partial \xi^k} + \Gamma_{kl}^k A^l \quad j, k, l = 1, 2, \dots, n$$

We can introduce a special property of the Christoffel symbols (Denis-Papin and Kaufman, 1966).

$$\Gamma_{kl}^k = \frac{1}{\sqrt{g}} \frac{\partial \sqrt{g}}{\partial \xi^l}$$

where \sqrt{g} is the determinant of g_{ij} (see in Eq. 2.27); finally we get:

$$\text{Div} \vec{A} = \frac{1}{\sqrt{g}} \cdot \frac{\partial(\sqrt{g} A^k)}{\partial \xi^k} \quad (2.44)$$

2.4.7 Choice of velocity components for complex geometry

Regarding the choice of the velocity components, one has to select either the Cartesian, or the contravariant, or the covariant components as primary variables.

For each of them there are both advantages and disadvantages. In order to better understand the differences, we are considering continuity equation in the area represented in Fig. 2.10. Differences between Cartesian, Covariant and contravariant components are represented by u , V_1 and V^1 respectively for the first component and v , V_2 and V^2 for the second one, using over a classical cell of staggered grid.

When we use Cartesian components of velocity on the physical space, the momentum equations in curvilinear coordinates satisfies the physical conservation laws (Shyy and Vu, 1991, Sharman et al., 1988). On the other hand, using the contravariant components does not guarantee the physical conservation in the momentum equations, but makes the equations simpler (Sheng and Hirsh, 1984, Sheng, 1990, Sheng et al., 2010).

In order to better understand the easy use of the contravariant components in the transport equation applied to Φ , the latter equation is presented using contravariant components (Eq. 2.45a) or Cartesian components (Eq. 2.45b).

$$\frac{\partial(\sqrt{g}\Phi)}{\partial t} + \frac{\partial(\sqrt{g}V^1\Phi)}{\partial \xi} + \frac{\partial(\sqrt{g}V^2\Phi)}{\partial \eta} = S\sqrt{g} \quad (2.45a)$$

$$\frac{\partial(\sqrt{g}\Phi)}{\partial t} + \frac{\partial(\sqrt{g}(uJ_{\eta\xi}^{yz} + vJ_{\eta\xi}^{zx})\Phi)}{\partial \xi} + \frac{\partial(\sqrt{g}(uJ_{\xi\xi}^{yz} + vJ_{\xi\xi}^{zx})\Phi)}{\partial \eta} = S\sqrt{g} \quad (2.45b)$$

In both cases, the quantity $\sqrt{g}\Phi$ is conserved, and the transport equation is said to be in strong conservation form (for exhaustive treatments of various conservation law forms, see (Sharman et al., 1988)). In Eq. 2.45a, the Jacobians of transformation are:

$$\begin{aligned} J_{\eta\zeta}^{yz} &= \sqrt{g}\xi_x & J_{\eta\zeta}^{zx} &= \sqrt{g}\xi_y & J_{\eta\zeta}^{xy} &= \sqrt{g}\xi_z \\ J_{\zeta\xi}^{yz} &= \sqrt{g}\eta_x & J_{\zeta\xi}^{zx} &= \sqrt{g}\eta_y & J_{\zeta\xi}^{xy} &= \sqrt{g}\eta_z \\ J_{\xi\eta}^{yz} &= \sqrt{g}\zeta_x & J_{\xi\eta}^{zx} &= \sqrt{g}\zeta_y & J_{\xi\eta}^{xy} &= \sqrt{g}\zeta_z \end{aligned} \quad (2.46)$$

In order to reduce the visual complexity of this equation 2.45b, one could solve it using the form given by 2.45a and simply define the contravariant velocities (Eq. 2.33a) as separate quantities to be pre-computed at each time-step and inserted during the integration.

According to Shyy and Vu (1991), even using contravariant and covariant components do not guarantee full conservation for the momentum equations. Shyy and Vu (1991) explains that the curvatures of the grid lines introduce extra source terms into the governing equations which cause the degrees of satisfaction of physical conservation sensitive to the non-uniformity and skewness of the mesh distribution (Fig. 2.12). Skewness is one quality criteria the computational grid, and varies between 0 for the best (for the orthogonal case) to 1 for the worst. According to Fig. 2.12, the mentioned extra source terms are more important on the mesh with equiangular skew (red) and less on the mesh with square shape.

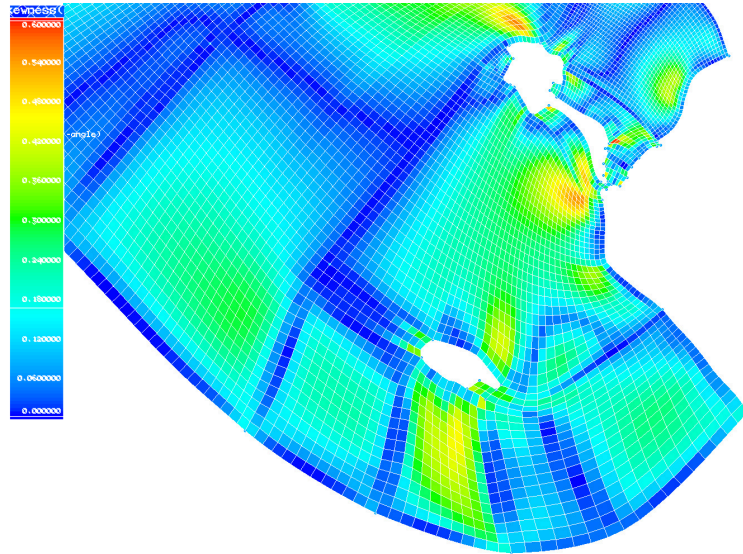


Figure 2.12: Skewness variation.

Though for the continuity equation, the contravariant components of velocity can maintain both the fully conservative form and compactness of the equation. The other conservation-law is called geometric conservation since the governing equations retain the conservation-law form but contain only the geometric quantities (Thomas and Lombard, 2012).

Hence using the contravariant component of velocity (Shyy and Vu, 1991) serves as a good case to test whether an algorithm can honor the geometric aspect of the conservation in a discrete form. In this study, we decide to use the contravariant component of velocity.

The following table 2.1 summarizes the points discussed above.

| Velocity Components | Momentum Equations | | | Continuity Equations |
|---------------------|--|--|---|--|
| | Convection | Pressure | Viscous | |
| Cartesian | satisfies both physical and geometric laws | satisfies both physical and geometric laws | satisfies physical but not geometric laws | satisfies both physical and geometric laws |
| contravariant | does not satisfy either law | satisfies both physical and geometric laws | does not satisfy either law | satisfies both physical and geometric laws |

Table 2.1: Choice of velocity components regarding the satisfaction of physical and geometric conservation form for momentum and continuity equations (Shyy and Vu, 1991).

2.4.7.1 Scale adjusting

Once we have defined the curvilinear coordinates (ξ, η) , we necessarily define increments along the lines $\xi = C^{te}$ or $\eta = C^{te}$. Actually new basis vectors are chosen so that these increments are uniform in the new coordinates system. Then their lengths are not necessarily unit and even are dimensionless. In standard vector calculus, the notations contra-variance and covariance do not interfere, but in the general curvilinear coordinate as the basis vectors are not unit nor dimensionless, the components v^j are not the physical velocity (Vreugdenhil, 2013). In tensor calculus, the physical magnitude $v(j)$ is obtained by multiplying the contravariant component by the corresponding basis vector module or by dividing the covariant component by the same module.

$$v(j) = \sqrt{\mathbf{g}_j \cdot \mathbf{g}_j} v^j = \sqrt{g_{jj}} v^j \quad (2.47a)$$

$$v^j = \frac{1}{\sqrt{\mathbf{g}_j \cdot \mathbf{g}_j}} v(j) = \frac{1}{\sqrt{g_{jj}}} v(j) \quad (2.47b)$$

There is no summation on j and $v(j)$ is the actual velocity components in the coordinate directions. It is reminded that in an orthogonal space:

$$\begin{aligned} g_{ij} &= \mathbf{e}_i \cdot \mathbf{e}_j = 0 & \text{if} & \quad i \neq j & \quad i, j = 1, 2, \dots, n \\ g_{jj} &= (\mathbf{e}_j)^2 & \text{when} & \quad \mathbf{e}_j = \sqrt{g_{jj}} & \quad j = 1, 2, \dots, n \end{aligned}$$

We will now modify the equations of Navier-Stokes using the boundary-fitted coordinate and tensorial hypothesis, completed by a tracer conservation equation to express the comparison between these equation on either the Cartesian and generalized curvilinear basis.

2.4.8 Continuity equation

In an incompressible fluid, the Eulerian description of the global conservation law of mass implies that the variations of the height of the water column are balanced by mass flow across the fixed walls of this water column if the environment remains continuous without density variation, according to the Boussinesq approximation.

$$\frac{\partial \zeta}{\partial t} + \text{Div}(D\vec{U}) = 0 \quad (2.48)$$

with ζ the elevation of the free surface, $D = \zeta + H$ the depth of the water column and \vec{U} the velocity field. This is the continuity equation, expressed independently of the coordinate system. As mentioned previously (Sec. 2.4.6), by using the results of the divergence operator, this equation can be written in curvilinear coordinates from contravariant components of the velocity field \vec{U} .

$$\frac{\partial \zeta}{\partial t} + \frac{1}{\sqrt{g}} \cdot \frac{\partial(\sqrt{g}Du^k)}{\partial x^k} + \frac{\partial D\omega}{\partial \sigma} = 0$$

which gives after development:

$$\frac{\partial \zeta}{\partial t} + \frac{1}{\sqrt{g}} \cdot \left(\frac{\partial(\sqrt{g}Du^1)}{\partial \xi} + \frac{\partial(\sqrt{g}Du^2)}{\partial \eta} \right) + \frac{\partial D\omega}{\partial \sigma} = 0 \quad (2.49)$$

where:

$$\begin{aligned} (x^1, x^2, x^3) &= (\xi, \eta, \sigma) \\ (u^1, u^2, u^3) &= (u, v, \omega) \end{aligned}$$

2.4.9 Equations of momentum conservation

Considering the Navier-Stokes equations solved in MARS-3D code (Sec. 2.2.1), the momentum equations in horizontal plane contains six main terms as presented here:

$$\overrightarrow{\mathbf{Acc}} + \overrightarrow{\mathbf{Cor}} = \overrightarrow{\mathbf{Pres}} + \overrightarrow{\mathbf{IPG}} + \overrightarrow{\mathbf{V}_{\text{Dif}}} + \overrightarrow{\mathbf{H}_{\text{Dif}}}$$

- $\overrightarrow{\mathbf{Acc}}$ Acceleration terms,
- $\overrightarrow{\mathbf{Cor}}$ Coriolis forcing,
- $\overrightarrow{\mathbf{Pres}}$ Pressure forcing,
- $\overrightarrow{\mathbf{IPG}}$ Internal Pressure Gradient,
- $\overrightarrow{\mathbf{V}_{\text{Dif}}}$ Vertical diffusion terms,
- $\overrightarrow{\mathbf{H}_{\text{Dif}}}$ Horizontal diffusion terms.

2.4.9.1 Cartesian coordinate

| direction | <i>isolines</i> ($y = c^{te}$) | <i>isolines</i> ($x = c^{te}$) |
|------------------|--|--|
| Acc | $\frac{du^1}{dt} = \frac{\partial u^1}{\partial t} + u^1 \frac{\partial u^1}{\partial x} + u^2 \frac{\partial u^1}{\partial y} + u^3 \frac{\partial u^1}{\partial \sigma}$ | $\frac{du^2}{dt} = \frac{\partial u^2}{\partial t} + u^1 \frac{\partial u^2}{\partial x} + u^2 \frac{\partial u^2}{\partial y} + u^3 \frac{\partial u^2}{\partial \sigma}$ |
| Cor | $-fu^2$ | fu^1 |
| Pres | $-g \frac{\partial \zeta}{\partial x} - \frac{1}{\rho_0} \frac{\partial p_{atm}}{\partial x}$ | $-g \frac{\partial \zeta}{\partial y} - \frac{1}{\rho_0} \frac{\partial p_{atm}}{\partial y}$ |
| IPG | $\frac{\partial}{\partial x} [D \int_{\sigma}^0 b \, d\sigma] + b \left(\sigma \frac{\partial D}{\partial x} - \frac{\partial H}{\partial x} \right)$ | $\frac{\partial}{\partial y} [D \int_{\sigma}^0 b \, d\sigma] + b \left(\sigma \frac{\partial D}{\partial y} - \frac{\partial H}{\partial y} \right)$ |
| V _{Dif} | $\frac{1}{D} \frac{\partial}{\partial \sigma} \left(\frac{N_z}{D} \frac{\partial u}{\partial \sigma} \right)$ | $\frac{1}{D} \frac{\partial}{\partial \sigma} \left(\frac{N_z}{D} \frac{\partial v}{\partial \sigma} \right)$ |
| H _{Dif} | $\frac{\partial}{\partial x} \left(\nu_x \frac{\partial u^1}{\partial x} \right) + \frac{\partial}{\partial y} \left(\nu_x \frac{\partial u^1}{\partial y} \right)$ | $\frac{\partial}{\partial x} \left(\nu_y \frac{\partial u^2}{\partial x} \right) + \frac{\partial}{\partial y} \left(\nu_y \frac{\partial u^2}{\partial y} \right)$ |

In Sec. 2.2, the Navier-Stokes equations have been written with the Boussinesq approximation in a standard Cartesian coordinate (x, y, σ) (Eq. 2.2 & 2.3).

Here we only consider the horizontal plane, which includes directions 1 and 2. The reason is that in this study the change of coordinates is limited to the change in horizontal plane and the third direction (vertical) is considered the same (σ coordinate) in both coordinate systems.

2.4.9.2 Generalized tensor notation

| direction | <i>isolignes</i> ($x^j = c^{te} \quad \forall j \neq i$) |
|------------------|---|
| Acc | $\frac{dv^i}{dt} = \frac{\partial v^i}{\partial t} + v^j \nabla_j v^i$ |
| Cor | $\varepsilon_{ij} f v_j$ |
| Pres | $-\frac{1}{\rho_0} (\rho_0 g \nabla^i \zeta + \nabla^i p_{atm})$ |
| IPG | $\nabla^i D \left(\int_{\sigma}^0 b \, d\sigma + \sigma b \right) + D \left(\int_{\sigma}^0 \nabla^i b \, d\sigma \right) - b \nabla^i H$ |
| V _{Dif} | $\frac{1}{D} \frac{\partial}{\partial \sigma} \left(\frac{N_z}{D} \frac{\partial v^i}{\partial \sigma} \right)$ |
| H _{Dif} | $\nabla^k (\nu \nabla_k (v^i))$ |

As described previously (Sec. 2.4.5.1), the vectorial law of momentum conservation is projected onto the covariant basis vectors (\mathbf{g}_i) on each direction, and therefore expressed for each of its contravariant components (\mathbf{v}^i).

2.4.9.3 Development in curvilinear coordinates

Unsteady and convective acceleration

$$\text{Acc}^i = \frac{\partial v^i}{\partial t} + v^j \nabla_j v^i = \frac{\partial v^i}{\partial t} + v^j \left(\frac{\partial v^i}{\partial x^j} + \Gamma_{jl}^i v^l \right) \quad (2.50)$$

$$\begin{aligned} \text{Acc}^1 = & \frac{\partial v^1}{\partial t} + v^1 \left(\frac{\partial v^1}{\partial \xi} + \Gamma_{11}^1 v^1 + \Gamma_{12}^1 v^2 + \Gamma_{13}^1 v^3 \right) \\ & + v^2 \left(\frac{\partial v^1}{\partial \eta} + \Gamma_{21}^1 v^1 + \Gamma_{22}^1 v^2 + \Gamma_{23}^1 v^3 \right) + v^3 \left(\frac{\partial v^1}{\partial \sigma} + \Gamma_{31}^1 v^1 + \Gamma_{32}^1 v^2 + \Gamma_{33}^1 v^3 \right) \end{aligned} \quad (2.51)$$

$$\begin{aligned} \text{Acc}^2 = & \frac{\partial v^2}{\partial t} + v^1 \left(\frac{\partial v^2}{\partial \xi} + \Gamma_{11}^2 v^1 + \Gamma_{12}^2 v^2 + \Gamma_{13}^2 v^3 \right) \\ & + v^2 \left(\frac{\partial v^2}{\partial \eta} + \Gamma_{21}^2 v^1 + \Gamma_{22}^2 v^2 + \Gamma_{23}^2 v^3 \right) + v^3 \left(\frac{\partial v^2}{\partial \sigma} + \Gamma_{31}^2 v^1 + \Gamma_{32}^2 v^2 + \Gamma_{33}^2 v^3 \right) \end{aligned} \quad (2.52)$$

According to tensorial calculus, all Γ_{ik}^j are zero if basis \vec{e}_j is fixed. In addition by definition of Christoffel symbol of the second kind, Γ_{ik}^j , if the i and k basis are perpendicular, the Γ_{ik}^j are all zero (Denis-Papin and Kaufman, 1966). That means:

$$\Gamma_{ij}^3 = \Gamma_{ji}^3 = \Gamma_{i3}^j = \Gamma_{3i}^j = 0 \quad (2.53)$$

Coriolis acceleration The horizontal component of the Coriolis acceleration is perpendicular to the displacement of a water particle. In E^2 plan, referring to the Sec. 2.4.7 on the definition of the different components of a vector, we find that the direction perpendicular to the first (second) basis vector \mathbf{g}^1 (\mathbf{g}^2) is the second (first) basis vector \mathbf{g}_2 (\mathbf{g}_1). We can write this in more detail as:

$$\text{Cor}^i = \varepsilon_{ij} f v_j$$

where f is the Coriolis parameter, v_j the covariant components of the velocity field and ε_{ij} the symbol of antisymmetry:

$$\varepsilon_{ik} = \begin{pmatrix} 0 & -1 \\ 1 & 0 \end{pmatrix}$$

Equation 2.8 is used to introduce the contravariant components of the velocity:

$$\text{Cor}^i = g_{kj} \varepsilon_{ij} f v^k \quad (2.54)$$

which gives for each direction

$$\text{Cor}^1 = g_{12} f v^1 + g_{22} f v^2 \quad (2.55)$$

$$\text{Cor}^2 = -g_{11} f v^1 - g_{21} f v^2 \quad (2.56)$$

Pressure forces

$$\text{Pres}^i = -\frac{1}{\rho_0} (\nabla^i p_{atm} + \rho_0 g \nabla^i \zeta)$$

The above expression uses the contravariant components of the derivative. As previously mentioned, the covariant and contravariant components of derivative are linked via covariant com-

ponents of the metric tensor \mathbf{g} .

$$\text{Pres}^i = -\frac{g^{ik}}{\rho_0} (\nabla_k p_{atm} + \rho_0 g \nabla_k \zeta) \quad (2.57)$$

A scalar (e.g. p_{atm} , ζ , ρ) is invariant during a change of coordinates and its value at a particular point is independent of the chosen coordinate framework. The components of the gradient are given by the partial derivatives.

$$\text{Pres}^i = -\frac{g^{ik}}{\rho_0} \left(\frac{\partial p_{atm}}{\partial x^k} + \rho_0 g \frac{\partial \zeta}{\partial x^k} \right)$$

$$\text{Pres}^1 = -\frac{g^{11}}{\rho_0} \left(\frac{\partial p_{atm}}{\partial \xi} + \rho_0 g \frac{\partial \zeta}{\partial \xi} \right) - \frac{g^{12}}{\rho_0} \left(\frac{\partial p_{atm}}{\partial \eta} + \rho_0 g \frac{\partial \zeta}{\partial \eta} \right) \quad (2.58)$$

$$\text{Pres}^2 = -\frac{g^{21}}{\rho_0} \left(\frac{\partial p_{atm}}{\partial \xi} + \rho_0 g \frac{\partial \zeta}{\partial \xi} \right) - \frac{g^{22}}{\rho_0} \left(\frac{\partial p_{atm}}{\partial \eta} + \rho_0 g \frac{\partial \zeta}{\partial \eta} \right) \quad (2.59)$$

Internal pressure gradient

$$\text{IPG}^i = \nabla^i D \left(\int_{\sigma}^0 b \, d\sigma + \sigma b \right) + D \left(\int_{\sigma}^0 \nabla^i b \, d\sigma \right) - b \nabla^i H$$

As explained previously, by using metric tensor \mathbf{g} , this equation can be rewritten in covariant form:

$$\text{IPG}^i = g^{ik} \left(\nabla_k D \left(\int_{\sigma}^0 b \, d\sigma + \sigma b \right) \right) + D \left(g^{ik} \int_{\sigma}^0 \nabla_k b \, d\sigma \right) - b g^{ik} \nabla_k H \quad (2.60)$$

$$\begin{aligned} \text{IPG}^1 &= g^{11} \left(\nabla_1 D \left(\int_{\sigma}^0 b \, d\sigma + \sigma b \right) \right) + g^{12} \left(\nabla_2 D \left(\int_{\sigma}^0 b \, d\sigma + \sigma b \right) \right) \\ &+ D \left(g^{11} \int_{\sigma}^0 \nabla_1 b \, d\sigma \right) + D \left(g^{12} \int_{\sigma}^0 \nabla_2 b \, d\sigma \right) - b g^{11} \nabla_1 H - b g^{12} \nabla_2 H \end{aligned} \quad (2.61)$$

$$\begin{aligned} \text{IPG}^2 &= g^{21} \left(\nabla_1 D \left(\int_{\sigma}^0 b \, d\sigma + \sigma b \right) \right) + g^{22} \left(\nabla_2 D \left(\int_{\sigma}^0 b \, d\sigma + \sigma b \right) \right) \\ &+ D \left(g^{21} \int_{\sigma}^0 \nabla_1 b \, d\sigma \right) + D \left(g^{22} \int_{\sigma}^0 \nabla_2 b \, d\sigma \right) - b g^{21} \nabla_1 H - b g^{22} \nabla_2 H \end{aligned} \quad (2.62)$$

Horizontal diffusion

$$\begin{aligned} \text{Difh}^i &= \nabla^j (\nu \nabla_k v^i) \\ \text{Difh}^i &= g^{jk} \nabla_j (\nu \nabla_k v^i) \end{aligned} \quad (2.63)$$

The first derivate, ∇_k , corresponds to the covariant derivative of the contravariant components of a vector and the second one, ∇_j , corresponds to the covariant derivative of a mixed tensor, once covariant and then contravariant.

$$\text{Difh}^i = \nu g^{jk} \nabla_j (\nabla_k v^i) + g^{jk} \nabla_k u^i \cdot \nabla_j \nu = \text{Difh}_u^i + \text{Difh}_\nu^i$$

Using the covariant derivatives of (i) contravariant components of a vector (Eq. 2.45b) and of (ii) a mixed tensor (Eq. 2.42), after using the Einstein summation convention, we get:

$$\begin{aligned} \text{Difh}_u^i = \nu g^{jk} & \left[\frac{\partial^2 v^i}{\partial x^j \partial x^k} + \Gamma_{kl}^i \frac{\partial v^l}{\partial x^j} + \Gamma_{jl}^i \frac{\partial v^l}{\partial x^k} - \Gamma_{jk}^l \frac{\partial v^i}{\partial x^l} \right. \\ & \left. + \left(\frac{\partial \Gamma_{kl}^i}{\partial x^j} + \Gamma_{jm}^i \Gamma_{kl}^m - \Gamma_{jk}^m \Gamma_{ml}^i \right) \cdot v^l \right] \end{aligned} \quad (2.64)$$

$$\text{Difh}_\nu^i = g^{jk} \frac{\partial \nu}{\partial x^j} \cdot \left(\frac{\partial v^i}{\partial x^k} + \Gamma_{kl}^i v^l \right) \quad (2.65)$$

Or, after full development, by taking advantage of the symmetry properties of the Christoffel coefficient ($\Gamma_{ik}^j = \Gamma_{ki}^j$) and simplification Eq. 2.53, we obtain ⁴:

$$\begin{aligned} \text{Difh}_u^i = \nu g^{11} & \left[2 \frac{\partial^2 v^i}{\partial \xi \partial \xi} + 2 \Gamma_{11}^i \frac{\partial u}{\partial \xi} + 2 \Gamma_{12}^i \frac{\partial v}{\partial \xi} - \Gamma_{11}^1 \frac{\partial v^i}{\partial \xi} - \Gamma_{11}^2 \frac{\partial v^i}{\partial \eta} \right. \\ & \left. + \frac{\partial \Gamma_{11}^i}{\partial \xi} \cdot u + \left(\frac{\partial \Gamma_{12}^i}{\partial \xi} + \Gamma_{11}^i \Gamma_{12}^1 + \Gamma_{12}^i \Gamma_{12}^2 - \Gamma_{11}^1 \Gamma_{12}^i - \Gamma_{11}^2 \Gamma_{22}^i \right) \cdot v \right] \\ + \nu g^{12} & \left[2 \frac{\partial^2 v^i}{\partial \xi \partial \eta} + \Gamma_{21}^i \frac{\partial u}{\partial \xi} + \Gamma_{22}^i \frac{\partial v}{\partial \xi} + \Gamma_{11}^i \frac{\partial u}{\partial \eta} + \Gamma_{12}^i \frac{\partial v}{\partial \eta} - \Gamma_{12}^1 \frac{\partial v^i}{\partial \xi} - \Gamma_{12}^2 \frac{\partial v^i}{\partial \eta} \right. \\ & \left. + \frac{\partial \Gamma_{21}^i}{\partial \xi} \cdot u + \left(\frac{\partial \Gamma_{22}^i}{\partial \xi} + \Gamma_{11}^i \Gamma_{22}^1 + \Gamma_{12}^i \Gamma_{22}^2 - \Gamma_{12}^1 \Gamma_{12}^i - \Gamma_{12}^2 \Gamma_{22}^i \right) \cdot v \right] \\ + \nu g^{21} & \left[2 \frac{\partial^2 v^i}{\partial \eta \partial \xi} + \Gamma_{11}^i \frac{\partial u}{\partial \eta} + \Gamma_{12}^i \frac{\partial v}{\partial \eta} + \Gamma_{21}^i \frac{\partial u}{\partial \xi} + \Gamma_{22}^i \frac{\partial v}{\partial \xi} - \Gamma_{21}^1 \frac{\partial v^i}{\partial \xi} - \Gamma_{21}^2 \frac{\partial v^i}{\partial \eta} \right. \\ & \left. + \left(\frac{\partial \Gamma_{11}^i}{\partial \eta} + \Gamma_{21}^i \Gamma_{11}^1 + \Gamma_{22}^i \Gamma_{11}^2 - \Gamma_{21}^1 \Gamma_{11}^i - \Gamma_{21}^2 \Gamma_{21}^i \right) \cdot u + \frac{\partial \Gamma_{12}^i}{\partial \eta} \cdot v \right] \\ + \nu g^{22} & \left[2 \frac{\partial^2 v^i}{\partial \eta \partial \eta} + 2 \Gamma_{21}^i \frac{\partial u}{\partial \eta} + 2 \Gamma_{22}^i \frac{\partial v}{\partial \eta} - \Gamma_{22}^1 \frac{\partial v^i}{\partial \xi} - \Gamma_{22}^2 \frac{\partial v^i}{\partial \eta} \right. \\ & \left. + \left(\frac{\partial \Gamma_{21}^i}{\partial \eta} + \Gamma_{21}^i \Gamma_{21}^1 + \Gamma_{22}^i \Gamma_{21}^2 - \Gamma_{22}^1 \Gamma_{11}^i - \Gamma_{22}^2 \Gamma_{21}^i \right) \cdot u + \frac{\partial \Gamma_{22}^i}{\partial \eta} \cdot v \right] \end{aligned} \quad (2.66)$$

⁴ $(x^1, x^2) = (\xi, \eta)$
 $(v^1, v^2) = (u, v)$

$$\begin{aligned}
\text{Difh}_u^1 = & \nu g^{11} \left[2 \frac{\partial^2 u}{\partial \xi \partial \xi} + \Gamma_{11}^1 \frac{\partial u}{\partial \xi} + 2 \Gamma_{12}^1 \frac{\partial v}{\partial \xi} - \Gamma_{11}^2 \frac{\partial u}{\partial \eta} \right. \\
& \left. + \frac{\partial \Gamma_{11}^1}{\partial \xi} \cdot u + \left(\frac{\partial \Gamma_{12}^1}{\partial \xi} + \Gamma_{12}^1 \Gamma_{12}^2 - \Gamma_{11}^2 \Gamma_{22}^1 \right) \cdot v \right] \\
& + \nu g^{12} \left[2 \frac{\partial^2 u}{\partial \xi \partial \eta} + \Gamma_{22}^1 \frac{\partial v}{\partial \xi} + \Gamma_{11}^1 \frac{\partial u}{\partial \eta} + \Gamma_{12}^1 \frac{\partial v}{\partial \eta} - \Gamma_{12}^2 \frac{\partial u}{\partial \eta} \right. \\
& \left. + \frac{\partial \Gamma_{21}^1}{\partial \xi} \cdot u + \left(\frac{\partial \Gamma_{22}^1}{\partial \xi} + \Gamma_{11}^1 \Gamma_{22}^1 + \Gamma_{12}^1 \Gamma_{22}^2 - \Gamma_{12}^1 \Gamma_{12}^1 - \Gamma_{12}^2 \Gamma_{22}^1 \right) \cdot v \right] \\
& + \nu g^{21} \left[2 \frac{\partial^2 u}{\partial \eta \partial \xi} + \Gamma_{11}^1 \frac{\partial u}{\partial \eta} + \Gamma_{12}^1 \frac{\partial v}{\partial \eta} + \Gamma_{22}^1 \frac{\partial v}{\partial \xi} - \Gamma_{21}^2 \frac{\partial u}{\partial \eta} \right. \\
& \left. + \left(\frac{\partial \Gamma_{11}^1}{\partial \eta} + \Gamma_{22}^1 \Gamma_{11}^2 - \Gamma_{21}^2 \Gamma_{21}^1 \right) \cdot u + \frac{\partial \Gamma_{12}^1}{\partial \eta} \cdot v \right] \\
& + \nu g^{22} \left[2 \frac{\partial^2 u}{\partial \eta \partial \eta} + 2 \Gamma_{21}^1 \frac{\partial u}{\partial \eta} + 2 \Gamma_{22}^1 \frac{\partial v}{\partial \eta} - \Gamma_{22}^1 \frac{\partial u}{\partial \xi} - \Gamma_{22}^2 \frac{\partial u}{\partial \eta} \right. \\
& \left. + \left(\frac{\partial \Gamma_{21}^1}{\partial \eta} + \Gamma_{21}^1 \Gamma_{21}^1 + \Gamma_{22}^1 \Gamma_{21}^2 - \Gamma_{22}^1 \Gamma_{11}^1 - \Gamma_{22}^2 \Gamma_{21}^1 \right) \cdot u + \frac{\partial \Gamma_{22}^1}{\partial \eta} \cdot v \right] \quad (2.67)
\end{aligned}$$

$$\begin{aligned}
\text{Difh}_u^2 = & \nu g^{11} \left[2 \frac{\partial^2 v}{\partial \xi \partial \xi} + 2 \Gamma_{11}^2 \frac{\partial u}{\partial \xi} + 2 \Gamma_{12}^2 \frac{\partial v}{\partial \xi} - \Gamma_{11}^1 \frac{\partial v}{\partial \xi} - \Gamma_{11}^2 \frac{\partial v}{\partial \eta} \right. \\
& \left. + \frac{\partial \Gamma_{11}^2}{\partial \xi} \cdot u + \left(\frac{\partial \Gamma_{12}^2}{\partial \xi} + \Gamma_{11}^2 \Gamma_{12}^1 + \Gamma_{12}^2 \Gamma_{12}^2 - \Gamma_{11}^1 \Gamma_{12}^2 - \Gamma_{11}^2 \Gamma_{22}^2 \right) \cdot v \right] \\
& + \nu g^{12} \left[2 \frac{\partial^2 v}{\partial \xi \partial \eta} + \Gamma_{21}^2 \frac{\partial u}{\partial \xi} + \Gamma_{22}^2 \frac{\partial v}{\partial \xi} + \Gamma_{11}^2 \frac{\partial u}{\partial \eta} + \Gamma_{12}^2 \frac{\partial v}{\partial \eta} - \Gamma_{12}^1 \frac{\partial v}{\partial \xi} - \Gamma_{12}^2 \frac{\partial v}{\partial \eta} \right. \\
& \left. + \frac{\partial \Gamma_{21}^2}{\partial \xi} \cdot u + \left(\frac{\partial \Gamma_{22}^2}{\partial \xi} + \Gamma_{11}^2 \Gamma_{22}^1 + \Gamma_{12}^2 \Gamma_{22}^2 - \Gamma_{12}^1 \Gamma_{12}^2 - \Gamma_{12}^2 \Gamma_{22}^2 \right) \cdot v \right] \\
& + \nu g^{21} \left[2 \frac{\partial^2 v}{\partial \eta \partial \xi} + \Gamma_{11}^2 \frac{\partial u}{\partial \eta} + \Gamma_{12}^2 \frac{\partial v}{\partial \eta} + \Gamma_{21}^2 \frac{\partial u}{\partial \xi} + \Gamma_{22}^2 \frac{\partial v}{\partial \xi} - \Gamma_{21}^1 \frac{\partial v}{\partial \xi} - \Gamma_{21}^2 \frac{\partial v}{\partial \eta} \right. \\
& \left. + \left(\frac{\partial \Gamma_{11}^2}{\partial \eta} + \Gamma_{21}^2 \Gamma_{11}^1 + \Gamma_{22}^2 \Gamma_{11}^2 - \Gamma_{21}^1 \Gamma_{11}^2 - \Gamma_{21}^2 \Gamma_{21}^2 \right) \cdot u + \frac{\partial \Gamma_{12}^2}{\partial \eta} \cdot v \right] \\
& + \nu g^{22} \left[2 \frac{\partial^2 v}{\partial \eta \partial \eta} + 2 \Gamma_{21}^2 \frac{\partial u}{\partial \eta} + 2 \Gamma_{22}^2 \frac{\partial v}{\partial \eta} - \Gamma_{22}^1 \frac{\partial v}{\partial \xi} - \Gamma_{22}^2 \frac{\partial v}{\partial \eta} \right. \\
& \left. + \left(\frac{\partial \Gamma_{21}^2}{\partial \eta} + \Gamma_{21}^2 \Gamma_{21}^1 + \Gamma_{22}^2 \Gamma_{21}^2 - \Gamma_{22}^1 \Gamma_{11}^2 - \Gamma_{22}^2 \Gamma_{21}^2 \right) \cdot u + \frac{\partial \Gamma_{22}^2}{\partial \eta} \cdot v \right] \quad (2.68)
\end{aligned}$$

$$\begin{aligned}
\text{Difh}_\nu^i = & g^{11} \frac{\partial \nu}{\partial \xi} \cdot \left(\frac{\partial v^i}{\partial \xi} + \Gamma_{11}^i u + \Gamma_{12}^i v \right) + g^{12} \frac{\partial \nu}{\partial \xi} \cdot \left(\frac{\partial u^i}{\partial \eta} + \Gamma_{21}^i u + \Gamma_{22}^i v \right) \\
& + g^{21} \frac{\partial \nu}{\partial \eta} \cdot \left(\frac{\partial v^i}{\partial \xi} + \Gamma_{11}^i u + \Gamma_{12}^i v \right) + g^{22} \frac{\partial \nu}{\partial \eta} \cdot \left(\frac{\partial v^i}{\partial \eta} + \Gamma_{21}^i u + \Gamma_{22}^i v \right) \quad (2.69)
\end{aligned}$$

$$\begin{aligned} \text{Difh}_\nu^1 &= g^{11} \frac{\partial \nu}{\partial \xi} \cdot \left(\frac{\partial u}{\partial \xi} + \Gamma_{11}^1 u + \Gamma_{12}^1 v \right) + g^{12} \frac{\partial \nu}{\partial \xi} \cdot \left(\frac{\partial u}{\partial \eta} + \Gamma_{21}^1 u + \Gamma_{22}^1 v \right) \\ &+ g^{21} \frac{\partial \nu}{\partial \eta} \cdot \left(\frac{\partial u}{\partial \xi} + \Gamma_{11}^1 u + \Gamma_{12}^1 v \right) + g^{22} \frac{\partial \nu}{\partial \eta} \cdot \left(\frac{\partial u}{\partial \eta} + \Gamma_{21}^1 u + \Gamma_{22}^1 v \right) \end{aligned} \quad (2.70)$$

$$\begin{aligned} \text{Difh}_\nu^2 &= g^{11} \frac{\partial \nu}{\partial \xi} \cdot \left(\frac{\partial v}{\partial \xi} + \Gamma_{11}^2 u + \Gamma_{12}^2 v \right) + g^{12} \frac{\partial \nu}{\partial \xi} \cdot \left(\frac{\partial v}{\partial \eta} + \Gamma_{21}^2 u + \Gamma_{22}^2 v \right) \\ &+ g^{21} \frac{\partial \nu}{\partial \eta} \cdot \left(\frac{\partial v}{\partial \xi} + \Gamma_{11}^2 u + \Gamma_{12}^2 v \right) + g^{22} \frac{\partial \nu}{\partial \eta} \cdot \left(\frac{\partial v}{\partial \eta} + \Gamma_{21}^2 u + \Gamma_{22}^2 v \right) \end{aligned} \quad (2.71)$$

Complications compared with the equations in Cartesian coordinates are fourfold:

- Christoffel symbols appear in the advective terms,
- The Coriolis term is more complicated.
- The pressure term in the i direction equation is not just the gradient in that coordinate direction and creates some difficulties with finite difference solver.
- The diffusion terms are much more complicated and some terms are being ignored without reducing the precision significantly.

Gourrion (2005) developed a test-case to evaluate the terms of diffusion. He simulated a channel in which one of the boundary was fixed and the other moved at a constant speed. It was expected to see the progressive training of the body of water. Gourrion concluded that the viscous terms were used mainly to stabilize the model. According to him, for realistic simulation, diffusion terms have been vastly simplified and only the second derivative uncrossed has been retained for each direction.

2.4.10 Passive tracer equation

The equation Eq. 2.9 was written in the form of an advection-diffusion of a non-conservative tracer in Cartesian coordinates. We can rewrite it in a more general way under vector notation:

$$\frac{\partial DC}{\partial t} + \text{Div} \left(D \vec{U} C \right) - D \text{Div} \left(K \text{Grad} C \right) = S_o - S_i \quad (2.72)$$

or furthermore under the tensorial notation we obtain:

$$\frac{\partial DC}{\partial t} + \nabla_k (D u^k C) - D \nabla_k (K \text{Grad}^k C) = S_o - S_i$$

$$\frac{\partial DC}{\partial t} + \nabla_k (D u^k C) - D K \nabla_k (\text{Grad}^k C) - D \nabla_k K \cdot \text{Grad}^k C = S_o - S_i \quad (2.73)$$

Using the properties of differential operators mentioned in the Sec. 2.4.6, we obtain:

$$\frac{\partial DC}{\partial t} + \frac{1}{\sqrt{g}} \cdot \frac{\partial(\sqrt{g} D u^k C)}{\partial x^k} - \frac{D K}{\sqrt{g}} \cdot \frac{\partial(\sqrt{g} g^{jk} \frac{\partial C}{\partial x^j})}{\partial x^k} - g^{jk} D \frac{\partial K}{\partial x^k} \cdot \frac{\partial C}{\partial x^j} = S_o - S_i \quad (2.74)$$

and finally, after developing the repeated indices, however, it is worth to be noted that the diffusion part also has been simplified:

$$\begin{aligned} \frac{\partial DC}{\partial t} + \frac{1}{\sqrt{g}} \cdot \left(\frac{\partial(\sqrt{g} D u^1 C)}{\partial \xi} + \frac{\partial(\sqrt{g} D u^2 C)}{\partial \eta} \right) \\ - \frac{D K}{\sqrt{g}} \cdot \left(\frac{\partial(\sqrt{g} g^{11} \frac{\partial C}{\partial \xi} + g^{21} \frac{\partial C}{\partial \eta})}{\partial \xi} - \frac{\partial(\sqrt{g} g^{12} \frac{\partial C}{\partial \xi} + g^{22} \frac{\partial C}{\partial \eta})}{\partial \eta} \right) \\ - D \frac{\partial K}{\partial \xi} \cdot \left(g^{11} \frac{\partial C}{\partial \xi} + g^{21} \frac{\partial C}{\partial \eta} \right) - D \frac{\partial K}{\partial \eta} \cdot \left(g^{12} \frac{\partial C}{\partial \xi} + g^{22} \frac{\partial C}{\partial \eta} \right) \\ + \frac{\partial D(\omega^* C - \frac{K}{D^2} \frac{\partial C}{\partial \sigma})}{\partial \sigma} = S_o - S_i \end{aligned} \quad (2.75)$$

Splitting mode

The unsteady Navier-Stokes equations are discretized on a non-orthogonal curvilinear, multi-block, body conforming mesh using a cell-centered finite volume method. The convective terms are discretized using centered scheme and MACHO variable extrapolation is used to provide second-order accuracy. Most primitive equation models use mode splitting schemes. This aims to solve free surface wave propagation (barotropic mode) and internal motion (internal mode) separately, with time steps that may be different. Because of their high celerity, surface gravity waves require small time steps to be properly solved through explicit numerical schemes, whereas internal waves with weaker celerity may be processed with larger time steps. The two modes are closely linked as the barotropic pressure gradient calculated with the external mode is prescribed to the internal mode. The ratio between internal and external time steps is around 10-50 (Lazure and Dumas, 2008). Most of the models apply a correction to the 3D predicted currents to ensure consistency. This corrector step consists in adding to the 3D predicted currents the local difference between the 2D (external mode) calculated currents and the vertical integration of the predicted 3D currents. In order to eliminate problems induced by the use of different schemes for the internal mode, external mode equations were rewritten to allow strictly identical discretization over both time and space for the internal mode. It focuses on the coupling between modes. An iterative procedure is used to provide full consistency between modes without any extra correction.

2.5 Discretization of equations

2.5.1 Introduction

This section is mostly devoted to the governing Navier-Stokes equations and describing of their discretization. Problems of ADI method with non-orthogonal curvilinear coordinate are discussed to some extent in this section as well. The indices i, j, k refer to the position in the ξ, η, σ direction.

Free surface elevation $\zeta(i, j)$ is located at the center of the cell (i, j) in the horizontal mesh(Fig. 2.13a).

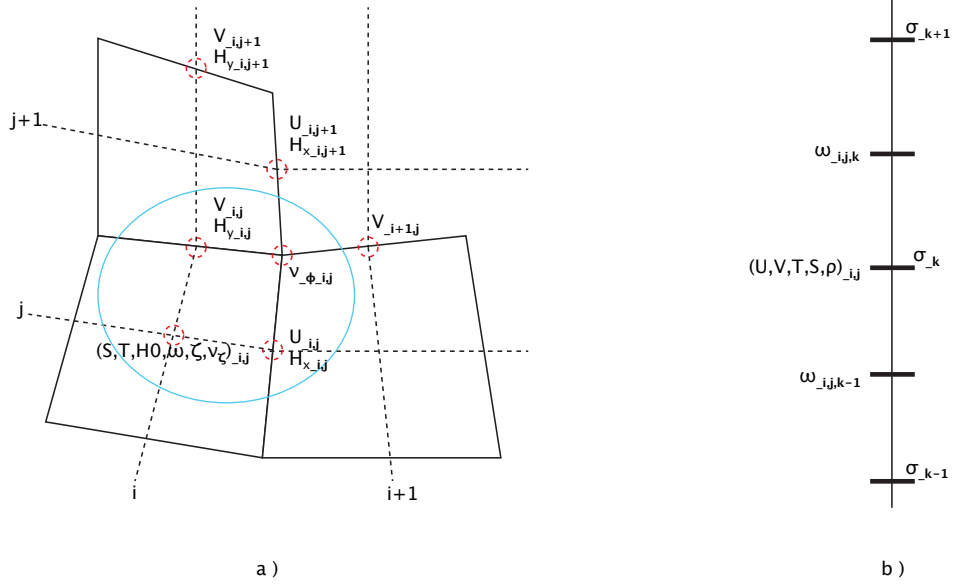


Figure 2.13: a) Variables positions in the Arakawa-C grid projected in a non-orthogonal curvilinear grid. b) Position of variables on the vertical axis.

The "zonal" velocity $U_{\phi_{i,j}}$ represent the orthogonal component averaged along the "east" side of the mesh (between centers indexed (i, j) , and $(i, j + 1)$) (Fig. 2.13a). The velocity located on the right side (to the East) of ζ keeps the same i index, while the nearest velocity point located on the west side of ζ is referred to $i - 1$ index. The same method is applied for the "meridian" velocity V .

The $V_{\phi_{i,j}}$ component is calculated by averaging along the "north" side of the mesh (between centers indexed (i, j) and $(i + 1, j)$) (Fig. 2.13a).

The following variables having the same i, j indices are located at the center of each mesh: ζ : free surface elevation (from a reference level; positive upwards); Concentration of any tracer (temperature or salinity included); D : water depth at the ζ position (already mentioned in Eq. 2.13); K_z, N_z : Vertical eddy diffusivity and viscosity; k : Turbulent kinetic energy, ω^* : Vertical velocity in sigma coordinates. The following variables are located at the same position as U (Zonal barotropic velocity), H_x : The bottom position in right side of mesh (with the same reference level as H); D_x : Height of the whole water column that is to say $D_x = H_x + 0.5(\zeta_{i,j} + \zeta_{i+1,j})$. The following variables are located at the same position as V (Meridian barotropic velocity); H_y : The bottom position in top side of mesh, D_y : Water depth.

This gives three different depth information (namely D, D_x, D_y) for each grid cell. The vertical discretization is also based on discretizing to a staggered grid. The center of the mesh, referred to 'k' index, is located at σ_k , from the bottom ($\sigma = -1$) up to the surface ($\sigma = 0$). At σ_k level the following variables are calculated in the Arakawa-C grid: concentration of tracers, S salinity, T temperature and density ρ .

Between these two cells, the vertical velocity computation point corresponding to index 'k' is located at $\sigma_{\omega k} = 0.5 * (\sigma_k + \sigma_{k+1})$. The following variables are calculated at the same horizontal location as $\sigma_{\omega k}$: K_z, N_z : eddy diffusivity and viscosity.

2.5.2 Adaptation of the ADI scheme to curvilinear coordinates, first step

In this section, the discretization of **barotropic** equations is developed in the general case of curvilinear coordinates systems.

Curvilinear equations of depth-integrated Navier-Stokes equations

In this study all equations were developed in 3D but for avoiding complex and fastidious writing, only the 2DH depth-integrated equations, modified by the same method are presented here. First, we start by presenting the Cartesian continuity equation (Eq. 2.1) in a general coordinates systems (Eq. 2.76).

$$\sqrt{g} \frac{\partial \zeta}{\partial t} + \frac{\partial (\sqrt{g} D U)}{\partial \xi} + \frac{\partial (\sqrt{g} D V)}{\partial \eta} = 0 \quad (2.76)$$

The Cartesian momentum equation (Eq. 2.2) for the j_{th} line, regarding the differential operators in general curvilinear system writes (Eq. 2.77):

Equations 2.76 & 2.77 synthetize the development of different terms as explained in Sec. 2.4.8 & 2.4.9, and express the simplifications which have been retained for the diffusion term.

$$\underbrace{\frac{\partial U}{\partial t}}_{\text{Acc}^1} + \underbrace{U \left(\frac{\partial U}{\partial x^1} + \Gamma_{11}^1 U + \Gamma_{12}^1 V \right) + V \left(\frac{\partial U}{\partial x^2} + \Gamma_{21}^1 U + \Gamma_{22}^1 V \right)}_{\text{NI}^1} - \underbrace{\frac{g_{12}}{\sqrt{g}} f U - \frac{g_{22}}{\sqrt{g}} f V}_{\text{Cor}^1} =$$

$$- \underbrace{g g^{11} \frac{\partial \zeta}{\partial x^1} - g g^{12} \frac{\partial \zeta}{\partial x^2}}_{\text{Pres}^1} - \underbrace{\frac{g \|\vec{u}\|}{S^2 D^{4/3}} U}_{\text{Frot}^1} + \underbrace{\nu_U g^{11} \frac{\partial^2 U}{\partial (x^1)^2} + \nu_U g^{22} \frac{\partial^2 U}{\partial (x^2)^2}}_{\text{Visc}^1} \quad (2.77)$$

2.5.2.1 Discrete equations along first ξ and second η axis

For the barotropic **ADI** resolution on a given j line, this leads to solve a linear tridiagonal system which evolves all along a predictor-corrector iterative process. First of all, it is useful to give a little explanation about the temporal scheme, in which a time-step between *time* n and *time* $n + 1$ is divided into two parts. During the first half time-step ($n \mapsto n + \frac{1}{2}$), the code starts by computing an explicit estimate of velocity components (here we note them $U^{n+\frac{1}{2},*}, V^{n+\frac{1}{2},*}$), in which the only semi-implicit terms are the bottom-stress. Then discretizing the continuity equation and momentum equation of the j_{th} line leads to a tridiagonal linear system for computing a first prediction of water surface $\zeta^{n+\frac{1}{2},*}$ and one of the final velocity component $U^{n+\frac{1}{2}}$. In the last part of first half time-step, in a tridiagonal linear system in j_{th} line the water elevation and the second final velocity component is computed ($\zeta^{n+\frac{1}{2}}, V^{n+\frac{1}{2}}$). In the following step ($n + \frac{1}{2} \mapsto n + 1$), a second estimation of velocities is computed first ($U^{n+1,*}, V^{n+1,*}$). Then, another use of the continuity and momentum equations is needed. However in j_{th} line this time, for computing a second prediction water surface $\zeta^{n+1,*}$ another final velocity component V^{n+1} . Finally, a second final surface water elevation and the other velocity component (ζ^{n+1}, U^{n+1}) are computed.

This predictor-corrector method is used to limit the errors due to splitting in two directions. In the following, the implicitly treated quantities are marked in bold (Lazure and Dumas, 2008).

Vertically integrated momentum equation along ξ direction (centered scheme) for estimating $U^{n+\frac{1}{2},*}$:

$$\overline{\mathbf{Acc}}^{\mathbf{1}} + \overline{\mathbf{NI}}^{\mathbf{1}} = \overline{\mathbf{Cor}}^{\mathbf{1}} + \overline{\mathbf{Pres}}^{\mathbf{1}} + \overline{\mathbf{Frot}}^{\mathbf{1}} + \overline{\mathbf{Visc}}^{\mathbf{1}} + \overline{\mathbf{Wind}}^{\mathbf{1}}$$

$$\mathbf{Acc}^1 \Rightarrow \frac{\mathbf{U}_{ij}^{n+\frac{1}{2},*} - U_{i,j}^n}{\Delta t/2} \quad (2.78)$$

$$\begin{aligned} \mathbf{NI}^1 \Rightarrow & U_{i,j}^n \cdot \left(\left[\frac{U^n}{2\Delta\xi} \right]_{i-1,j}^{i+1,j} + \Gamma_{11}^1 U_{i,j}^n + \Gamma_{12}^1 V_{i,j-U}^n \right) \\ & + V_{i,j-U}^n \cdot \left(\frac{1}{2} \left(\text{ms} \cdot \left[\frac{U^n}{\Delta\eta} \right]_{i,j-1}^{i,j} + \text{mn} \cdot \left[\frac{U^n}{\Delta\eta} \right]_{i,j}^{i,j+1} \right) + \Gamma_{21}^1 U_{i,j}^n + \Gamma_{22}^1 V_{i,j-U}^n \right) \end{aligned} \quad (2.79)$$

$$\mathbf{Cor}^1 \Rightarrow (f_u)_{ij} \left(\frac{g_{12}}{\sqrt{g}} U_{i,j}^n + \frac{g_{22}}{\sqrt{g}} V_{i,j-U}^n \right) \quad (2.80)$$

$$\text{Pres}^1 \Rightarrow -g \left(\frac{g^{11}}{\Delta\xi} [\zeta^n]_{i,j}^{i+1,j} + \frac{g^{12}}{\Delta\eta} d\zeta_{i,j-U}^n \right) - \frac{1}{\rho} \left(\frac{g^{11}}{\Delta\xi} [P_a^n]_{i,j}^{i+1,j} + \frac{g^{12}}{\Delta\eta} dP_{a\ i,j-U}^n \right) \quad (2.81)$$

$$\text{Frot}^1 \Rightarrow - (ft)_{ij} \left(\beta_2 \mathbf{U}^{n+\frac{1}{2},*}_{i,j} + \beta_1 U_{i,j}^n \right) \quad (2.82)$$

$$\begin{aligned} \text{Visc}^1 \Rightarrow & \frac{g^{11}}{\Delta\xi} \left(\left[\nu \frac{U^n}{\Delta\xi} \right]_{i,j}^{i+1,j} - \left[\nu \frac{U^n}{\Delta\xi} \right]_{i-1,j}^{i,j} \right) \\ & - \frac{g^{22}}{\Delta\eta} \left(\text{ms} \cdot \left[\nu \frac{U^n}{\Delta\eta} \right]_{i,j-1}^{i,j} - \text{mn} \cdot \left[\nu \frac{U^n}{\Delta\eta} \right]_{i,j}^{i,j+1} \right) \end{aligned} \quad (2.83)$$

$$\text{Wind}^1 \Rightarrow \frac{1}{D_x^n \rho} (\tau_{s\xi})_{i,j}^n \quad (2.84)$$

$V_{i,j-U}^n$, $d\zeta_{i,j-U}^n$, $dP_{a\ i,j-U}^n$ are some functions that are performed to obtain the values of the second velocity component, water levels and pressure in the middle of the right face of the mesh(Fig. 2.13).

- $V_{i,j-U}^n = f_{V2U} (V_{ij}^n, V_{i+1j}^n, V_{ij-1}^n, V_{i+1j-1}^n, i, j, U^n)$,
- $d\zeta_{i,j-U}^n = f_{\nabla\zeta}^U (\zeta_{ij}^n, \zeta_{i+1j}^n, \zeta_{ij+1}^n, \zeta_{i+1j+1}^n, \zeta_{ij-1}^n, \zeta_{i+1j-1}^n, i, j)$,
- $dP_{a\ i,j-U}^n = f_{\nabla P_a}^U (P_{a\ ij}^n, P_{a\ i+1j}^n, P_{a\ ij+1}^n, P_{a\ i+1j+1}^n, P_{a\ ij-1}^n, P_{a\ i+1j-1}^n, i, j)$,
- $\beta_1, \beta_2 =$ implicit and explicit coefficients ($\beta_1 + \beta_2 = 1$),

The coefficients **ms** and **mn** are designed to represent the (im)possibility of local north-south exchange.

- **ms** = south wall (1 when it is open and 0 when it is close),
- **mn** = north wall (1 when it is open and 0 when it is close),
- $(f_u)_{ij} = 2\Omega \sin\phi_u$ (Coriolis parameter in the right face of the staggered grid),
- $(ft)_{ij} = \frac{0.5 \cdot \Delta t \cdot \|\vec{u}\|}{D_x^n} \cdot \min \left[\left(\frac{\kappa}{\ln \left(\frac{D_x^n}{e \cdot z_0} \right)} \right)^2, 0.1 \right]$,
- $\|\vec{u}\| = g_{11} U_{i,j}^n \cdot U_{i,j}^n + (g_{12} + g_{21}) U_{i,j}^n \cdot V_{i,j-U}^n + g_{22} V_{i,j-U}^n \cdot V_{i,j-U}^n$,
- $(\tau_{s\xi})_{i,j}^n = BU11_{i,j} \cdot (\tau_{sx})_{i,j}^n + BU12_{i,j} \cdot (\tau_{sy-x})_{i,j}^n$, the wind stress on the surface in the ξ direction,
- $D_x^n = H_x + \zeta_x^n$.

Vertically integrated momentum equation along η (centered scheme) for estimating $V^{n+\frac{1}{2},*}$:

$$\overrightarrow{\text{Acc}^2} + \overrightarrow{\text{NI}^2} = -\overrightarrow{\text{Cor}^2} + \overrightarrow{\text{Pres}^2} + \overrightarrow{\text{Frot}^2} + \overrightarrow{\text{Visc}^2} + \overrightarrow{\text{Wind}^2}$$

$$\text{Acc}^2 \Rightarrow \frac{\mathbf{V}_{ij}^{n+\frac{1}{2},*} - V_{i,j}^n}{\Delta t/2} \quad (2.85)$$

$$\begin{aligned} \text{NI}^2 \Rightarrow & V_{i,j}^n \cdot \left(\left[\frac{V^n}{2\Delta\eta} \right]_{i,j-1}^{i,j+1} + \Gamma_{21}^2 U_{i,j-V}^n + \Gamma_{22}^2 V_{i,j}^n \right) \\ & + U_{i,j-V}^n \cdot \left(\frac{1}{2} \left(\text{mo} \cdot \left[\frac{V^n}{\Delta\xi} \right]_{i-1,j}^{i,j} + \text{me} \cdot \left[\frac{V^n}{\Delta\xi} \right]_{i,j}^{i+1,j} \right) + \Gamma_{11}^2 U_{i,j-V}^n + \Gamma_{12}^2 V_{i,j}^n \right) \end{aligned} \quad (2.86)$$

$$\text{Cor}^2 \Rightarrow (f_v)_{ij} \left(\frac{g_{11}}{\sqrt{g}} U_{i,j-V}^n + \frac{g_{21}}{\sqrt{g}} V_{i,j}^n \right) \quad (2.87)$$

$$\text{Pres}^2 \Rightarrow -g \left(\frac{g^{22}}{\Delta\eta} [\zeta^n]_{i,j}^{i,j+1} + \frac{g^{21}}{\Delta\xi} d\zeta_{i,j-V}^n \right) - \frac{1}{\rho} \left(\frac{g^{22}}{\Delta\eta} [P_a^n]_{i,j}^{i,j+1} + \frac{g^{21}}{\Delta\eta} dP_{a\ i,j-V}^n \right) \quad (2.88)$$

$$\text{Frot}^2 \Rightarrow - (ft)_{ij} \left(\beta_2 \mathbf{V}^{n+\frac{1}{2},*}_{i,j} + \beta_1 V_{i,j}^n \right) \quad (2.89)$$

$$\begin{aligned} \text{Visc}^2 \Rightarrow & \frac{g^{22}}{\Delta\eta} \left(\left[\nu \frac{V^n}{\Delta\xi} \right]_{i,j}^{i,j+1} - \left[\nu \frac{V^n}{\Delta\eta} \right]_{i,j-1}^{i,j} \right) \\ & - \frac{g^{11}}{\Delta\xi} \left(\text{mo} \cdot \left[\nu \frac{V^n}{\Delta\xi} \right]_{i-1,j}^{i,j} - \text{me} \cdot \left[\nu \frac{V^n}{\Delta\xi} \right]_{i,j}^{i+1,j} \right) \end{aligned} \quad (2.90)$$

$$\text{Wind}^2 \Rightarrow \frac{1}{D_y^n \rho} (\tau_{s\eta})_{i,j}^n \quad (2.91)$$

$U_{i,j-V}^n$, $d\zeta_{i,j-V}^n$, $dP_{a\ i,j-V}^n$ are some functions that are performed to obtain the values of the second velocity component, water levels and pressure in middle of the top side of the mesh (Fig. 2.13).

- $U_{i,j-V}^n = f_{U2V} (U_{i,j}^n, U_{i,j+1}^n, U_{i-1,j}^n, U_{i-1,j+1}^n, i, j, V^n)$,
- $d\zeta_{i,j-V}^n = f_{\nabla\zeta}^V (\zeta_{i,j}^n, \zeta_{i+1,j}^n, \zeta_{i,j+1}^n, \zeta_{i+1,j+1}^n, \zeta_{i-1,j}^n, \zeta_{i-1,j+1}^n, i, j)$,
- $dP_{a\ i,j-V}^n = f_{\nabla P_a}^V (P_{a\ ij}^n, P_{a\ i+1j}^n, P_{a\ ij+1}^n, P_{a\ i+1j+1}^n, P_{a\ i-1j}^n, P_{a\ i-1j+1}^n, i, j)$,
- $\beta_1, \beta_2 = \text{implicit and explicit coefficients } (\beta_1 + \beta_2 = 1)$,

The coefficients **mo** and **me** are representing the (im)possibility of local west-east exchange.

- **mo** = west wall (1 when it is open and 0 when it is closed),
- **me** = east wall (1 when it is open and 0 when it is closed),

- $(ft)_{ij} = \frac{0.5 \cdot \Delta t \cdot \|\vec{u}\|}{D_y^n} \cdot \min \left[\left(\frac{\kappa}{\ln \left(\frac{D_y^n}{e \cdot z_0} \right)} \right)^2, 0.1 \right],$
- $\|\vec{u}\| = g_{11} U_{i,j_V}^n \cdot U_{i,j_V}^n + (g_{12} + g_{21}) U_{i,j_V}^n \cdot V_{i,j}^n + g_{22} V_{i,j}^n \cdot V_{i,j}^n,$
- $(f_v)_{ij} = 2\Omega \sin \phi_v$, Coriolis parameter in the right side of the staggered grid,
- $(\tau_{s\eta})_{i,j}^n = BV22_{i,j} \cdot (\tau_{sy})_{i,j}^n + BV21_{i,j} \cdot (\tau_{sx_y})_{i,j}^n$, the wind stress on the surface in the η direction,
- $D_y^n = H_y + \zeta_y^n.$

Here, the continuity and momentum equations are rewritten in a linear discretized form for each mesh (i, j) of a common line j and used in the initial part of each first half time-step $(n + \frac{1}{2})$. For computing the first horizontal velocity component at the time step $n + \frac{1}{2}$, one needs to resolve the continuity and momentum equations simultaneously using estimated the velocity components $(U_{i,j}^{n+\frac{1}{2},*}, V_{i,j}^{n+\frac{1}{2},*})$ and the estimated value of the free surface elevation $(\zeta_{i,j}^{n+\frac{1}{2},*})$ over the ξ direction. As mentioned previously (Sec. 2.5.2.1), the step after explicit estimation of the velocity components $(U_{i,j}^{n+\frac{1}{2},*}, V_{i,j}^{n+\frac{1}{2},*})$ is the estimate of the free surface elevation $(\zeta_{i,j}^{n+\frac{1}{2},*})$ for which the continuity equation is used:

$$\begin{aligned} \sqrt{g} \frac{\zeta_{i,j}^{n+\frac{1}{2},*} - \zeta_{i,j}^n}{\Delta t/2} + \left[\frac{\sqrt{g} D_x^n}{\Delta \xi} \left(\alpha_p U^n + \alpha_n \mathbf{U}^{n+\frac{1}{2}} \right) \right]_{i-1,j}^{i,j} \\ + \left[\frac{\sqrt{g} D_y^n}{\Delta \eta} \left(\alpha_p V^n + \alpha_n V^{n+\frac{1}{2},*} \right) \right]_{i,j-1}^{i,j} = 0 \end{aligned} \quad (2.92)$$

with $\alpha_n + \alpha_p = 1$.

After rearrangements we obtain:

$$\begin{aligned} \zeta_{i,j}^{n+\frac{1}{2},*} + \frac{\alpha_n}{2(\sqrt{g})_{i,j}^\zeta} \frac{\Delta t}{\Delta \xi} \left[\sqrt{g} D_x^n \mathbf{U}^{n+\frac{1}{2}} \right]_{i-1,j}^{i,j} = \zeta_{i,j}^n - \frac{\alpha_p}{2(\sqrt{g})_{i,j}^\zeta} \frac{\Delta t}{\Delta \xi} \left[\sqrt{g} D_x^n U^n \right]_{i-1,j}^{i,j} \\ - \frac{\alpha_p}{2(\sqrt{g})_{i,j}^\zeta} \frac{\Delta t}{\Delta \eta} \left[\sqrt{g} D_y^n V^n \right]_{i,j-1}^{i,j} \\ - \frac{\alpha_n}{2(\sqrt{g})_{i,j}^\zeta} \frac{\Delta t}{\Delta \eta} \left[\sqrt{g} D_y^n V^{n+\frac{1}{2},*} \right]_{i,j-1}^{i,j} \end{aligned} \quad (2.93)$$

The modifications from one iteration to another are highly localized within a part of the right-hand side of the system. That means the lower upper (LU) factorization is performed only once, until the convergence is reached. The resolution at each iteration consists in updating the

right-hand side (RHS) vector; this is done by splitting this RHS into two parts: one explicit and one implicit (Lazure and Dumas, 2008). This could be written formally in the following way:

$$\begin{pmatrix} b_{1,j} & c_{1,j} & 0 & \cdots & 0 \\ a_{2,j} & b_{2,j} & c_{2,j} & \ddots & 0 \\ 0 & \ddots & \ddots & \ddots & 0 \\ \vdots & \ddots & \ddots & \ddots & c_{n-1,j} \\ 0 & \cdots & 0 & a_{n,j} & b_{n,j} \end{pmatrix} \begin{pmatrix} u_{1,j} \\ \zeta_{2,j} \\ \vdots \\ \zeta_{imax-1,j} \\ u_{imax,j} \end{pmatrix} = \begin{pmatrix} d_{1,j} \\ d_{2,j} \\ \vdots \\ d_{imax-1,j} \\ d_{imax,j} \end{pmatrix}$$

the upper equations can be rewritten in the form of a linear tridiagonal system (Eq. 2.94):

$$\text{Continuity : } a_{\zeta} \mathbf{U}_{i-1,j}^{n+\frac{1}{2}} + b_{\zeta} \zeta_{i,j}^{n+\frac{1}{2},*} + c_{\zeta} \mathbf{U}_{i,j}^{n+\frac{1}{2}} = d_{\zeta} \quad (2.94)$$

$$a_{\zeta} = -\frac{\alpha_n}{2(\sqrt{g})_{i,j}^{\zeta}} \frac{\Delta t}{\Delta \xi} (\sqrt{g} D_x^n)_{i-1,j} \quad (2.95)$$

$$b_{\zeta} = (f_{wet})_{i,j} \quad (2.96)$$

$$c_{\zeta} = \frac{\alpha_n}{2(\sqrt{g})_{i,j}^{\zeta}} \frac{\Delta t}{\Delta \xi} (\sqrt{g} D_x^n)_{i,j} \quad (2.97)$$

$$\begin{aligned} d_{\zeta} = & \zeta_{i,j}^n \cdot f_{wet} p_{i,j} - \frac{\alpha_p}{2(\sqrt{g})_{i,j}^{\zeta}} \frac{\Delta t}{\Delta \xi} \left((\sqrt{g} D_x^n U^n)_{i,j}^U - (\sqrt{g} D_x^n U^n)_{i-1,j}^U \right) \\ & - \frac{\alpha_p}{2(\sqrt{g})_{i,j}^{\zeta}} \frac{\Delta t}{\Delta \eta} \left((\sqrt{g} D_y^n V^n)_{i,j}^V - (\sqrt{g} D_y^n V^n)_{i,j-1}^V \right) \\ & - \frac{\alpha_n}{2(\sqrt{g})_{i,j}^{\zeta}} \frac{\Delta t}{\Delta \eta} \left((\sqrt{g} D_y^n V^{n+\frac{1}{2},*})_{i,j}^V - (\sqrt{g} D_y^n V^{n+\frac{1}{2},*})_{i,j-1}^V \right) \end{aligned} \quad (2.98)$$

with

- $(f_{wet})_{i,j}^{\zeta^{n+\frac{1}{2},*}}$ = The real fraction of the wet part of each cell is estimated and used in the continuity, momentum and tracer equations to improve the realistic aspect of wet-drying.

The next step consists in resolving the momentum equation to find out the value of first velocity component $\mathbf{U}^{n+\frac{1}{2}}$. To keep it simple, only the form of tridiagonal system over ξ direction is presented hereafter (Eq. 2.99):

$$\text{Momentum Eq. over } (\xi) : a_v \zeta_{i,j}^{n+\frac{1}{2},*} + b_v \mathbf{U}_{i,j}^{n+\frac{1}{2}} + c_v \zeta_{i+1,j}^{n+\frac{1}{2},*} = d_v \quad (2.99)$$

$$a_v = -\alpha_n \frac{g\Delta t}{2\Delta\xi} (g^{11})_{i-1,j} \quad (2.100)$$

$$b_v = \left(1 + (ft)_{ij} \beta_2 \Delta t\right)_{i,j} \quad (2.101)$$

$$c_v = \alpha_n \frac{g\Delta t}{2\Delta\xi} (g^{11})_{i,j} \quad (2.102)$$

$$d_v = \quad (2.103)$$

- Time evolution

$$U_{i,j}^n$$

- Bottom stress

$$- (ft)_{ij} \cdot \beta_1 \cdot U_{i,j}^n$$

- Coriolis

$$+ (fu)_{ij} \cdot \frac{\Delta t}{2} \left(\frac{g_{22}}{\sqrt{g}} V_{i,j-U}^{n+\frac{1}{2},*} + \frac{g_{12}}{\sqrt{g}} U_{i,j}^{n+\frac{1}{2},*} \right)$$

- Sea surface pressure gradient

$$- g \cdot \frac{\Delta t}{2} \left(\alpha_p \left(\frac{g^{11}}{\Delta\xi} [\zeta^n]_{i,j}^{i+1,j} \right) + \frac{g^{12}}{\Delta\eta} d\zeta_{i,j-U}^n \right)$$

- First non-linear advection term "ududξ"

$$- \frac{\Delta t}{2} \cdot udud\xi$$

- Second non-linear advection term "vdudη"

$$- \frac{\Delta t}{2} \cdot vdud\eta$$

- Viscosity along ξ

$$+ \frac{\Delta t}{2} \cdot \frac{g^{11}}{\Delta\xi} \left(\left[\nu \frac{U^n}{\Delta\xi} \right]_{i,j}^{i+1,j} - \left[\nu \frac{U^n}{\Delta\xi} \right]_{i-1,j} \right)$$

- Viscosity along η

$$+ \frac{\Delta t}{2} \cdot \frac{g^{22}}{\Delta\eta} \left(mn \cdot \left[\nu \frac{U^n}{\Delta\eta} \right]_{i,j}^{i,j+1} - ms \cdot \left[\nu \frac{U^n}{\Delta\eta} \right]_{i,j-1} \right)$$

- Wind stress

$$+ \frac{\Delta t}{2} \cdot \frac{1}{D_x^{n+\frac{1}{2},*} \rho} (\tau_{s\xi})_{i,j}^n$$

- Atmospherical pressure gradient

$$- \frac{\Delta t}{2\rho} \left(\frac{g^{11}}{\Delta\xi} [P_a^n]_{i,j}^{i+1,j} + \frac{g^{12}}{\Delta\eta} dP_a^n_{i,j-U} \right)$$

with:

- $d\zeta_{i,j-U}^{n+\frac{1}{2},*} = f_{\nabla\zeta}^U \left(\zeta_{ij}^{n+\frac{1}{2},*}, \zeta_{i+1j}^{n+\frac{1}{2},*}, \zeta_{ij+1}^{n+\frac{1}{2},*}, \zeta_{i+1j+1}^{n+\frac{1}{2},*}, \zeta_{ij-1}^{n+\frac{1}{2},*}, \zeta_{i+1j-1}^{n+\frac{1}{2},*}, i, j \right),$
- $dP_a^n_{ij-U} = f_{\nabla P_a}^U \left(P_a^n_{ij}, P_a^n_{i+1j}, P_a^n_{ij+1}, P_a^n_{i+1j+1}, P_a^n_{ij-1}, P_a^n_{i+1j-1}, i, j \right),$

- $(ft)_{ij} = \frac{0.5 \cdot \Delta t \cdot \|\vec{u}\|}{D_x^{n+\frac{1}{2},*}} \cdot \min \left[\left(\frac{\kappa}{\ln \left(\frac{D_x^{n+\frac{1}{2},*}}{e \cdot z_0} \right)} \right)^2, 0.1 \right],$
- $\|\vec{u}\| = g_{11} U_{i,j}^n \cdot U_{i,j}^n + (g_{12} + g_{21}) U_{i,j}^n \cdot V_{i,j-U}^n + g_{22} V_{i,j-U}^n \cdot V_{i,j-U}^n,$
- $(f_v)_{ij} = 2\Omega \sin \phi_v$, Coriolis parameter,
- $udud\xi = U_{i,j}^{n+\frac{1}{2},*} \cdot \alpha_n \cdot \left(\left[\frac{U^{n+\frac{1}{2},*}}{2\Delta\xi} \right]_{i-1,j}^{i+1,j} + \Gamma_{11}^1 U_{i,j}^{n+\frac{1}{2},*} + \Gamma_{12}^1 V_{i,j-U}^{n+\frac{1}{2},*} \right)$
 $+ U_{i,j}^{n+\frac{1}{2},*} \cdot \alpha_p \cdot \left(\left[\frac{U^n}{2\Delta\xi} \right]_{i-1,j}^{i+1,j} + \Gamma_{11}^1 U_{i,j}^n + \Gamma_{12}^1 V_{i,j-U}^n \right),$
- $vdud\eta = V_{i,j-U}^{n+\frac{1}{2},*} \cdot \alpha_n \cdot \left(\frac{1}{2} \left(\text{ms} \cdot \left[\frac{U^{n+\frac{1}{2},*}}{\Delta\eta} \right]_{i,j-1}^{i,j} + \text{mn} \cdot \left[\frac{U^{n+\frac{1}{2},*}}{\Delta\eta} \right]_{i,j}^{i,j+1} \right) + \Gamma_{21}^1 U_{i,j}^{n+\frac{1}{2},*} + \Gamma_{22}^1 V_{i,j-U}^{n+\frac{1}{2},*} \right)$
 $+ V_{i,j-U}^{n+\frac{1}{2},*} \cdot \alpha_p \cdot \left(\frac{1}{2} \left(\text{ms} \cdot \left[\frac{U^n}{\Delta\eta} \right]_{i,j-1}^{i,j} + \text{mn} \cdot \left[\frac{U^n}{\Delta\eta} \right]_{i,j}^{i,j+1} \right) + \Gamma_{21}^1 U_{i,j}^n + \Gamma_{22}^1 V_{i,j-U}^n \right),$
- $(\tau_{s\xi})_{i,j}^n = BU11_{i,j} \cdot (\tau_{sx})_{i,j}^n + BU12_{i,j} \cdot (\tau_{sy-x})_{i,j}^n,$
- $D_x^{n+\frac{1}{2},*} = H_x + \zeta_y^{n+\frac{1}{2},*}.$

The third part of the first half time-step is devoted to compute the final free surface elevation $\zeta_{ij}^{n+\frac{1}{2}}$ and the second final velocity component $V_{ij}^{n+\frac{1}{2}}$, using the equations of continuity and momentum along η . Here, the continuity and momentum equations are rewritten in a linear discretized form for each mesh (i, j) of a common line i :

$$\text{Continuity} : a_\zeta \mathbf{V}_{i,j-1}^{n+\frac{1}{2}} + b_\zeta \zeta_{i,j}^{n+\frac{1}{2}} + c_\zeta \mathbf{V}_{i,j}^{n+\frac{1}{2}} = d_\zeta \quad (2.104)$$

$$a_\zeta = -\frac{\alpha_n}{2(\sqrt{g})_{i,j}^\zeta} \frac{\Delta t}{\Delta\eta} (\sqrt{g} D_y^l)_{i,j-1} \quad (2.105)$$

$$b_\zeta = (fwet)_{i,j} \quad (2.106)$$

$$c_\zeta = \frac{\alpha_n}{2(\sqrt{g})_{i,j}^\zeta} \frac{\Delta t}{\Delta\eta} (\sqrt{g} D_y^l)_{i,j} \quad (2.107)$$

$$d_\zeta = \zeta_{i,j}^n \cdot (fwetp)_{i,j} - \frac{\alpha_p}{2(\sqrt{g})_{i,j}^\zeta} \frac{\Delta t}{\Delta\eta} \left((\sqrt{g} D_y^l V^n)_{i,j}^V - (\sqrt{g} D_y^l V^n)_{i-1,j}^V \right)$$

$$- \frac{\alpha_p}{2(\sqrt{g})_{i,j}^\zeta} \frac{\Delta t}{\Delta\xi} \left((\sqrt{g} D_x^l U^n)_{i,j}^U - (\sqrt{g} D_x^l U^n)_{i-1,j}^U \right)$$

$$- \frac{\alpha_n}{2(\sqrt{g})_{i,j}^\zeta} \frac{\Delta t}{\Delta\xi} \left((\sqrt{g} D_x^l U^{n+\frac{1}{2}})_{i,j}^U - (\sqrt{g} D_x^l U^{n+\frac{1}{2}})_{i-1,j}^U \right) \quad (2.108)$$

For momentum equation over (η)

$$\text{Momentum equation over } (\eta) : a_v \zeta_{i,j}^{n+\frac{1}{2}} + b_v \mathbf{V}_{i,j}^{n+\frac{1}{2}} + c_v \zeta_{i,j+1}^{n+\frac{1}{2}} = d_v \quad (2.109)$$

$$a_v = -\alpha_n \frac{g\Delta t}{2\Delta\eta} (g^{22})_{i,j-1} \quad (2.110)$$

$$b_v = \left(1 + (ft)_{ij} \beta_2 \Delta t\right)_{i,j} \quad (2.111)$$

$$c_v = \alpha_n \frac{g\Delta t}{2\Delta\eta} (g^{22})_{i,j} \quad (2.112)$$

$$d_v = \quad (2.113)$$

- Time evolution

$$V_{i,j}^n$$

- Bottom stress

$$- (ft)_{ij} \cdot \beta_1 \cdot V_{i,j}^n$$

- Coriolis

$$- (fv)_{ij} \cdot \frac{\Delta t}{2} \left(\frac{g_{11}}{\sqrt{g}} U_{i,j-V}^{n+\frac{1}{2}} + \frac{g_{21}}{\sqrt{g}} V_{i,j}^{n+\frac{1}{2},*} \right)$$

- Sea surface pressure gradient

$$- g \cdot \frac{\Delta t}{2} \left(\alpha_p \left(\frac{g^{22}}{\Delta\xi} [\zeta^n]_{i,j}^{i,j+1} \right) + \frac{g^{21}}{\Delta\eta} d\zeta_{i,j-V}^n \right)$$

- First non-linear advection term "vdrv\eta"

$$- \frac{\Delta t}{2} \cdot vdrv\eta$$

- Second advection non-linear term "udvdx"

$$- \frac{\Delta t}{2} \cdot udvdx$$

- Viscosity along η

$$+ \frac{\Delta t}{2} \cdot \frac{g^{22}}{\Delta\eta} \left(\left[\nu \frac{V^n}{\Delta\eta} \right]_{i,j}^{i,j+1} - \left[\nu \frac{V^n}{\Delta\eta} \right]_{i,j-1}^{i,j} \right)$$

- Viscosity along ξ

$$+ \frac{\Delta t}{2} \cdot \frac{g^{11}}{\Delta\eta} \left(me \cdot \left[\nu \frac{V^n}{\Delta\xi} \right]_{i,j}^{i+1,j} - mo \cdot \left[\nu \frac{V^n}{\Delta\xi} \right]_{i-1,j}^{i,j} \right)$$

- Wind stress

$$+ \frac{\Delta t}{2} \cdot \frac{1}{D_y^l \rho} (\tau_{s\eta})_{i,j}^n$$

- Atmospherical pressure gradient

$$- \frac{\Delta t}{2\rho} \left(\frac{g^{22}}{\Delta\eta} [P_a^n]_{i,j}^{i,j+1} + \frac{g^{21}}{\Delta\eta} dP_a^n_{i,j-V} \right)$$

with:

- $d\zeta_{i,j_V}^n = f_{\nabla\zeta}^V (\zeta_{ij}^n, \zeta_{i+1j}^n, \zeta_{ij+1}^n, \zeta_{i+1j+1}^n, \zeta_{i-1j}^n, \zeta_{i-1j+1}^n, i, j),$
- $dP_{a\ ij_V}^n = f_{\nabla P_a}^V (P_a^{ij}, P_a^{i+1j}, P_a^{ij+1}, P_a^{i+1j+1}, P_a^{i-1j}, P_a^{i-1j+1}, i, j),$
- $(ft)_{ij} = \frac{0.5 \cdot \Delta t \cdot \|\vec{u}\|}{D_y^{n+\frac{1}{2},*}} \cdot \left(\frac{\kappa}{\ln\left(\frac{D_y^{n+\frac{1}{2},*}}{e \cdot z_0}\right)} \right)$
- $\|\vec{u}\| = g_{11} U_{i,j_V}^{n+\frac{1}{2}} \cdot U_{i,j_V}^{n+\frac{1}{2}} + (g_{12} + g_{21}) U_{i,j_V}^{n+\frac{1}{2}} \cdot V_{i,j}^n + g_{22} V_{i,j}^n \cdot V_{i,j}^n,$
- $vdvd\eta = V_{i,j}^{n+\frac{1}{2},*} \cdot \left(\alpha_n \cdot \left[\frac{V^{n+\frac{1}{2},*}}{2\Delta\eta} \right]_{i,j-1}^{i,j+1} + \Gamma_{22}^2 V_{i,j}^{n+\frac{1}{2},*} + \Gamma_{21}^2 U_{i,j_V}^{n+\frac{1}{2},*} \right)$
 $+ V_{i,j}^{n+\frac{1}{2},*} \cdot \left(\alpha_p \cdot \left[\frac{V^n}{2\Delta\eta} \right]_{i,j-1}^{i,j+1} + \Gamma_{22}^2 V_{i,j}^n + \Gamma_{21}^2 U_{i,j_V}^n \right)$
- $udvd\xi = U_{i,j_V}^{n+\frac{1}{2},*} \cdot \alpha_n \cdot \left(\frac{1}{2} \left(\text{mo} \cdot \left[\frac{V^{n+\frac{1}{2},*}}{\Delta\xi} \right]_{i-1,j}^{i,j} + \text{me} \cdot \left[\frac{V^{n+\frac{1}{2},*}}{\Delta\xi} \right]_{i,j}^{i+1,j} \right) + \Gamma_{12}^2 V_{i,j}^{n+\frac{1}{2},*} + \Gamma_{11}^2 U_{i,j_V}^{n+\frac{1}{2},*} \right)$
 $+ U_{i,j_V}^{n+\frac{1}{2},*} \cdot \alpha_p \cdot \left(\frac{1}{2} \left(\text{mo} \cdot \left[\frac{V^n}{\Delta\xi} \right]_{i-1,j}^{i,j} + \text{me} \cdot \left[\frac{V^n}{\Delta\xi} \right]_{i,j}^{i+1,j} \right) + \Gamma_{12}^2 V_{i,j}^n + \Gamma_{11}^2 U_{i,j_V}^n \right),$
- $(\tau_{s\eta})_{i,j}^n = BV22_{i,j} \cdot (\tau_{sy})_{i,j}^n + BV21_{i,j} \cdot (\tau_{sx_y})_{i,j}^n,$
- $D_x^l = \alpha_p \cdot D_x^n + \alpha_n \cdot D_x^{n+\frac{1}{2},*},$
- $D_y^l = \alpha_p \cdot D_y^n + \alpha_n \cdot D_y^{n+\frac{1}{2},*}$

Emerging zones

In the case of emerging zones (surface elevation inferior or equal to bottom height), a test is made which imposes $a_v = 0$, $c_v = 0$ and $d_v = 0$, sets the velocity U to zero, while preserving the linear form of the relation. The usual matrix resolution can then be coded for the whole domain, irrespective of the existence of permanent or occasional land barriers (Lazure and Salomon, 1991b).

2.5.3 Principal difficulties using the ADI scheme with curvilinear coordinates

2.5.3.1 Estimate of the pressure gradient in decoupling rows (columns) of ADI curvilinear scheme

In general coordinates, we have to put aside traditional thinking that a X-gradient (Y-gradient) of the vectorial quantity (*e.g.* zonal momentum) only involves finite differences in the

X-direction (Y-direction). Indeed, a gradient in one direction contains both derivatives in both directions so that the usual ADI scheme used in MARS-3D needs to be modified in order to maintain the uncoupling between rows and columns. As a matter of fact, subdivides the global linear system to be solved into sub-linear systems are for each line or column (the straight forward discretization discretization of the ADI with coupled rows through to $\nabla\zeta$ (Fig. 2.14) that involves only unknowns of the considered rows (or columns), that is to say u^{n+1}, ζ^{n+1} for rows (v^{n+1}, ζ^{n+1} for columns).

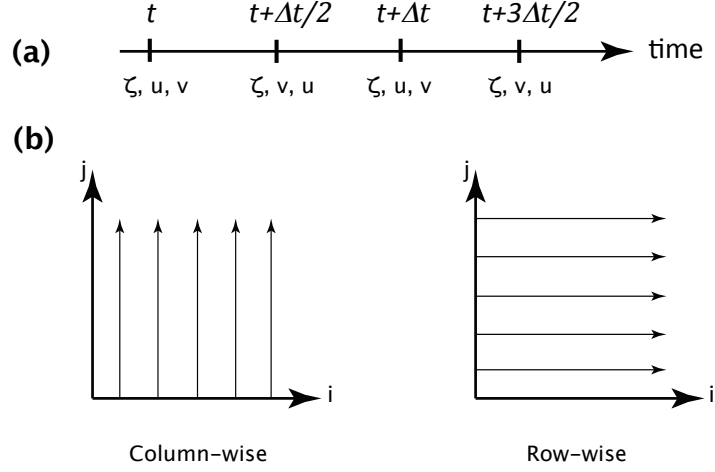


Figure 2.14: ADI semi-implicit resolving variable with respect to the direction (Lazure and Dumas, 2008).

The problem with the curvilinear coordinate system is that the variable is required in two separate directions (ξ, η) at the same time. This is due to the added partition of differential operators in the curvilinear coordinate system which has been shown in a previous section (Sec. 2.4.6).

$$\nabla A_{ij}^{n+1} = \frac{1}{\sqrt{g}} \cdot \frac{\partial(\sqrt{g}A_{i,j}^k)}{\partial \xi^k} = \frac{1}{\sqrt{g}} \cdot \frac{\partial(\sqrt{g}A_{i,j}^1)}{\partial \xi^1} + \frac{1}{\sqrt{g}} \cdot \frac{\partial(\sqrt{g}A_{i,j}^2)}{\partial \xi^2} \quad \text{with } k = 1, 2 \quad (2.114)$$

\mathbf{A} could be any variable, that we need to compute its divergence over the first and second axis. Here we rewrite the formula mentioned above for computing surface elevation on the right side of the Arrakawa C-grid, where we compute U component of velocity (Eq. 2.115).

$$\nabla_{\zeta_{ij}}^{n+1} = \frac{1}{\sqrt{gz}} \cdot \frac{\partial(\sqrt{g_U^{11}} \zeta_{i,j}^{n+1})}{\partial \xi} + \frac{1}{\sqrt{gz}} \cdot \frac{\partial(\sqrt{g_U^{12}} \Delta \zeta_{i,j}^{n+1})}{\partial \eta} \quad (2.115)$$

Computing pressure gradient and surface elevation over the first coordinate axis (ζ) involves more cells in general coordinates than in Cartesian coordinates; black dashed rectangular show the discretized cells which intervene in the first component of gradient and orange-dashed rectangular present the cells used on second components (see Fig. 2.15).

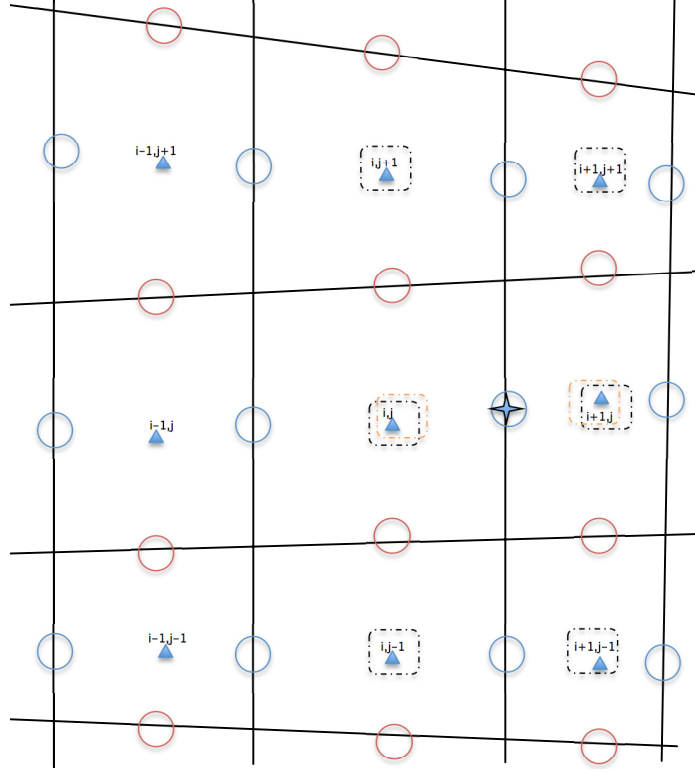


Figure 2.15: Arrakawa C-grid, divergence at "star" point over the first axis, orange-dashed rectangles show the cells involved in the first component of gradient and black-dashed rectangles present the cells used in the second components.

Therefore we can not solve the continuity and momentum equations with implicit cross derivative. Here, to calculate the velocity in row (column) direction during the $\{n + \frac{1}{2}\}$ th time-step, we use pressure gradient in the $\{n\}$ th time-step for the cross direction. The reason is that an implicit discretization of this term would prevent to solve Navier-Stokes equations by inverting sub-linear systems, as commonly achieved through the ADI scheme. Therefore, using non-orthogonal curvilinear grid is not compatible with ADI in the standard form.

In the version of MARS-3D curvilinear adapted to curvilinear coordinates, the complementary terms ($d\zeta_{i,j_V}^{n+\frac{1}{2}}$, $d\zeta_{i,j_U}^{n+\frac{1}{2},*}$) are estimated explicitly, which means the scalar field of free surface elevation is interpolated on the nodes of the mesh before being treated in the same manner as the pressure gradient ($dP_a^n_{i,j_U}$, $dP_a^n_{i,j_V}$) principal term (Eq. 2.103 and 2.113). Along the closed borders, the elevation is extrapolated from inside the area by a polynomial fitting of order 4. It is also important to note that these terms have generally an order of magnitude lower comparing to the pressure gradient. We can therefore expect that the quality of the interpolation method has little impact on the overall outcome of a simulation.

Depending on the skewness of the grid mesh, these cross derivative terms can become significant and can affect the numerical stability as well as the accuracy of the numerical method used for the solution (Erturk and Dursun, 2007). In our application of the model, it

has been chosen to limit the range of skew angle (α) to $60^\circ \leq \alpha \leq 120^\circ$ (see chapter 3).

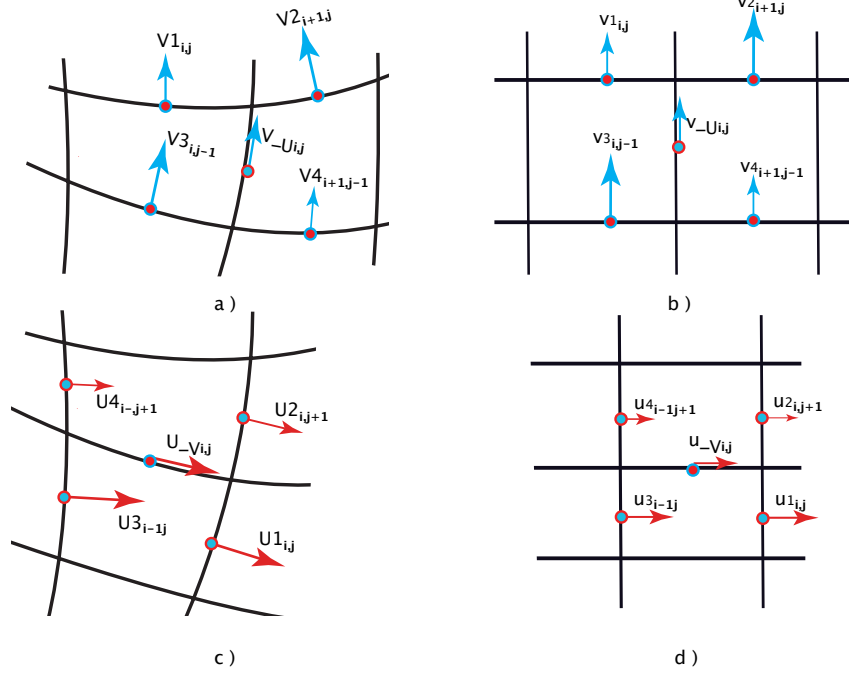


Figure 2.16: a) Interpolation of V component of Arakawa-C grid in U position in curvilinear coordinate meshes b) Interpolation of V component of Arakawa-C grid in U position in Cartesian coordinate meshes c) Interpolation of U component of Arakawa-C grid in V position in curvilinear coordinate meshes d) Interpolation of U component of Arakawa-C grid in V position in Cartesian coordinate meshes.

2.5.3.2 Estimation of the main Coriolis term

In contrast to the pressure gradient cross term, for the component of the Coriolis force, it is the main term which requires an interpolation. Obviously the quality of the interpolation method has a significant impact on the quality of simulation for this term. On the Cartesian coordinate, direction associated with a component of velocity is uniform (Fig. 2.16b & d). Contrary to the Cartesian coordinate, in curvilinear coordinates, the direction varies in the field (Fig. 2.16a & c).

Indeed, the identical interpolation used in Cartesian coordinates (simple averaging of the relevant component in the four adjacent cells) introduces an additional error which is due to the fact that variations of the direction of the velocity components are not included. Therefore, a new interpolation method is here proposed. This new method, accounts for the direction of components used for the interpolation. Fig. 2.16 shows the position of the variables U_i , V_i (velocity components in curvilinear coordinates in the adjacent meshes, $(i = 1, 2, 3, 4)$) and u_i , v_i

(velocity components in Cartesian coordinate in the adjacent meshes, $i = 1, 2, 3, 4$).

$$\begin{aligned}
U1_{-V} &= {}^V B_1^1 u1_{-V} + {}^V B_2^1 v1_{-V} \\
&= \frac{{}^V B_1^1}{4} (u1 + u2 + u3 + u4) + {}^V B_2^1 ({}^V A_1^2 U1_{-V} + {}^V A_2^2 V1_{-V}) \\
&= \frac{{}^V B_1^1}{4} ({}^1 A_1^1 U1 + {}^1 A_2^1 V1 + {}^2 A_1^1 U2 + {}^2 A_2^1 V2 + {}^3 A_1^1 U3 + {}^3 A_2^1 V3 + {}^4 A_1^1 U4 + {}^4 A_2^1 V4) \\
&\quad + {}^V B_2^1 ({}^V A_1^2 U1_{-V} + {}^V A_2^2 V1_{-V}) \\
&= \frac{{}^V B_1^1}{4} ({}^1 A_1^1 U1 + {}^2 A_1^1 U2 + {}^3 A_1^1 U3 + {}^4 A_1^1 U4) + \frac{{}^V B_1^1}{4} ({}^1 A_2^1 + {}^2 A_2^1 + {}^3 A_2^1 + {}^4 A_2^1) V1_{-V} \\
&\quad + {}^V B_2^1 ({}^V A_1^2 U1_{-V} + {}^V A_2^2 V1_{-V}) \tag{2.116}
\end{aligned}$$

$$\begin{aligned}
V1_{-U} &= {}^U B_1^2 u1_{-U} + {}^U B_2^2 v1_{-U} \\
&= \frac{{}^U B_2^2}{4} (v1 + v2 + v3 + v4) + {}^U B_1^2 ({}^U A_1^1 U1_{-U} + {}^U A_2^1 V1_{-U}) \\
&= \frac{{}^U B_2^2}{4} ({}^1 A_2^2 V1 + {}^1 A_1^2 U1 + {}^2 A_2^2 V2 + {}^2 A_1^2 U2 + {}^3 A_2^2 V3 + {}^3 A_1^2 U3 + {}^4 A_2^2 V4 + {}^4 A_1^2 U4) \\
&\quad + {}^U B_1^2 ({}^U A_1^1 U1_{-U} + {}^U A_2^1 V1_{-U}) \\
&= \frac{{}^U B_2^2}{4} ({}^1 A_2^2 V1 + {}^2 A_2^2 V2 + {}^3 A_2^2 V3 + {}^4 A_2^2 V4) + \frac{{}^U B_2^2}{4} ({}^1 A_1^2 + {}^2 A_1^2 + {}^3 A_1^2 + {}^4 A_1^2) U1_{-U} \\
&\quad + {}^U B_1^2 ({}^U A_1^1 U1_{-U} + {}^U A_2^1 V1_{-U}) \tag{2.117}
\end{aligned}$$

finally we obtain:

$$\begin{aligned}
U1_{-V} &= \left(\frac{{}^V B_1^1}{4} ({}^1 A_1^1 U1 + {}^2 A_1^1 U2 + {}^3 A_1^1 U3 + {}^4 A_1^1 U4) \right. \\
&\quad \left. + \frac{V1_{-V}}{4} ({}^V B_1^1 * ({}^1 A_2^1 + {}^2 A_2^1 + {}^3 A_2^1 + {}^4 A_2^1) + 4 * {}^V B_2^1 {}^V A_2^2) \right) / (1 - {}^V B_2^1 {}^V A_1^2) \tag{2.118}
\end{aligned}$$

$$\begin{aligned}
V1_{-U} &= \left(\frac{{}^U B_2^2}{4} ({}^1 A_2^2 V1 + {}^2 A_2^2 V2 + {}^3 A_2^2 V3 + {}^4 A_2^2 V4) \right. \\
&\quad \left. + \frac{U1_{-U}}{4} ({}^U B_2^2 * ({}^1 A_1^2 + {}^2 A_1^2 + {}^3 A_1^2 + {}^4 A_1^2) + 4 * {}^U B_1^2 {}^U A_1^1) \right) / (1 - {}^U B_1^2 {}^U A_2^1) \tag{2.119}
\end{aligned}$$

with

- $w_i = {}^U A_1^1 U_i + {}^U A_2^1 V_i \sim {}^U A_1^1 U_i + {}^U A_2^1 V1_{-V}$, approximation for reducing the cost of interpolation.
- $V1_{-V} = V1$, second contravariant component of velocity at the mesh where interpolation takes place.

- $v1_{_V} = v1$, second Cartesian component of velocity at the node where interpolation takes place.
- $vi = {}^V A_1^2 Ui + {}^V A_2^2 Vi \sim {}^V A_1^2 U1_{_U} + {}^V A_2^2 Vi$, approximation for reducing the cost of interpolation.
- $U1_{_U} = U1$, first contravariant component of velocity at the mesh where interpolation takes place.
- $u1_{_U} = u1$, first Cartesian component of velocity at the node which interpolation takes place.

The estimated values of $V1_{_U}$ and $d\zeta_{i,j}_{_U}$ at the calculation point U, or $U1_{_V}$ and $d\zeta_{i,j}_{_V}$ at the calculation point V, is made by linear interpolation between the 6(4) adjacent values for $d\zeta_{i,j}$ (U or V). Close to the boundaries of the domain and for each adjacent values corresponding to a point in the land, a one-dimensional linear extrapolation (potentially square) of the physical associated quantity, is performed when needed. The above described interpolation method for the velocity components has been very effective (refer to the next chapter). However since the terms $(1 - {}^V B_2^1 {}^V A_1^2)$ and $(1 - {}^U B_1^2 {}^U A_2^1)$ appear in the denominator, these estimators (Eq. 2.118 & 2.119) can locally tend towards 0. This depends on the shape of the grid, and in cases of occurrence should be replaced by a simple linear interpolation of the velocity components (the usual method served in the Cartesian interpolation).

2.6 Preliminary tests of equations

2.6.1 Introduction

This section intends to test the equations previously determined in order to verify their consistency and possibly guide in choosing the best discretization scheme. For this simplified configuration we have a prior knowledge of the result that are implemented here. This test case has been proposed by Gourrion (2005) and has been updated for this study.

When the discontinuities develop in the numerical solution, between linear conservation (mass and momentum) and quadratic conservation (energy and potential enstrophy), the linear conservation is a essential (Vreugdenhil, 2013). For checking conservation over mass and momentum equations, the behavior of two Kelvin waves in a periodic rectangular basin has been examined. Actually a solution of this problem is known in the simplified case of very small

amplitude waves. The linear approximation only deals with the interaction of Coriolis force and pressure gradient.

2.6.2 Tracer Advection

2.6.2.1 One-dimensional Test

For the tracer balance equation, only the advection has been tested. In a one-dimensional space, a Gaussian distribution of a dissolved substance is applied by a uniform velocity (10 cm.s^{-1}) in the absence of physical process of diffusion. A correct modelling of the process should reproduce the average displacement of the structure (Gaussian) with a minimum deformation. A numerical diffusion is likely to be generated, at a rate controlled by the ratio $\frac{U\Delta t}{\Delta x}$.

In addition to the validation of equations, the principal objective of this test is to illustrate possible modifications in the form of structure induced by the local mesh sizes, stretching ratio and stretching direction. To do so, we consider a steady current $U = 10 \text{ cm.s}^{-1}$ through a simple channel, 1000 m long. Four different grids are used: two uniform grids ($\Delta x_1 = 2$ m and $\Delta x_2 = 8$ m) and two variables grids in which Δx gradually varies from 2 to 8 or from 8 to 2.

1. $\Delta x = \Delta x_1 = 2$
2. $\Delta x = \Delta x_2 = 8$
3. $\Delta x = \frac{\Delta x_1 + \Delta x_2}{2} + \frac{\Delta x_2 - \Delta x_1}{2} * \tanh((\xi - \xi_0)/\xi_r)$
4. $\Delta x = \frac{\Delta x_1 + \Delta x_2}{2} - \frac{\Delta x_2 - \Delta x_1}{2} * \tanh((\xi - \xi_0)/\xi_r)$

where ξ is the coordinate in the computing space, ξ_r is fitted to the width of the structure of dissolved substance and ξ_0 is the center location of the stretching zone in physical space. It is important to mention that the four simulations use the same time step $\Delta t = \frac{x_1}{U}$.

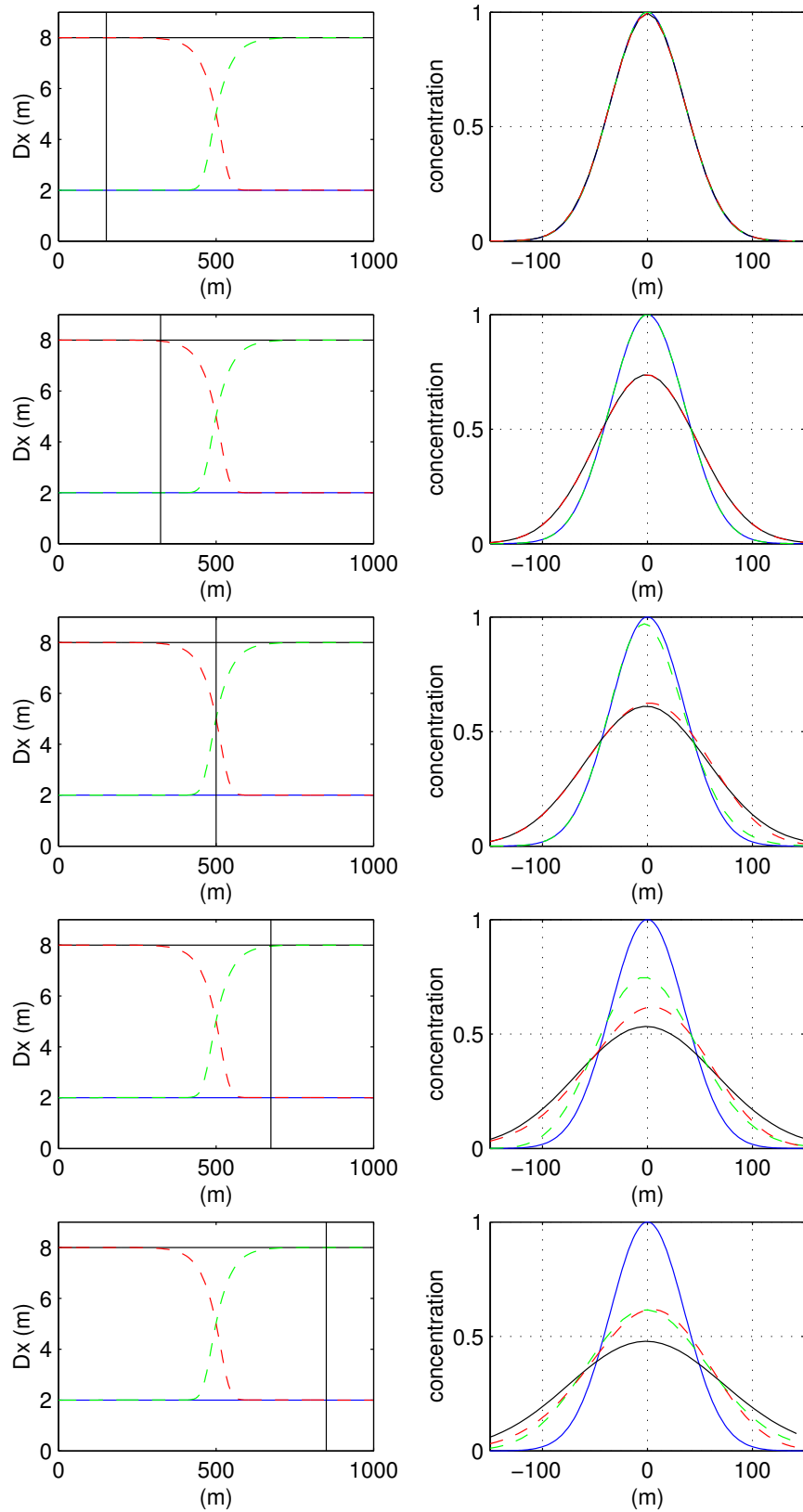


Figure 2.17: One-dimensional advection of a Gaussian structure of concentration for four different grids (black, blue, red and green) at five different moments. Left: value of the grid step throughout the entire area for the different grids (1_{blue} , 2_{black} , 3_{red} , 4_{green}) and theoretical position of the center of the structure (vertical black line ξ_0). Right: structure of the concentration field for each grids in the mobile basis vectors related to the theoretical position of the center of the structure.

Results are presented in Fig. 2.17 which shows that the structure remains centered in the mobile benchmark (Fig. 2.17, right). It is therefore advected in average with the theoretical speed. Hence, the modification of the equation of conservation for any tracer, proposed for using a curvilinear grid is satisfactory.

When the ratio $\frac{U\Delta t}{\Delta x}$ is equal to 1 (blue curve), the model is able to maintain the shape of the Gaussian structure over the time. For the lowest value of the ratio (Fig. 2.17, black curve), the synchronous model is not perfect and the shape of the transported structure is deformed over the time.

With a uniform time step, the diffusion rate in a regular grid, is dependent on the intensity of the velocity field while in irregular grids, it becomes a function of $\frac{U}{\Delta x}$.

As the local mesh size can control numerical diffusion, the mesh size gradients (in the regular grid) also can generate asymmetric deformations of the affected structure: green and red curves show that the convected pattern generally retains a memory of the mesh changes encountered; deformation of initial shape is further on the side which has passed longer time over the coarse meshes (Duhaut et al., 2008).

2.6.2.2 Two-dimensional Test

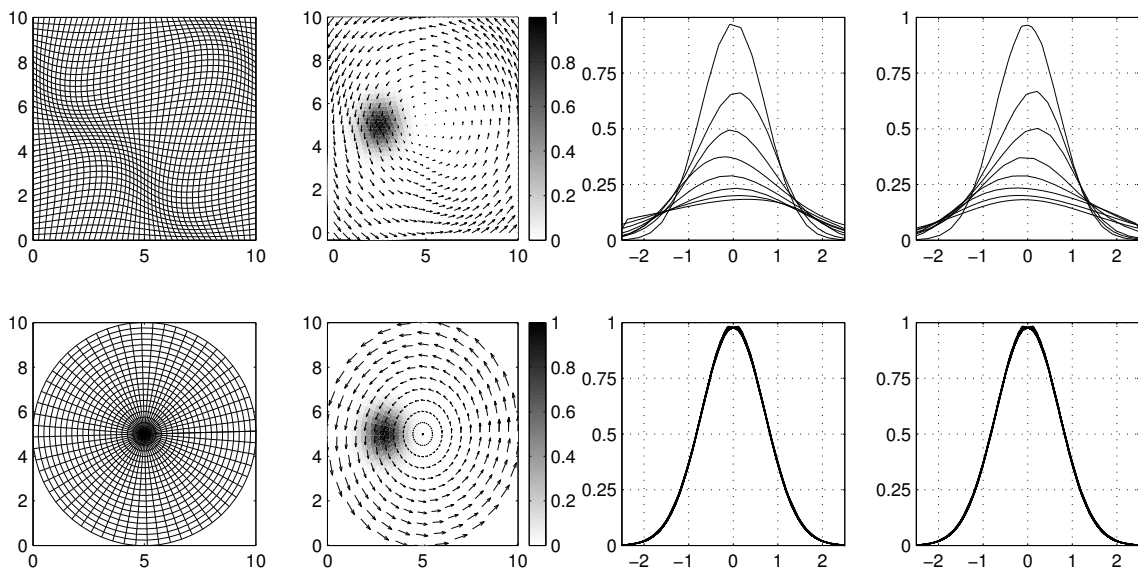


Figure 2.18: Two-dimensional advection a Gaussian isotropic structure of dissolved substance in a circular velocity field during one rotation period (one curve every 1/8th rotation) and for two different grids. Top: distorted mesh (non-orthogonal). Bottom: cylindric mesh (orthogonal). From left to right: grid / velocity field + initial condition / cross-section according to the orthonormal mobile axes (centered on the theoretical position of structure center).

A Gaussian and isotropic distribution of dissolved substance is transported in a circular velocity field corresponding to a "solid rotation", once again without considering the physical

process of diffusion. This test aims to show the potential of an irregular grid for minimizing numerical diffusion phenomena, but also to illustrate the role of the flow inclination with respect to the grid line in numerical diffusion (the larger inclination, the larger diffusion) (Date, 2005).

As in the one-dimensional case, the non-uniformity of the parameter $U/\Delta x$ together with a uniform time step lead to inevitable numerical diffusion. The curves of Fig. 2.18a-3 & a-4 show that the structure is deformed and seriously flattened after a cycle of rotation, the maximum concentration at the center being reduced by %80. In the case of stationary transport problem, nevertheless it may be possible to define a grid consistent with the velocity field, in order to provide uniform $U/\Delta x$ parameter. For the rotating flow of Fig. 2.18, a cylindrical grid centered on the fluid rotation axis satisfies the criterion (Fig. 2.18b). Fig. 2.18b-3 & b-4, show that numerical diffusion may vanish in the case of steady flow. This result is totally in agreement with those of Maliska and Czesnat (2003), who noticed that the numerical diffusion could be significantly reduced by aligning the grid axes with main stream directions.

2.7 Implementation of curvilinear terms in the general MARS-3D computing code

It has been chosen to develop a version of the MARS-3D code for non-orthogonal curvilinear coordinates as close as possible to the "Cartesian" version. This has been achieved by adding the required additional terms in equations under the use of a dedicated "CPP key" (Fortran 95) which activates or not the extra terms (depending on the key value) when compiling the program. In addition, all terms and coefficients related to metrics are computed from the grid definition within a pre-processing step.

It should be noted that changes made in the code (MARS-3D), with the aim that the numerical resolution of curvilinear on a regular grid gives exactly the same result as the resolution of Cartesian equations.

Chapter 3

3D modelling of hydrodynamics in South Brittany and the Loire Estuary: implementation, configuration and validation of the model

3.1 Introduction

The evaluation of the model performance is an important aspect of a model development process that has received large attention in the literature dedicated to geophysical fluid dynamics. The issue is to choose a procedure for determining: 1) the model accuracy, the extent to which model-predicted events approach a corresponding set of independently obtained reliable observations (usually measured); 2) the extent to which the model's behavior is consistent with existing scientific theory (Willmott et al., 1985). In this chapter we first describe the implementation of a curvilinear grid in our study area, and the configuration of the MARS-3D code for our application. The model implementation includes three main sections: parameterization, forcing, and boundary conditions. In addition this chapter deals with the validation of the MARS-3D model while using a curvilinear grid. The validation analyzes the model reliability based on three different types of measurement for hydrodynamic processes. The first set of measurements is the water surface elevation from tidal gauges at fixed stations. The second one is the water velocity profile collected from a moored Acoustic Doppler Current Profiler (ADCP). Third, computed salinity and temperature are being compared to measurements at different stations inside and out of the Loire Estuary.

3.2 Generation of a curvilinear grid for the study area

The "plasticity" of a non-orthogonal curvilinear grid can satisfy numerous criteria and therefore optimizing the computational grid is a difficult exercise, much more than meshing with a regular Cartesian grid, and even more complicated than building an unstructured grid such as those used by finite element models for which many "mesh generators" are available (mesh generation software). Here we have retained the Pointwise software, implemented by the **SIREHNA** society.

3.2.1 Choice of Lambert coordinates

The mesh coordinates have been transformed from Latitude and Longitude to the "extended Lambert II" coordinates system, a conformal conic projection which preserves angles, because the computation of the distances between points is simpler in this coordinate system. Therefore, we converted the various files used for the generation of our grid, which initially had different coordinates systems, into the "Lambert II extended".

3.2.2 Definition of Study area boundaries

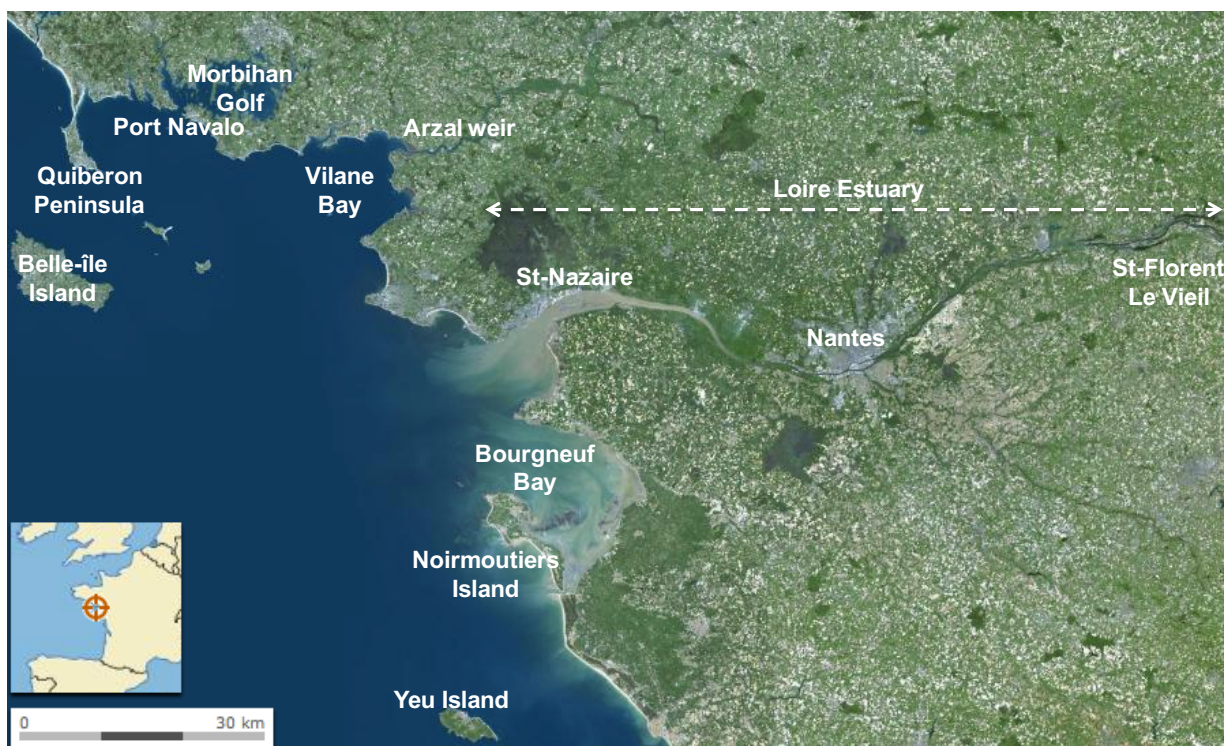


Figure 3.1: Aerial view of the whole Loire Estuary, included in the study area (the image is taken from the website www.geoportail.fr).

The study area to be meshed includes the French-Atlantic coastal area from the Quiberon Peninsula and the Belle-Île island westwards to the islands of Noirmoutier and Yeu southwards. The computational grid has to include the whole Loire Estuary up to the upper limit of tide propagation, located approximately at Saint Florent Le Vieil (Fig. 3.1).



Figure 3.2: Coastline in Atlantic parts of the study area.

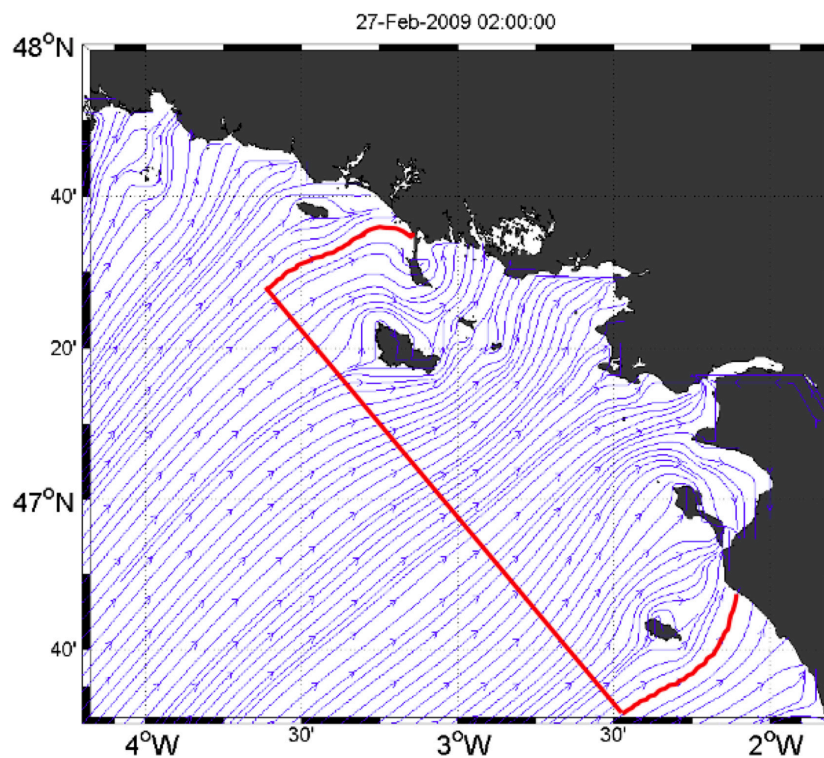


Figure 3.3: Streamlines at maximum tidal flood, the study area boundary is represented by the red line.

Similarly, the tidal section of the Vilaine estuary, up to Arzal weir is included in the domain, as well as the Morbihan Gulf which communicates with the coastal area through a very narrow strait near Port Navalo.

For the coastal zone we used the coast lines issued from the file "France-CoastLine" (Fig. 3.2) and for the open sea we defined an imaginary line which encompasses the islands and all the areas of interest (Fig. 3.3).

The next step was to define the principal longitudinal and transversal lines of the grid structure. As mentioned the main longitudinal lines, were constructed empirically and follow the main direction of the tidal flow (Fig. 3.3). Fig. 3.4 shows the boundaries of the different domains used for the mesh generation (189 domains). The boundaries of each domain are colored according to the mesh size along these boundaries (ΔS , in meters).

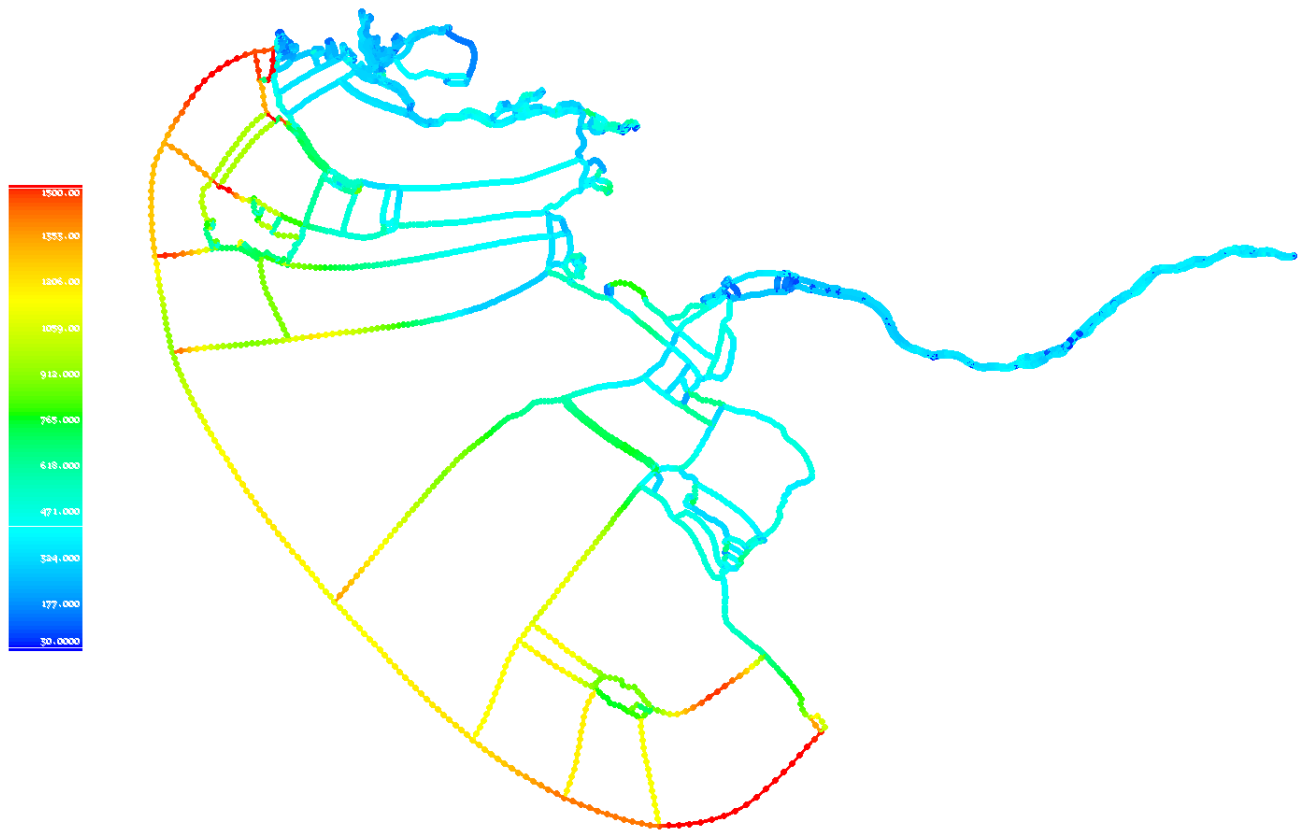


Figure 3.4: Splitting of the study area into 189 domains, colors indicate the mesh sizes along the domain borders.

3.2.3 Construction criteria of the grid

A certain number of criteria guides the construction of the mesh of our study area. By using the graphical interface of Point-wise software progressively and after multiple iterations, we achieved the geometrical parameters of the mesh, as well as the angles between the grid lines, mesh sizes, their asymmetry and the rate of variation (angle and dimension) from each cell to its neighbors. Adopted criteria are followings:

- The mesh contours should be oriented parallel or orthogonal to the streamlines: in the estuary (in-shore), streamlines are often parallel to the bathymetric contours; off-shore, often they are often perpendicular to the coastline (Fig. 3.3); we have also sought to "follow" the direction of the paleovalley of the Loire River, to respect the hydrodynamic continuity around the bathymetric pit already mentioned and clearly visible in Fig. 3.5;
- Use of the possibility to extend the mesh in the direction of the tidal current resulting in a less severe CFL stability criterion;
- Respect of specific maximum mesh size, provided for different sectors;
- Ramping mesh lengths (no more than 20% from a cell to another);
- Reduction of the meshes obliquity (skewness¹) with typical angles between 60° and 120°, in order not to give too much weight to cross derivatives for which the numerical scheme has not been optimized;
- Compliance with the continuity of the grid around the islands (same number of meshes on each side of an island) to be compatible with the structure of the mesh.

One of the principal particularity of using non-orthogonal curvilinear grids was using the isobath contours for generation of the principal direction of meshes. In the Loire estuary, bathymetric contours (Fig. 3.5 & 3.6) have been used to build the orientation of the grid.

¹According to Sec. 2.6.2.2, the mathematical check on the respect of continuity confirms that our numerical solution is indeed accurate at the considered skew angles and aspect ratio.

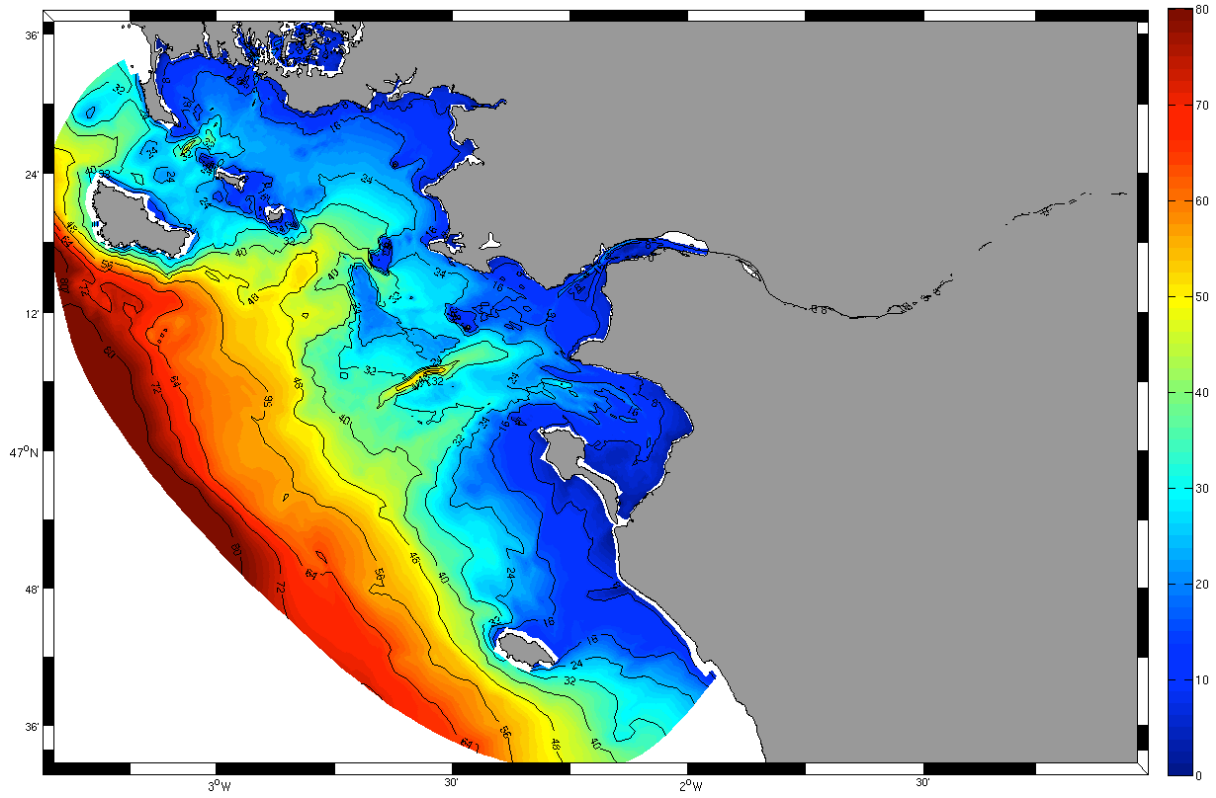


Figure 3.5: Bathymetry of the coastal zone Loire-Vilaine.

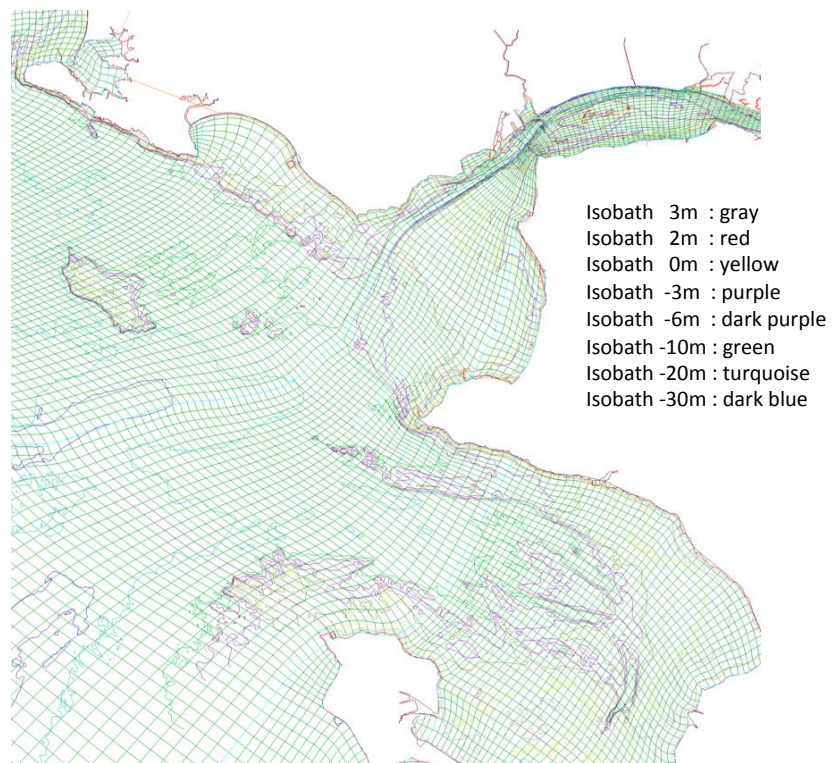


Figure 3.6: Part of the computational grid localized at the mouth of the Loire Estuary, superposed with isobath contours.

In addition, it has been chosen to respect sharp capes of some islands by splitting some grid lines into two branches having the same set of indices, as shown on Fig. 3.7 below: in particular, an extensive examination of the mesh orthogonality (skewness) was produced to comply with the complex geometric imposed by the coastline, the islands and the depth contours while maintaining a continuity between the different sub-areas of the mesh.

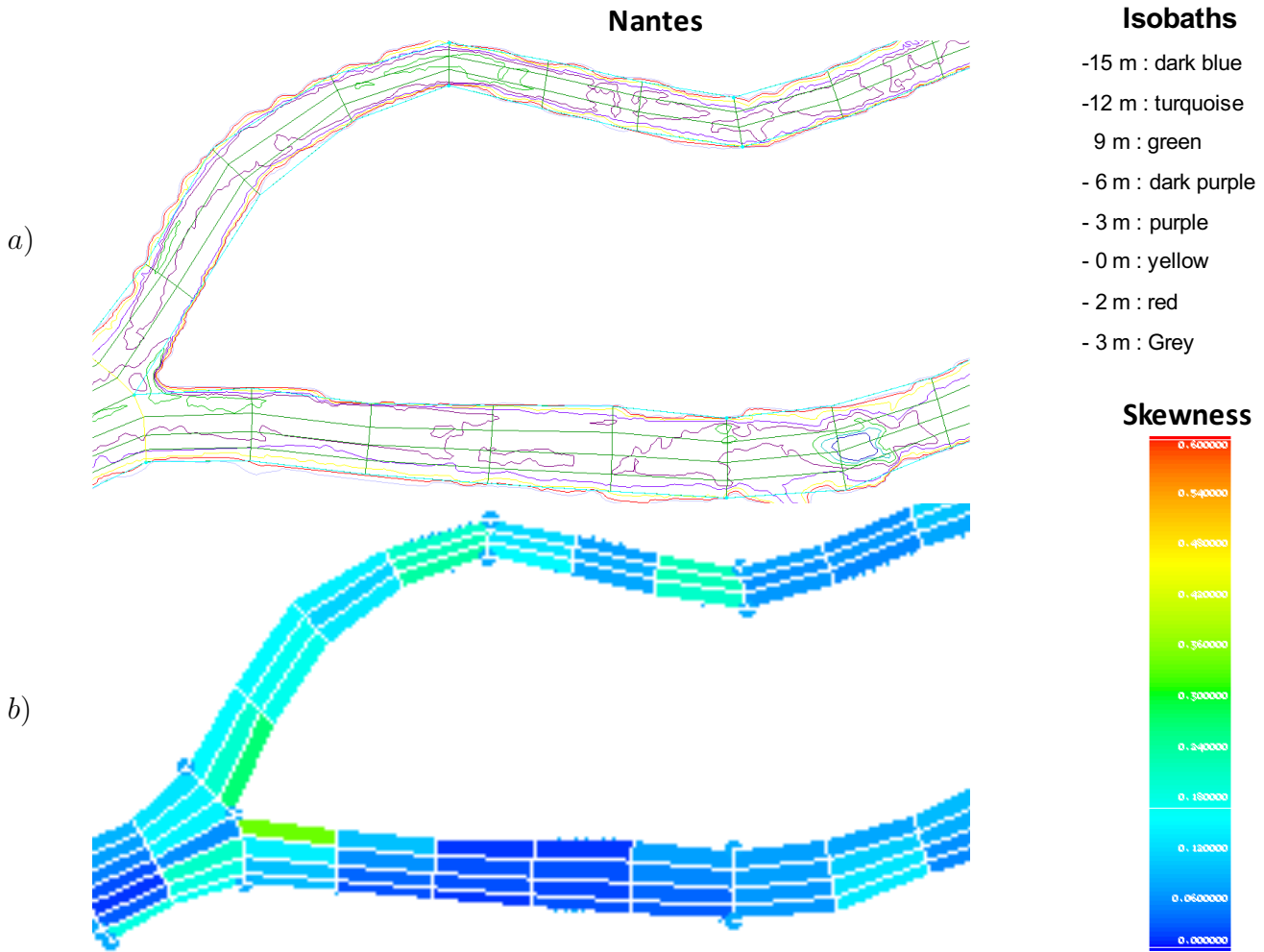


Figure 3.7: Details of the computational grid in the Loire Estuary, around the Nantes Island; a) superposition of the grid and isobath contours b) skewness, the colors represent the obliquity.

The whole area is divided into contiguous domains, inside which the grid building is automatically optimized, following mesh specifications that are selected on domain borders. Frequently, these borders are common to contiguous domains (Fig. 3.4 & 3.8). These borders, or baselines, were constructed empirically, following the main direction of the tidal current. The orthogonality is maintained as much as possible, in particular near boundaries. In addition, the size variation of contiguous meshes was limited to 20% in agreement with the requirement previously listed. An example of base lines distribution at the mouth of the Loire estuary is given

in Fig. 3.9.

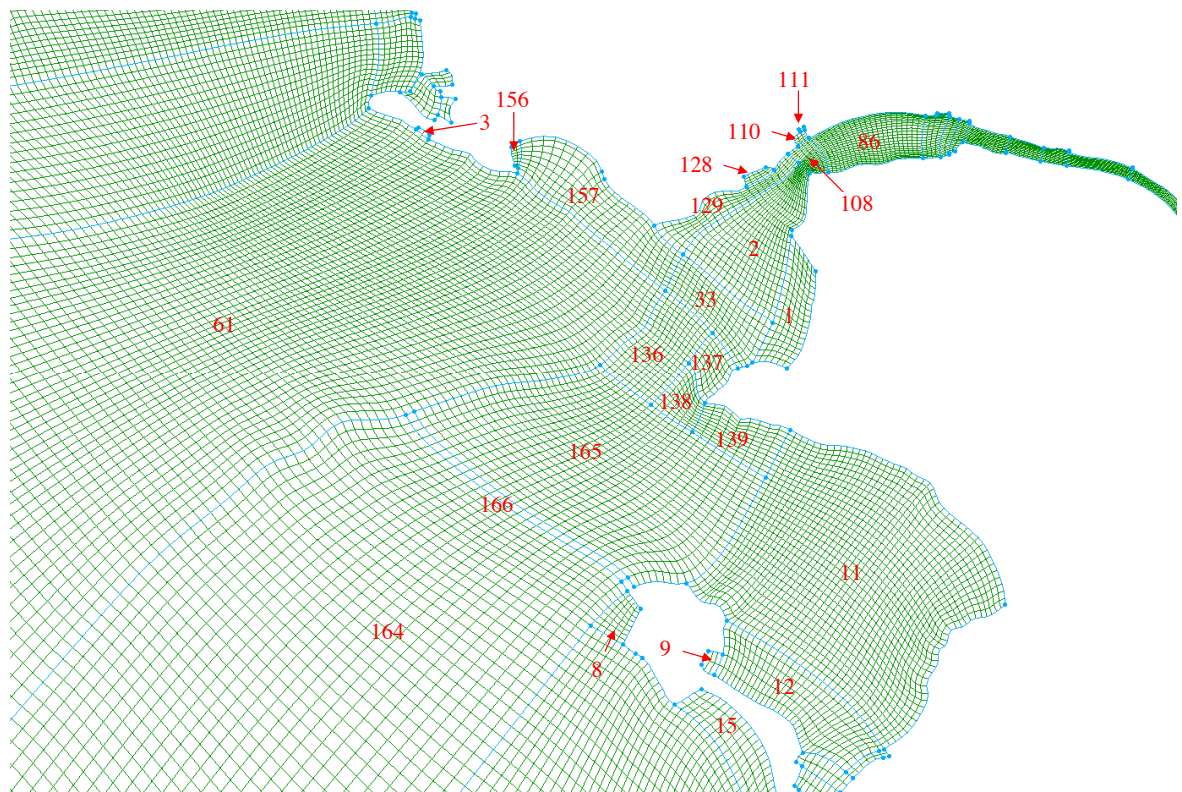


Figure 3.8: Zoom of the grid at the mouth of the Loire Estuary. Baselines (in blue) are used to divide the area into smaller blocks, the numbers indicate each block.

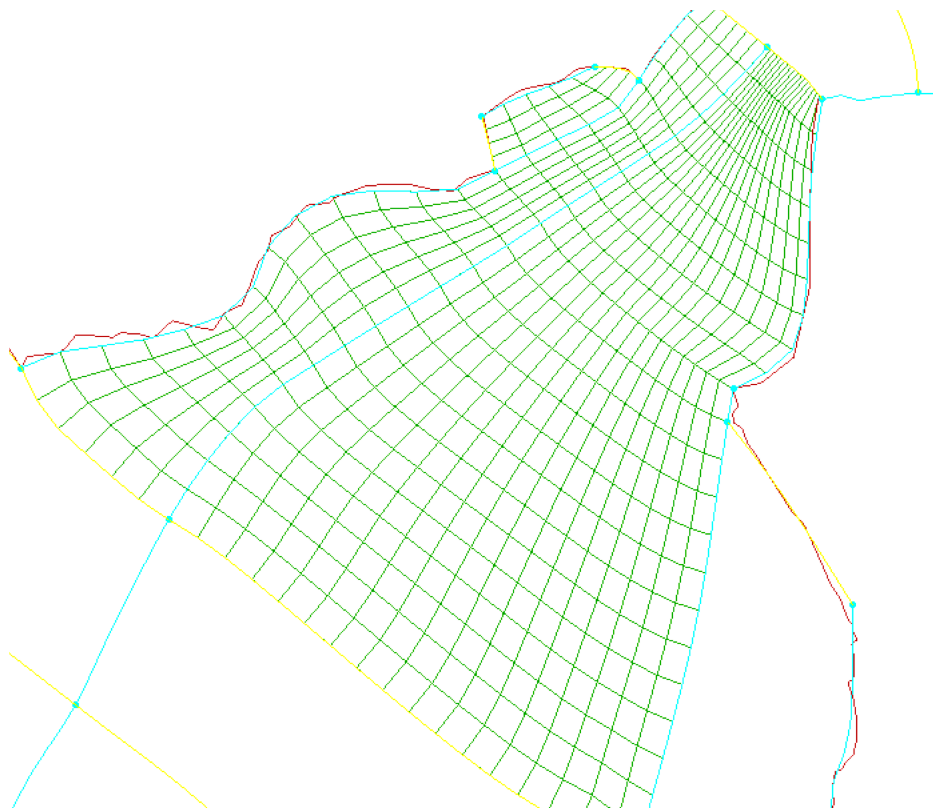


Figure 3.9: Illustration of the progressive mesh size criterion to a typical cross-section of the Loire Estuary.

3.2.4 Mesh sizes and orthogonality

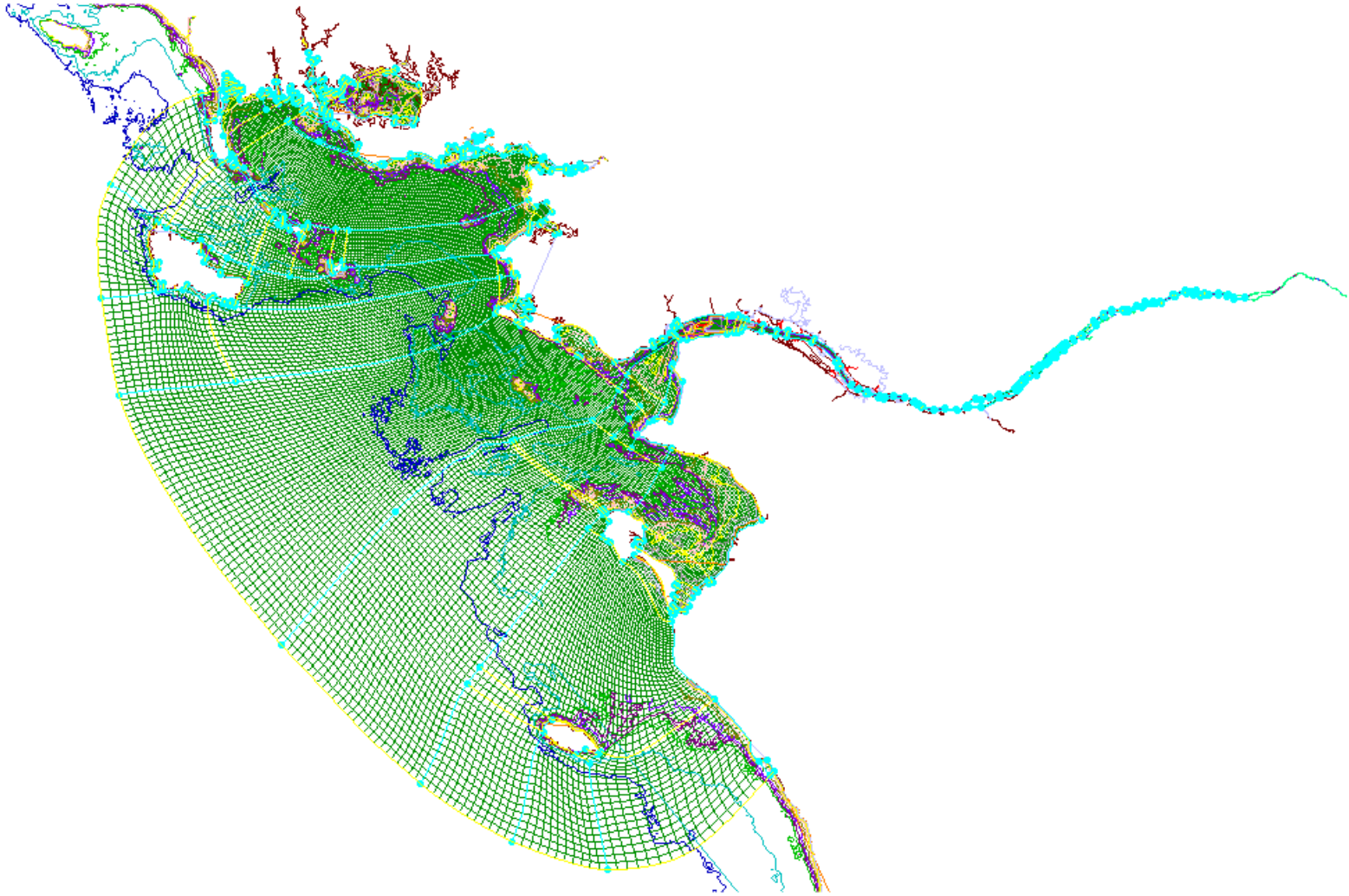


Figure 3.10: General view of the grid with depth contours and coastline, blue lines present the principal domains.

In addition to the previous requirements, constraints on minimum or maximum mesh size have been defined for different areas of the computation grid. These are summed up in the table below. The progressiveness, expressed as the length ratio between successive meshes is limited to 10% (exceptionally 15%) in some regions with the strong current, particularly in the mouth of the Loire Estuary (Fig. 3.10). The elongation, is the ratio between the two dimensions of a mesh, is favored in the case where the current is systematically aligned along one of the dimensions of the curvilinear coordinates.

The guideline values of the mesh dimensions by sectors are summarized in the following table:

| Place | | Size / number of mesh | |
|---------------|--|---|--|
| | | length | width |
| Atlantic area | | 1.5 km maximum close the sea boundary | |
| | | About 250 m in the inner bays | |
| | | About 500 m around the islands | |
| Loire Estuary | Upstream and downstream of Nantes | 500 m when the stream is "channelized" | Between 30 and 100 m depending on the location, in order to keep 6 to 8 meshes through the cross section |
| | | Reduction down to 250 m when is forced by the coastline (presence of islands or meanders for example) | |
| | Upstream of the Martiniere channel | 250 to 350 m with refinement if needed | |
| | From the Martiniere canal to Saint-Nazaire | ≈ 300 m | About 100 m at Paimboeuf, and 200 m off the Loire Estuary |

Table 3.1: Sizes of meshes used in different sectors of computational grid.

Skewness

In a non-orthogonal grid, when the governing equations are reformulated in general curvilinear coordinates, cross derivative terms appear in the equations (Sec. 2.5.3.1).

Depending on the skewness (which quantifies the orthogonality) of meshes in the grid, these cross derivative terms can be very significant and can affect the numerical stability as well as the accuracy of the numerical method used for the solution (Erturk and Dursun, 2007).

According to Lee and Tsuei (1992), skewness and smoothness (change in size) affect the truncation error and have most important influence on the mesh quality. However, the effects of mesh skewness on the quality of the numerical solution and on the procedure to obtain the solution of full Navier–Stokes or even linear advection–diffusion equations are still not well illustrated (You et al., 2006).

The skewness of the grid, representing the deviation from orthogonality, has been evaluated according to the following expression, computed for each quad mesh characterized by θ_{max} and θ_{min} the maximum and minimum angles at the mesh corners:

$$\text{Skewness (for a quad)} = \max \left[\frac{\theta_{max} - 90}{90}, \frac{90 - \theta_{min}}{90} \right] \quad 0_{(best)} \leq \text{Skewness} \leq 1_{(worst)}$$

When generating the grid, skewness was limited to 0.6 in the sharpest corner, and about 85% of meshes had a skewness lower than 0.4. The skewness distribution is illustrated on Fig. 3.11 (see also Fig. 3.7 for the Loire Estuary).

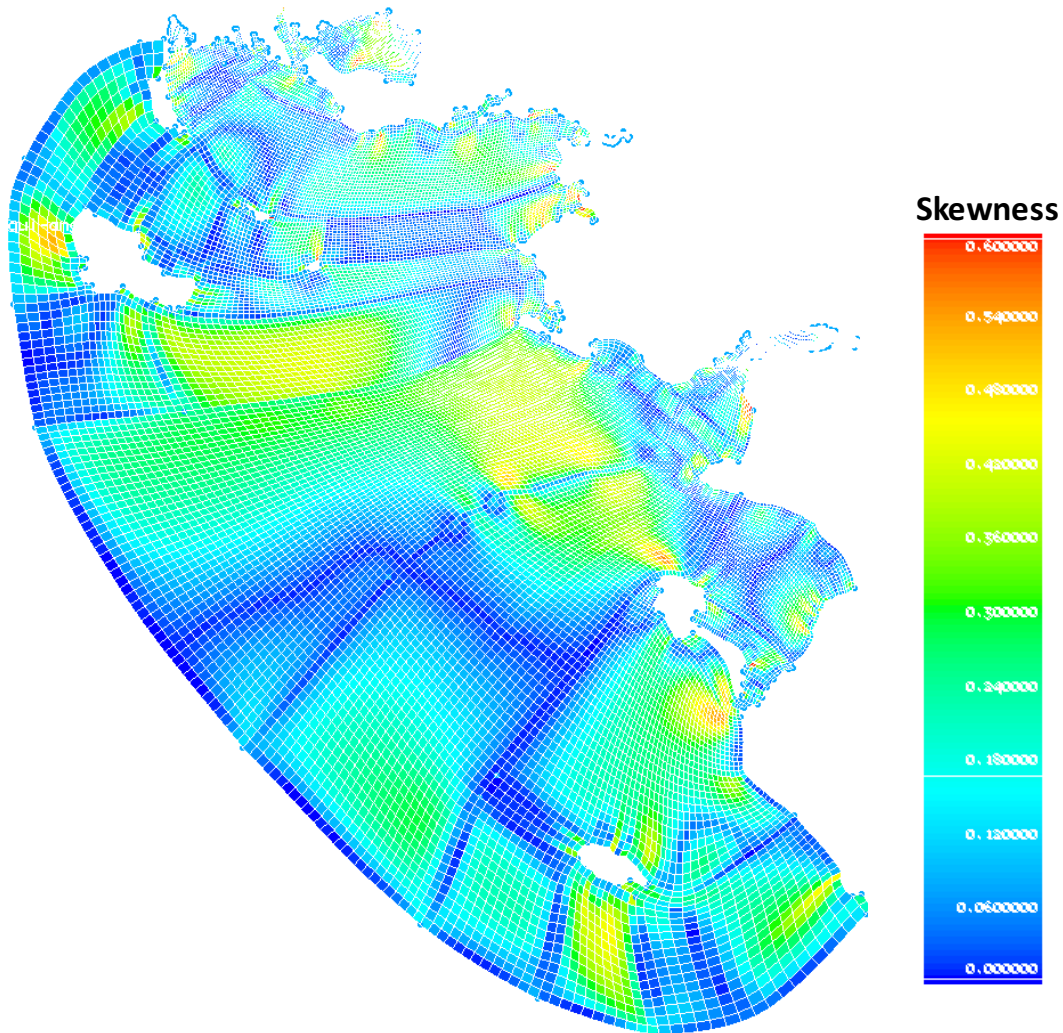


Figure 3.11: General view of the non-orthogonal curvilinear grid: orthogonality gap.

Figure 3.11 shows the entire grid Skewness; each mesh is colored according to its deviation from orthogonality (criterion of inclination "skewness"): a perfectly orthogonal mesh has a skewness of 0, and a "crushed mesh" (totally deformed) has a skewness equal 1. In the figure presented here, the color scale ranges from 0 (dark blue) to 0.6 (red).

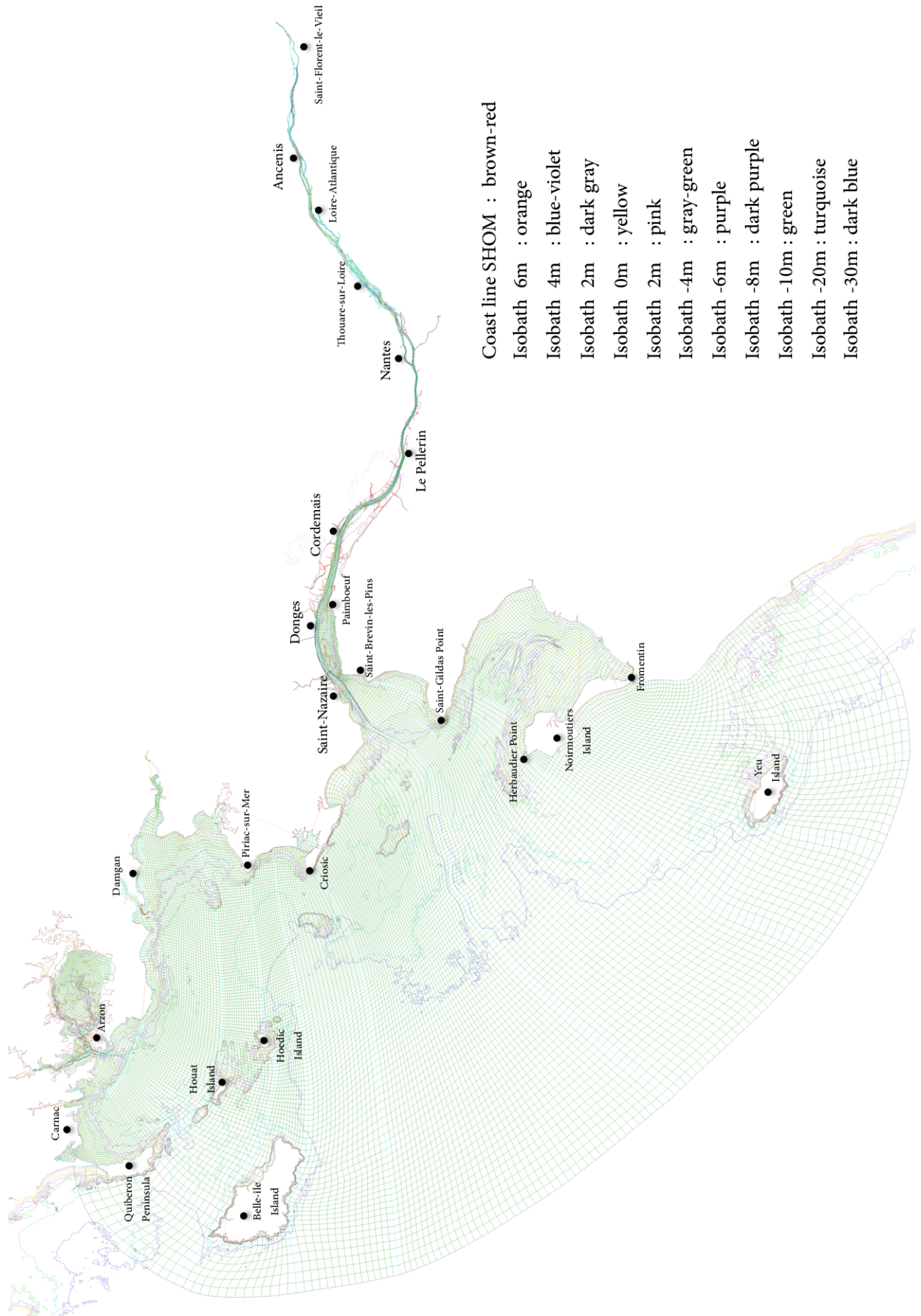


Figure 3.12: General view of the grid with depth contours and coastline.

3.2.5 Generation of final grid

Naturally, all criteria could not be full-filled at the same time because they were not always compatible. A compromise has been elaborated by successive iterations. Figure 3.12 shows the entire grid, overlapped with coastlines and depth contours. As shown on this figure (blue lines), boundaries have been selected in order to have main streamlines either parallel or orthogonal to the boundary. The final grid has 25801 meshes. More detailed views of the grid superimposed on depth contours are shown in Khojasteh et al., (2011).

Finally, the computational domain matrix used in MARS-3D has a dimension of 467 x 252 meshes. It is shown in Fig. 3.13.

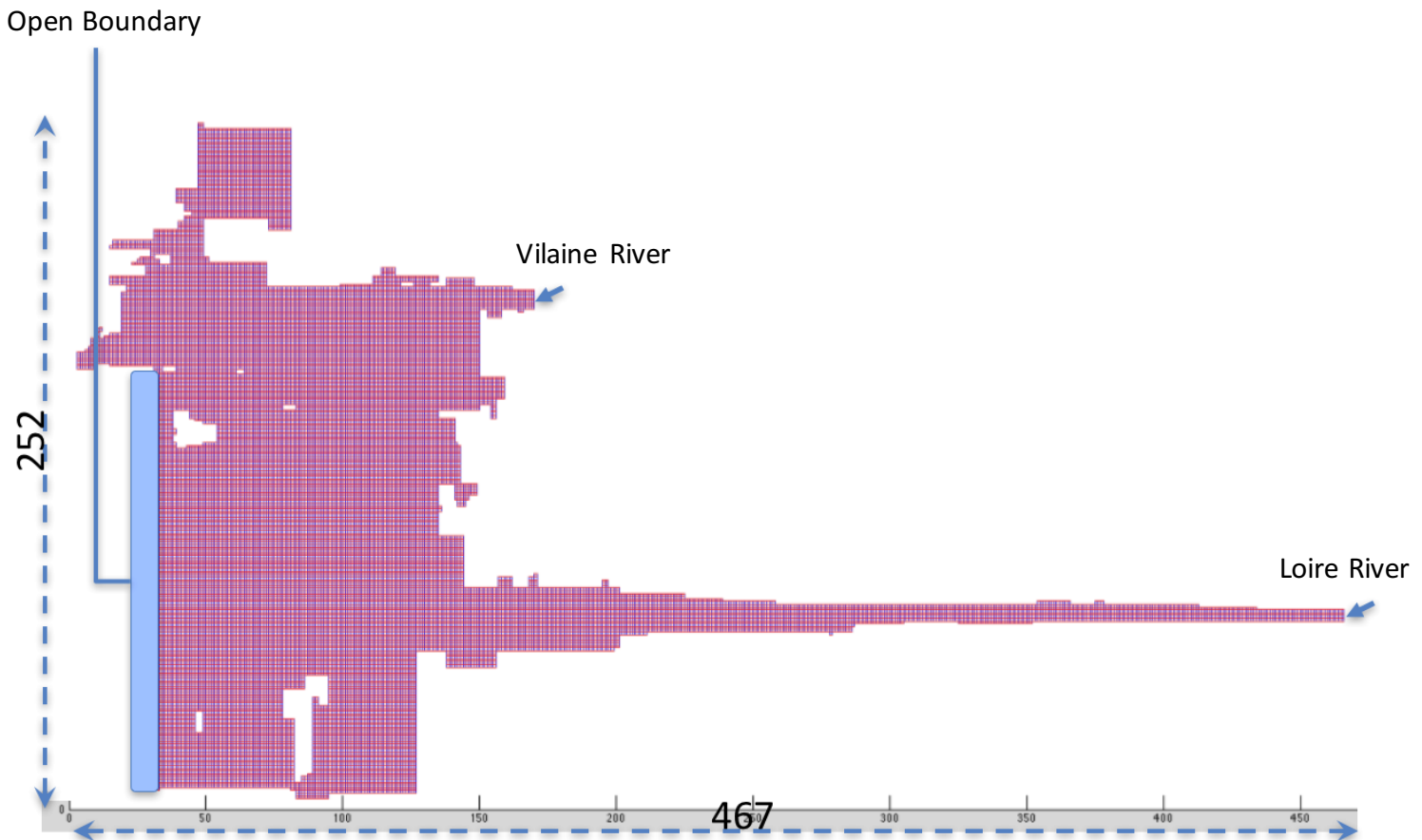


Figure 3.13: Study area in transformed computational grid.

3.2.6 Geometric coefficients and bathymetry interpolation

Once the grid is realized using the Pointwise software, its geometric coefficients have to be computed (metric tensor and different transformation coefficients are being used in the MARS-3D hydrodynamic code, Sec. 2.4.9.3). A possible approach to estimate these local derivatives

is to use the finite-differences methods. The adopted approach, to compute the transformation coefficients uses "spline functions" (Khojasteh et al., 2011). The spline functions are a device for approximating the shape of a curvilinear stochastic function without the necessity of pre-specifying the mathematical form of the function (Suits et al., 1978). The case of multiple islands along the Loire River is particular (see Fig. 3.14), because two banks of a given island, geographically separated, may correspond to border lines having the same index in the matrix of certain coefficients. The red line on Fig. 3.14 shows such an example of double geographic position for same matrix coordinates. A solution has been developed by doubling the required matrix coefficients, distinguishing their northern and southern uses.

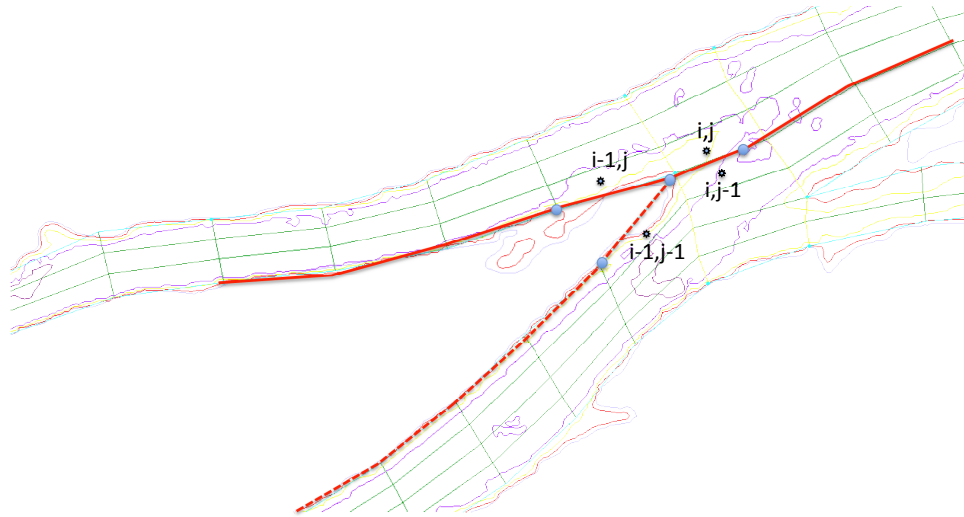


Figure 3.14: Example of grid splitting around an island.

In the case of non-overlapping areas, the "spline" method may produce discontinuities of geometric parameters near boundaries. When these areas are pre-assembled, continuity problems may rise in case of a narrow strip land (such as the Quiberon peninsula or some islands in the upper reach of Loire Estuary with one mesh wide), while a cubic spline interpolation function uses several adjacent meshes. In a first step, we reassemble all the areas in a unique matrix, operate the spline function over the whole area and replace calculated coefficients at the non-overlapping domain by changing the derivative order and precision criteria (more information about calculating geometric parameter is given in Khojasteh et al., (2011)).

All these interpolations were produced with Matlab software. The grid generated by "Pointwise" contains several domains (actually 189 domains, Fig. 3.4). Each of them contains one set of lines I and one set of lines J, defined the position of the grid with two matrices $X(i,j)$ and $Y(i,j)$ for the coordinates of each node (i,j) in real space. The first step consists in assembling these matrices of different domains and form single X and Y matrices for the entire grid.

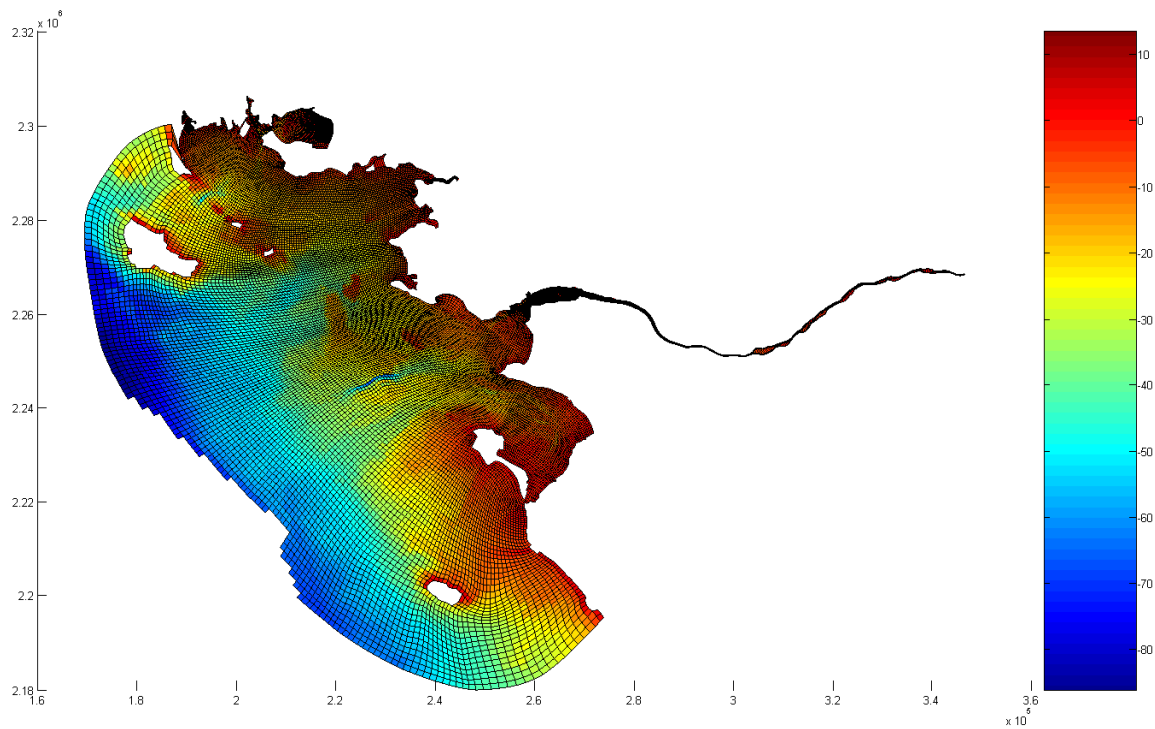


Figure 3.15: General view of the grid after projection on the bathymetry.

The second operation is an interpolation of bathymetric height in each point of the grid from different files (mixing information from digital terrain models (DTM) at different resolutions (Fig. 3.16)). The vertical references of various bathymetry files are different: the reference of marine sections is hydro-graphic reference level (corresponding to the lower tidal level), while the bathymetry files upstream and downstream of Nantes refer to the IGN69 level, which is situated 2.75 m above the hydro-graphic reference level at St-Nazaire. The bathymetry file of marine section has been corrected in order to have the IGN69 level as a unique reference for our whole domain. Figures 3.15 and 3.17 show the bathymetry obtained after this second step. Coordinates are expressed in "Lambert II extended" and water depths refer to the IGN69 level. The third operation consists in transforming coordinates of all bathymetry references from the Lambert II system to the WGS84 ² system. The principal reason for this choice is that the offshore section is the largest ones (greenish blue color, see in Fig. 3.16) and MARS-3D convention. Finally, the last step is the generation of the metric tensor, consisting of covariant and contra-variant transformation coefficients of different points of meshes, for the curvilinear adaptation of Navier-Stokes equations. Computation of all the coefficients used in this study

²WGS84 (World Geodetic Survey 1984) is an Earth-centered, Earth-fixed terrestrial reference system and geodetic datum. WGS84 is based on a consistent set of constants and model parameters that describe the Earth's size, shape, and gravity and geomagnetic fields, and is the reference system for the Global Positioning System (GPS).

is expressed in Khojasteh et al., (2011).

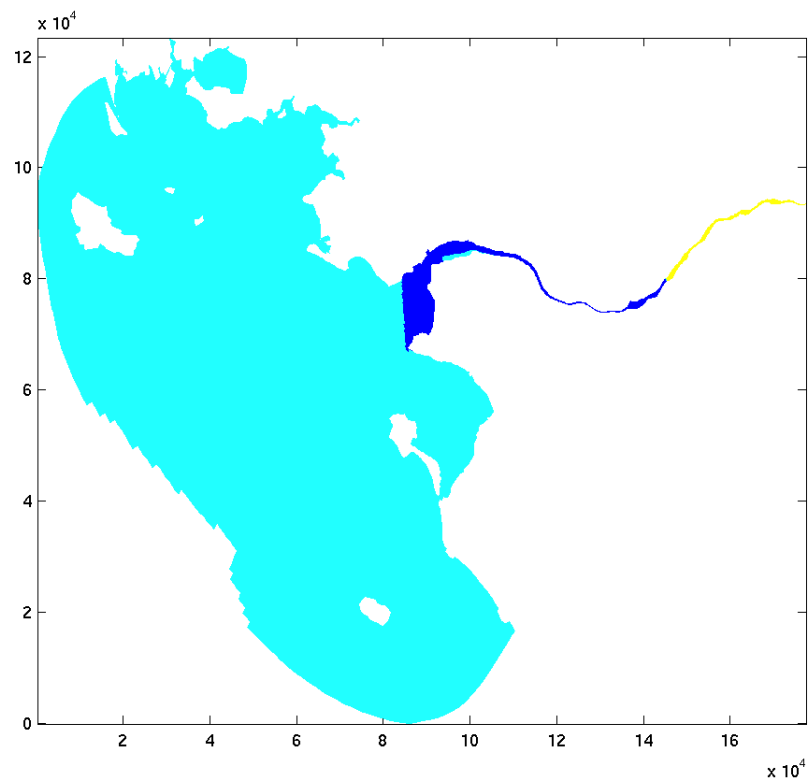


Figure 3.16: Different references used for interpolation of bathymetry; greenish blue color: "WGS84"; dark blue: "Lambert II extended"; yellow: "Lambert II extended".

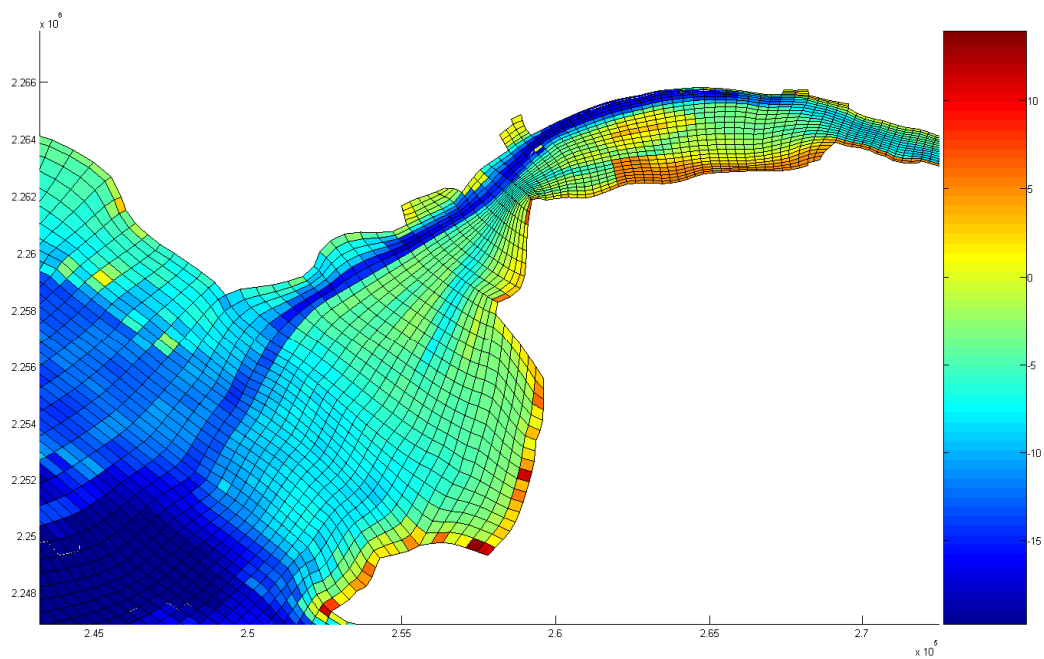


Figure 3.17: View of the grid in the area of the Loire mouth, and representation of bathymetric information for each mesh.

3.3 Model configuration

3.3.1 Vertical grid

The MARS model uses the reduced vertical coordinate system named **sigma**, which has the advantage of following the topography of the ocean floor and to keep the same number of layers whatever the bathymetry and the surface level. The **sigma** coordinates are defined as:

$$\sigma = \frac{z - \zeta}{\zeta + H} \quad (3.1)$$

here σ is the vertical coordinate, $H(x, y)$ the bottom position and $\zeta(x, y, t)$ the sea surface elevation. z and σ increase upward. Levels are freely chosen between $\sigma = -1$ ($z = -H$) at the sea floor and $\sigma = 0$ ($z = \zeta$) at the sea surface depending on the desired vertical refinement.

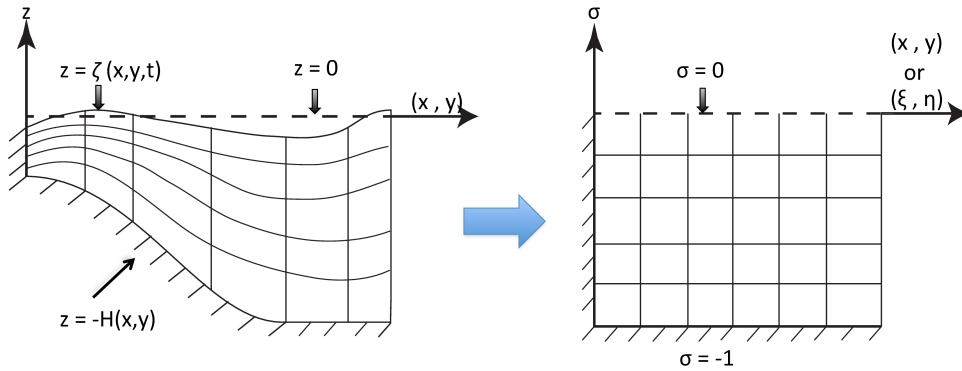


Figure 3.18: Transformation into sigma coordinates.

The figure 3.18 shows the change of coordinate system. The number of levels is identical regardless of the water depth, the layers' thickness varies in space and even in time according to variations of surface elevation. In this study we choose 10 vertical layers with equal thickness in sigma coordinates.

3.3.2 Forcing

3.3.2.1 Tide

The tidal harmonic constants (amplitudes and phases) used as boundary conditions come from the CST-FRANCE model developed by SHOM (Le Roy and Simon, 2003), which is a numerical model of the Bay of Biscay adjusted by tide gauges at sea. 115 harmonic components are provided by this model on a rectangular grid (4 km resolution), among which 8 waves are dominant (M2, N2, S2, K2, O1, K1, P1, Q1). At the open boundary, sea surface elevations are

imposed. They result from the sum of astronomical tides and the average sea surface estimated at Saint-Nazaire station.

Tidal forcing data have been computed for the full year 2007 and the beginning of 2008 (until April) at each boundary nodes of the model, with a time step of 15 minutes. The curvilinear boundary condition requires the interpolation of sea surface elevation data which was achieved with a Fortran based software called EXTRACT (developed in Dyneco-Physed Lab, IFREMER).

3.3.2.2 Storm surges and other open sea conditions

Storm surges on the coast of France often come from storms occurring in the North Atlantic Ocean, so that it is important to consider a sufficiently large area to model this parameter correctly. A regional model of the bay of Biscay is used to compute storm surges at a representative location of the sea boundary, chosen at the same latitude as St-Nazaire. This storm surge is computed as the water elevation difference between two simulations of the MARS model applied to the bay of Biscay, one with meteorological forcing (tide harmonic FES (Lyard et al., 2006) including fresh water inputs and meteorological forcings (Saha et al., 2010)), the other without meteorological forcing (Fig. 3.19).

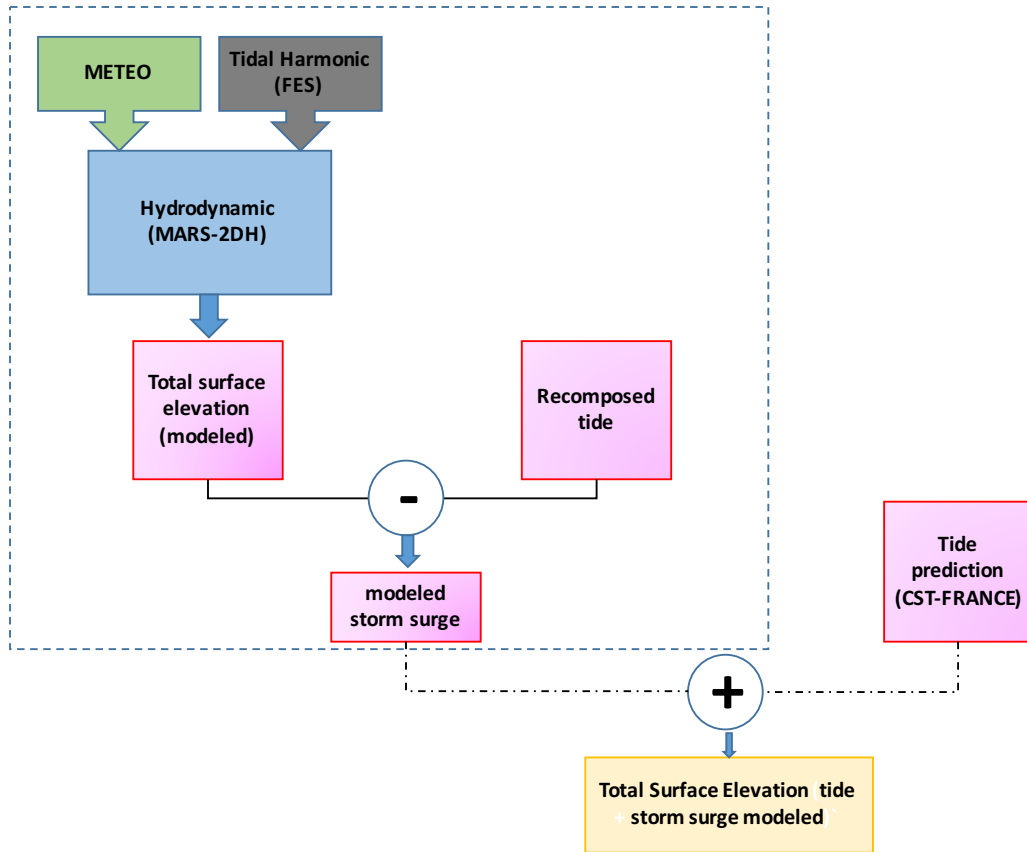


Figure 3.19: Reconstitution of the total SSE (predicted atmospheric tide + storm surge), modeled by MARS-2DH (Lazure and Dumas, 2008).

Last, temperature and salinity are forced on the boundary when water fluxes are shoreward. These information were captured from a regional 3D model of the bay of Biscay (the Manga MARS-3D model, with a 4 km horizontal resolution and 10 layers on vertical). The inputs of Gironde River, likely to be significant at the boundary of our study area, particularly via the influence on density gradient. For this reason, the results issue from the nesting model are interpolated along the open boundary.

3.3.2.3 Wind forcing and other meteorological forcing

Forcing of real wind and atmospheric pressure was introduced in the model from simulations with the meteorological ARPEGE model (MétéoFrance). Considering the mesh resolution of the ARPEGE model (spatial resolution of 0.25 degree with a temporal resolution of 6 hours), two points were located in the study area. One of them is close to the mouth of the Loire estuary ($47^{\circ} 12' 26''\text{N}$, $2^{\circ} 20' 7''\text{W}$). The other available point is situated at the Talus semaphore, on Belle-île Island. Although winds in this region are mostly uniform (see Chapter 4), both of these points are spatially interpolated/extrapolated in each mesh of the entire grid. Simultaneously,

surface heat fluxes are extracted from the meteorological model and similarly interpolated. With mixing conditions in the water column, these fluxes constitute the main forcing for sea temperature variations in the area.

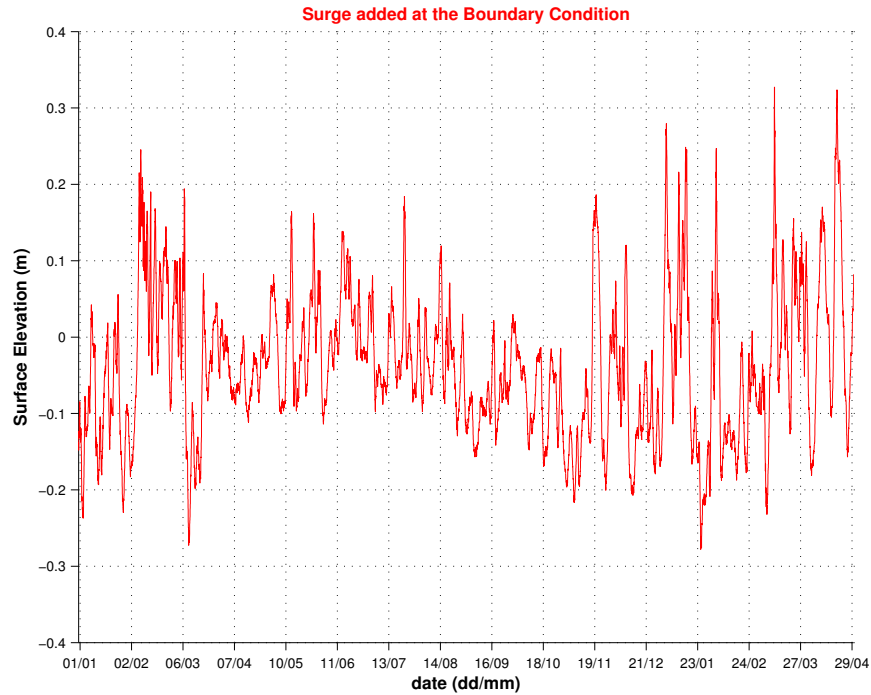


Figure 3.20: Surge considered at the open boundary between 01/01/2007 and 29/04/2008.

3.3.2.4 River discharges

The simulated period includes the whole year 2007 and the beginning of 2008 (till April), because of the availability of validation measurements and because of the representativity of different forcing variations during this period (this will be explained in chapter 4).

Fig. 3.21 shows the Loire and Vilaine discharges during 01/01/2007 - 29/04/2008. The daily discharge measured at Montjean (on the Loire River) is imposed at the upstream boundary of the model (Saint-Florent). The river outflow is assumed to have a steady salinity of 0.002 PSU, while its daily-averaged temperature is provided by measurements at Montjean. A daily outflow of the Vilaine River is also accounted for, ignoring the time variations within the day that could be induced by the functioning of gates at Arzal weir, the upstream end of the Vilaine Estuary. Fig. 3.21 indicates that the Loire discharge actually varies between 200 to 4000 m³/s and the Vilaine discharge varies between 15 to 600 m³.

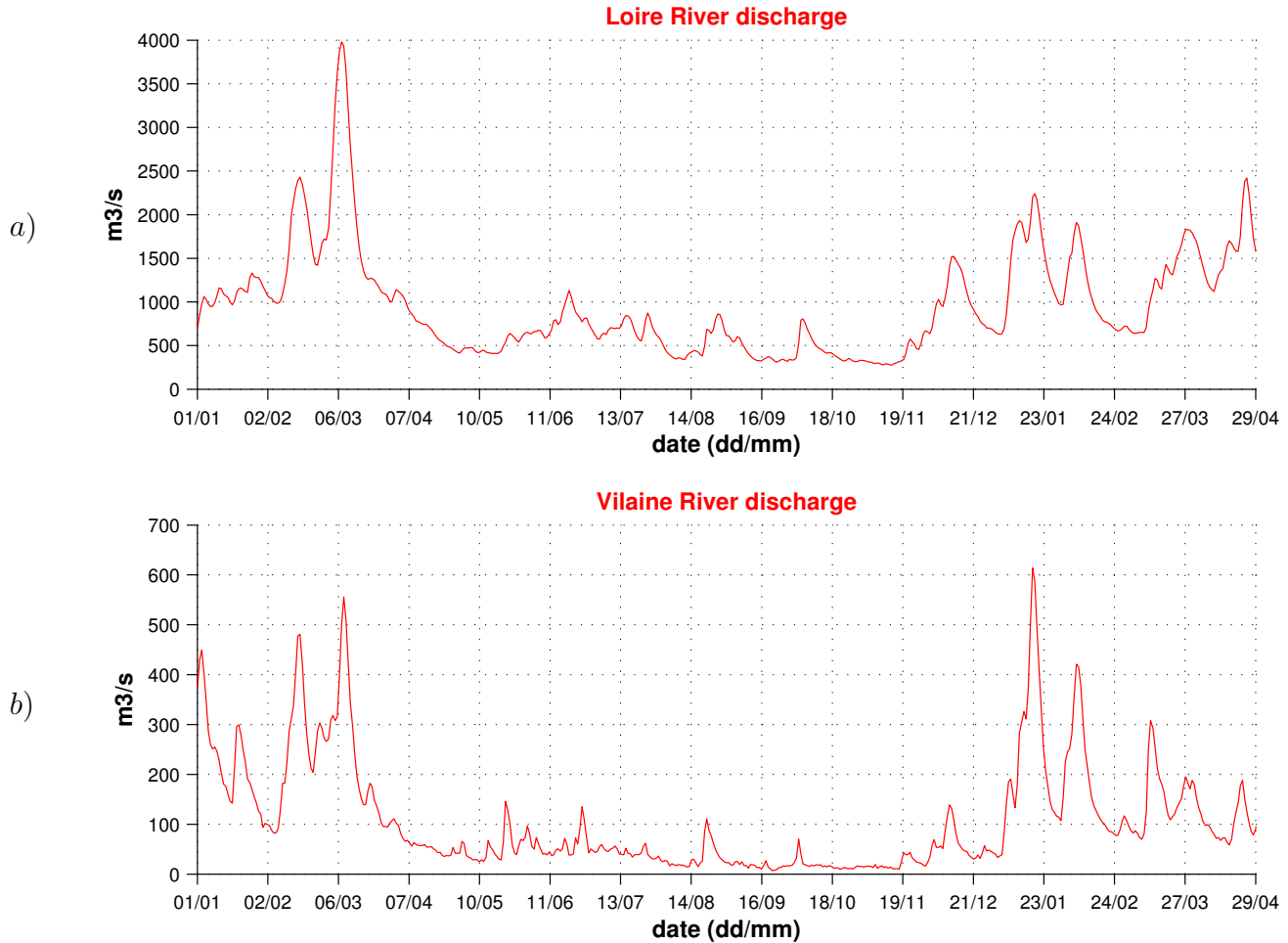


Figure 3.21: River discharges in the study area between 01/01/2007 and 29/04/2008; a) Loire, b) Vilaine.

3.3.3 Parameterization

Bottom friction

Coastal hydrodynamic models are very sensitive to the bottom friction, especially in shallow areas and estuaries. In our model, bottom friction is parameterized with a roughness length (Z_0), assuming a logarithmic profile in the bottom layer. This parameter has to be fitted so as to simulate actual tidal variations of water level in different regions, as measured by tide gauges. We considered seven tide gauges data, provided by the "Grand Port Maritime" de Nantes-St-Nazaire (GPMNSN), located at Saint-Gildas heap point, Saint-Nazaire, Donges, Cordemais, Le-Pellerin and Nantes.

IFREMER measurements near Le Croisic are also used for validation. The surficial sediment nature is likely to influence the bed roughness; in addition, this sediment nature may change in the estuary according to the position of the turbidity maximum, which is dependent on the Loire river flow (Le Hir and Thouvenin, 1992, Sanchez et al., 2000). Finally, following

an approach adopted by SOGREAH (ARTELIA in the present days) for a previous estuarine modelling in the Loire estuary (Walther et al., 2009), it has been chosen to have a roughness length which directly depends on the river flow (Fig. 3.22).

The defined roughness length for different regions of the estuary is given in Fig. 3.22, while it remains uniform in the offshore area

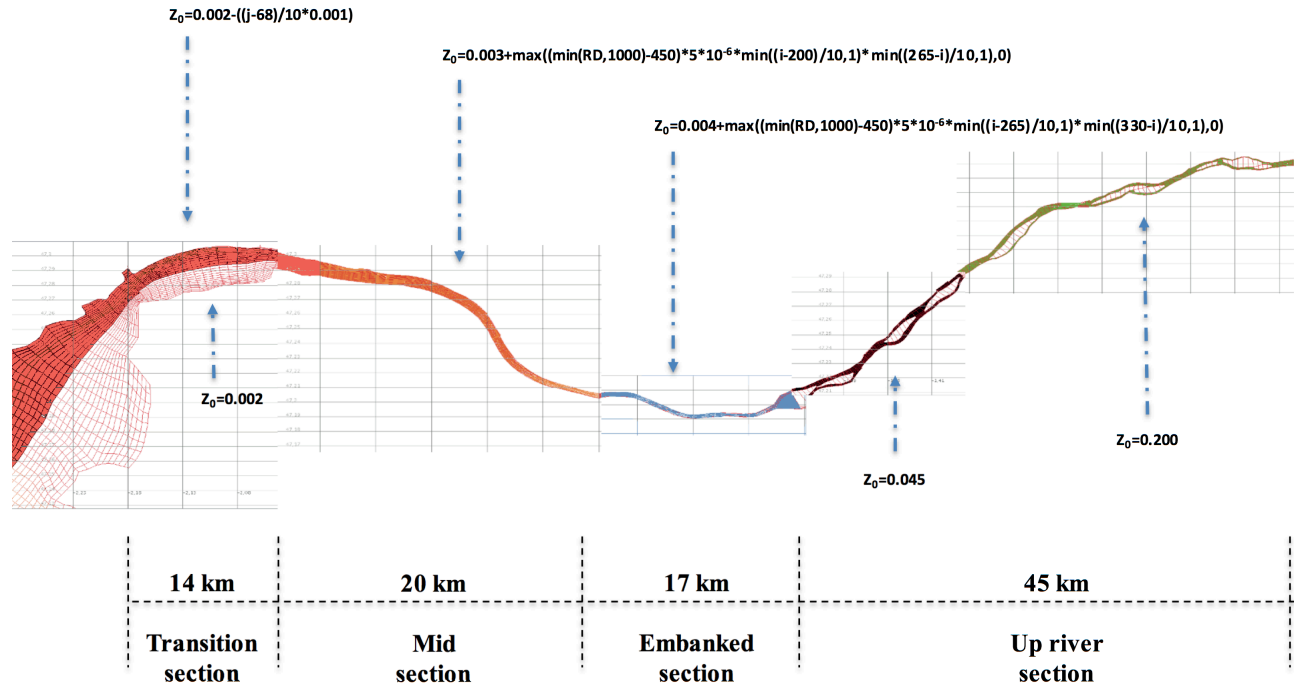


Figure 3.22: Distribution of the bottom roughness length in different reaches of the Loire estuary. 1) red: main channel in the estuary mouth 2) orange, blue: sectors where the roughness is dependent on Loire River Discharge (RD); 'i' (resp. 'j') represent a number of computing cell in the longitudinal (resp. transverse) direction, increasing eastward (resp. northward).

Vertical mixing

The occurrence of stratifications, the transport of passive tracers, the location of the up-stream limit of salinity, the location of turbidity maximum and more generally the characterization of hydrological structures are dependent on the turbulent closure and its parameterization. In our model, and following Tessier (Tessier, 2006), the Gaspar turbulent closure is chosen, and some adjustment of the Schmidt-Prandtl number has been proceeded to increase momentum mixing and avoid excessive current stratification when the water column is stratified ($Prt = N_z/K_z > 1$, instead of 1, in the basic formulation).

Time steps

Our model uses a variable time step, adjusted every 3 hours by checking that $\max(CFL) < 0.6$, where $\max(CFL)$ is the maximum value of the Courant Friedrich Lewy parameter (see Chap. 2) through the whole computational domain. However, a maximum time step of 25

seconds is respected, in order to avoid any convergence loss of the model.

3.4 Validation

3.4.1 Introduction

The statistic parameter most often used to quantify pattern similarity (phases) is the correlation coefficient. Considering two variables, f_n and r_n , which are defined at N discrete points (in time and/or space), the correlation coefficient R between f and r is defined as (Taylor, 2001):

$$Corr = \frac{\frac{1}{N} \sum_{n=1}^N (f_n - \bar{f})(r_n - \bar{r})}{SD_f SD_r} \quad (3.2)$$

where the letter f indicates the model field, r indicates the measured field, the over-bar indicates the average, and SD is the standard deviation. The correlation coefficient is limited in the range $-1.0 \leq R \leq 1.0$. In general, as the pattern (phase) between two time dependent signals approaches agreement, R approaches 1.0 which means that the two fields have the same centered pattern of variation. However, from the correlation coefficient alone it is difficult to determine whether two patterns have the same amplitude of variation. For this reason, another statistic parameter often used to quantify differences between two fields is the RMS, which for fields f and r is defined by:

$$RMS = \left[\frac{1}{N} \sum_{n=1}^N (f_n - r_n)^2 \right]^{1/2} \quad (3.3)$$

In order to isolate patterns differences from mean differences between two fields, one can compute the 'bias' which is defined as the difference between the means of the two fields:

$$\bar{E} = \bar{f} - \bar{r},$$

The distance between both series is proportional to the unbiased Root-Mean-Square-Error (RMSE) which is defined by:

$$RMSE = \left\{ \frac{1}{N} \sum_{n=1}^N [(f_n - \bar{f}) - (r_n - \bar{r})]^2 \right\}^{1/2} \quad (3.4)$$

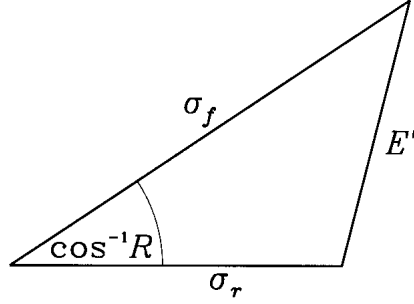


Figure 3.23: Geometric relationship between the correlation coefficient R , the unbiased pattern RMS error E' , and the standard deviations SD_f and SD_r of the model (test) and measured (reference) fields, respectively (Taylor, 2001).

The correlation coefficient and the RMS difference provide complementary statistical information quantifying the correspondence between two patterns, but for a more complete characterization of the fields the standard deviations of the fields must also be given (Taylor, 2001). According to Taylor (2001), all the four above statistics (Corr, RMSE, SD_f , and SD_r) are useful for patterns comparison, and it is possible to display all of them on a single, easily interpreted diagram.

$$RMSE^2 = SD_f^2 + SD_r^2 - 2 \times SD_f \times SD_r \times Corr, \tag{3.5}$$

3.4.2 Sea Surface Elevation

Several simulations have been performed to validate the tidal wave propagation, by changing the bed roughness in different regions. However a small change in bed roughness could influence the up-stream, therefore it was impossible to find a constant value for all the estuary. Finally, we chose the best case for the entire Loire Estuary based on the statistic parameter.



Figure 3.24: Tide gauges positions.

The spring tidal range at the entrance of the Loire Estuary exceeds 5m at Saint-Gildas and Saint-Nazaire; further upstream of Donges, it can reach 5.5m and even exceed 6.5m in Nantes during flood.

The comparison between predicted elevations and observed ones in the whole period of analysis (1 June to 22 Dec 2007) along the estuary from Saint-Gildas to Nantes (see Fig. 3.25) is presented in Table 3.2. In terms of statistics, for stations located at the entrance of the Loire River (Saint-Gildas, Saint-Nazaire, Donges), the amplitude is well reproduced, with errors in the range of 11 to 13 cm (Table 3.2) and a correlation of 99.6%. For the stations located upstream (Cordemais, Le-Pellerin and Nantes), discrepancies between model and data are larger, the error being included in the range 21-24 cm and 98% till 99%, for amplitudes and correlation respectively (Table 3.2). Getting more and more upstream, due to different factors, the accuracy of calculated tidal wave is reduced.

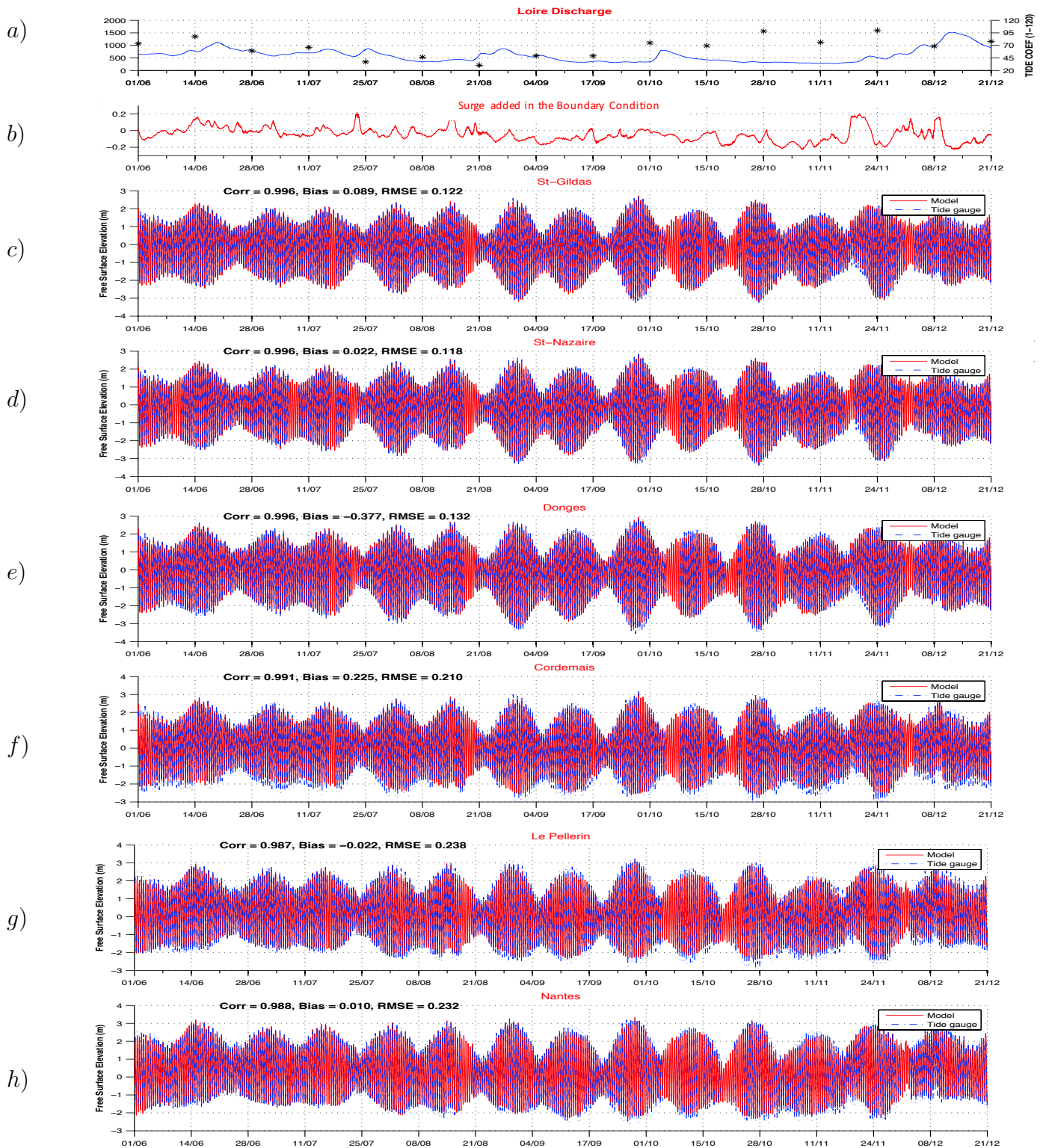


Figure 3.25: Superposition of measured (blue) and modeled (red) surface elevation from 1 June 2007 to 22 December 2007 for all tidal gauge stations; a) right side corresponds to the Loire discharge and left side to the tide coefficient, b) storm surge level; SSL at St-Gildas (c) , at St-Nazaire (d), at Donges (e), at Cordemais (f), at Le-Pellerin (g), at Nantes (h).

| Station | RMSE during severe Spring tide | Interval | RMSE during severe Neap tide | interval | RMSE during the whole periode |
|---------------|--------------------------------|---------------|------------------------------|---------------|-------------------------------|
| Saint-Gildas | 10.7 cm | 20/09 - 04/10 | 9.6 cm | 14/09 - 28/09 | 12.2 cm |
| Saint-Nazaire | 11.1 cm | 20/09 - 04/10 | 9.81 cm | 14/09 - 28/09 | 11.8 cm |
| Donges | 12.6 cm | 20/09 - 04/10 | 11.3 cm | 14/09 - 28/09 | 13.2 cm |
| Cordemais | 19.6 cm | 20/09 - 04/10 | 18.2 cm | 14/09 - 28/09 | 21 cm |
| Le Pellerin | 23.2 cm | 20/09 - 04/10 | 22.6 cm | 14/09 - 28/09 | 23.8 cm |
| Nantes | 25.3 cm | 20/09 - 04/10 | 25.9 cm | 05/12 - 19/12 | 23.2 cm |

Table 3.2: Statistical errors of surface elevation at different stations of tidal gauges.

We assumed that main factors affecting the accuracy of the simulated water level in the Loire Estuary are the Loire discharge, a possible variation of the bottom roughness, the quality of the boundary information (tidal components and storm surge) and wind forces (Fig. 3.26 & 3.27). For identifying the most important factor, we applied two kinds of analysis.

In the first one, for understanding the weight of the tide, we tested the performance of the model on two periods, one during a spring tide the other on neap tide. We choose two periods in which the Loire River discharges were relatively low (to avoid multiple factors of level variations), from 14/09 to 28/09 for a severe neap tide (see Fig. 3.28) and from 20/09 to 04/10 for a severe spring tide (see Fig. 3.29).

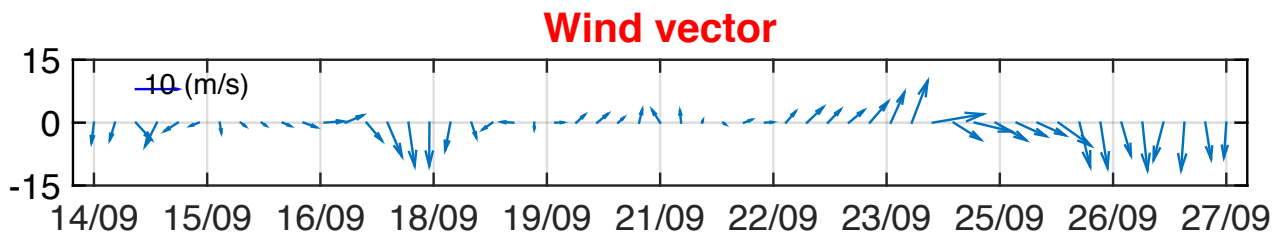


Figure 3.26: Wind forcing during neap tide from 14 Sep 2007 to 28 Sep 2007.

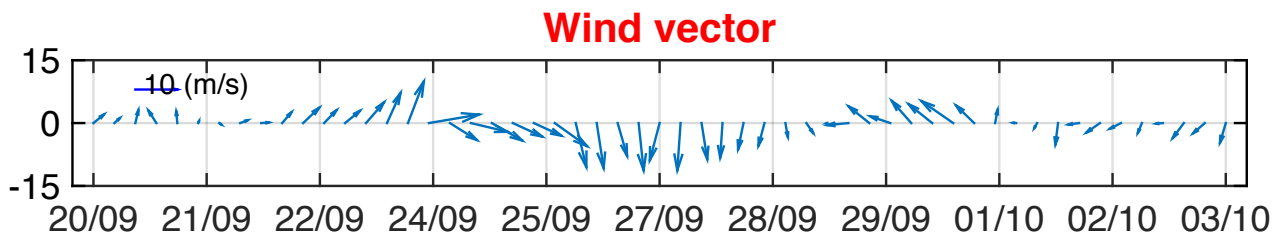


Figure 3.27: Wind forcing during spring tide from 20 Sep 2007 to 4 Oct 2007.

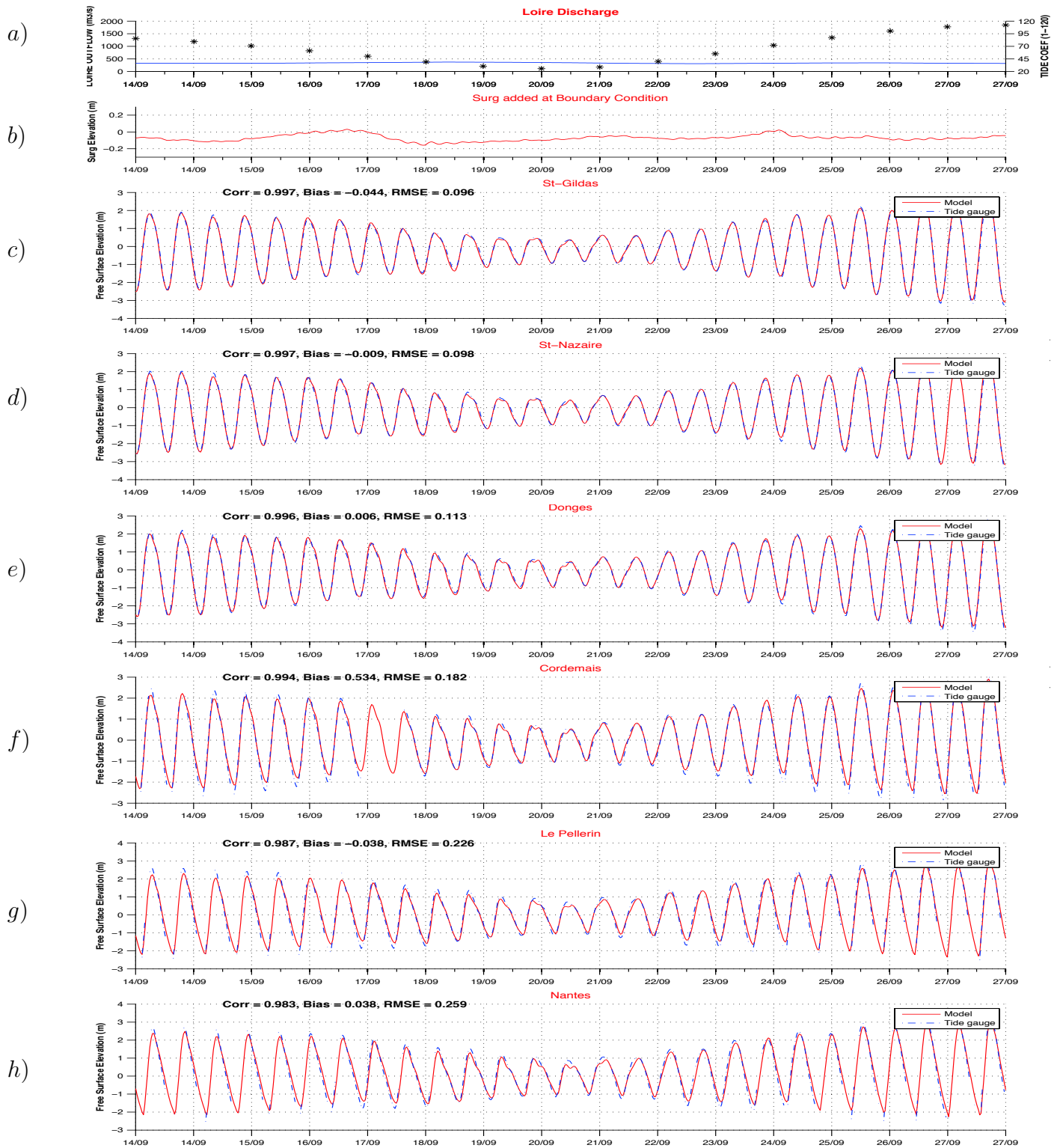


Figure 3.28: Superposition of measured (blue) and modeled (red) surface elevation from 14 Sep 2007 to 28 Sep 2007 (neap tide) for all tidal gauge stations; a) right side corresponds to the Loire discharge and left side to the tide coefficient, b) storm surge level; SSL at St-Gildas (c) , at St-Nazaire (d), at Donges (e), at Cordemais (f), at Le-Pellerin (g), at Nantes (h).

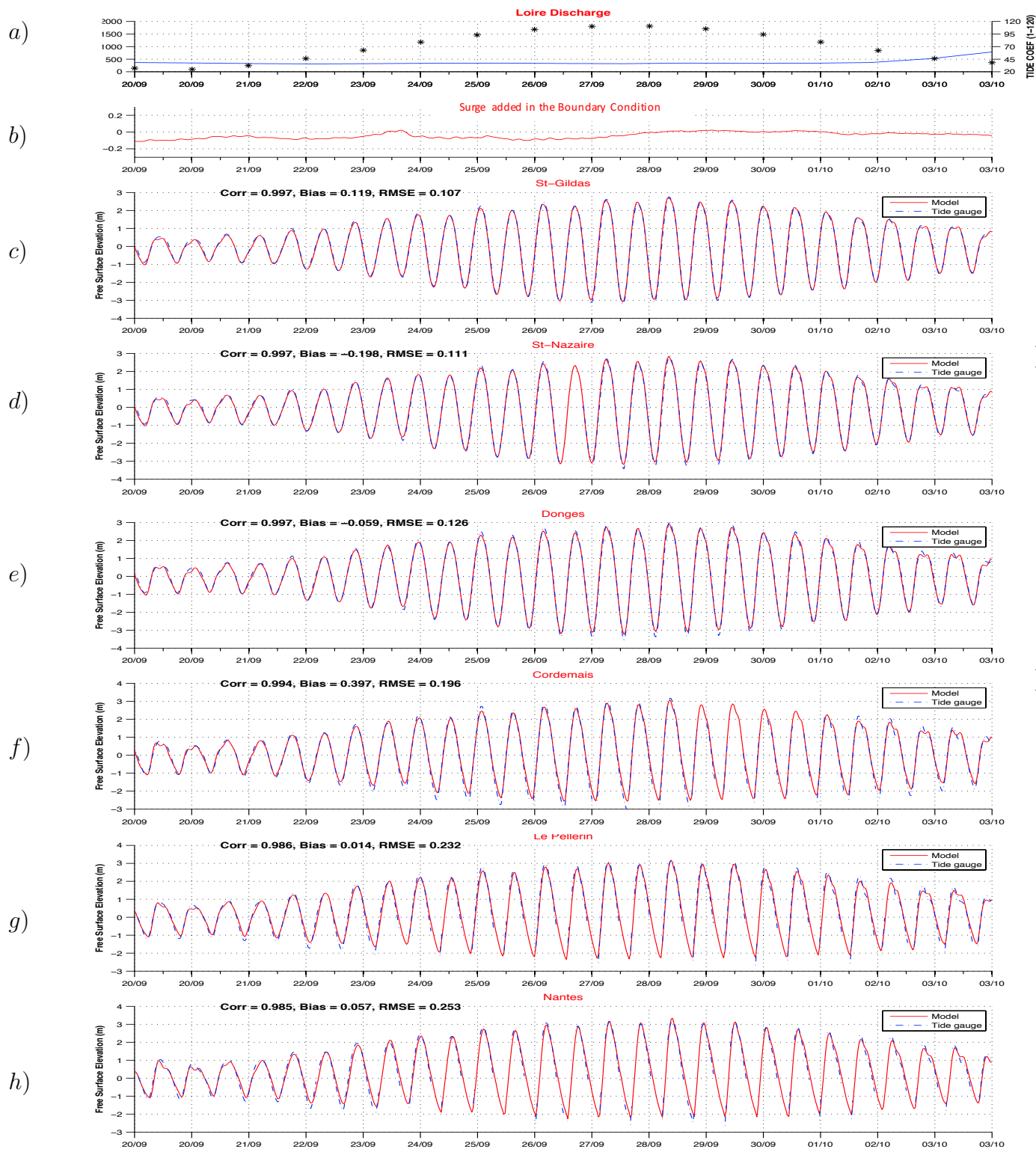


Figure 3.29: Superposition of measured (blue) and modeled (red) surface elevation from 20 Sep 2007 to 4 Oct 2007 (spring tide), for all tidal gauge stations; a) right side corresponds to the Loire discharge and left side to the tide coefficient, b) storm surge level; SSL at St-Gildas (c), at St-Nazaire (d), at Donges (e), at Cordemais (f), at Le-Pellerin (g), at Nantes (h).

The results for each period are presented in Table 3.2. Comparing the neap (Fig. 3.28, orange column in Table 3.2) and spring tides (Fig. 3.29, yellow column in Table 3.2) shows that the error is nearby the same on neap and spring tides. As we can see, the effect of tidal regime (RMSE difference between yellow and orange columns) is more important in the entrance of estuary.

The second tidal analysis, consists in computing RMSE on mobile 14 days window in order to know for which forcing the best and the worst RMSE occur (Table. 3.3).

| Station | Best RMSE | Interval | WORST RMSE | interval |
|---------------|-----------|---------------|------------|---------------|
| Saint-Gildas | 8.62 cm | 07/06 - 21/06 | 13.67 cm | 05/12 - 19/12 |
| Saint-Nazaire | 7.66 cm | 11/06 - 25/06 | 12.01 cm | 08/06 - 22/06 |
| Donges | 9.27 cm | 06/06 - 20/06 | 13.54 cm | 03/12 - 17/12 |
| Cordemais | 12.95 cm | 05/06 - 19/06 | 21.4 cm | 04/12 - 18/12 |
| Le Pellerin | 14.42 cm | 11/06 - 25/06 | 24.34 cm | 05/12 - 19/12 |
| Nantes | 16.27 cm | 05/06 - 19/06 | 26.38 cm | 05/12 - 19/12 |

Table 3.3: The best and the worst surface elevation RMSE computed in different stations.

It seems that the model performs significantly better when the Loire river flow is low than when it is large. In addition, Table 3.3 shows that the highest RMSE (the worst) for surface elevation occurs in the period from 3-19 Dec 2007, corresponding to a stormy weather and strongly variable wind forces (see Fig. 3.30). On the other hand, since 5 June till 25 (lowest RMSE), the order of magnitude of wind forcing is lower and in the large period of this interval the variation of wind direction is almost null (Fig. 3.31).

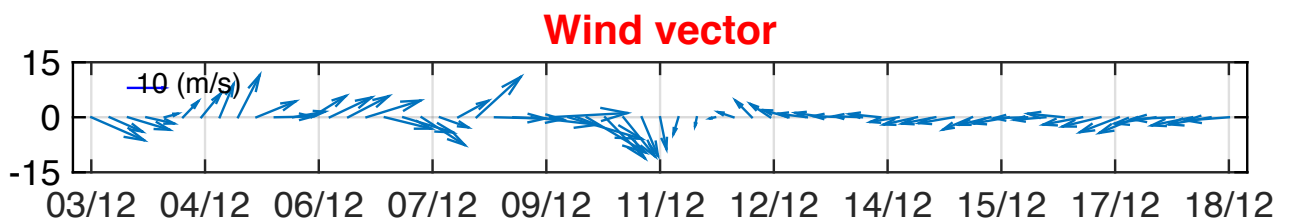


Figure 3.30: Wind forcing from 3 to 19 Dec 2007.

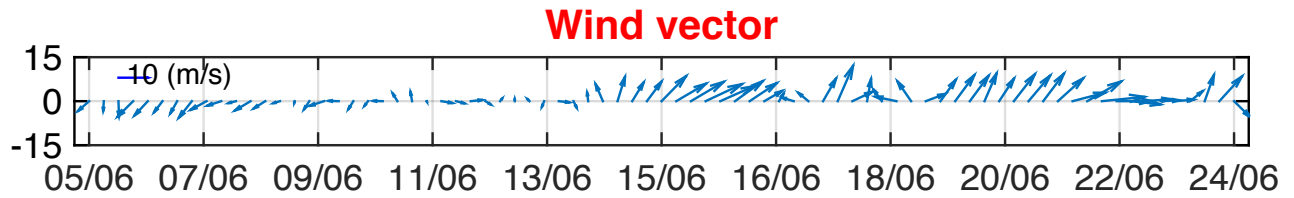


Figure 3.31: Wind forcing from 5 to 25 Jun 2007.

According to Tables 3.2 and 3.3, it is observed that the rate of error is greater upstream, probably the propagation distance from the open sea is longer, and because the relative section variations are higher. Water elevation also depends on the river discharge, the result of free surface level may depend on the ability of the model to properly evacuate freshwater, this evacuation resulting from a 3D circulation. Data from tide gauge was available upstream of Nantes, and a qualitative validation of our model could be achieved by a comparison with the results of the SOGREAH model (ARTELIA) (Walther et al., 2009).

Finally, it is concluded that the wind forces play an important role on the accuracy of the computed water elevation in this region and this effect can not be neglected. In general, the rate of RMSE has been 15% higher when the wind forces were neglected and 5% higher without considering the storm surge.

3.4.3 Salinity



Figure 3.32: Le-Pellerin, Paimboeuf and Le Croisic stations.

In this section, the accuracy of the resolution advection-diffusion equations used for a curvilinear non-orthogonal grid is analyzed. In-situ observation data (salinity and temperature) provided by GIP-Loire from various stations such as Paimboeuf and Le-Pellerin, as well as data from the ADCP situated at Le Croisic (Fig. 3.32), are used to validate the advection-diffusion equations used for tracer propagation. The salinity data, which are measured 1 meter below the surface level, have been compared to the model, from which the results at the same depth have been extracted.

3.4.3.1 Le-Pellerin

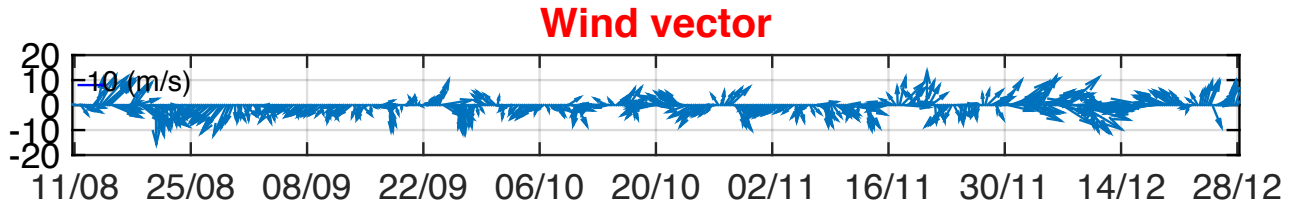


Figure 3.33: Wind forces from 11/08 to 28/12.

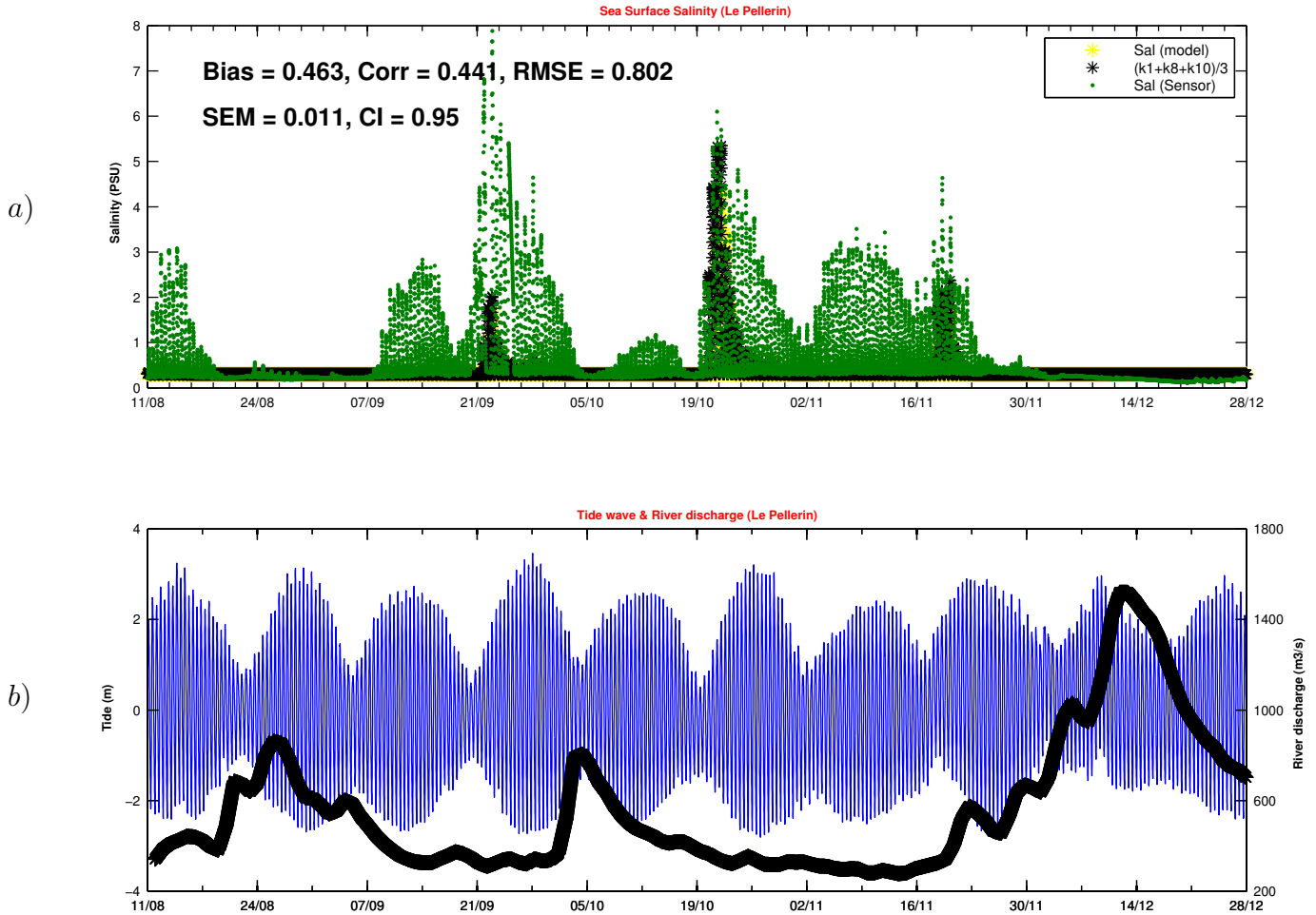


Figure 3.34: Comparison between computed and observed salinity at Le-Pellerin station; a) green points indicate the measured values, yellow ones the estimated value at the same depth and black ones present a mean value among 3 layers $(k_1+k_8+k_{10})/3$, k_1 indicates the first layer (at the bottom) and k_{10} , 10_{th} layer (at the surface) b) Water level (blue) at Le-Pellerin station and Loire River discharge (black).

As shown in Fig. 3.32, Le-Pellerin is close to the upstream boundary of the salt-water intrusion. According to Fig. 3.34 'a', the comparison between observations and computations shows an underestimation of simulated salinities on low flow, which means that the model hardly reproduces the upstream salt-water intrusion, but the gap is not so important because some salinity peaks are simulated and the salinity range remains very low (during 20-29/10 and 14-18/11).

The remarkable drop in salinity at Le-Pellerin during the periods 20/08-08/09 and 15/11-28/12 is due to the increase in Loire River discharge. Based on real data, the salinity of "fresh" water input upstream has been fixed at 0.2 PSU.

3.4.3.2 Paimboeuf

Figure 3.35 compares the in-situ observed salinity and the one estimated by the model at Paimboeuf station, situated in the medium reach of the Loire Estuary (Fig. 3.32). Measured and simulated salinities strongly vary with the tidal phase, both within the semi-diurnal cycle and along the neap-spring tidal cycle. The model well reproduces changes along these cycles, and seems more accurate on spring tides than on neap tides. The reason is probably related to the structure of salinity stratification.

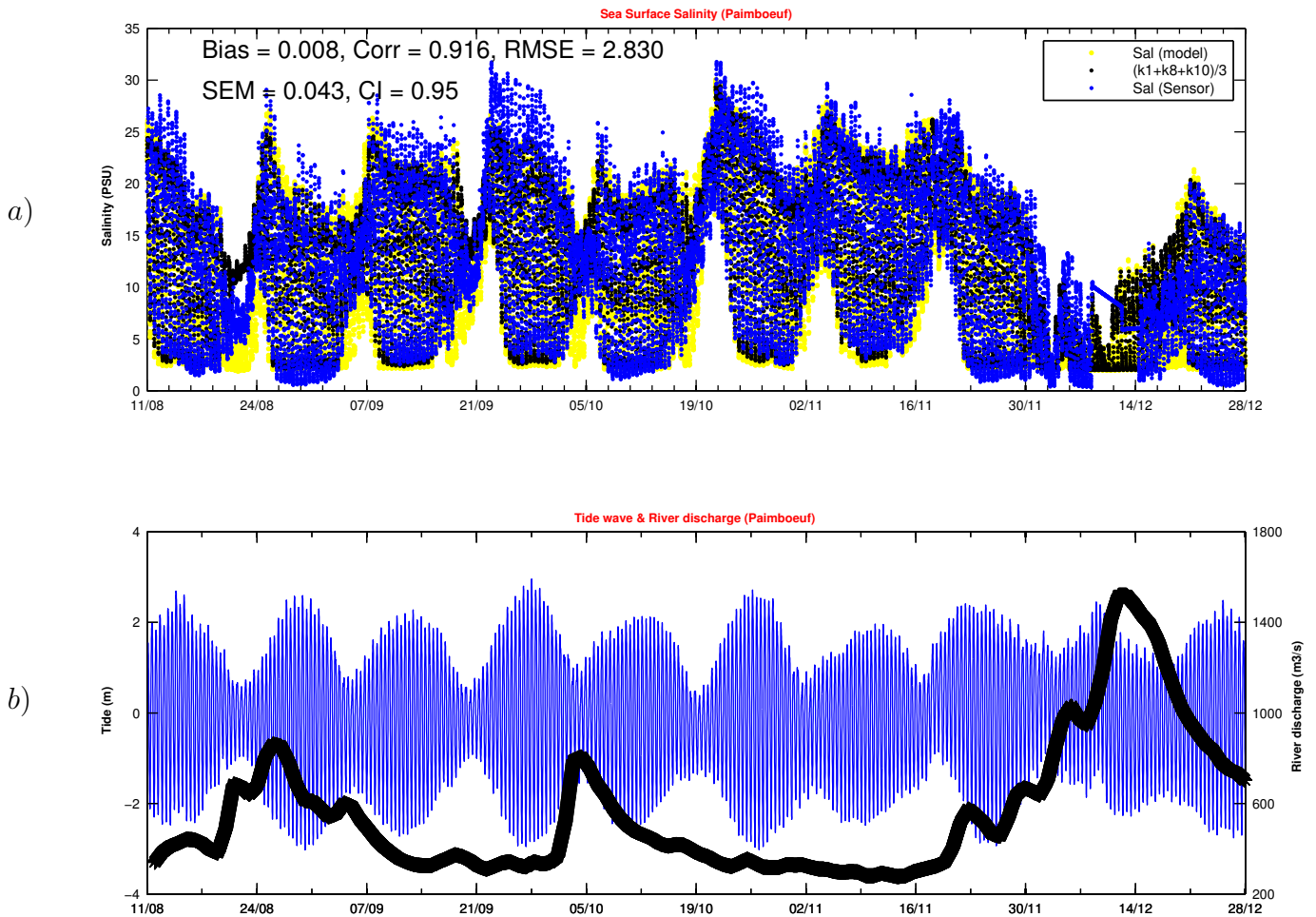


Figure 3.35: Comparison of salinity measurements and simulations by MARS-3D at Paimboeuf station, a) blue points indicate the measured values, yellow ones the estimated value at the same depth and black ones present a mean value among 3 layers $(k_1+k_8+k_{10})/3$, k_1 indicates the first layer (at the bottom) and k_{10} , 10th layer (at the surface); b) Water level (blue) at Paimboeuf station and Loire River discharge (black).

There is no remarkable difference between salinity in the surface layer (yellow point), and the

vertically averaged one (black point). This can be due to the water homogeneity in this region during the spring tides. The main reasons behind the homogeneous characteristic of the water are a high magnitude of tidal force (~ 5 m) and probably coincided with sudden changes in the amplitude and direction of wind force at this time of the year. According to Fig. 3.35, the model is able to display the penetration of the seawater into the mouth and upstream of the river, fairly well. However, considering the amplitude, the results of this part have been slightly underestimated.

The Fig. 3.35 b, shows that a strong increase of river discharge induces a net decay of salinity (*e.g* around mid-December). This feature is well reproduced by the model.

3.4.3.3 Le Croisic

Surface salinity has been recorded with a CTD probe at the same location as a bottom ADCP, south of Le Croisic (lon = -3.06 W , lat = 47.51 N). Measurements and results from the MARS-3D model are plotted on Fig. 3.37: during the period of 27/11 till 16/12 a sudden decrease of salinity occurs near the ADCP station, which is mainly due to rapid changes in the wind direction (Fig. 3.36) and leads to a sudden change of direction of the river plume. This induces a strong salinity variation within a day around the 11th December. As it is indicated in the Fig. 3.37, the model reproduced these sudden changes in a matter of a few hours in a fairly good manner. Although the location of the ADCP is relatively far away from the entrance of the Loire Estuary, the model has been capable to reproduce the phase as well as the order of magnitude of this sudden change in the salinity of water mass. Statistics of the model performance in salinity gradient have been computed. As shown in Fig. 3.37, the correlation between in-situ and computed salinities is significant: considering the confidence interval of 95%, the correlation coefficient is equal to 93% and the bias is really low (0.007). The RMSE (root mean square error) is 0.92 PSU: considering the sudden change of around 12 PSU, the amount of error is acceptable.

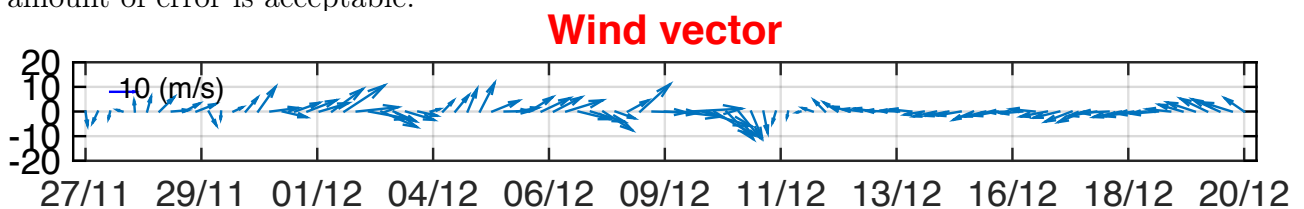


Figure 3.36: Wind forces from 27/11 to 20/12.

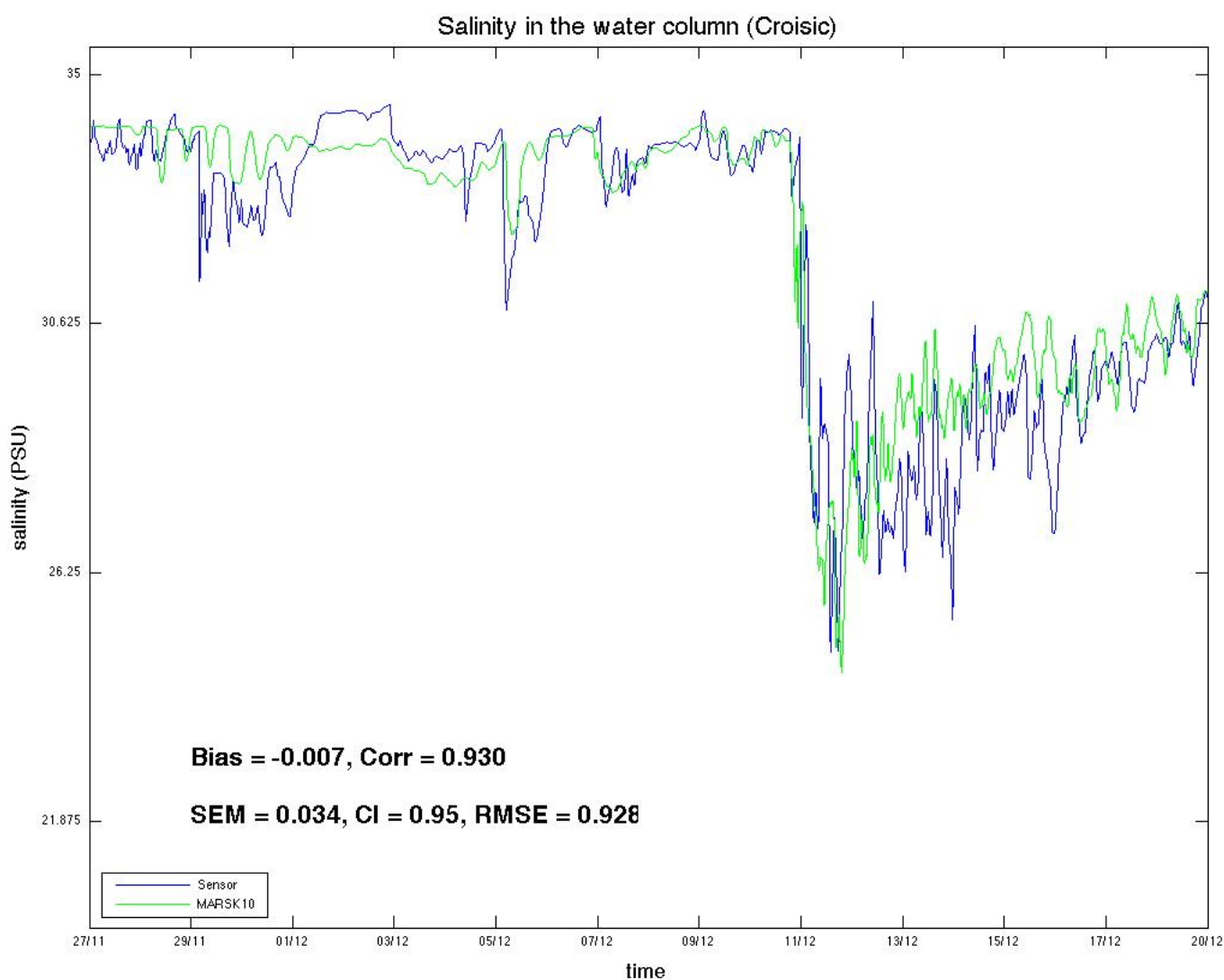


Figure 3.37: Blue represents the amount of salinity measured by ADCP 1m below free water surface; green shows the model's estimated salinity (between layer 10 and 9) which interpolated at the same depth.

3.4.4 Temperature

The accuracy of the simulation of advection-diffusion processes has also been evaluated through temperatures, by comparing MARS-3D results to measurements at three stations (Le Croisic, Cordemais, Le-Pellerin). For the simulations, temperature measured at Belle-Vue, upstream Nantes, have been assigned to the fresh water input as upstream boundary condition.

3.4.4.1 Le-Pellerin

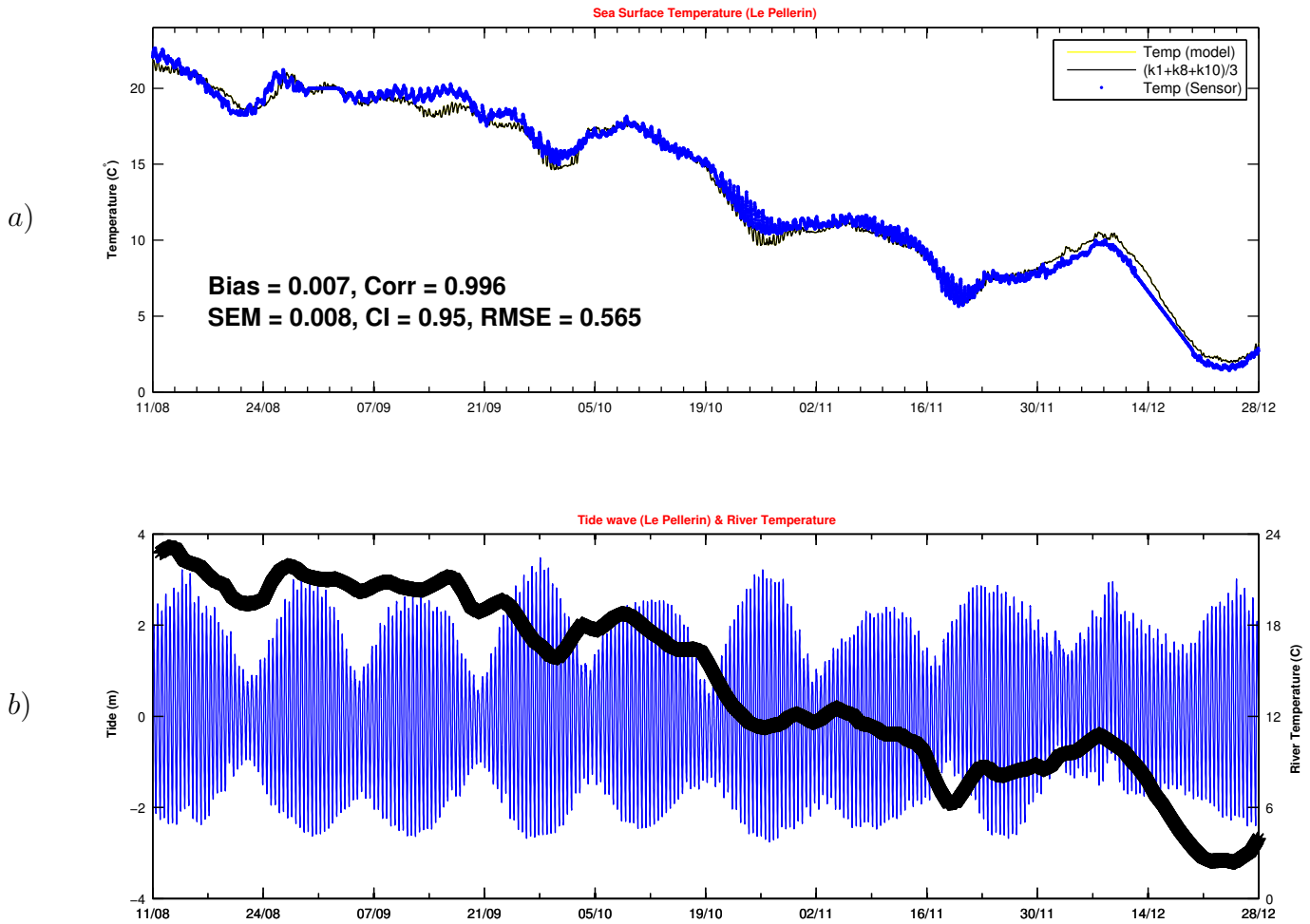


Figure 3.38: Observed and predicted temperature at Le-Pellerin station 1m below the water surface, model (yellow), black (measurement) (a), and b) Water level (blue) at Le-Pellerin station and the Loire River temperature (black).

Upstream in the Loire Estuary, the changes in the river's temperature are more affected the river temperature, and experience a slight shift. However, the order of magnitude is still very close to reality.

As indicated in Fig. 3.38 the model simulates the temperature variation in the Loire Estuary with a high level of accuracy. The correlation coefficient is 99.6% and $RMSE = 0.6 \text{ }^{\circ}\text{C}$. At Le-Pellerin too, temperature variations are mainly controlled by temperature variation of the river in upstream (given in Fig. 3.38b).

Reasons for having the more accurate temperature compared to the salinity may be a less contrast between the river and coastal ocean temperatures and perhaps an additional control by heat exchanges at the surface.

3.4.4.2 Paimboeuf

Figure 3.39 a, compares the computed temperature from the model and the measurement near the surface at Paimboeuf station.

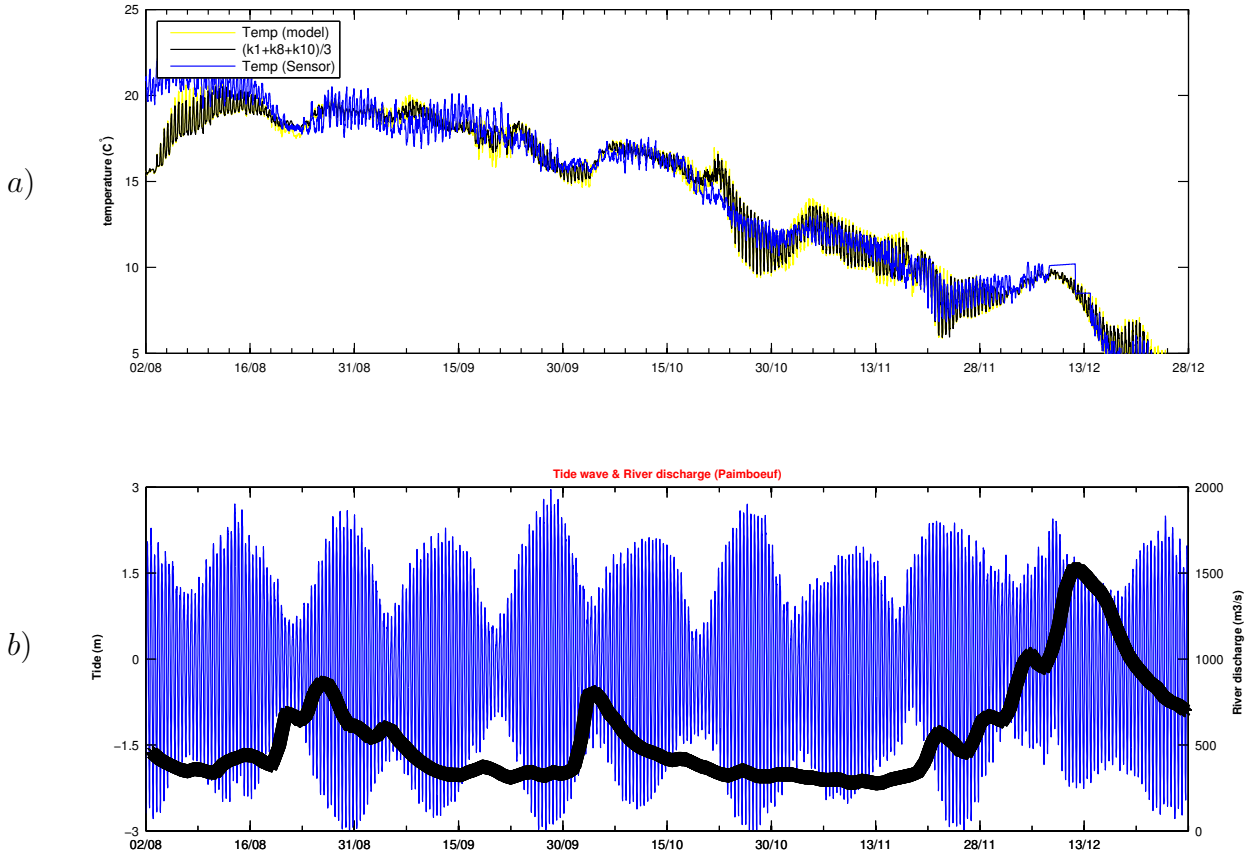


Figure 3.39: Observed and predicted temperature at Paimboeuf station 1m below the water surface, model (yellow), blue (measurement) (a), and b) Water level (blue) at Paimboeuf station and Loire River discharge (black).

However, the superposition of the both graphs admits the accuracy of the model in reproducing the temperature variation near the mouth of the Loire Estuary. Statistics of the model performance produce a correlation coefficient of 98% and a RMSE of 0.7 °C, which is relatively good for modeling in this coastal region and estuary.

Temperature changes are directly related to the river discharge and temperature as well as to the tidal range. The change in surface water temperature is mainly related to the upstream water temperature and discharge, the sudden decrease occurs during the increase of river discharge.

3.4.4.3 Le Croisic

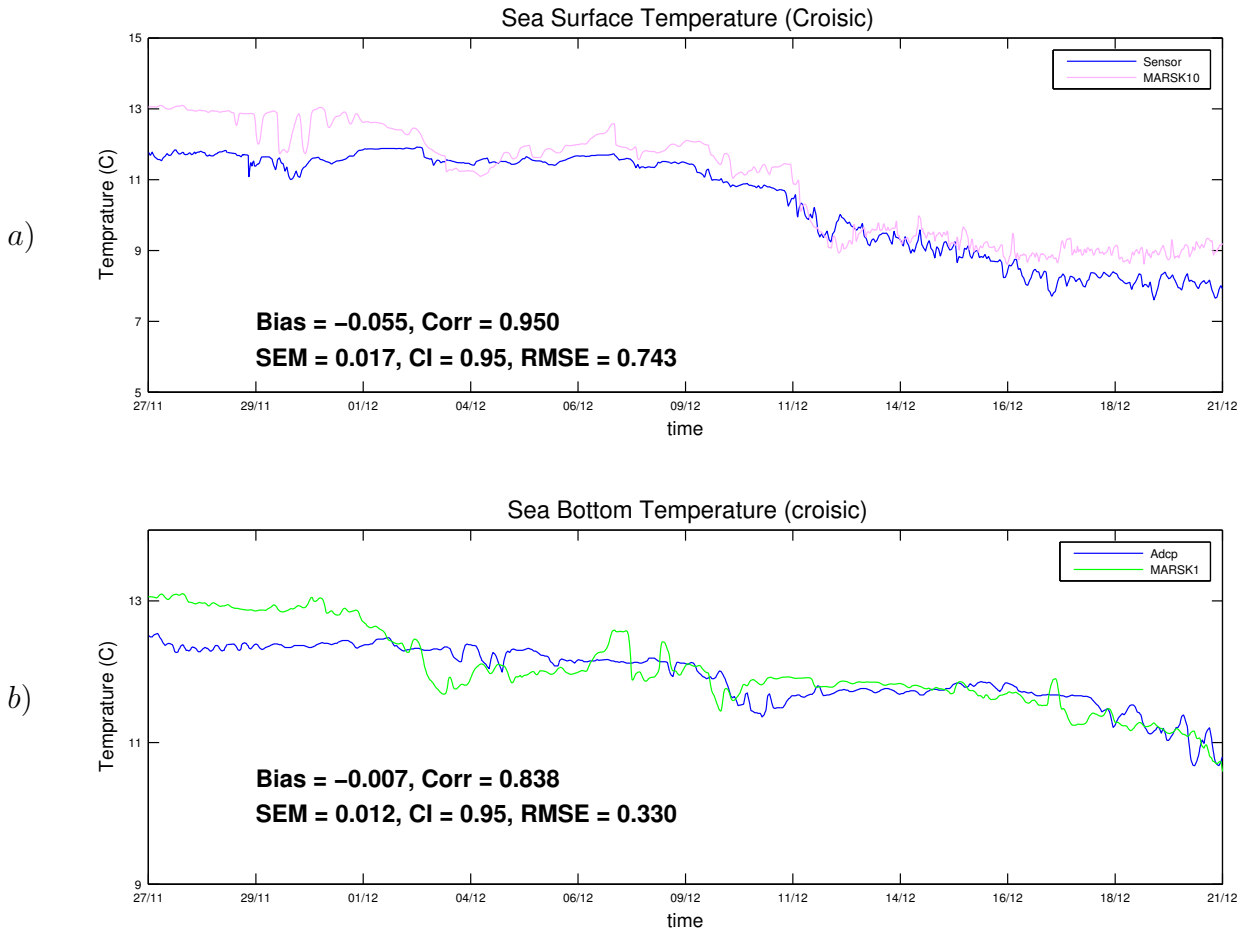


Figure 3.40: Observed and predicted temperature at Le Croisic station 1m below the water surface (a), and b) 1.45m above the bottom.

From 27/11 to 21/12, measured and simulated temperatures are compared in the surface layer (1m below the water surface) and in the bottom layer (Fig. 3.40). This is a very interesting interval in which we have a variation of 4 °C close to the surface and 2 °C near the bottom in a short period (about one month). The model has been able to simulate the changes caused by the variations in the river plume direction, river discharge and even the effects of up-welling in an acceptable manner. It appears that at the beginning of the represented period, observations show a slightly stratification while the model does not. As we can see in Fig. 3.40a, the model is more accurate near the surface in terms of phase and better to reproduce the order of magnitude the variation near the sea bed.

An important point is that temperature of the Le Croisic station at the surface varies with a delay of about two days corresponding to the variation of Loire River temperature measured at Belle-Vue station next to Nantes (see in Fig. 3.39b & Fig. 3.40a, especially on 14 Dec).

3.4.4.4 Satellite images (SST)

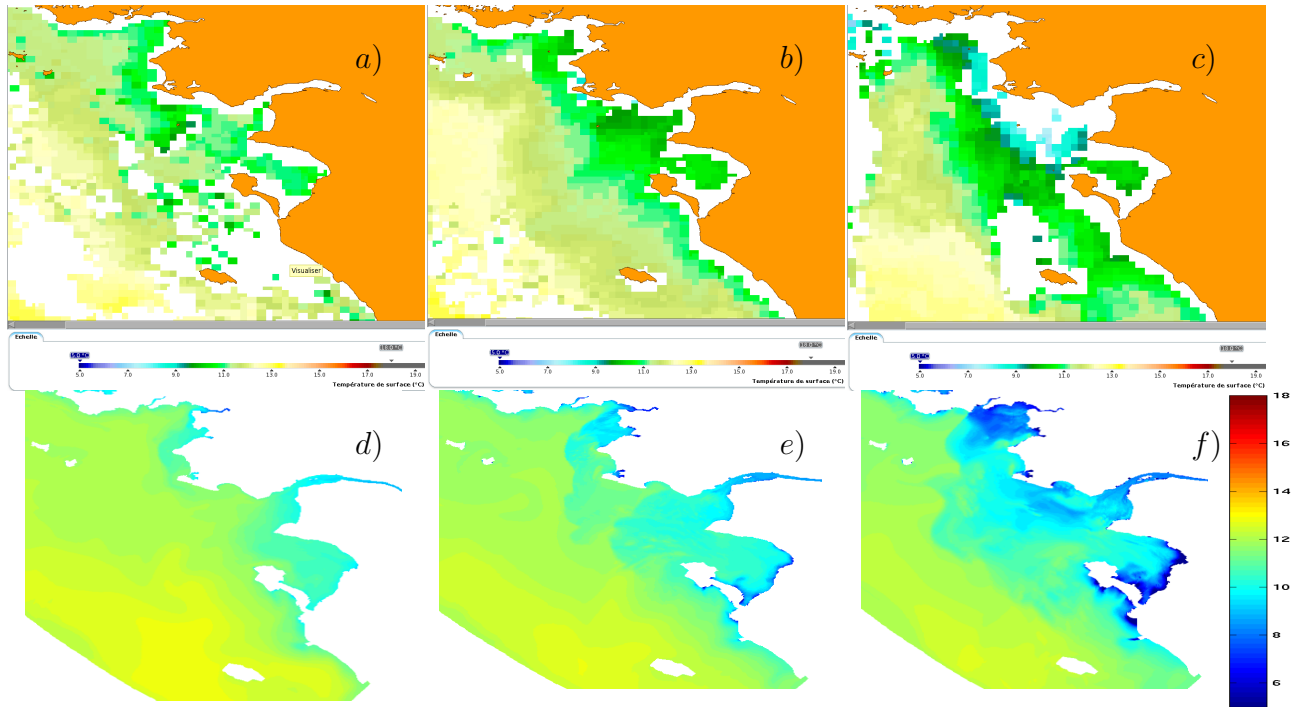


Figure 3.41: Comparison between a Sea Surface Temperature (SST) satellite (NOAA) image and surface results of the MARS-3D model on 10-12/12/2007 2h; a) satellite Image 10/12 b) satellite Image 11/12 c) satellite Image 12/12 d) MARS-3D 10/12 e) MARS-3D 11/12 f) MARS-3D 12/12 .

According to the Fig. 3.41, it appears that the MARS-3D model is capable to reproduce the Sea Surface Temperature contrast, even in the particular evenement like on 10-12 Dec 2007 in which the wind directions have changed dramatically (see Fig. 3.30). At the entrance of the Loire Estuary, the SST difference is less than $0.5\text{ }^{\circ}\text{C}$, and this difference reaches its maximum ($0.7\text{ }^{\circ}\text{C}$) close to the open boundary.

3.4.5 Velocity

3.4.6 Flow patterns of the Estuary

As mentioned earlier, using a curvilinear mesh allows to refine the desired velocity field (Fig. 3.42) in the area of interest. It also helps increasing the accuracy of the calculated values and reducing the grid orientation effects, as numerical diffusion (Maliska and Raithby, 1983, Maliska and Raimundo, 1981). For sampling the curvilinear equations all vectorial variables (as flow patterns) are calculated on the contra-variant based components. A comparison between computed and measured currents in the water column during 5 weeks at a fixed station near Le Croisic where an ADCP had been moored is represented on Fig. 3.43 & 3.45. This figure and other comparisons (not shown here) reveal a rather satisfactory simulation of flow patterns

was done.

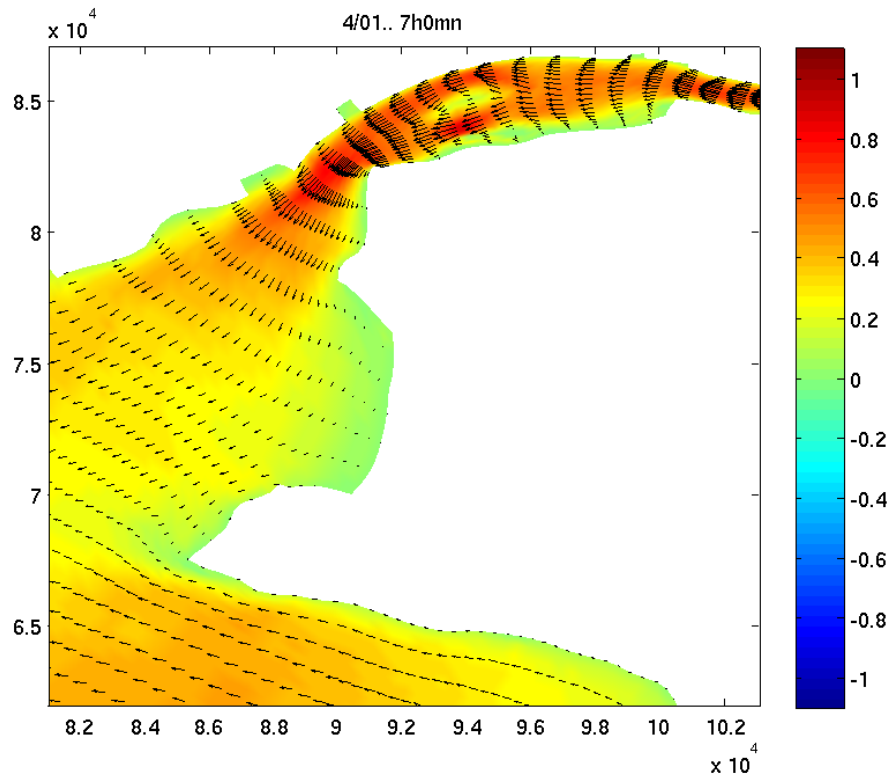


Figure 3.42: Flow pattern at the mouth of the Loire Estuary.

As stated earlier, the accuracy of 3D model should be checked on several factors such as the tide magnitude (spring or neap), storm surge and local wind.

From 03/Dec until 10/Dec Fig. 3.43b indicates a remarkable change in current velocity at different layers of water. As shown in the graph, the model was capable to reproduce this current velocity satisfactorily. Comparing Fig. 3.43c & d, an underestimation of the magnitude of the velocity is observed in lower layers, especially on spring tide (*e.g* from 24/Nov until 28/Nov). On the other hand, a small overestimation of the flow velocity is observed episodically, for instance between 1th and 4th Dec or from 15/Dec to 18/Dec.

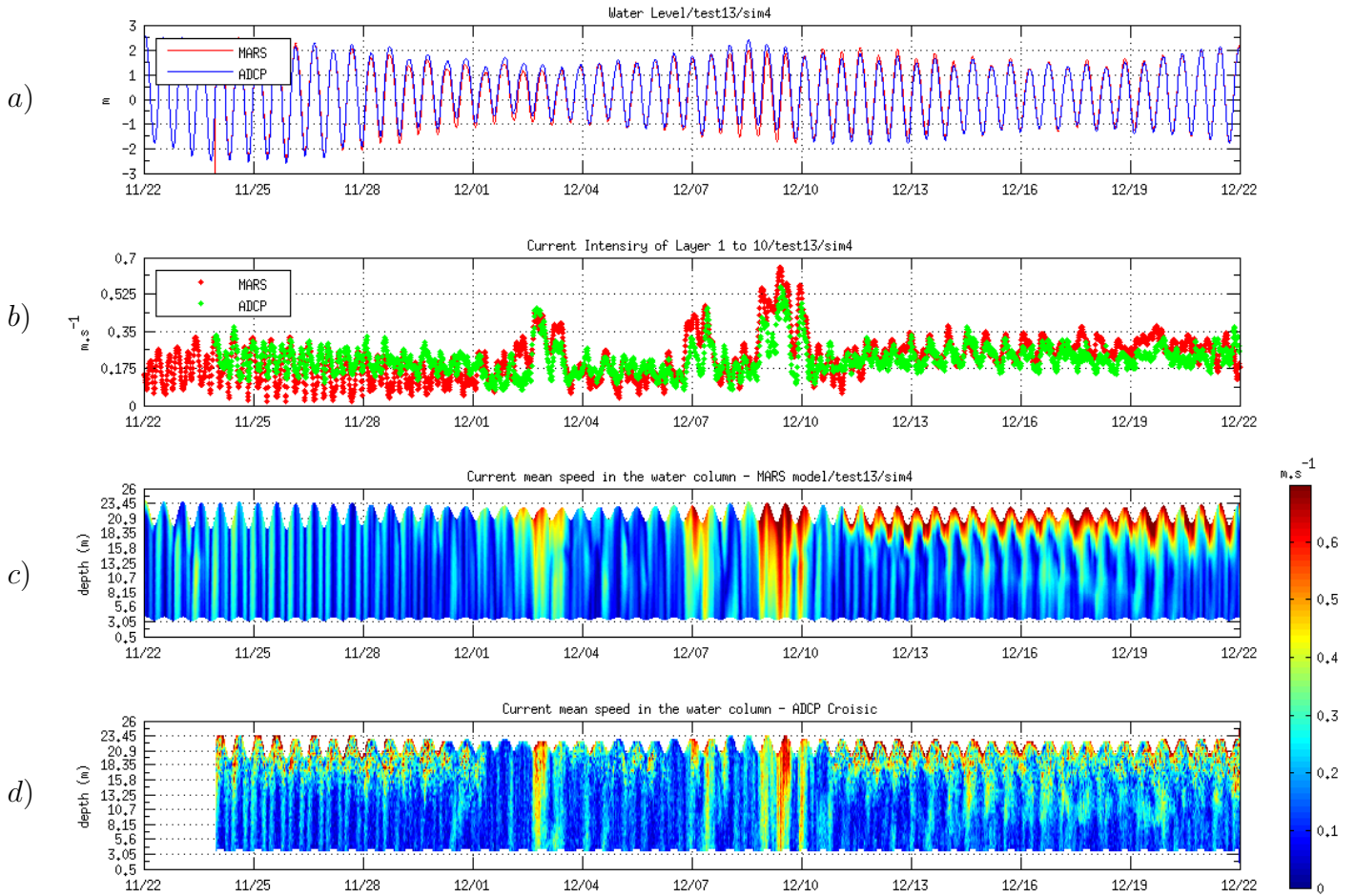


Figure 3.43: Comparison between measured and simulated current magnitude at Le Croisic station; a) observed and predicted water level variations; b) observed and predicted depth-averaged velocity (average of 10 σ layers for computation, average of 0.50 m layers for the ADCP measurements); c) predicted current intensity; d) observed (ADCP) velocity intensity.

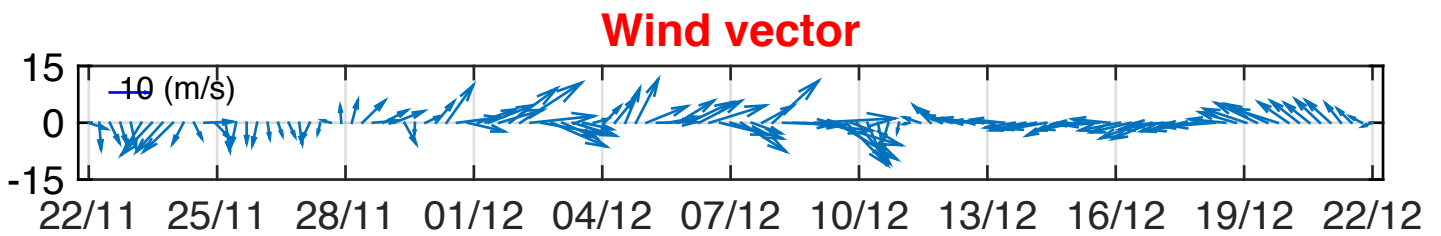


Figure 3.44: Wind vectors from 22 Nov to 22 Dec 2007.

Generally speaking, Fig. 3.43 reveals very strong variations of the flow intensity which are not related to the tide, but are actually induced by wind variations (Fig. 3.44). The agreement between observations and model results is remarkable, in terms of averaged values as well as vertical structure. In particular, between December 12 and 22, a strong vertical gradient in surface layers can be seen in both measurements and computations. Fig. 3.45b compares observed and measured current directions averaged in the water column. The comparison is

between an average of 10 layers used in the model and a variable number of 0.5m layers given by the ADCP.

During the first period until the 1st of December, the agreement between model and observations is not so good, the model producing a rotating flow, which concerns the whole column, while depth-averaged measurements show an oscillation between -60° and $+45^\circ$ and some stratification. But in December, the agreement is again remarkable, all changes of direction, both in time and according to the vertical, are very well simulated, despite their strong intensities.

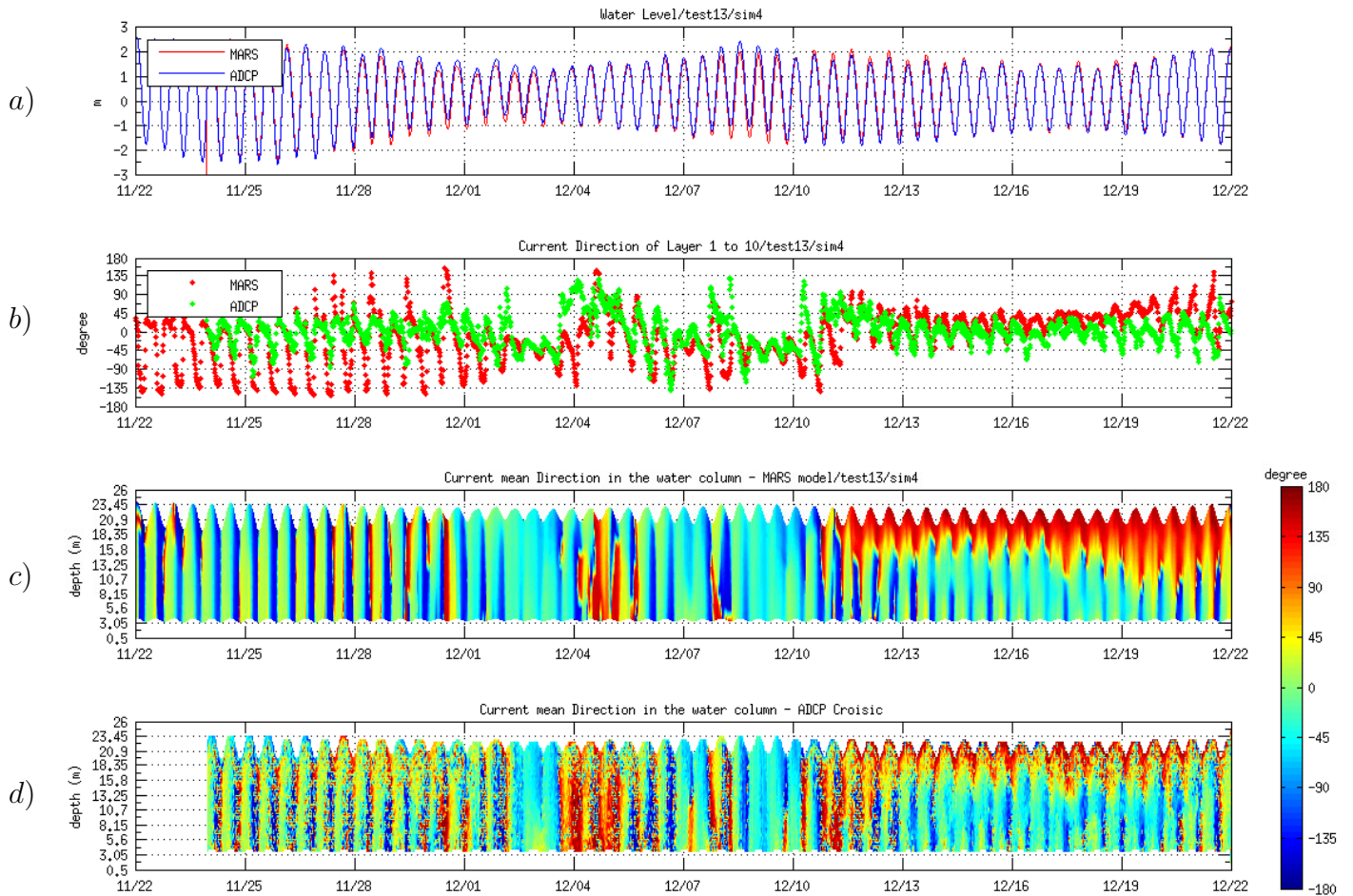


Figure 3.45: Comparison between measured and simulated current direction at Le Croisic station (all data come from the ADCP situated at Le Croisic); a) observed and predicted water level variations, b) observed and predicted depth-averaged velocity direction (average of 10 layers for simulated currents), c) predicted velocity direction, d) observed (ADCP) velocity direction.

According to the Fig. 3.45, it seems that the model shows vertical changes under the surface deeper than measurements from the ADCP. This could be due to the fact that the model uses less layers than the ADCP. Therefore, the results could probably be improved by adding vertical layers or rearranging the resolution close to the surface (using generalized sigma coordinates). By this way, the effect of wind on the surface layer could be modeled more accurately.

In terms of statistics, calculated RMSE for the direction of currents at different vertical levels is less than 20% for 80% of the considered time period. The flow intensity is simulated with a standard error no more than 8% in more than 90% of time.

Fig. 3.46 presents imaginary trajectories of particles that would have the same velocity as the ones measured by the ADCP or produced by the model at the location of the ADCP, at any time from 08/Dec to 12/Dec (4 days). The exercise is conducted for the surface and bottom layers at Le Croisic. Such an analysis provides a general view of the accuracy and productivity of the curvilinear MARS-3D model. The selected period is the one when a remarkable velocity change in the water column was observed. As mentioned earlier, the change was both in the magnitude and direction of the current velocity (see Fig. 3.43 & Fig. 3.45). Fig. 3.46 indicates a great similarity between observations and measurements, as well as an inversion of residual velocities, for both surface and near bottom particles. The difference of surface and bottom residual displacement is interesting; waters flow in the SSE direction at the surface and in the E direction near the bottom. After the wind-induced reversal, the surface and bottom directions seem in agreement.

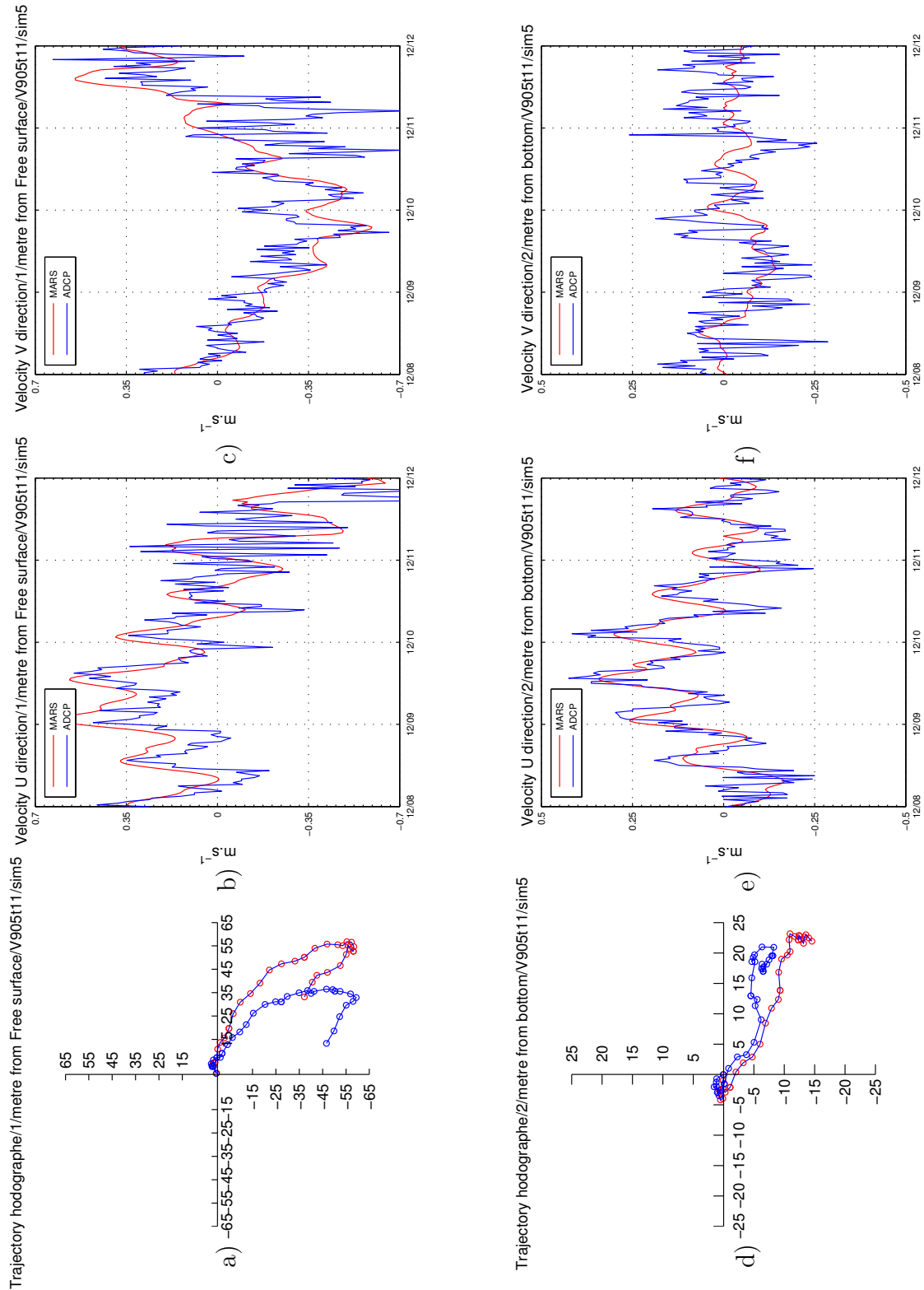


Figure 3.46: Imaginary particle trajectories a) observed and predicted particle trajectory near the surface between 8/12 till 12/12/2007 (axis captions: in km) b) observed and predicted U component near surface, c) observed and predicted V component near surface, d) observed and predicted particle trajectory near bottom e) observed and predicted U component near bottom, f) observed and predicted V component near bottom.

The Fig. 3.46 is complemented by the comparison between observed and simulated velocity components during the same period. Tidal fluctuations appear more clearly on the west-east components (Fig 3.46b & e), while the comparison is a bit less good for south-north components (Fig 3.46c & f). At the end of the fourth day the distance between imaginary particles the one related to measured velocity in blue and the one related to the simulated velocity in red, is less than 7 km.

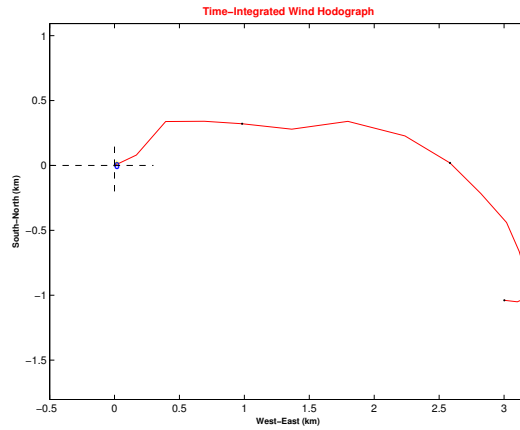


Figure 3.47: Time-integrated wind hodograph from 8 to 12 December 2007.

In addition, trajectories do not present tidal variations, which means that wind-induced velocities are much more significant than tidal induced velocities. The wind reversal during the same period is represented by the wind hodograph on Fig. 3.47.

This comparison of model results with observations at Le Croisic shows that the MARS-3D model is able to satisfactorily reproduce the current velocity, its vertical structure and both the tidal current and the effects of wind, so that the model can be considered as validated.

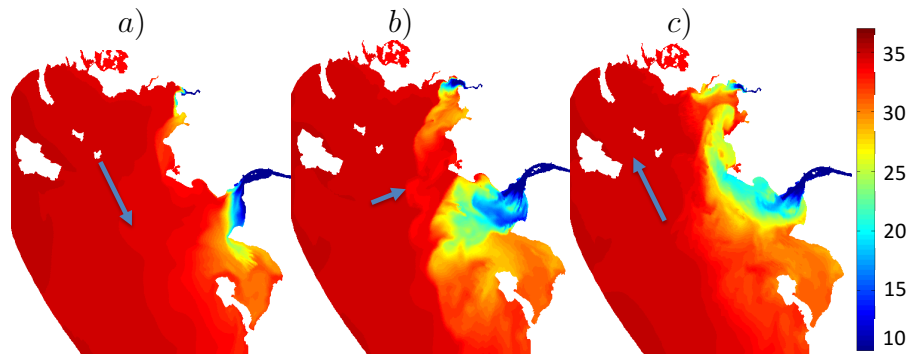


Figure 3.48: Change the direction of the plume of the Loire, between 10 and 12 December; a) 10 Dec 10h, b) 11 Dec 10h, c) 12 Dec 10h.

As previously talked about the time interval between 10 to 12 December, Fig. 3.48 illustrates the tipping of the Loire River plume propagation induced by wind, which leads to a sudden change in salinity (12 PSU) near the Le-Croisic station (see Fig. 3.37).

Chapter 4

General circulation and Water flow patterns

Introduction

This chapter presents a general scheme of water circulation in the Loire Estuary and its adjacent waters. Since forcing combination is changing very quickly, steady states are never reached, especially considering the wind and meteorological forcing. For this reason, the descriptions of circulation schemes are based on a realistic sequence lasting 7 months (01/06 until 31/12/2007).

In the first section this sequence is analyzed. In particular the representativeness of the period is considered, in terms of river regime and wind forcing. The second section presents the instantaneous and residual tidal currents. The third section illustrates the density circulation induced by main rivers and its likely impact on the particle exchanges. The fourth part represents the influence of wind over the circulation frame and the river plumes. The last and more detailed section of this chapter discusses the variability of water and fresh-water fluxes through different cross sections in the study area, using multiple simulated configurations. In order to understand the role of specific forcing, alternative simulations have been run, simplifying some other forcing. Thus, to obtain the results provided in this chapter, around 80 simulations were performed. A quarter of these simulations were performed with realistic forcing, while the others have been run schematically.

A brief presentation of the time series of forcing is given below. In the case of schematic simulations, to have a better realization of each factor, the specific factor has been omitted and the result is compared with the one obtained with the whole realistic forcing.

The forcing considered for these realistic simulations are tide, storm surge, rivers flow, wind, salinity and temperature along the open boundary. It should be noted that even when conside-

ring "realistic simulations", some forcing has been neglected or simplified: for instance, wave forcing is ignored, and meteorological forcing is considered uniform over the study area.

4.1 Overview of the forcing time series from June to December 2007

The period chosen for the realistic simulation is based on the availability of measurements for model validation. The aim of this section is to describe the different forcing and show how representative they are.

Time series of tide, storm surge, river discharges, wind, salinity and temperature at the sea boundary from June to December 2007 are presented in Fig. 4.1. This figure is reproduced on a movable transparent insert in order to allow its superposition with the time evolution of model results and thus to facilitate results analysis.

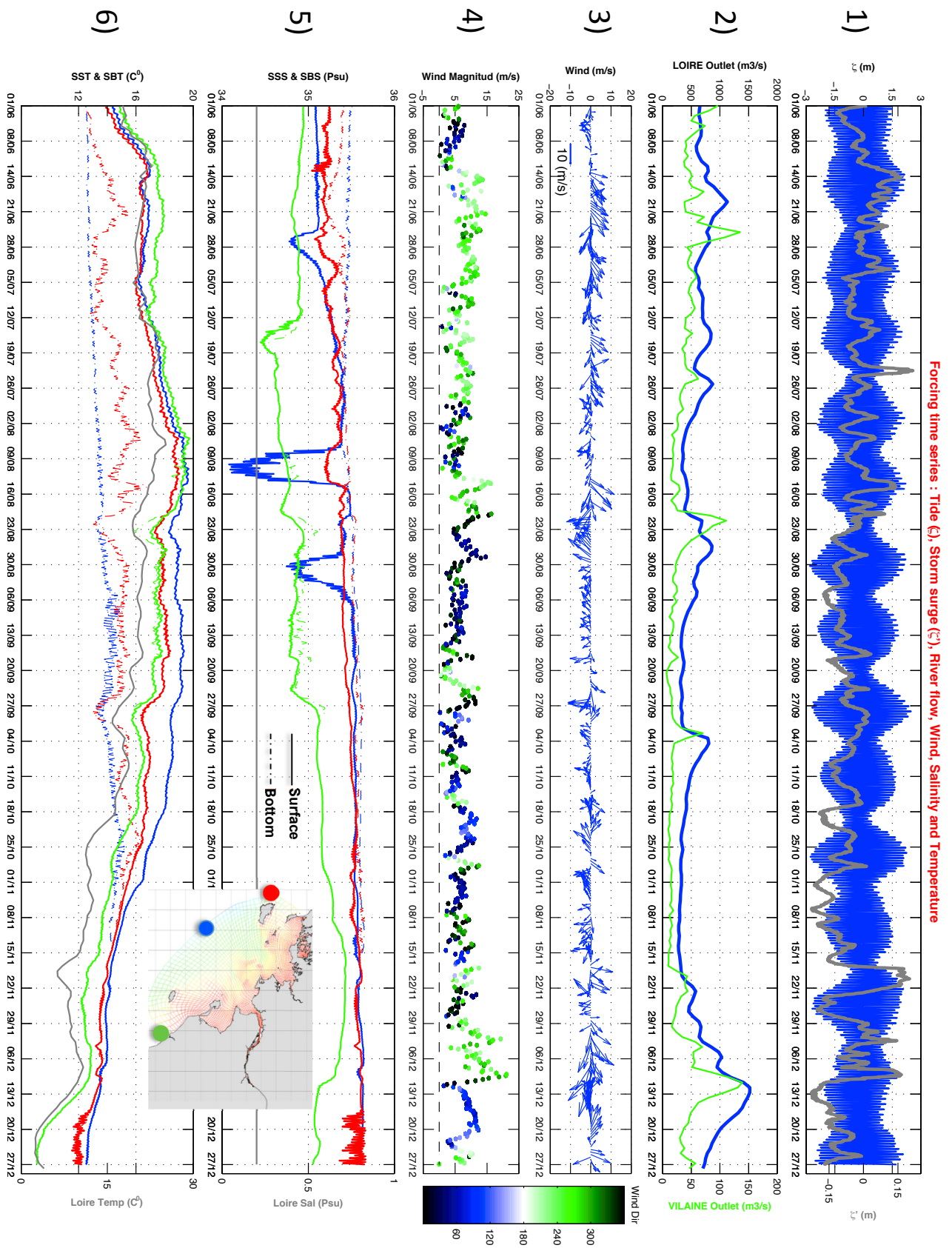


Figure 4.1: Forcing time series includes: 1) tide (blue) and surge (gray), 2) rivers discharges (Loire in blue, Vilaine in green), 3 and 4) wind (magnitude and direction), 5) salinity at the sea boundary and 6) surface and bottom temperatures.

4.1.1 Tidal and Surge waves

The upper graph (graph 1) of Fig. 4.1 shows a superposition of tidal and storm surge waves during the selected period. The blue color curve on this graph represents the tidal wave. Data for this curve are from a larger model represented as "Rank1" in Fig. 4.2 and are located on the open boundary of our model at the latitude of Saint-Nazaire. During the whole period (01/06-28/12) the tidal amplitude ranges from 1 m (severe neap tide on 20/09) up to 5.5 m (perigean spring tide on 27/10). Between 15 Nov and 12 Dec the tide elevation is strongly modified while the storm surge reaches two maxima. This period will be discussed later in this chapter.

The grey curve represents the storm surge on the open boundary at the same latitude as Saint-Nazaire. This curve is computed as the water level deviation from two depth-averaged simulations of the "Rank1" model (Fig. 4.2), considering or not the wind and atmospheric pressure. This storm surge has been uniformly added to the tide level at the open boundary (considering that its deformation is negligible along the open boundary).



Figure 4.2: Configurations Mars2D model for current and storm surge levels (Ifremer, 2010a).

The variation of the surge wave as simulated in our local model in different places of the estuary is shown in Fig. 4.3. According to this figure, there are some points to be considered. The first is that the effect of storm surge can be felt until Ancenis, although its magnitude is very attenuated. The second, comparing graph "a" and "b", we found that while the wind

blows from S-SW to NW (green points) the amplitude of surge storm is amplified in the Loire Estuary until Nantes. On the other hand, during winds from NE to SE the magnitude of the surge wave is not modified in a tangible way. Most of the time in the selected period, the surge waves are intensified upstream in the Loire Estuary until Nantes; even when the surge at the sea boundary is mainly negative for instance from 2 to 10 of December, the surge experiments a positive shift in the estuary, except for eastern winds.

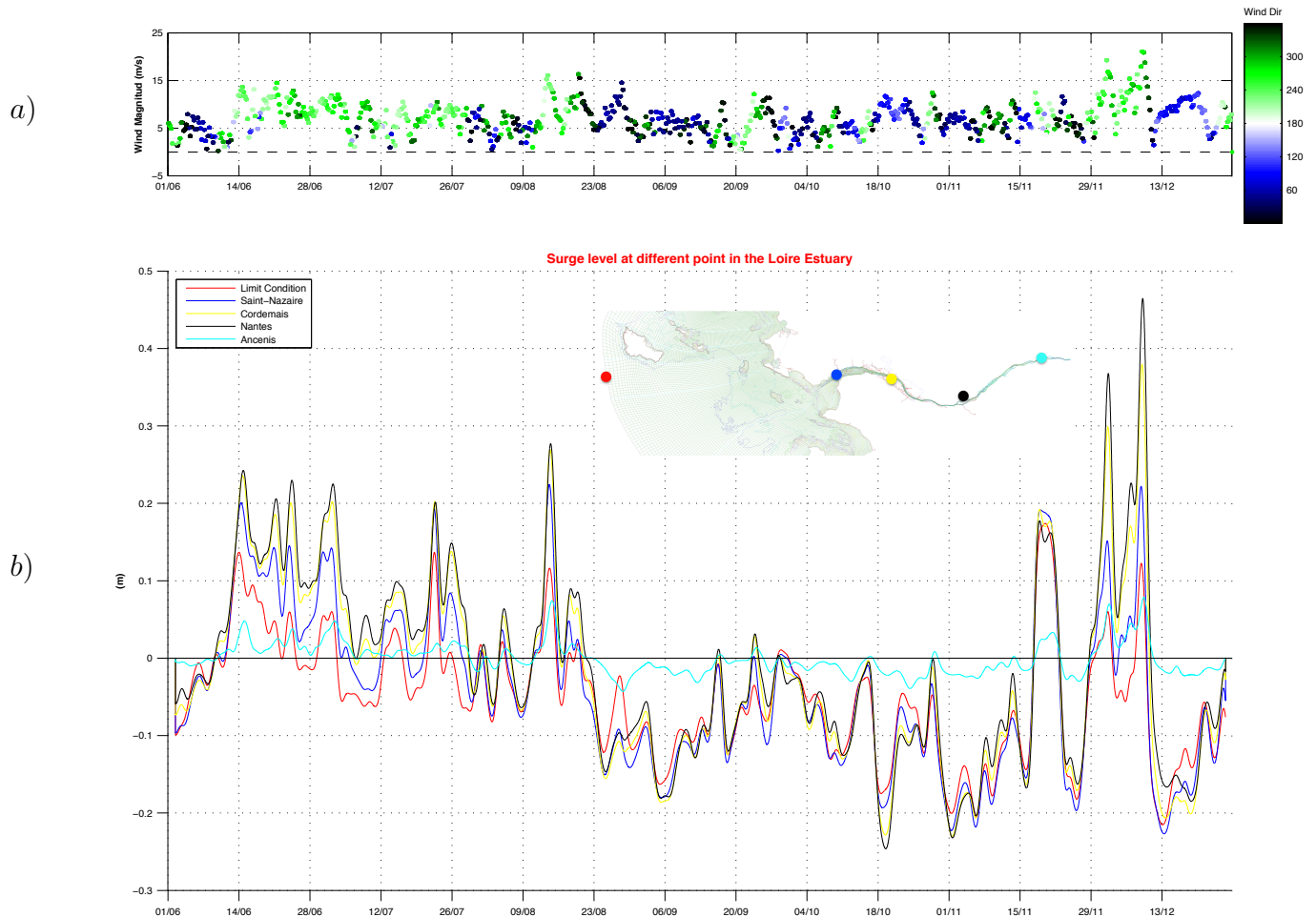


Figure 4.3: Computed storm surges level in the study area; a) wind forcing, b) surge wave at the Open Boundary (forcing in red) and computed at different locations in the Loire Estuary, represented by 4 other colors.

blue: Saint-Nazaire; yellow: Cordemais;
black: Nantes; cyan: Ancenis.

4.1.2 River discharge

The Loire and Vilaine discharges during the selected realistic period are shown in Fig. 4.1 graph 2. At the beginning of these time series (01/06 to 28/12), the Loire outflow varies from 500 to 1100 m³/s, around the Loire average annual discharge (\simeq 900 m³/s). Low discharge

(300-400 m³/s) is observed from August till November. However, two exceptional events are observed, one from August 22th to 31th with a magnitude of 800 m³/s, and the other from October 4th to 9th with a magnitude of 750 m³/s. From mid-December during few days a small flood is experienced in the order of 1500 m³/s. The Vilaine flow rate is very low compared to the Loire River and experiences a variation in the order of 30 to 50 m³/s most of the time. A substantial change can be noticed from mid-November in which the Vilaine discharge reaches 140 m³/s, for a short period of time. It appears that maximum values for both river discharges occur in a similar time frame, with a phase-lag depending on precipitation occurrences in the respective watersheds. High rates of Vilaine River flow generally occur before the Loire peaks, which can be coherent with the smaller watershed of the Vilaine River. The occurrence of the opposite case is unlikely but an example can be seen on 25th June (see in Fig. 4.1), probably due to non simultaneous rains in the respective regions.

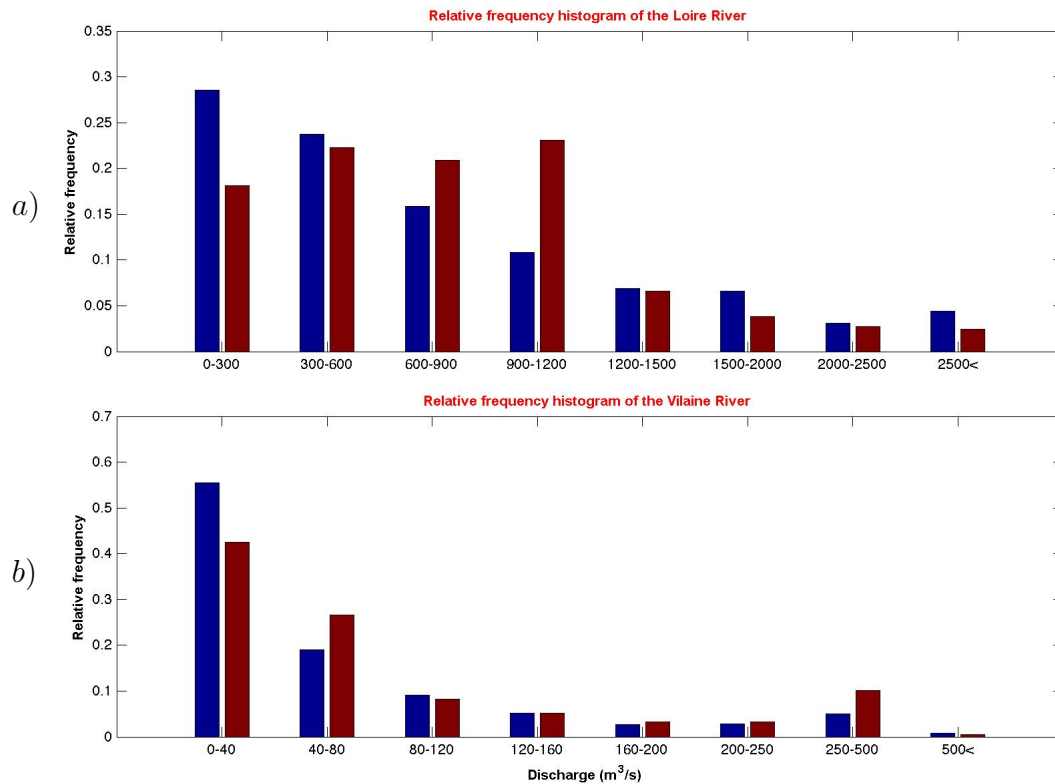


Figure 4.4: Relative frequency histogram of the Loire and Vilaine River discharges:
a) Loire River discharge from 1984 to 2009 (blue) and for selected period in 2007 (red);
b) Vilaine River discharge from 2003 to 2013 (blue) and for selected period in 2007 (red);

The relative frequency histogram of the Loire and Vilaine flow rates is shown in Fig. 4.4, to demonstrate the representativeness of the selected time interval for our study. Indeed, the histograms of the Loire and Vilaine discharges during the selected period in 2007 are very similar to the one computed for long periods (25 years for the Loire, 10 years for the Vilaine).

For each river, three representative values have been computed, mean and representative low and high flows. Mean flow is based on the annual mean flow over several hydrological years (from 1984 to 2009 for Loire and from 2003 to 2013 for Vilaine). The mean flows are 900 and 70 m^3/s , respectively for the Loire and Vilaine rivers. Low discharge representative for low river flow has been computed as mean value of 90 lower discharge daily records during these same years (25 years for the Loire River and 10 years for the Vilaine River).

These representative low discharges are 300 and 30 m^3/s , respectively for the Loire and Vilaine Rivers. Similarly, the representative high flow is computed as the average of 90 upper daily flows; they range 2000 and 180 m^3/s .

These representative values are shown by blue horizontal lines for each river (see Fig. 4.5) together with the simulation period, in gray rectangles.

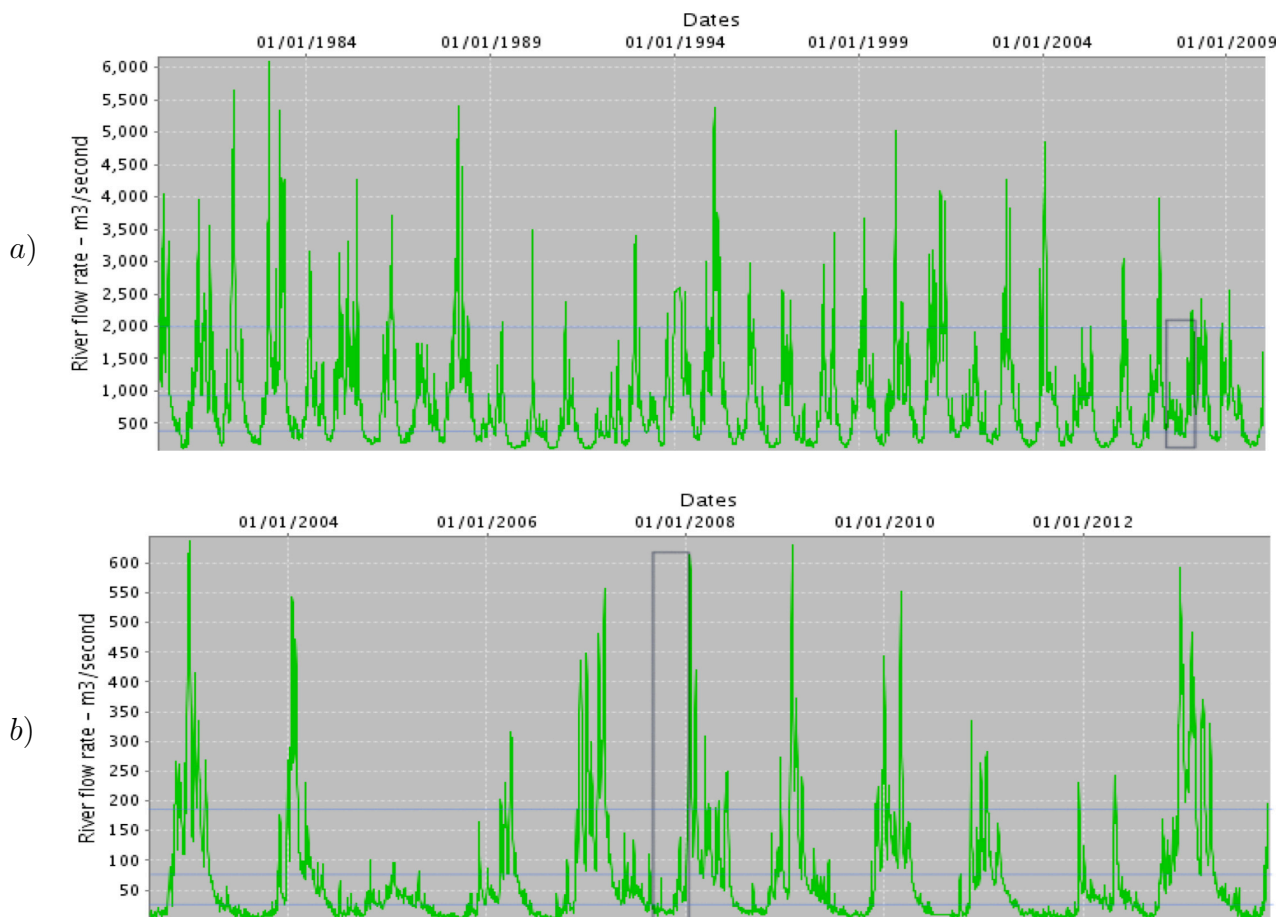


Figure 4.5: Chronology of the Loire and Vilaine River discharges:
a) Chronology of the Loire River discharge from 1980 to 2009;
b) Chronology of the Vilaine River discharge from 2003 to 2013;

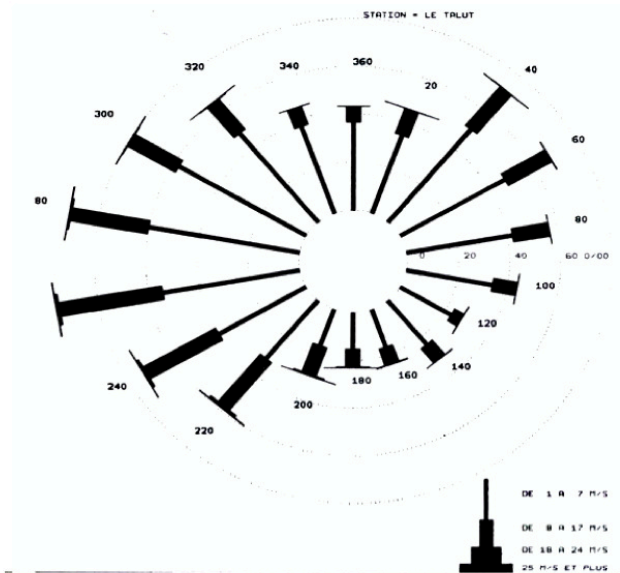
4.1.3 Wind Forces

According to Lazure & Jegou (1998), the wind forces are regarded as the main sources of energy for mixing the water column in the temporarily stratified shallow waters. Furthermore, as explained in Sec. 1.1.2.1, related to the Bay of Biscay, the seasonal wind cycle is characterized by two regimes, one in autumn and winter when the wind mainly blows from the SW and one in spring and summer with winds from the NW sector (Pingree and Le Cann, 1990). Since the NW wind is upwelling-favorable, it tends to push the low-salinity surface waters southwards and towards the open sea. Therefore, it is crucial to choose appropriate time interval in order not to miss the main effect of winds on the circulation in our study area which is part of Biscay Bay.

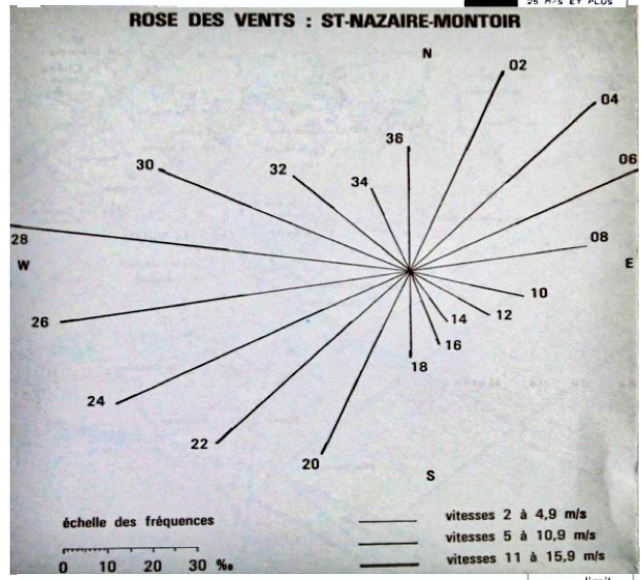
4.1.3.1 Wind roses

The analysis of past two decades wind data collected and recorded by Meteo-France at Belle-Ile station (Fig. 4.6 a), indicates a high wind variability in amplitude and direction. Ascensio et al. (1987), exhibited the annual frequency of winds direction and intensity averaged over the period 1951-1980 at Chassiron station located on Oleron Island, south of our study area, that can be synthesized as: 26.6% from NE quadrant, 16.3% from SE quadrant, 20.3% from SW quadrant, 33.3% from NW quadrant and 3.7% calm. Averaging wind over a year shows that 74% of the energy provided by the wind originated from West (NW + SW) and 55% originated from North (NW + NE) (Auby et al., 1994). Fig. 4.6 shows wind roses at two different stations (Belle-Ile & Saint-Nazaire); they are very similar with dominant winds from N-W and S-W, and also from N-E. In addition, according to Lazure et al. (2008), the similarity between Chassiron and Belle-Ile has been observed, so that the assumption of uniform wind over the whole study area is reasonable. Fig. 4.6 represents the wind rose corresponding to the whole selected period for our simulation; data come from a meteorological simulation, run by MétéoFrance. Actually the wind rose looks like the one deduced from 30 years' observation, meaning that our selected period has a good representativity.

a)



b)



c)

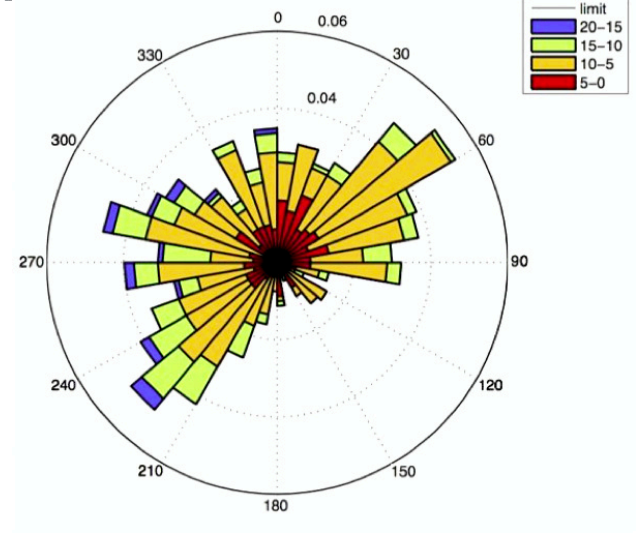


Figure 4.6: a) Winds Roses average annual frequency measured at Belle-Ile, calculated for the years 1951 to 1980 (Ascensio et al., 1987). b) Annually averaged Wind Rose measured at ST-NAZAIRE-MONTOIR (CARTE IGN, institut Geographique National, 1985). c) Wind rose near Le-Croisic (ARPEGE grid point) for the simulated period from 01/Jun to 28/Dec/2007.

Splitting a characteristic episode and analyses of induced circulation patterns

In Fig. 4.1, wind forcing is shown in two different forms, vectors on one hand (Fig. 4.1.3) and a cloud of dots (wind intensity) on the other (Fig. 4.1.4). Wind vectors give a qualitative overview of the wind direction and intensity. On graph 4 (Fig. 4.1), different colors represent the direction from which wind is blowing. To analyze this time period, trends can be summarized by using a time-integrated wind hodograph (Fig. 4.7). The wind forcing can be categorized into four main periods; the first is between 01/06 and 19/08 (days 1 to 82 in Fig. 4.7), the second period is from late august to mid-November (days 83 to 169), the third one is from 16/11 till 08/12 (days 170 to 192) and the last period is from 09/12 to 28/12 (days 193 to 211).

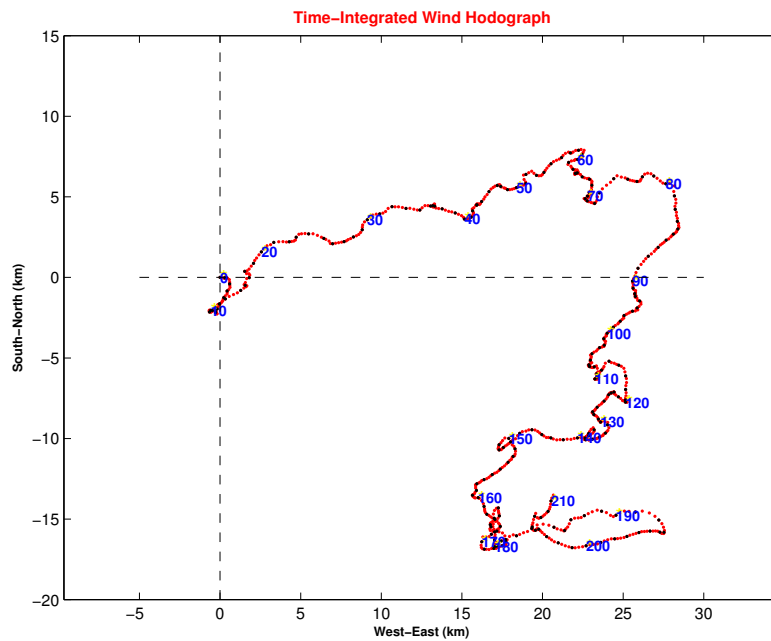


Figure 4.7: Time-integrated wind hodograph for the selected period (from 1st June to 28th December 2007), in blue: numbers of days since 1st June.

To illustrate the characteristic of each period, four wind roses have been drawn (Fig. 4.8). In the first subinterval from June 1th to August 19th (Fig. 4.8 part A), South-Westerly (SW) winds are dominant. These winds blow over a long period of time. In the second subinterval from August 20th to November 15th (Fig. 4.8 part B), a calm period with a large diversity of directions is observed in which the North-Easterly (NE) winds are privileged. The low intensity of wind and therefore its negligible effect on the regional circulation during this time period make it easier to analyze the effect of other essential elements of forcing on coastal circulation and water mass exchanges such as density gradient and tidal currents.

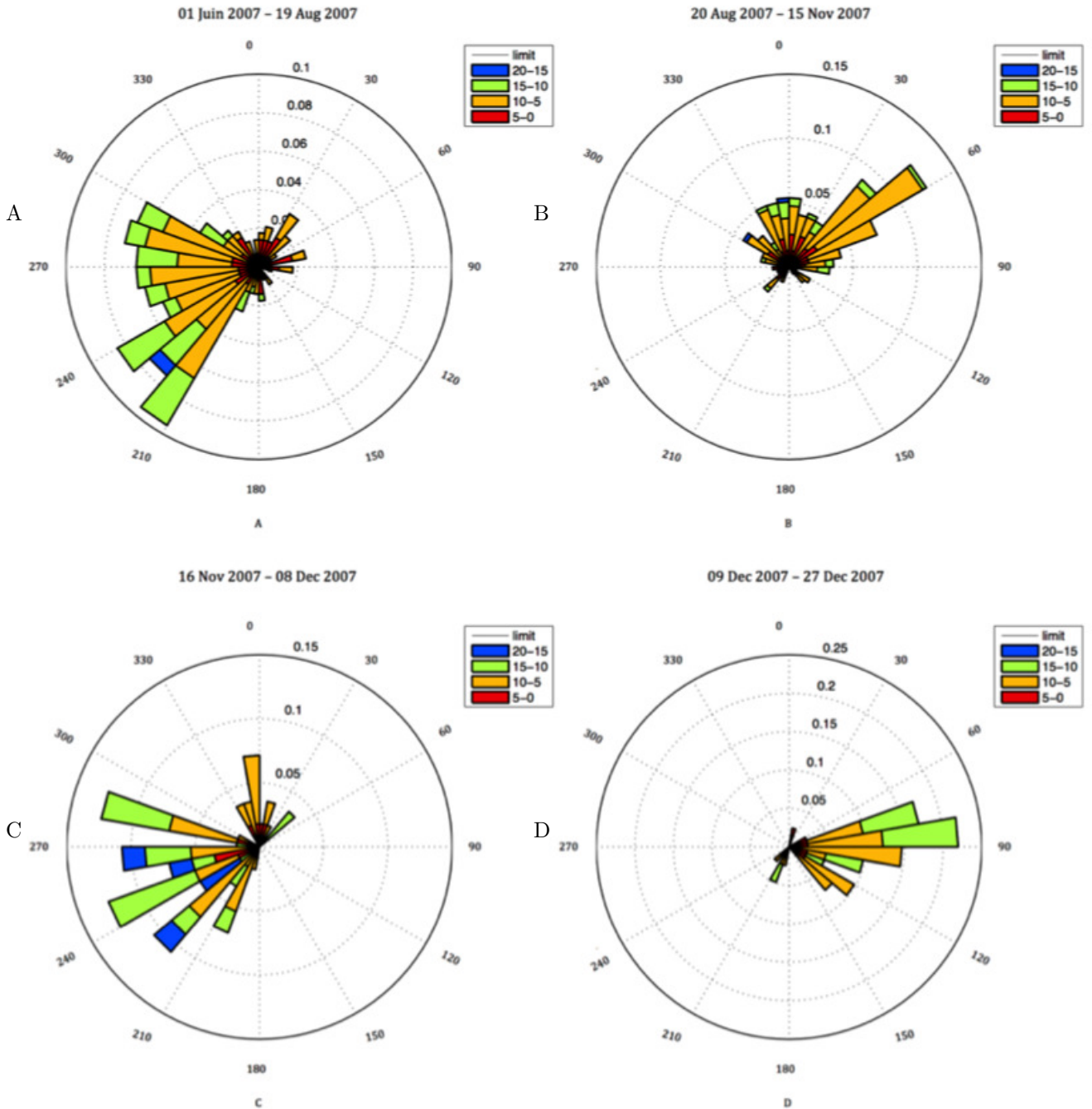


Figure 4.8: Statistical distribution of winds next to Loire Estuary (47.27° N, 2.56° W), computed from a model ARPEGE of Meteo-France (resolution: 0.5°). Reference for the four roses; radial coordinate: probability; red: winds between 0 and 5 m/s, orange: wind between 5 and 10 m/s, green: wind between 10 and 15 m/s, blue: wind between 15 and 20 m/s.

During the third time-interval from November 16th to December 8th (Fig. 4.8 part C), W and SW winds are dominant with large magnitude (mostly between 10-15 (m/s) reaching 15-20 (m/s) on some days). Finally, during the last time-interval from December 9th to 27th (Fig. 4.8, part D), a sudden change of wind direction is observed from West to East.

4.1.4 Salinity and Temperature

The graph 5 of Fig. 4.1, presents the salinity that is provided by a regional configuration of the MARS-3D model (Rank1 in Fig. 4.2) on three locations at the open boundary (blue, red, and green, with corresponding locations on the small map included in Fig. 4.1). The value of salinity is considered constant in the Loire River, equal to 0.2 PSU (gray line) in shallow coastal waters. At the southern boundary (green curve) the salinity is between 34.4-35.2 PSU. The vertical gradient of salinity remains below 0.2 PSU at this location. In the middle of the open boundary, episodic haline stratifications are present, with a considerable salinity decay in surface waters during 07/08-13/08 and 28/08-04/09. Haline stratifications is lower in the northern boundary (red curves), which are located farther from the Loire mouth, compared to the blue ones. These episodes seem to occur after eastern or north-eastern wind events following westerly wind. In late December, due to the increase of Vilaine and Loire River discharges, we can observe tidal variations of salinity near Belle-Ile Island (max 0.3 PSU).

Fig. 4.1, graph 6, shows the temperature variations at the same locations along the offshore boundary. The temperature variation of the Loire River, measured once a day at Mauve-Sur-Loire, appears in gray line. Temperature stratifications are very strong farther northward along the open boundary, in deeper areas and far away from the shore. The offshore temperature variations on the green, blue and red points during the entire period of analysis are 10, 8 and 7 °C, respectively while the variation of Loire River temperature during this period reaches 18 °C (the corresponding scales are different in Fig. 4.7). Thus the temperature variation during the selected period are representative of actual seasonal variations in the area.

4.2 Tidal circulation

In addition to the impact of the tidal wave on the marine environment, the alteration of the transient and residual flow velocities must be evaluated in detail since they constitute the driving force on important environmental processes such as sediment, pollutant transport, and nutrient dispersion.

4.2.1 Instantaneous tidal current during a spring tide

In this section, we will begin with the analysis of instantaneous tidal current during an ordinary spring tide provided by a simulation without wind forcing nor river discharge.

Fig. 4.9 and 4.10, represent the instantaneous tidal current near the water surface, few hours before and after high water level (Fig. 4.9) or low water level (Fig. 4.10). Colors represent the intensity of tidal current in each computational point while vectors present its direction and intensity for some locations. Some regions experience rather large velocities (more than 0.8 m/s). These regions are: the entrance of the Loire Estuary between St-Gildas and Paimboeuf, the opening of Bourgneuf Bay next to Herbaudière Point, the south of the Quiberon Peninsula (especially in the Teignouse Strait), the strait between Houat and Hoedic Islands, near the South-East coast of Belle-Ile Island and the entrance of the Morbihan Gulf at Port Navalo. Generally, the current velocity is weak (less than 10 cm/s) in the Mor-Braz area (Vilaine Estuary, Quiberon Bay and Morbihan Gulf), around Le-Croisic and in the south part of Bourgneuf Bay. Fig. 4.9 and 4.10 illustrate that the maximum velocity occurs around mid-tide (about three hours before and after high tide). Maximum current velocity (up to 2 m/s) is observed in three regions, Loire Estuary entrance, La-Teignouse Strait and port Navalo. Due to the high instantaneous current velocity, the local residence times are very short in these regions. Instantaneous current velocity in Bourgneuf Bay is strongly variable (between Saint-Gildas and L'Herbaudière points, it sometimes exceeds 1 m/s, while inside the Bourgneuf Bay the maximum intensity does not exceed to 0.5 m/s).

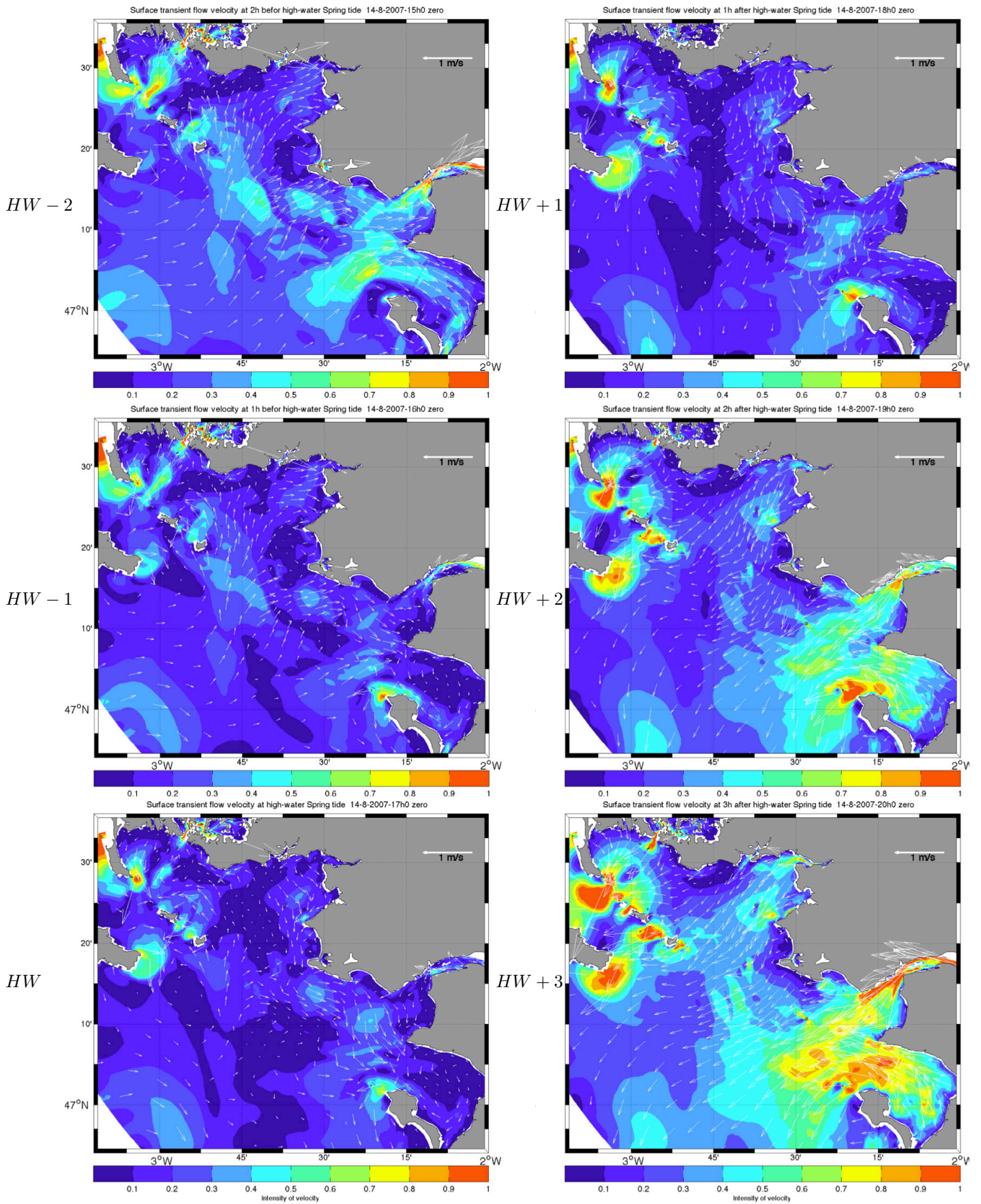


Figure 4.9: Surface tidal current during a spring tide on 14/08/2007 in a simulation without wind and river discharge from 2h before High-Water (HW) to 3h after HW.

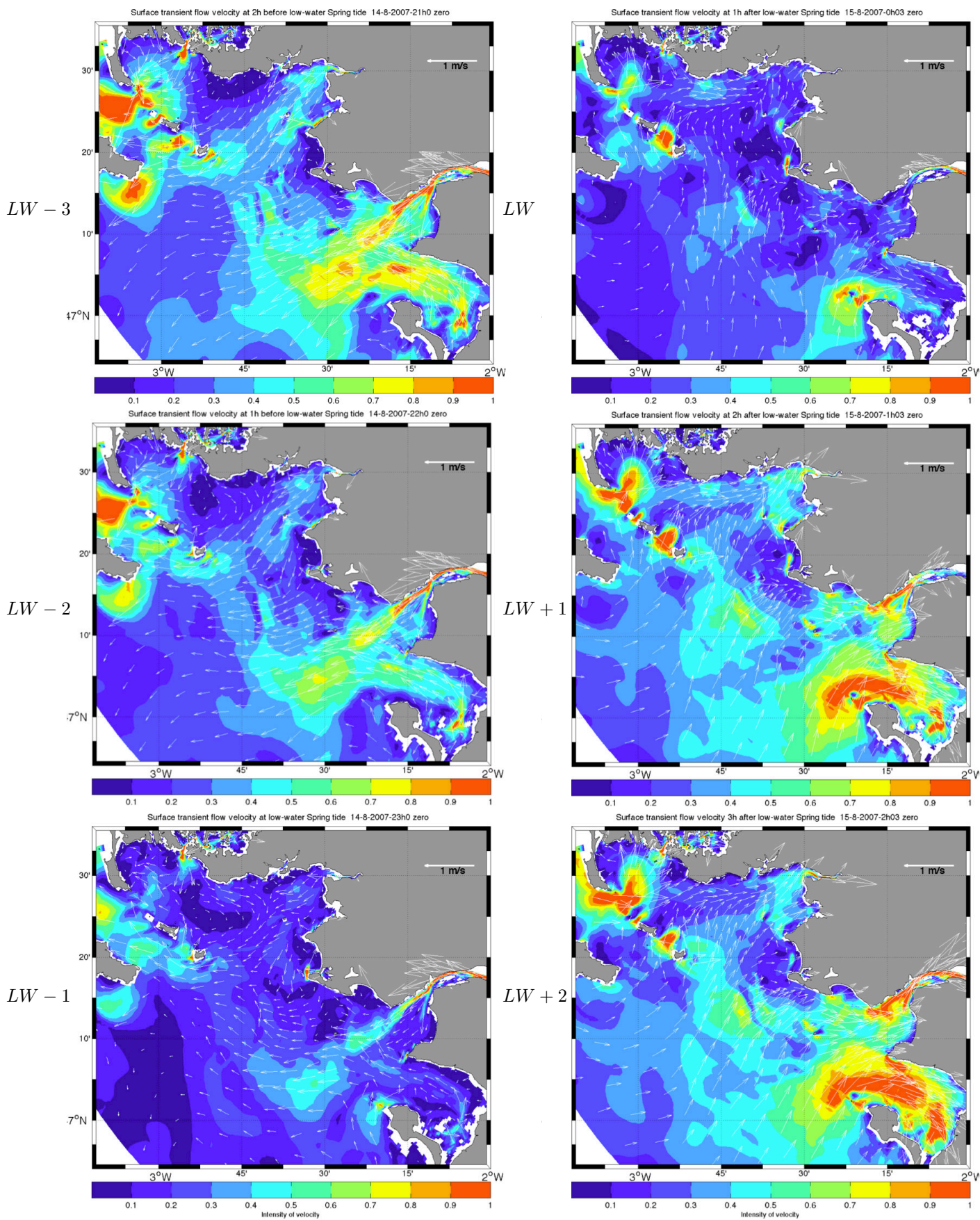


Figure 4.10: Surface tidal current during a spring tide on 15/08/2007 in a simulation without wind and river discharge from 3h before Low-Water (LW) to 2h after LW.

4.2.2 Maximum peak currents velocity during spring tides

The distribution of maximum currents is shown in Fig. 4.11. White isobaths indicate the variation of bathymetry.

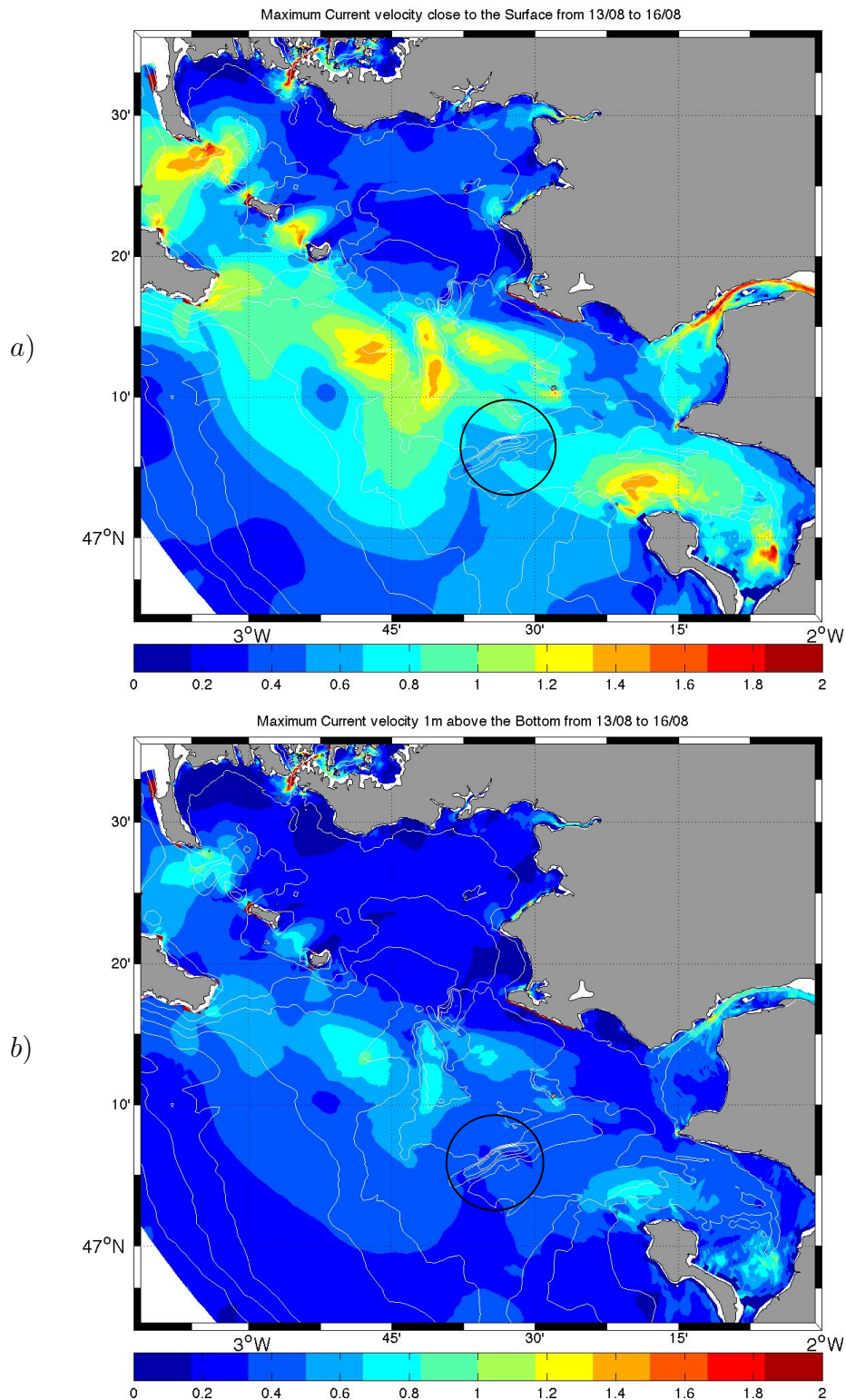


Figure 4.11: Maximum instantaneous currents between 13 to 16/08 with constant low river flow (Loire 300 m³/s, Vilaine 20 m³/s), without wind; a) close to the surface b) 1 meter above the bottom

In some regions, particularly around the Loire Estuary, the Mor-Braz islands and the entrance of the Morbihan Gulf, we can infer the relationship between the influence of bathymetry variation in the area with the maximum instantaneous current velocity. Maximum bottom currents represent main forcing on sediment dynamics and their distribution could be related to the sediment nature. An important feature in Fig. 4.11 is a relative strong bottom velocity (50 cm/s) in the clayed area of the ancient Loire Valley between shelves on each side. Such a substantial flow helps us to understand why this hole (more than 40 meters) has not been filled over the years (it has been shown in the figure by a black circle).

4.2.3 Residual tidal current during a spring tide

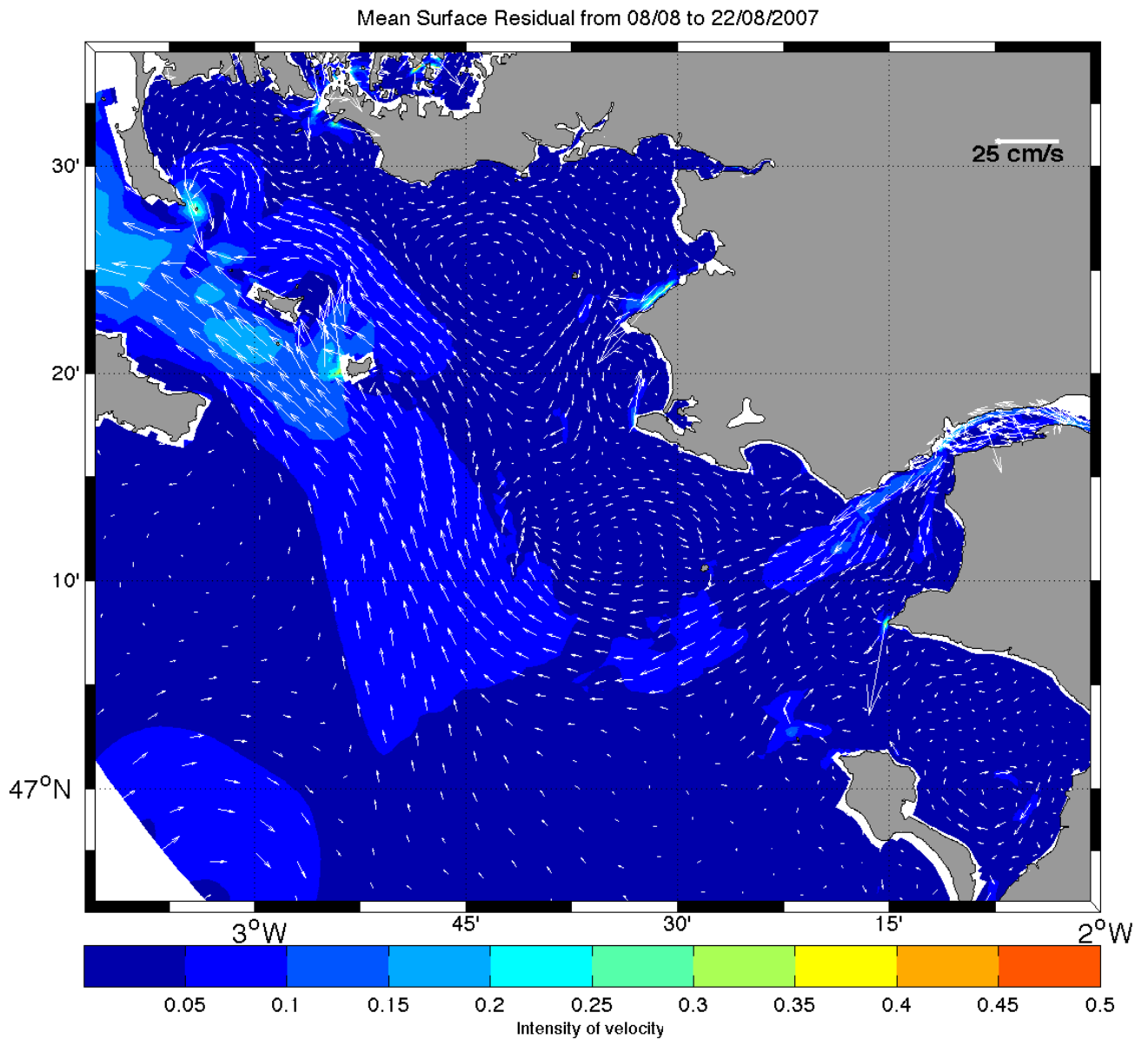


Figure 4.12: Surface residual tidal current during a whole neap/spring tidal cycle, from 08/08 to 14/08/2007, this simulation started from 01/06, constant low river discharge (Loire 300 m³/s, Vilaine 20 m³/s), without wind forcing.

In order to analyze the effect of tidal currents over long periods, the residual tidal current are considered by filtering alternate flows, using a numerical filter operating over a 72 hour window specifically fit to tidal forcing (Demerliac, 1974).

According to Fig. 4.12, in most of the study area the mean flow induced by tidal currents, without any effect of the wind forcing, remains low (less than 10 cm/s), except in the region between Quiberon Peninsula and the east bank of Belle-Ile Island where residual flow is oriented S-E and in the entrance of the Loire Estuary where it is clearly seawards near surface.

4.3 Density circulation

4.3.1 Residual circulation without wind

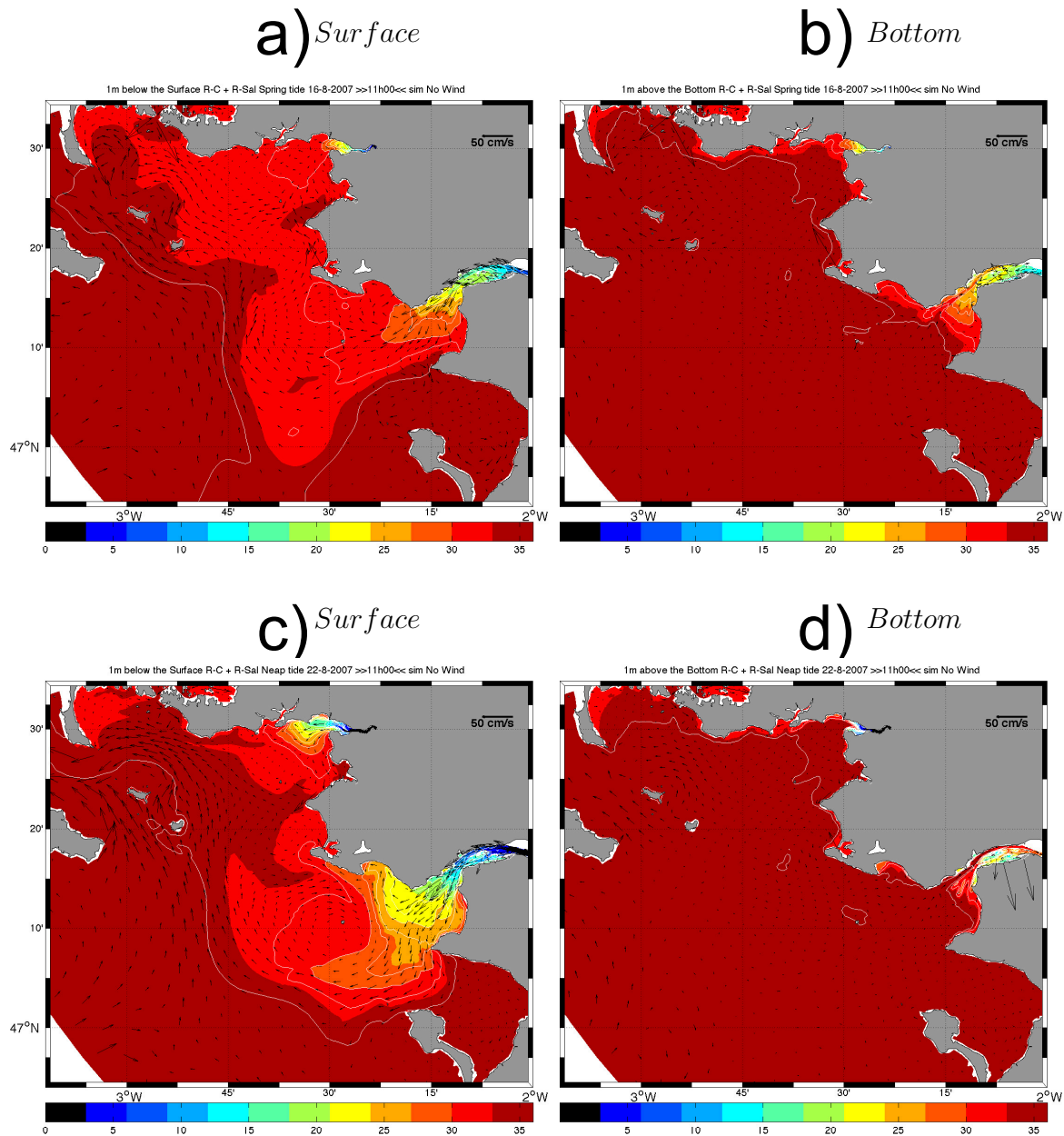


Figure 4.13: Residual salinity and current during spring tide (16/08) and neap tide (22/08) by considering real river flow 440 and 680 m³/s, respectively, without wind forces: a) at the surface during spring tide (16/08); b) at the sea-bed during spring tide (16/08); c) at the surface during neap tide (22/08); d) at the sea-bed during neap tide (22/08).

The density circulation is generated by salinity (mainly) and temperature gradients. Such a circulation can be visualized by a tidally-averaged (residual) current distribution and salinity plumes in coastal areas and especially the mouths of estuaries.

According to the Fig. 4.13, it is clear that when tide currents are not influenced by wind forces, river plumes tend to distribute northward at the surface. Our result is in conformity with Lazure and Jégou (1998).

In order to determine the stratification amplitude, we selected 4 different points, the first one is situated close to Saint-Nazaire harbor, the three others are respectively 5 km, 10 km and 20 km offshore from Saint-Nazaire. Surface and bottom salinity differences in these four points are respectively 6, 4, 6 and 4 PSU during spring tide and 26, 20, 12 and 9 PSU during neap tide which confirms that stratifications are larger on neap than during spring tides when stronger tidal currents induce mixing.

Constant river discharges

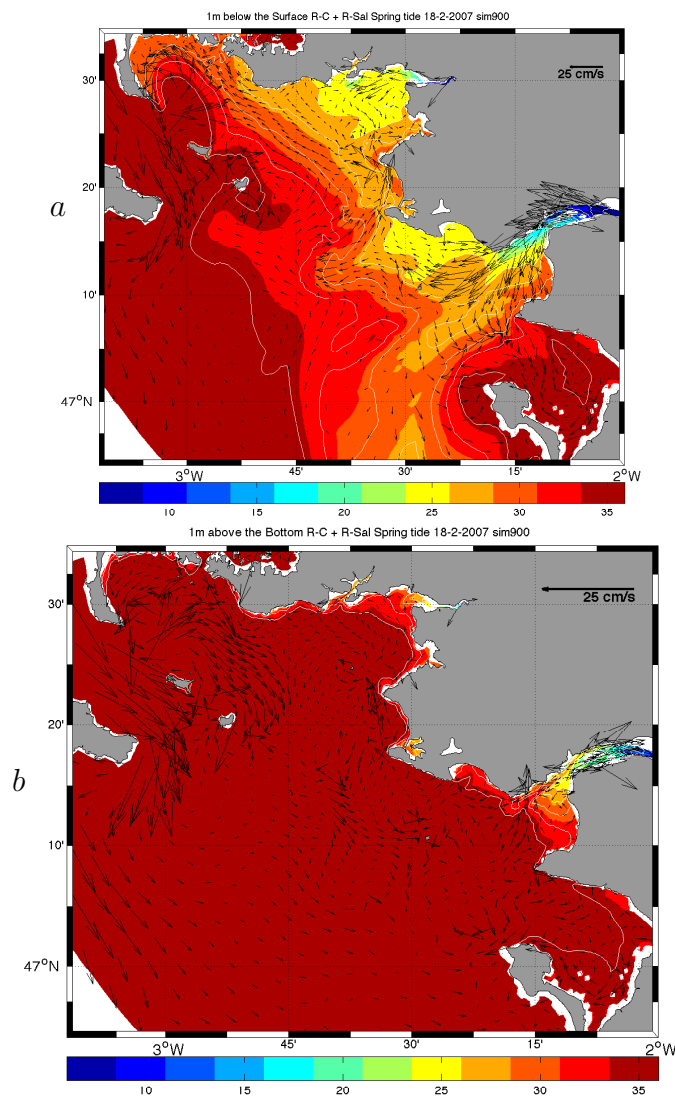


Figure 4.14: Residual salinity and current during spring tide (18/02) with a constant mean-flow (Loire 900 m³/s, Vilaine 70 m³/s);
a) Residual salinity over the surface layer and residual flow computed 1 meter below the surface,
b) Residual salinity in the bottom layer and residual current computed 1 meter above the bottom.

Another example of density-induced currents is shown in Fig. 4.14, with steady river discharge in order to avoid its variation effects.

Comparing Fig. 4.14a and b illustrates the opposite directions of flow near surface and near bottom at the entrance of the Loire and vilaine estuaries. In addition, this figure demonstrates that the river plume propagation tendency in the absence of wind forcing is divided into two main directions: the first one is northward, along the coast and the other is westward bypassing the Noirmoutier Island.

4.3.2 Wind-induced circulation

To show the effect of wind regime, we selected two periods of time for which the wind direction was stabilised during at least one tidal cycle (Sec. 4.1), in order to allow filtering the tide and to compare the results with previous ones that show the tidal residual and the density induced circulation (Fig. 4.13).

As the Demerliac (Demerliac, 1974) filter operates with a window of ± 36 hours, we also present the variation of wind every 6 hours during this 72h period. For both scenario a series of wind vectors in the interval of 36 hours before and after is shown. By comparing Fig. 4.15 and 4.13 (parts a & c), the influence of atmospheric forces on the propagation of Loire and Vilaine rivers plume is clearly demonstrated. This influence is much lower on the sea floor, but still not negligible (parts b & d). As we noticed for Fig. 4.13, stratification of surface and bottom level is more important during neap tide in the presence of wind forcing (see in Fig. 4.15).

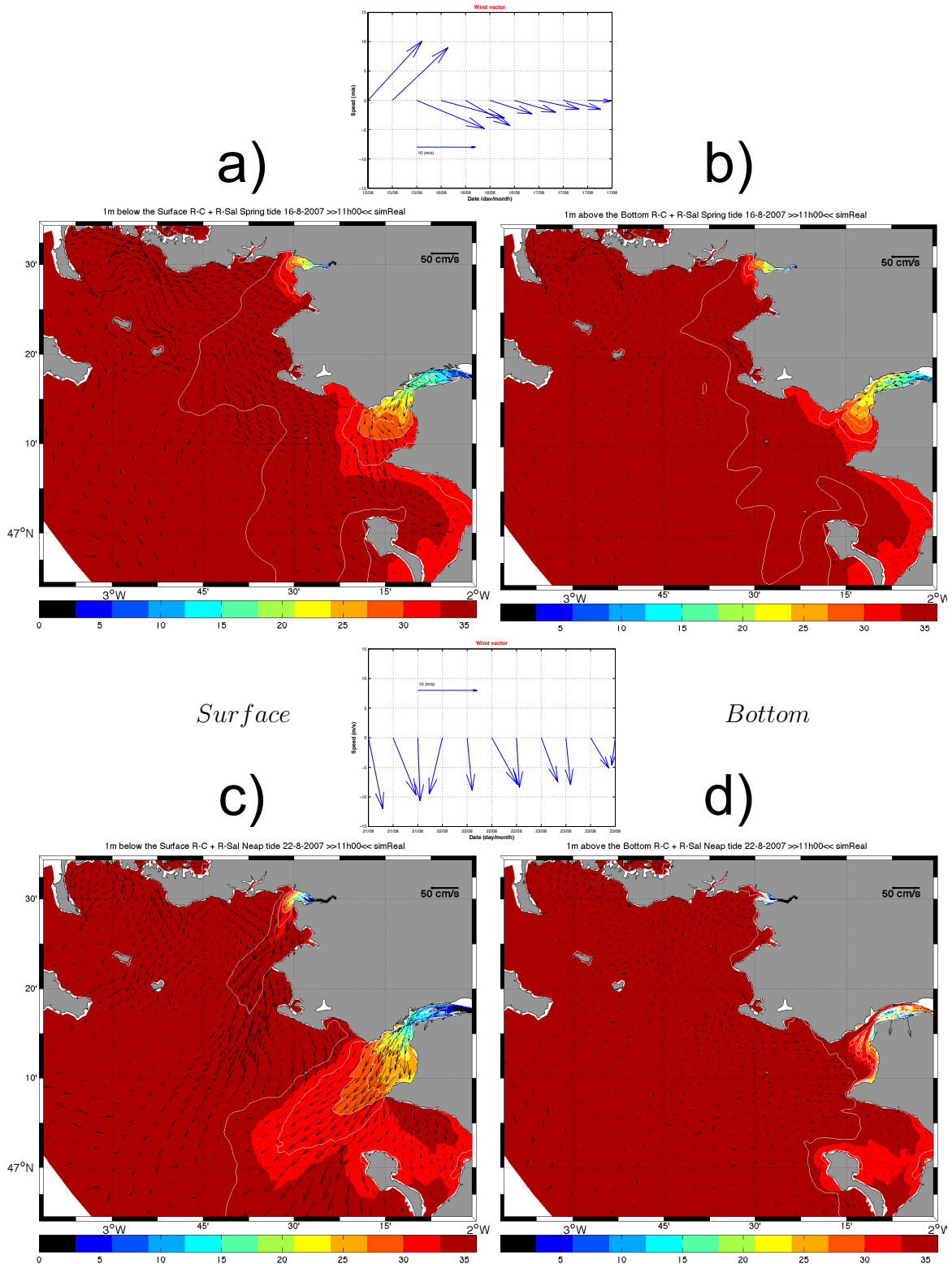


Figure 4.15: Residual salinity and current during spring tide (16/08) and neap tide (22/08) by considering real river-flow and wind forcing; a) at the surface during spring tide (16/08); b) at the sea-bed during spring tide (16/08); c) at the surface during neap tide (22/08); d) at the sea-bed during neap tide (22/08); Wind features displayed on top of each scenario present wind variation 36 hours before and after the indicated date with a time step of 6h (10 m/s wind vector is shown as an amplitude reference)

4.4 Water fluxes

4.4.0.1 Flux presentation

The objective of this section is to better understand the influence of forcing conditions (wind, tide and river discharge) on Water Fluxes in specific location (surface or bottom and deeper or shallower segments of each section).

To analyze the exchange between the Loire Estuary and the adjacent bays, the study area is divided into three main regions. Water and freshwater exchanges are examined in these regions through fluxes across their boundary.

Three sections are considered St-Nazaire, Bourgneuf and Mor-Braz. The areas are represented in Fig. 4.16 with an imaginary boundary for computing exchanges with the adjacent seas. According to research carried out over these areas, the main origin of residual flux is not clear whether it is tidally-induced or it is generated by meteorological events, particularly for both Mor-Braz and Bourgneuf areas.

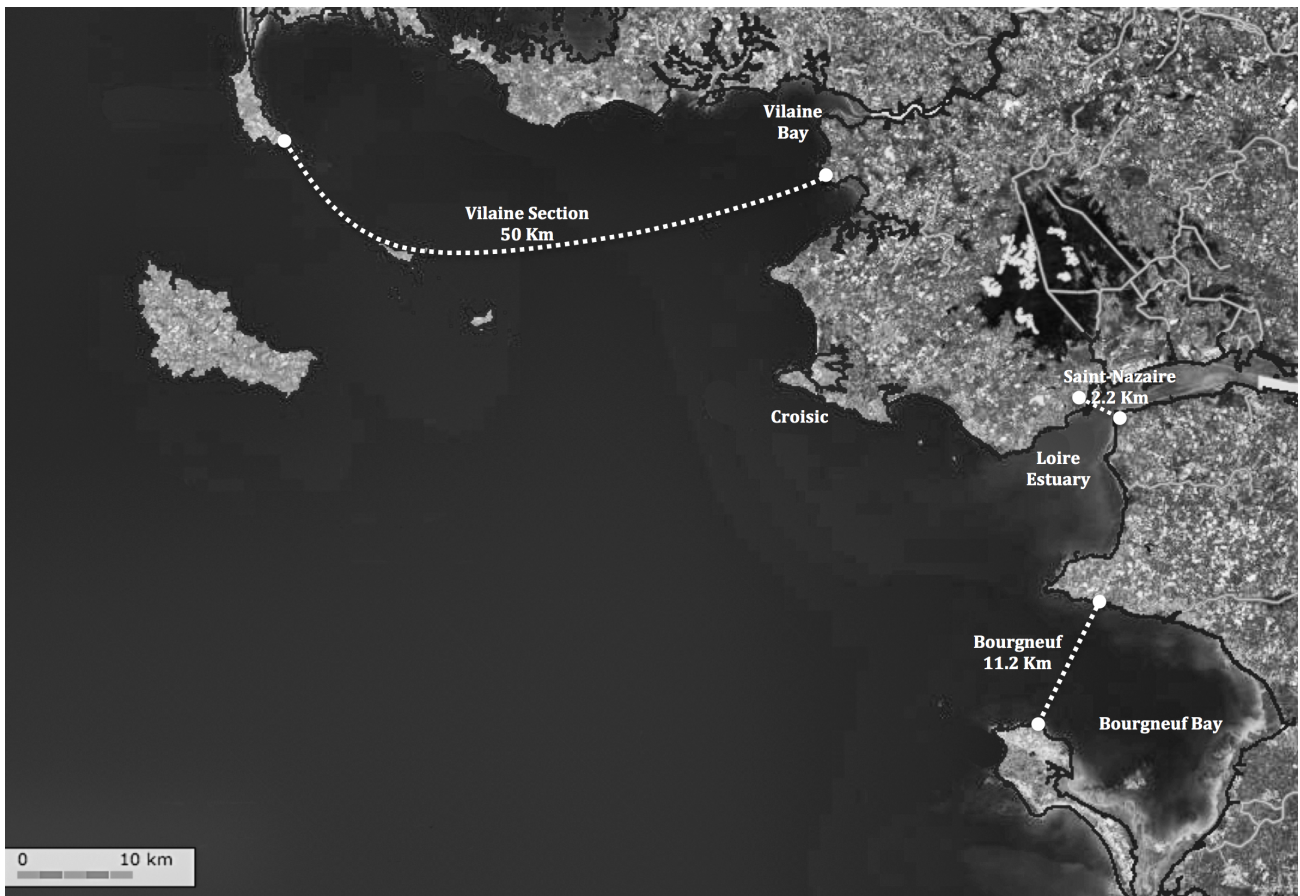


Figure 4.16: Vilaine (50 Km), Saint-Nazaire (2.2 Km) and Bourgneuf (11.2 Km) sections.

For each section (subsection) two kinds of flux have been computed. The first one, based on total water exchanges and the second one computed as the fresh water exchanges. Most figures (*e.g.* Fig. 4.20) in this section are related to the time evolution of fluxes through their subsections (sub-section). All of them consist of seven graphs that represent:

- a) the depth-integrated flux passing through the cross-section without filtering tide waves,
- b) the residual Water Flux over the first 1m below the surface (here "residual" means after filtering the tidal variation, using the Demerliac filter (Demerliac, 1974)),
- c) the time-integration of quantity represented in graph 'b',
- d) the residual Water Flux over the first 1m above the bottom,
- e) the time-integration of quantity represented in graph 'd',
- f) the depth-integrated Residual Water Flux (i.e. similar to 'a' after tide filtering using the Demerliac filter (Demerliac, 1974)),
- g) the time-integration of quantity represented in graph 'f'.

4.4.0.2 Flux analyses

Flux analysis was performed by setting up some assumptions. The initial conditions are identical for all simulations and for the comparison of freshwater flux, a salinity of 35.5 PSU is assumed for ocean water. As it was mentioned in Chap. 2, each coordinate of vector velocity is contravariant, in our method, which means it was computed perpendicular at each lateral border of meshes.

-Expression of Water Flux:

$$FW_x(t, k, i, j) = Uz(t, k, i, j) * \sqrt{g_u(i, j)} * \frac{(H_x(i, j) + xe(t, i, j))}{10}$$

$$FW_y(t, k, i, j) = Vz(t, k, i, j) * \sqrt{g_v(i, j)} * \frac{(H_y(i, j) + xe(t, i, j))}{10}$$

-Expression of Fresh Water Flux:

$$FWF_x(t, k, i, j) = \frac{(35.5 - SAL(t, k, i, j))}{35.5} * Uz(t, k, i, j) * \sqrt{g_u(i, j)} * \frac{(H_x(i, j) + xe(t, i, j))}{10}$$

$$FWF_y(t, k, i, j) = \frac{(35.5 - SAL(t, k, i, j))}{35.5} * Vz(t, k, i, j) * \sqrt{g_v(i, j)} * \frac{(H_y(i, j) + xe(t, i, j))}{10}$$

-Velocity components integrated over one meter above the bottom:

$$U_{1mf}(1, t, i, j) = Uz(k = 1, t, i, j) * \frac{\ln(\frac{1}{z_0})}{\ln(\frac{0.5 * (H_x(i, j) + xe(t, i, j))}{z_0 * (\text{nb layers} = 10)})}$$

$$V_{1mf}(1, t, i, j) = Vz(k = 1, t, i, j) * \frac{\ln(\frac{1}{z_0})}{\ln(\frac{0.5*(H_y(i,j)+xe(t,i,j))}{z_0*(nb\ layers=10)})}$$

$FWF_x(t, k, i, j)$, $FWF_y(t, k, I, j)$ are instantaneous fluxes passing throughout the westward and eastward directions of each mesh; $U_{1mf}(k, t, i, j)$ is the mean velocity from the bed up to 1 meter above the bottom, while Uz and Vz are the velocity components computed for the lower layer.

By integrating over the section and vertically we obtain the whole water or freshwater flux instantaneously passing over chosen section. The Demerliac filter (Demerliac, 1974) helps us to eliminate the tidal oscillation in the WF and FWF exchanges.

- t, k, i, j = represent the time, level and position indexes,
- $SAL(t, k, i, j)$ = Salinity,
- $Uz(t, k, i, j)$ = Contravariant velocity computed by the model which is not in m/s scale,
- $Uz(t, k, i, j) \times \sqrt{g_u(i, j)}/dy(i, j)$ = Adjusted contravariant velocity m/s,
- $\sqrt{g_u(i, j)}$ = metric tensor used for adjusting the orders of magnitude,
- $H_x(i, j)$ = depths over the x direction,
- $U_{1mf}(1, t, i, j)$ = Contravariant vector velocity coordinates 1 meter above the bottom,
- $z_0 = 0.002$ (bottom roughness)

4.4.1 Water and Fresh-Water Fluxes at Saint-Nazaire

The St-Nazaire section has been selected as it represents the mouth of the estuary, and then the exchanges with the coastal sea. Analyzing fluxes through this section enables to investigate for which conditions (of wind, tide, river discharge) and where (surface, bottom, northern and deeper section or southern and shallower section) water is flowing in either direction, and possibly distinguishing fresh water and total mass of water. The former indicates what the fate of any conservative constituent in the river is likely to be, whereas the latter is an indicator of residual flow, and can gives an idea of residual transport of fine suspended sediment particles.

Fig. 4.17 shows the Saint-Nazaire section. This section is the entrance of transition part of the Loire estuary, it includes 24 meshes in the entire cross-section among which 15 meshes are related to south subsection (shallow segment). Meshes are about 1 km wide. The north subsection (deep segment, 1.2 km) is larger than the shallow segment. This cross-section is represented in Fig. 4.18 and 4.19 .



Figure 4.17: Saint-Nazaire cross-section, divided into a deep (1.2 Km) and a shallow (1.0 Km) subsections.

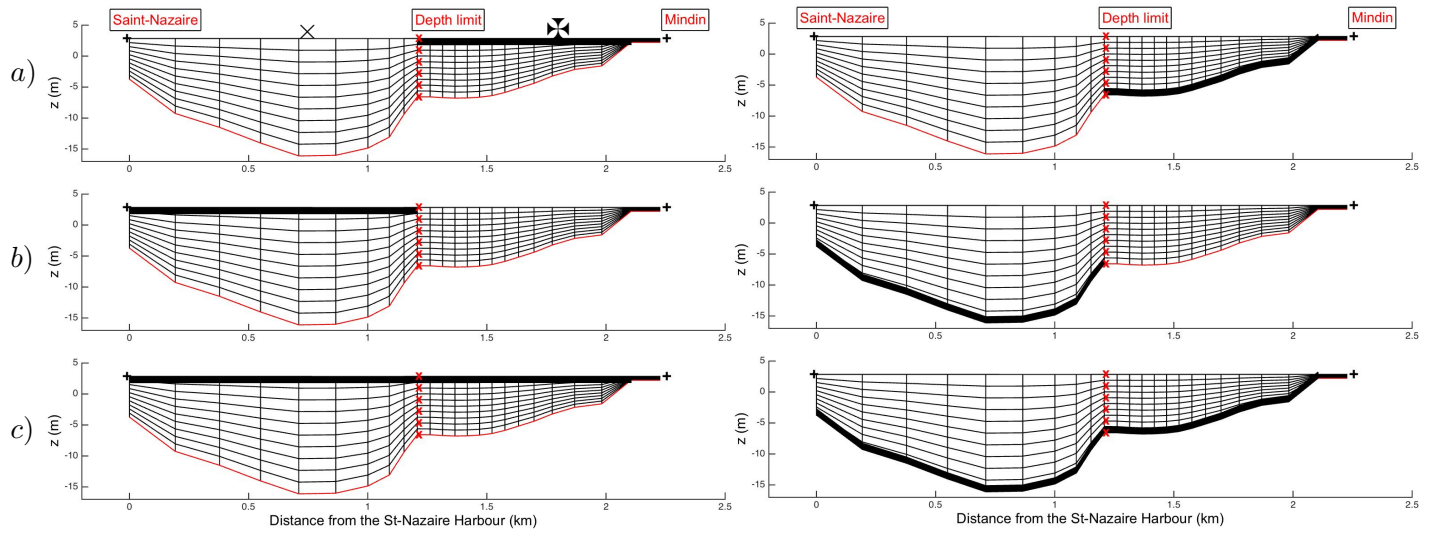


Figure 4.18: Schematic view of the cross-section in which (Fresh) Water Flux is calculated over the first 1m below the surface in St-Nazaire section (two point indicated by \times and \otimes are chosen for the vertical profiles of hydrological characteristics):

- a) surface Flux computed through the shallow subsection
- b) surface Flux computed through the deep sub-section
- c) surface Flux computed through the overall section.

Figure 4.19: Schematic view of the cross-section in which (Fresh) Water Flux is calculated over the first 1m above the bottom in St-Nazaire section:

- a) bottom Flux computed through the shallow subsection
- b) bottom Flux computed through the deep sub-section
- c) bottom Flux computed through the overall section.

4.4.1.1 Water Flux (WF) and Fresh-water Flux (FWF) in Saint-Nazaire section (overall)

The water fluxes and fresh water fluxes through the Saint-Nazaire section are respectively shown in Fig. 4.20 and 4.24.

Tidal fluxes

Water fluxes through the whole section (Fig. 4.20a) depict the tidal oscillation at the mouth of the Loire estuary, and point out the (linear) flux variation according to the tidal amplitude, with a maximum of about 25000 m³/s on spring flood (against a maximum of 21000 m³/s on spring ebb, much more than the river discharge (between 300 and 2000 m³/s). The residual water flux, after filtering tide by using the Demerliac (1974) filter (Fig. 4.20f) is strongly related to the river flow, as required for continuity considerations, and does not show large variations, neither with the tidal amplitude, nor with the meteorological forcing. Only small fluctuations can be noticed, some of them correlated with the tide amplitude (from late August until mid-November, the net flux seawards seems maximum before neap tide, *i.e.* around the end of the amplitude decreasing phase) and other anomalies being in relation with the storm surge (see Fig. 4.1): *e.g.* on July 22, November 18 and December 9.

Fresh water fluxes

The instantaneous Fresh Water Fluxes (FWF) strongly vary with the river discharge, but non linearly (Fig. 4.24a): for instance, on last spring tide of October, the FWF reaches about 15000 m³/s for a river flow of 2000 m³/s, while it is about 7000 m³/s when the river flow is nearly 7 times lower (300 m³/s).

This can be linked to the average salinity values near the mouth, which oscillate around 18 PSU or 26 PSU for respective steady river discharges of 2000 m³/s and 300 m³/s (Fig. 4.23). These mean depth-averaged salinities correspond to salinity deficits (in comparison with the offshore reference concentration of 35.5 PSU) of 17.5 PSU and 9.5 PSU respectively, in the proportion of FWF. It is also remarkable that the tidal fluxes of fresh water are much larger than the river discharge, as they involve a mass of fresh water temporarily accumulated in the area. In terms of tide-residual fresh water fluxes (Fig. 4.24f), results are very similar to the residual water fluxes: the residual fluxes oscillate around the respective river discharge (saving the continuity), but oscillations appear a bit larger, probably because fresh water is preferentially located near the water surface, which is more sensitive to the meteorological forcing.

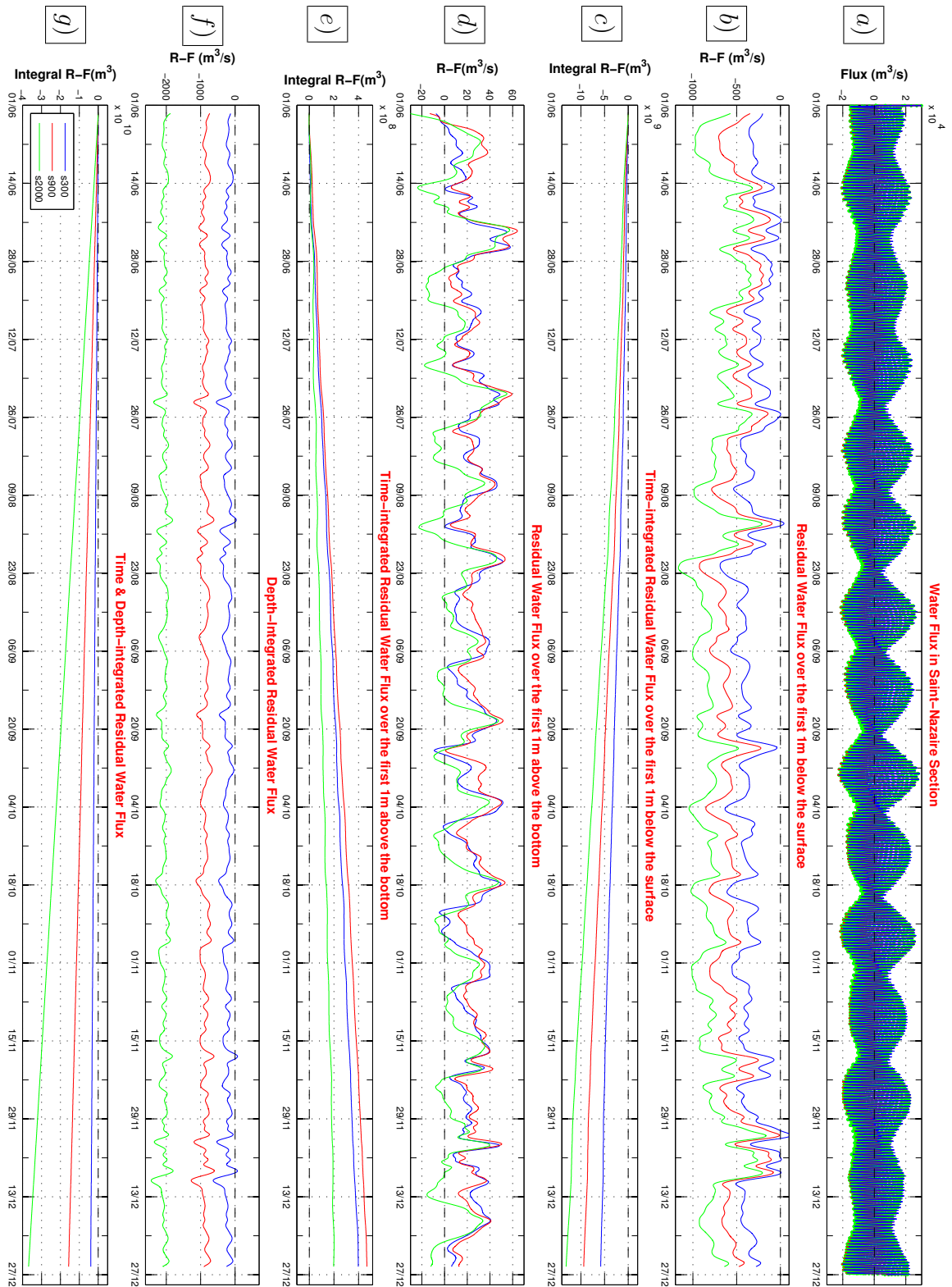


Figure 4.20: Water exchange in the St-Nazaire cross-section, three simulations are shown; positive value means landward and the negative means seaward. The color coding is as follows:

- Blue: a semi-realistic situations with real meteorological conditions (wind, salinity, temperature), actual bathymetry and low flow (300, 20 m³/s as constant discharges of Loire and Vilaine rivers).
- Red: a semi-realistic situations with real meteorological conditions (wind, salinity, temperature), actual bathymetry and average flow (900, 70 m³/s as constant discharges of Loire and Vilaine rivers).
- Green: a semi-realistic situations with real meteorological conditions (wind, salinity, temperature), actual bathymetry and flood flow (2000, 180 m³/s as constant discharges of Loire and Vilaine rivers).

Vertical distribution of water fluxes

However, the vertical distribution of the total water or fresh water residual flux reveals strong contrasts between surface and bottom, with larger fluctuations than after vertical integration. Near bottom, the water flux is clearly oriented upwards, whatever the river discharge, in agreement with the bottom residual current represented in Fig. 4.21b and is clearly correlated with the tidal amplitude (Fig. 4.20d). The maximum upwards flux occurs at the end of the period of decreasing tidal amplitude, before or around neap tide, may be in relation with more stratified waters, and then a stronger expression of estuarine circulation. Results are very similar for river discharges of 300 and 900 m³/s, while the flux is globally shifted downstream when the river flow is 2000 m³/s. In the latter case, bottom residual flow can be oriented downwards on spring (more precisely, at the end of the amplitude increase period), even if it remains oriented upwards in the long term (Fig. 4.20e).

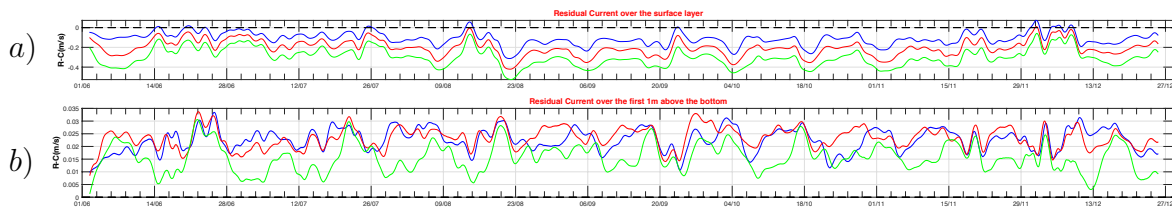


Figure 4.21: Averaged residual current; a) near the surface, b) over the first 1m above the bottom; The color coding is as follows:

- Blue: low flow (300, 20 m³/s as constant discharges of Loire and Vilaine rivers).
- Red: average flow (900, 70 m³/s as constant discharges of Loire and Vilaine rivers).
- Green: flood flow (2000, 180 m³/s as constant discharges of Loire and Vilaine rivers).

Near surface (Fig. 4.20b), residual water fluxes are always oriented offshore and show strong variations in relation with the tidal amplitude, presenting a maximum on neap, in agreement with the opposite maximum near bottom and the likely stratification at this time (actually, it seems that the phase of the flux is in advance on the tidal amplitude, may be because the residual circulation takes place when stratification is developing, not necessarily when the tidal amplitude is minimum). The residual water flux also varies significantly with the wind. As reminded in Fig. 4.22, the wind is mainly blowing from the WSW sector until mid-August, pushing surface waters to the shore, while in the following months (from late August until mid-November) it blows from NNE, enhancing the offshore surface water flux at St-Nazaire. It can be noticed that when the wind is onshore, residual fluxes are less dependent on the river flow than when the wind blows from the NE: in the former case the stratification is likely to be attenuated, while it should be reinforced in the latter one.

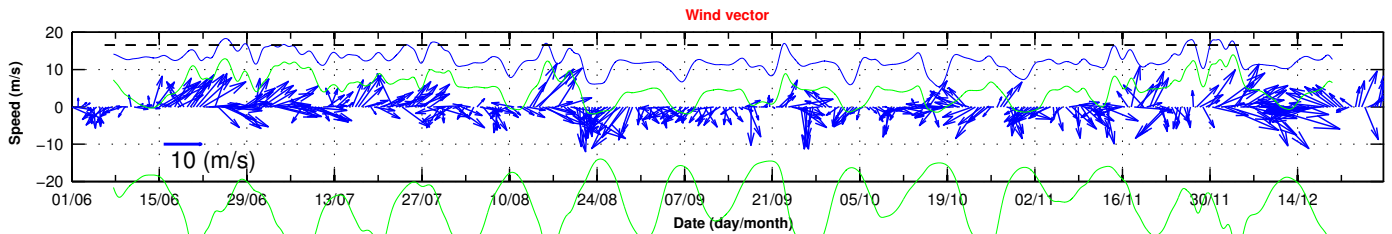


Figure 4.22: Time-evolution of wind speed from 01/June until 28/December nearby Le-Croisic according to the ARPEGE meteorological model.

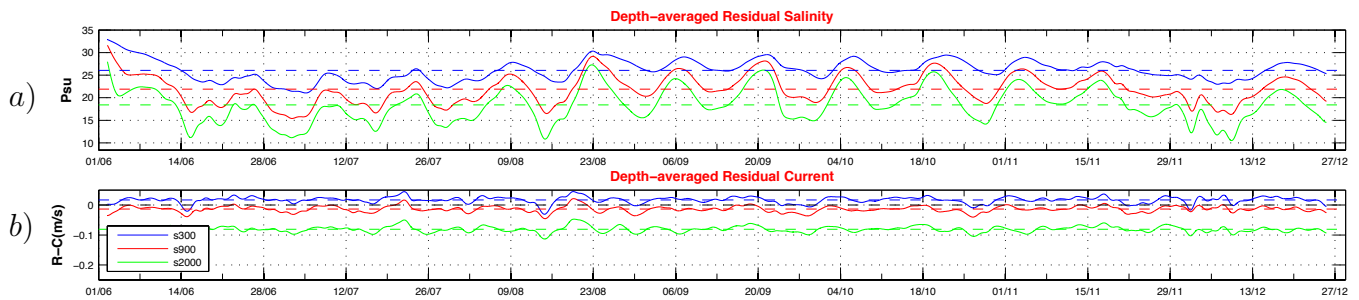


Figure 4.23: Depth-averaged Residual Salinity and Current at the mouth of Loire Estuary, dashed-line present the mean value of each curve respectively with a same color. The color coding is as follows:
 -Blue: low flow (300, 20 m³/s as constant discharges of Loire and Vilaine rivers).
 -Red: average flow (900, 70 m³/s as constant discharges of Loire and Vilaine rivers).
 -Green: flood flow (2000, 180 m³/s as constant discharges of Loire and Vilaine rivers).

Vertical distribution of fresh water fluxes

Residual FWF are very similar to the residual water fluxes near the surface, in terms of mean values and tide-induced or meteo-induced variations (Fig. 4.24b & 4.20b), although the salinity is non negligible at St-Nazaire. This can be due to a lower salinity on ebb than on flood, which compensates the reduced asymmetry between ebb and flood fluxes because each of these fluxes is reduced when considering the fresh water part only.

Close to the bottom, residual FWF behave differently from the total water fluxes. The difference of salinity between ebb (lower salinity) and flood (higher salinity) explains that the FWF is more oriented seawards. Actually, residual FWF is slightly upwards on low river regime, slightly seawards on mean river regime and clearly seawards on high river regime (Fig. 4.24e), but 40 times lower than in the first meter below the surface (Fig. 4.24c and e). Similarly to residual water fluxes, the variation of residual FWF with tidal amplitude is clearer when the river flow is high, probably because the stratification changes are likely to be enlarged in this case.

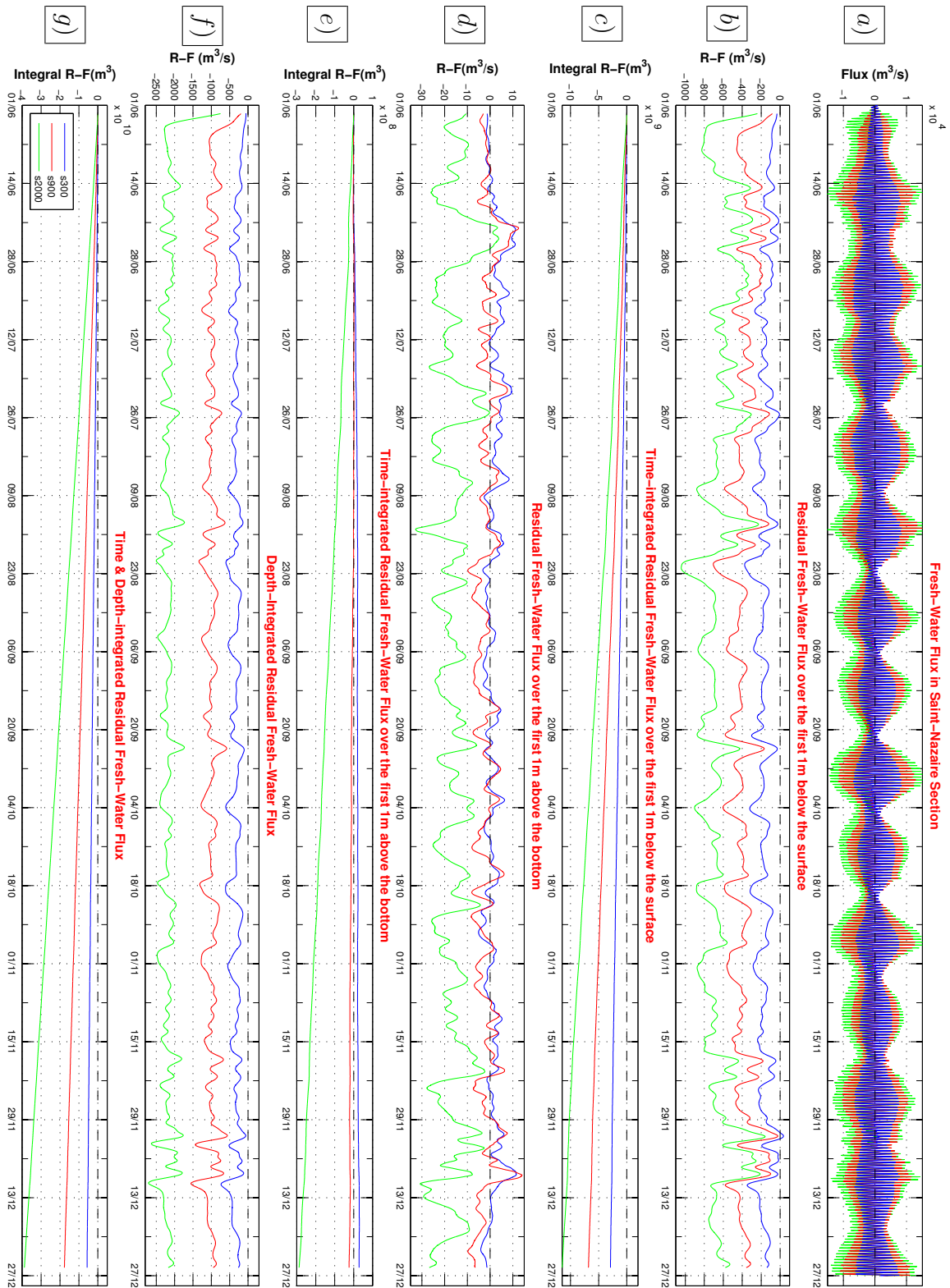


Figure 4.24: Fresh-Water exchange in the St-Nazaire cross-section, three simulations are shown; positive value means landward and the negative means seaward. The color coding is as follows:

- Blue: a semi-realistic situations with real meteorological conditions (wind, salinity, temperature), actual bathymetry and low flow (300, 20 m³/s as constant discharges of Loire and Vilaine rivers).
- Red: a semi-realistic situations with real meteorological conditions (wind, salinity, temperature), actual bathymetry and average flow (900, 70 m³/s as constant discharges of Loire and Vilaine rivers).
- Green: a semi-realistic situations with real meteorological conditions (wind, salinity, temperature), actual bathymetry and flood flow (2000, 180 m³/s as constant discharges of Loire and Vilaine rivers).

Vertical profiles analysis in Saint-Nazaire section

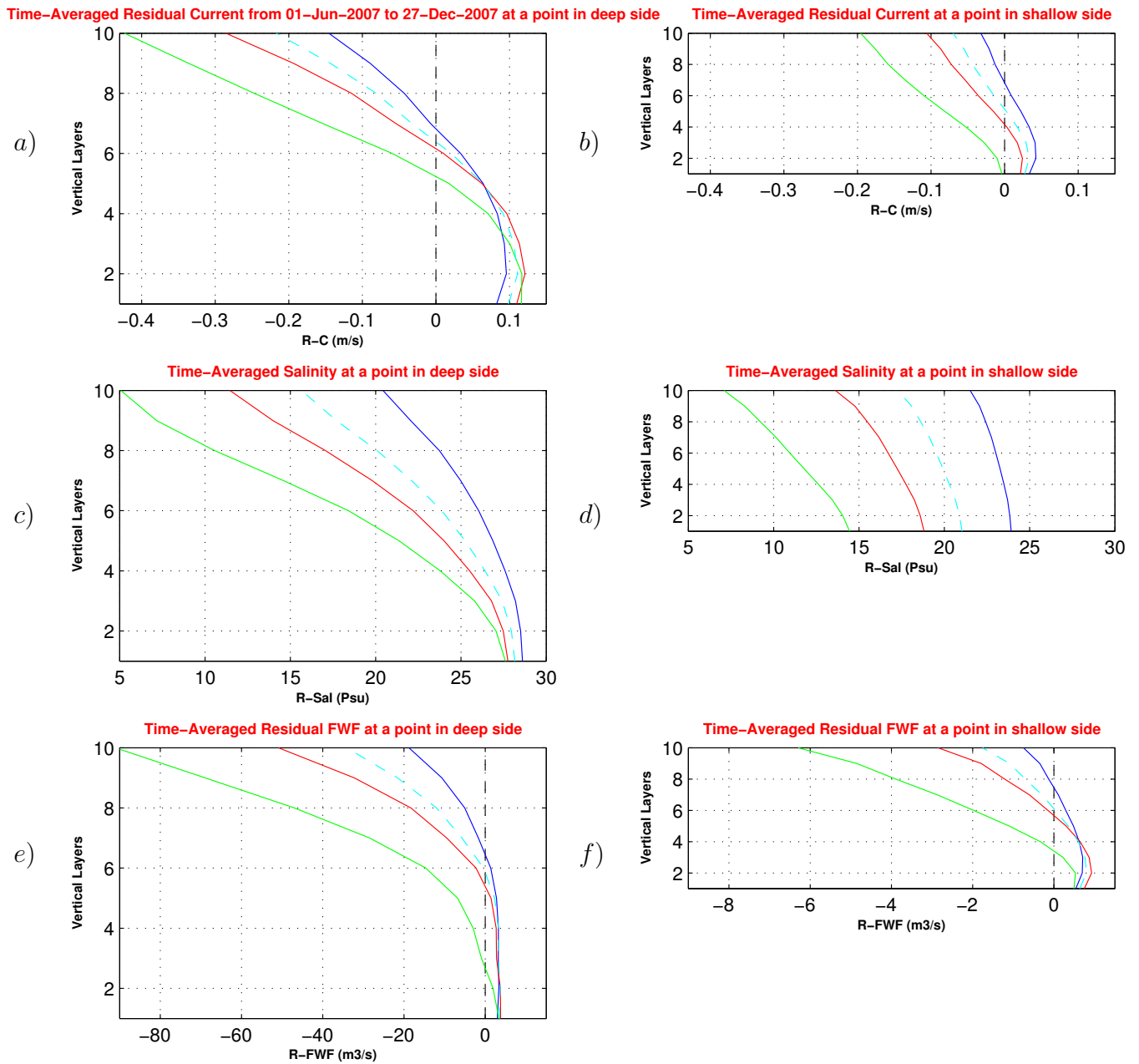


Figure 4.25: Representative vertical profiles of hydrological characteristics across the Saint-Nazaire section, averaged over seven months. Left hand side: in the deep part; Right hand side: in the shallow part. a) and b) Residual current; c) and d) Time-averaged salinity; e) and f) Time-averaged residual Fresh water Fluxes. Colors correspond to the different river discharges (blue: low, red: mean, green: high and cyan/dashed: real), Positive fluxes or currents are entering the Loire Estuary.

Residual currents, time-averaged salinity and FWF profiles in the middle of each subsection (locations are indicated by symbols in Fig. 4.18) are represented in Fig. 4.25.

Salinity profile is severely stratified in the deep part and moderately stratified in the shallow part, but residual flow profiles show a water exit near the surface and an opposite mean current

in bottom layers, more developed in the deep subsection. As a consequence, FWF is clearly oriented seawards near the surface (especially in the deepest part in northern subsection) and landward in bottom or intermediate layers, especially in the shallow subsection. The fresh water exchanges are nearly linearly dependent on the Loire River discharge. A valuable and remarkable point is the similarity of the shape of the curve in constant average flow (red curve) and the one related to the real flow (cyan/dashed curve) which allows us to conclude that the average flow constitutes a representative case.

4.4.1.2 North/south distribution of water flux at the estuary mouth

The mouth of the Loire estuary is characterized by a North-South asymmetry (Fig. 4.17), with a deep channel in the northern side (1.2 km wide) and shallow waters in the southern one (1 km wide). The respective fluxes in these two complementary subsections (Fig. 4.18) are presented in Fig. 4.26 and 4.27. Instantaneous fluxes are about three times larger in northern subsection than in the southern one (Fig. 4.26a & 4.27a). Total residual fluxes (depth-integrated) are not simply a ratio of the flux through the whole St-Nazaire section : on low river regime, it is slightly upwards in the southern part and downwards in the northern one, with a strong modulation with tide amplitude : upwards on spring, downwards on neap. This feature may be not independent of stratification effects, as the shallower southern part is hydrologically closer to the upper part of the northern subsection (see Fig. 4.25).

Looking at fluxes near bottom reveals that in the northern subsection, the tidal modulation is the same whatever the river flow (Fig. 4.26d), while the net input of water is larger for mean and high river flow (Fig. 4.26e). In the southern subsection, the net bottom flux (integrated over the period) is in the same range as in the North for low and mean river flow, while it remains null when the river flow is high (Fig. 4.27e). Lastly, residual fluxes in the surface layer indicate similar trends in both subsections (and then similar to trends for the whole section (Fig. 4.20b), with dependence on winds, river flow and tidal amplitude.

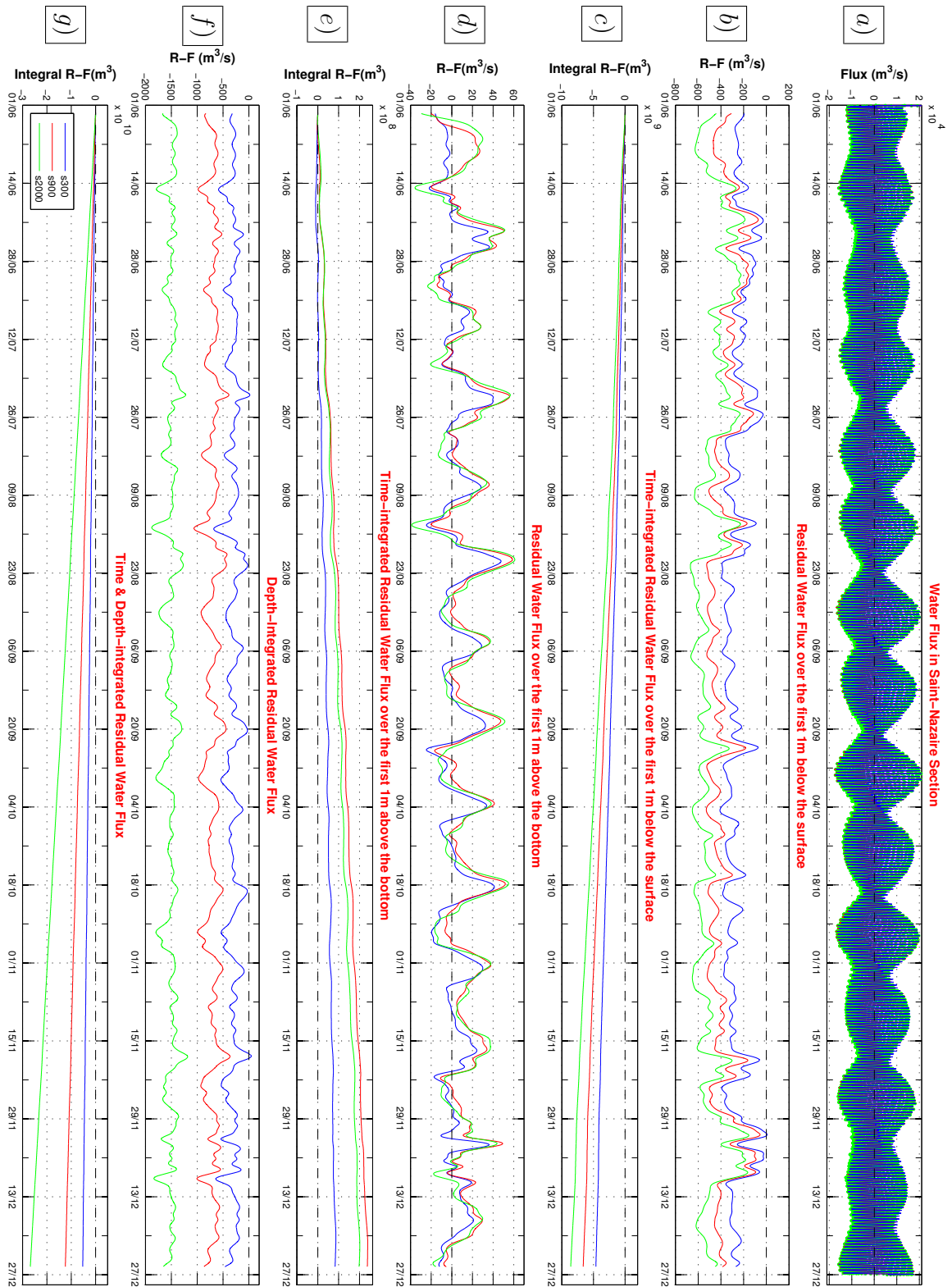


Figure 4.26: Water exchange in the St-Nazaire north-section (deep), three simulations are shown; positive value means landward and the negative means seaward. The color coding is as follows:

- Blue: a semi-realistic situations with real meteorological conditions (wind, salinity, temperature), actual bathymetry and low flow (300, 20 m³/s as constant discharges of Loire and Vilaine rivers).
- Red: a semi-realistic situations with real meteorological conditions (wind, salinity, temperature), actual bathymetry and average flow (900, 70 m³/s as constant discharges of Loire and Vilaine rivers).
- Green: a semi-realistic situations with real meteorological conditions (wind, salinity, temperature), actual bathymetry and flood flow (2000, 180 m³/s as constant discharges of Loire and Vilaine rivers).

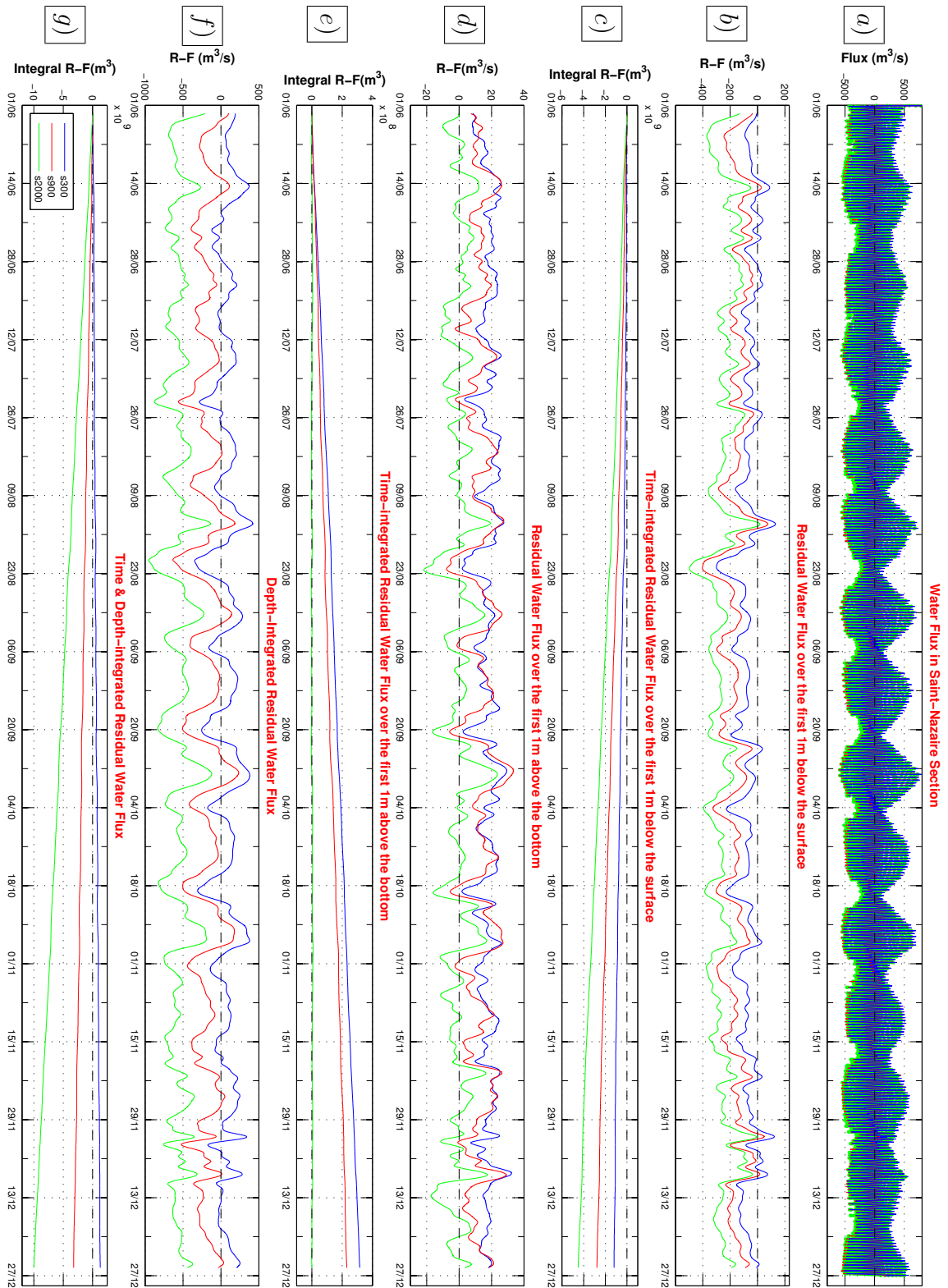


Figure 4.27: Water exchange in the St-Nazaire south-section (shallow), three simulations are shown; positive value means landward and the negative means seaward. The color coding is as follows:

- Blue: a semi-realistic situations with real meteorological conditions (wind, salinity, temperature), actual bathymetry and low flow (300, 20 m^3/s as constant discharges of Loire and Vilaine rivers).
- Red: a semi-realistic situations with real meteorological conditions (wind, salinity, temperature), actual bathymetry and average flow (900, 70 m^3/s as constant discharges of Loire and Vilaine rivers).
- Green: a semi-realistic situations with real meteorological conditions (wind, salinity, temperature), actual bathymetry and flood flow (2000, 180 m^3/s as constant discharges of Loire and Vilaine rivers).

4.4.1.3 North/south distribution of fresh water flux at the estuary mouth

Instantaneous FWF are approximately distributed in the two subsections in the proportion 2/3 (North) and 1/3 (South) (Fig. 4.28a & 4.29a), which indicates a higher contribution of the southern part compared with the exchange of instantaneous WF.

According to Fig. 4.28g and 4.29g, net residual FWF is much higher (4.5 times larger) in the northern subsection than in the southern one (for a constant discharge of 2000 m³/s during 6 months: 32109 m³ compared with 7109 m³). However, it should be noted that the surface of vertical section of deep subsection (16.55 m²) is 3.7 times wider than the shallow one (4.45 m²) according to Fig. 4.18. In particular, on low river flow, the net FWF is zero in the southern subsection. Relative tidal fluctuations are also much more intense (Fig. 4.29f). Considering the vertical distribution of FWF in both subsections, a net import of fresh water is obtained in the southern one near the bottom, but in a low range, while the net flux is seawards near the surface, and also near the bottom in the northern subsection. These results illustrate a strong sensitivity of fresh water pathways to the location we are considering and to the physical forcing.

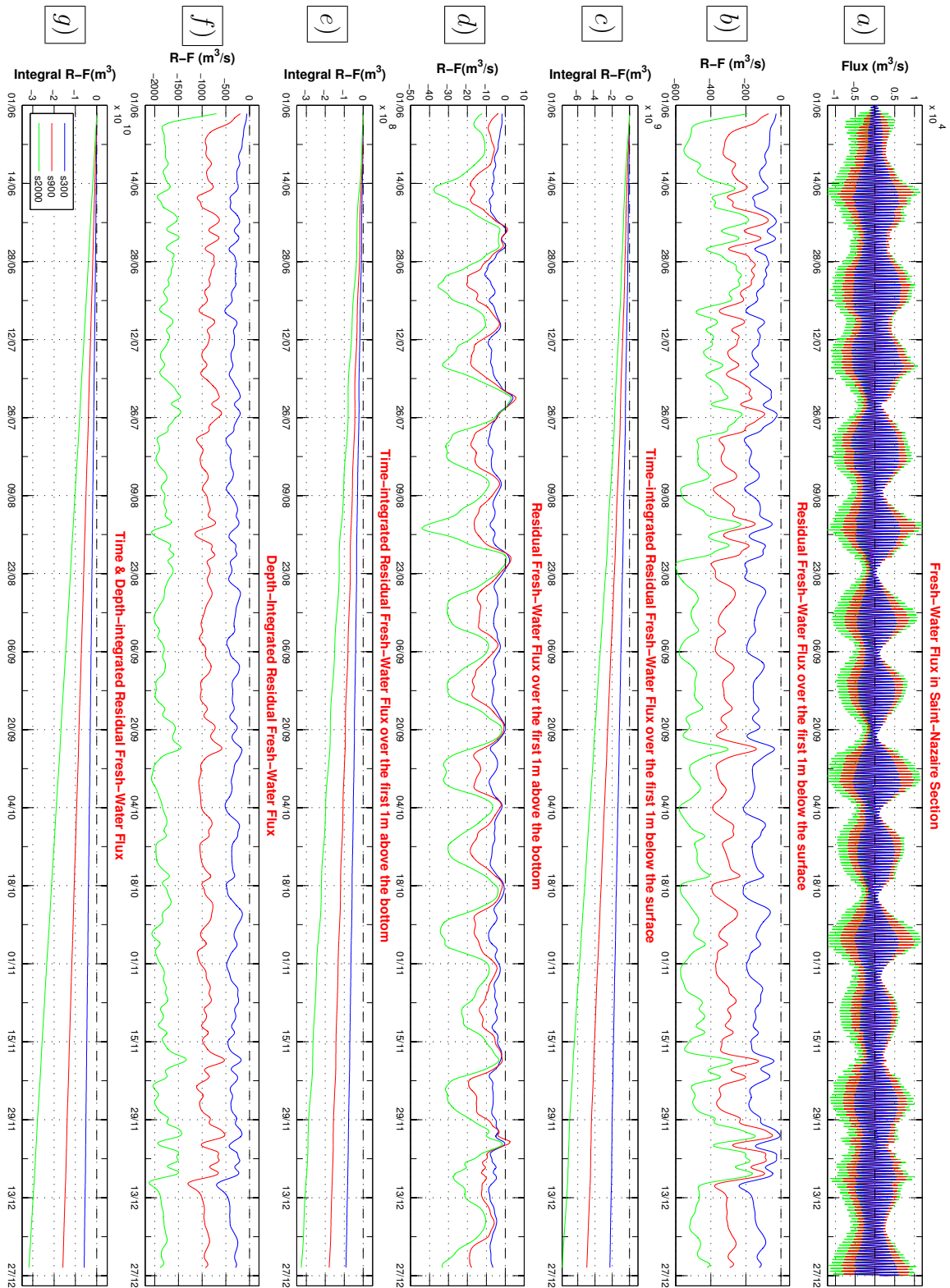


Figure 4.28: Fresh-Water exchange in the St-Nazaire north-section (deep), three simulations are shown; positive value means landward and the negative means seaward. The color coding is as follows:

- Blue: a semi-realistic situations with real meteorological conditions (wind, salinity, temperature), actual bathymetry and low flow (300, 20 m^3/s as constant discharges of Loire and Vilaine rivers).
- Red: a semi-realistic situations with real meteorological conditions (wind, salinity, temperature), actual bathymetry and average flow (900, 70 m^3/s as constant discharges of Loire and Vilaine rivers).
- Green: a semi-realistic situations with real meteorological conditions (wind, salinity, temperature), actual bathymetry and flood flow (2000, 180 m^3/s as constant discharges of Loire and Vilaine rivers).

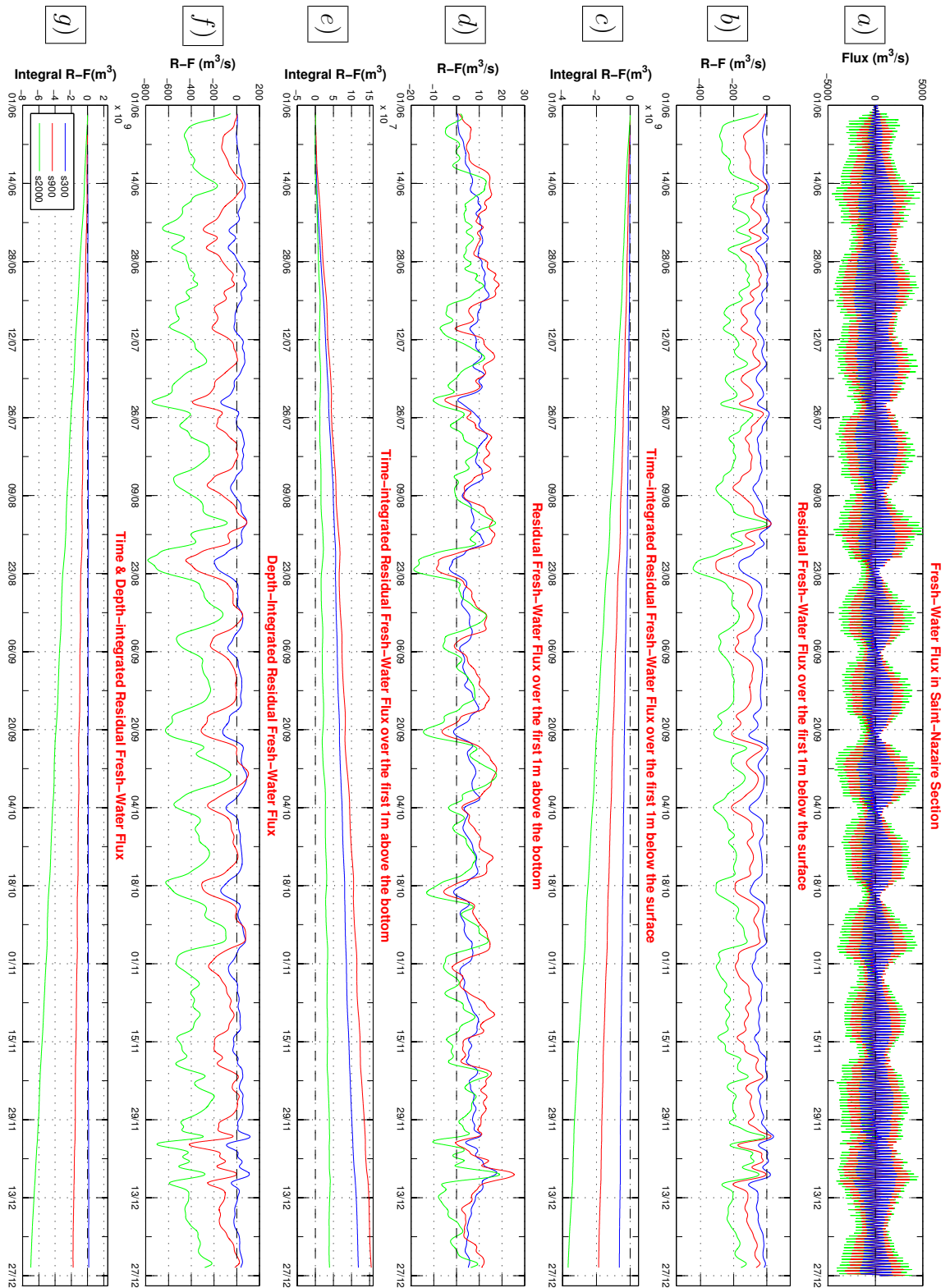


Figure 4.29: Fresh-Water exchange in the St-Nazaire south-section (shallow), three simulations are shown; positive value means landward and the negative means seaward. The color coding is as follows:

- Blue: a semi-realistic situations with real meteorological conditions (wind, salinity, temperature), actual bathymetry and low flow (300, 20 m^3/s as constant discharges of Loire and Vilaine rivers).
- Red: a semi-realistic situations with real meteorological conditions (wind, salinity, temperature), actual bathymetry and average flow (900, 70 m^3/s as constant discharges of Loire and Vilaine rivers).
- Green: a semi-realistic situations with real meteorological conditions (wind, salinity, temperature), actual bathymetry and flood flow (2000, 180 m^3/s as constant discharges of Loire and Vilaine rivers).

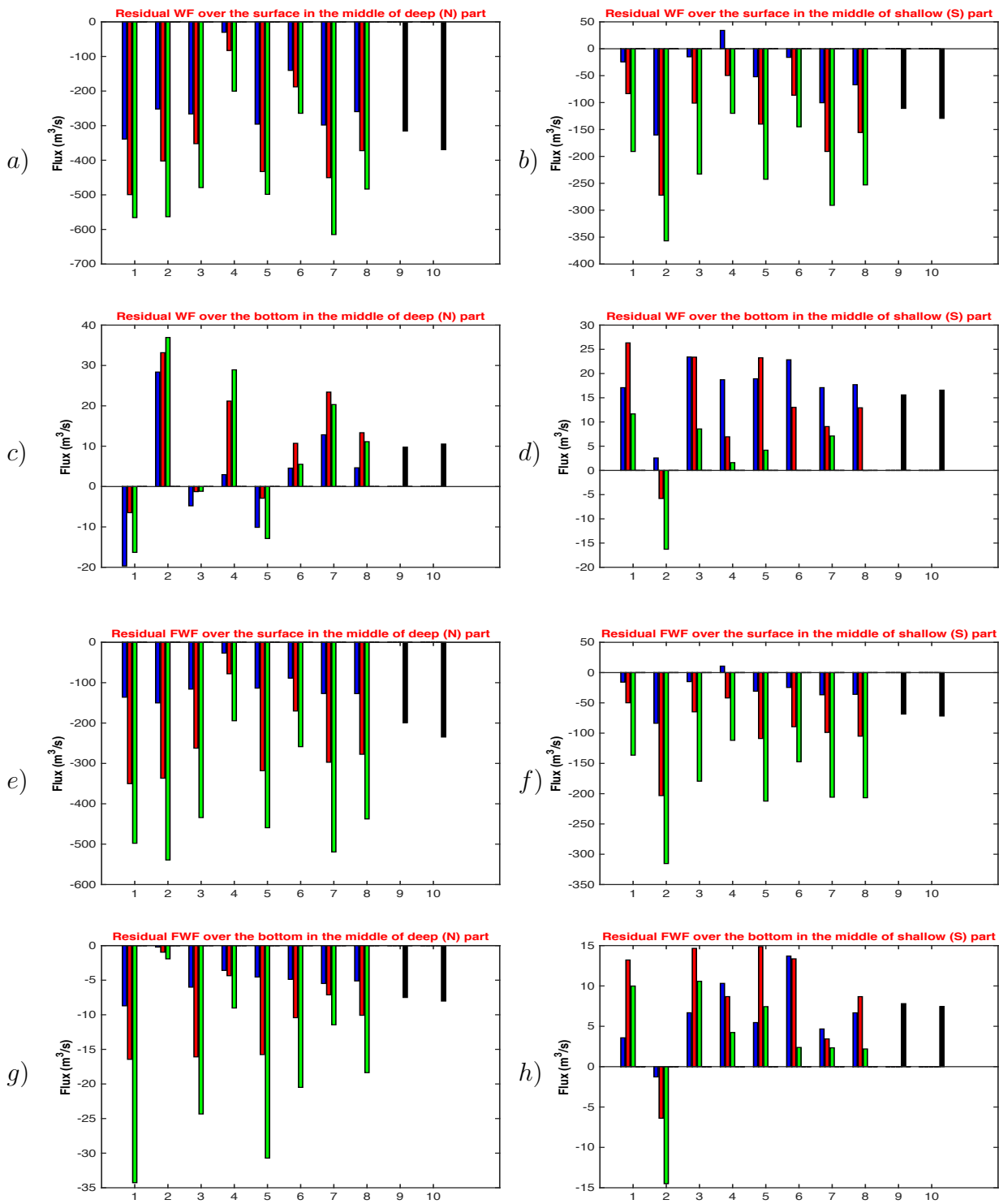


Figure 4.30: Water and freshwater exchanges in the St-Nazaire cross-section for 10 scenarios:

| | |
|--|--|
| 1) Spring tide without wind forcing (~Oct 26); | 6) West wind (July 7, ~mean tide); |
| 2) Neap tide without wind forcing (~Sep 20); | 7) East wind (Dec 17, ~mean tide); |
| 3) South wind (Jun 13, ~spring tide); | 8) Averaged over 7 months with real wind forcing; |
| 4) S-W wind (Jun 21, ~neap tide); | 9) Averaged over 7 months with real river regime and wind forcing; |
| 5) North wind (Sept 25, ~spring tide); | 10) Averaged over 7 months with real river regime but no wind forcing. |

The Fig. 4.30 synthesizes the residual fluxes of water and fresh water for different tide or wind scenarios and typical river regimes, in 4 different locations in the Saint-Nazaire cross-section: in the middle of northern subsection (deep) and in the middle of southern subsection (shallow), either near surface or near bottom. Scenarios are numbered from one to ten. The first two scenarios describe the tidal residual flux, scenarios 3 to 7 show the effect of typical wind. Scenarios 1 to 8 consider 3 steady river regimes (low: $300 \text{ m}^3/\text{s}$, mean: $900 \text{ m}^3/\text{s}$ and high river discharge $2000 \text{ m}^3/\text{s}$ respectively, in blue, red and green). The 8th scenario averages the effect of tide and real wind over 7 months, while the last two scenarios consider the real river discharge in 2007, either without wind (scenario 10) or with actual wind forcing (scenario 9). Each value is computed as the average of Water Flux (WF) or Fresh Water Flux (FWF) passing through one mesh in a given period of time over which the wind forcing is approximatively steady (scenarios 1 to 7) or not (scenarios 8 to 10). Values are positive when fluxes are upwards.

Many features can be deduced from this figure, in agreement with the time series presented before, but in a more synthesized way. Comparing scenarios 8 and 9 of Fig. 4.30, it appears that fluxes through the St-Nazaire section of the Loire Estuary, accounting for river flow variations, look like fluxes obtained with a medium steady river flow, whatever the type and location of flux is considered.

This reinforces the significance of analyses of steady river flow situations presented in the previous section. In addition, the strong analogy between the long term results (7 months, whose forcing variations have been demonstrated to be representative in Sec. 4.1) obtained when accounting for wind forcing or not indicates that on long term, the wind forcing does not influence the time-averaged fluxes (scenarios 9 and 10 in Fig. 4.30). A contrast between neap and spring tide results shows that the tidal forcing strongly amplifies fluxes.

In the northern sub-section, fluxes near the surface do not differ from spring to neap, but bottom water fluxes are clearly seawards on spring, and strongly upwards on neap, whatever the river regime. The latter has more influence on fresh water fluxes, which are strongly seawards near the surface as well as near the bottom on spring but also near the bottom on neap tides (with very small values). Considering the southern sub-section, total water fluxes and freshwater fluxes are seawards over the whole column on neap tide, but on spring they are clearly upwards near the bottom.

Scenarios 3 to 7 give ideas of wind influence on these fluxes. Near the surface, only southwest and west winds (scenarios 4 and 6) seem to influence fluxes, reducing the export of water (in case of low river flow, an import of fresh water is even observed for a SW wind (scenario 4)). Near the bottom, it appears difficult to identify the influence of wind, because fluxes are strongly influenced by the tidal amplitude (and finally not so much by wind direction).

4.4.2 Evolution of Water Flux in Saint-Nazaire section following the change of bathymetry after engineering works in 1984's

The estuarine circulation which consists of a seawards water flux near surface and an upwards water flux near bottom downstream the salinity intrusion is proportional to the square of the water height (Hir, 1980). Then deepening the channel is likely to enhance the estuarine circulation and reinforce the bottom residual flow.

In order to analyse a possible consequence of the navigation channel deepening between St-Nazaire and Donges around 1984, two specific simulations have been run. Both consider the river regime variations and other realistic forcing of the year 2007, but with the present-day bathymetry or with a simplified bathymetry before 1984, schematized by a smaller water depth in the navigation channel (actually the upper bed elevation is 9 m below low-water level instead of 13 m nowadays) (Fig. 4.31). In figures 4.32, 4.33 and 4.34, the results of these simulations are presented in red (channel depth before 1984) and green (channel depth after 1984). In order to compare with results previously presented, results with the present-day bathymetry, but a steady river regime [average river flow for Loire ($900 \text{ m}^3/\text{s}$) and Vilaine ($70 \text{ m}^3/\text{s}$)], already presented in the previous section are reminded by blue curves.

Fig. 4.32, 4.33 and 4.34 present the time evolution of fresh water fluxes (FWF) in the whole St-Nazaire section (see Fig. 4.32), in the northern/deep subsection (Fig. 4.33) and in the shallow/southern subsection (Fig. 4.34).

Considering the whole section, FWF do not change near the surface (Fig. 4.32b & c), nor after depth-integrating (Fig. 4.32f & g), but near bottom, fluxes are qualitatively modified, although their intensity is very low: it appears that after dredging, the time-integrated bottom FWF are clearly upwards the estuary, while they were nearly null before (Fig. 4.32e).

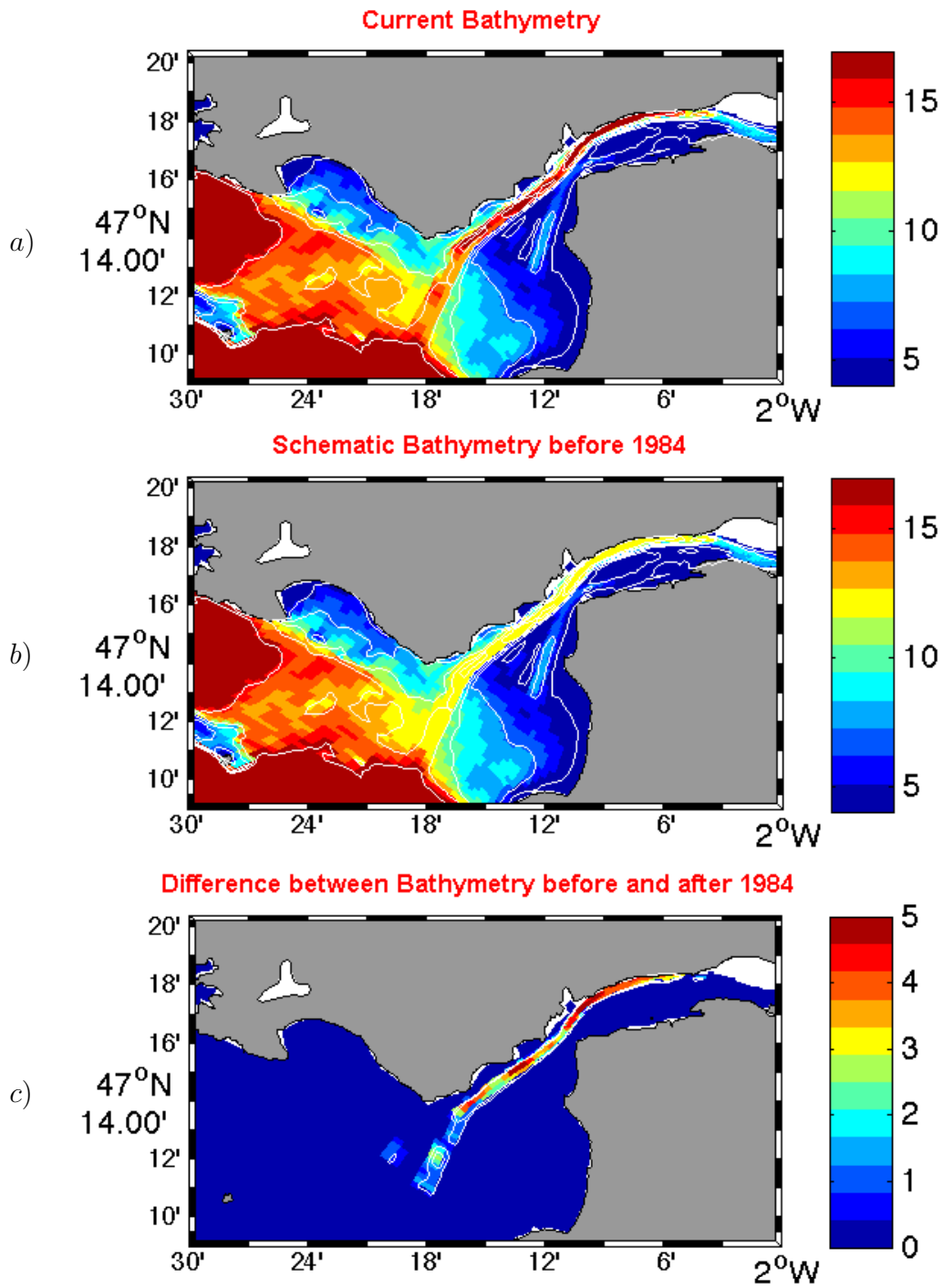


Figure 4.31: a) Actual bathymetry in St-Nazaire section, b) Schematic Bathymetry in St-Nazaire section before the engineering works in 1984, c) difference between bathymetry before and after 1984

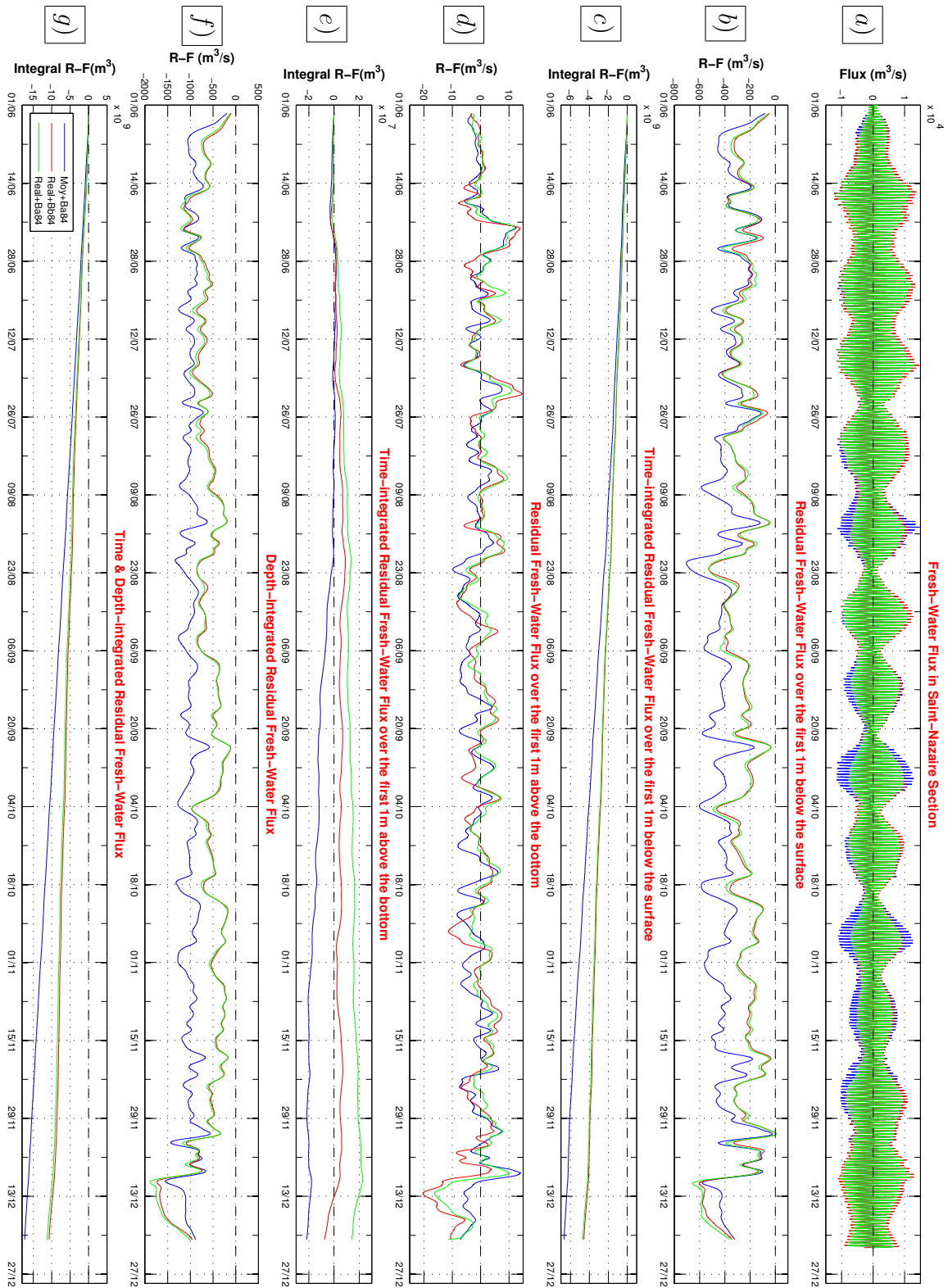


Figure 4.32: Fresh water exchange in the Saint-Nazaire cross-section, three simulations are shown. The color coding is as follows:

- Blue: mean outflow of Loire ($900 \text{ m}^3/\text{s}$) and Vilaine ($70 \text{ m}^3/\text{s}$), wind, and present day bathymetry are taken into account.
- Red: real outflow of both rivers, wind; bathymetry in principal channel which is 3 meter higher than nowadays and represents the depth before channel dredging. Here, maximum depth of main channel is 9m.
- Green: a semi-realistic situations such as real meteorological conditions, river discharges, and present day bathymetry are the elements taken into account here.

The effect of channel deepening on the FWF is more sensitive when splitting the section into the northern and the southern parts. In the former (Fig. 4.33), the bottom flux is clearly shifted upwards (Fig. 4.33d & e), as suspected from the theory, but also the surface flux is slightly shifted upwards, so that the seawards depth-integrated fresh water flux is attenuated. On the opposite, bottom and surface FWF are shifted downwards in the southern channel, as well as the depth-integrated fresh water flux. Differences between the northern and the southern subsections nearly compensate, in agreement with the very low change of FWF for the whole St-Nazaire section.

This means that a slight shearing of fresh water fluxes would have occurred after channel deepening, with a trend for upwards shift of the flux in the northern subsection, and a downwards shift in the southern one. It should be noticed that these differences remain low, and much lower than the effect of tides and river regime change (*i.e.* the differences between the blue and green curves in Fig. 4.33g and 4.34g), or even less than the effect of the wind: nevertheless, these differences are steady. In addition, as the bottom flux is more strongly altered, the bottom current is likely to have increased in the upwards direction after dredging and changed the sediment flux with an intensity that does not vary linearly with the flow. An opposite trend could be obtained in the southern subsection, but probably with smaller velocities. A specific attention should be paid to these features as far as sediment transport is concerned.

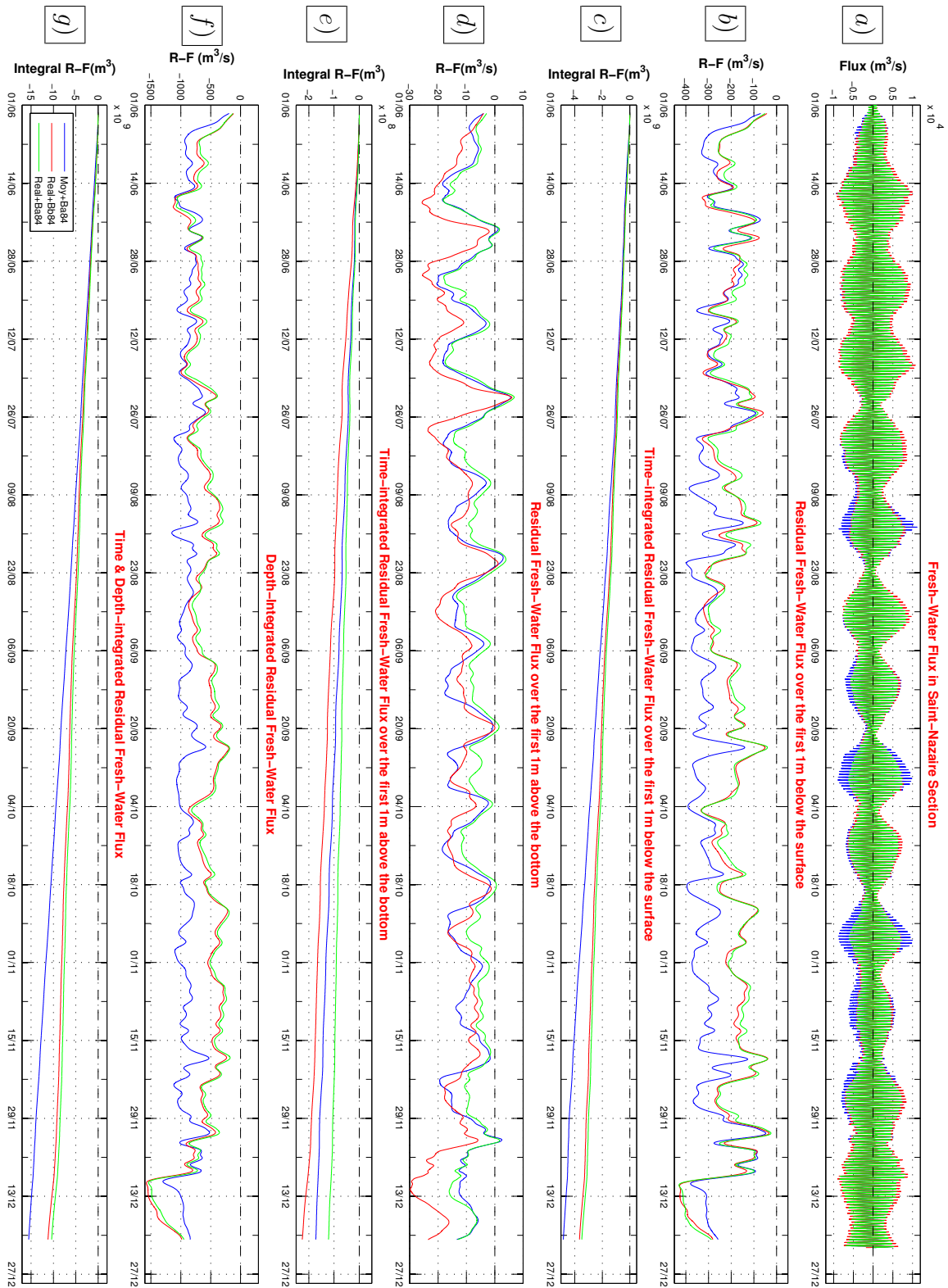


Figure 4.33: Fresh water exchange in the deep sub-section in St-Nazaire. The color coding is as follows:
 -Blue: mean outflow of Loire (900 m³/s) and Vilaine (70 m³/s), wind, and present day bathymetry are taken into account.

-Red: real outflow of both rivers, wind; bathymetry in principal channel which is 3 meter higher than nowadays and represents the depth before channel dredging. Here, maximum depth of main channel is 9m.

-Green: a semi-realistic situations such as real meteorological conditions, river discharges, and present day bathymetry are the elements taken into account here.

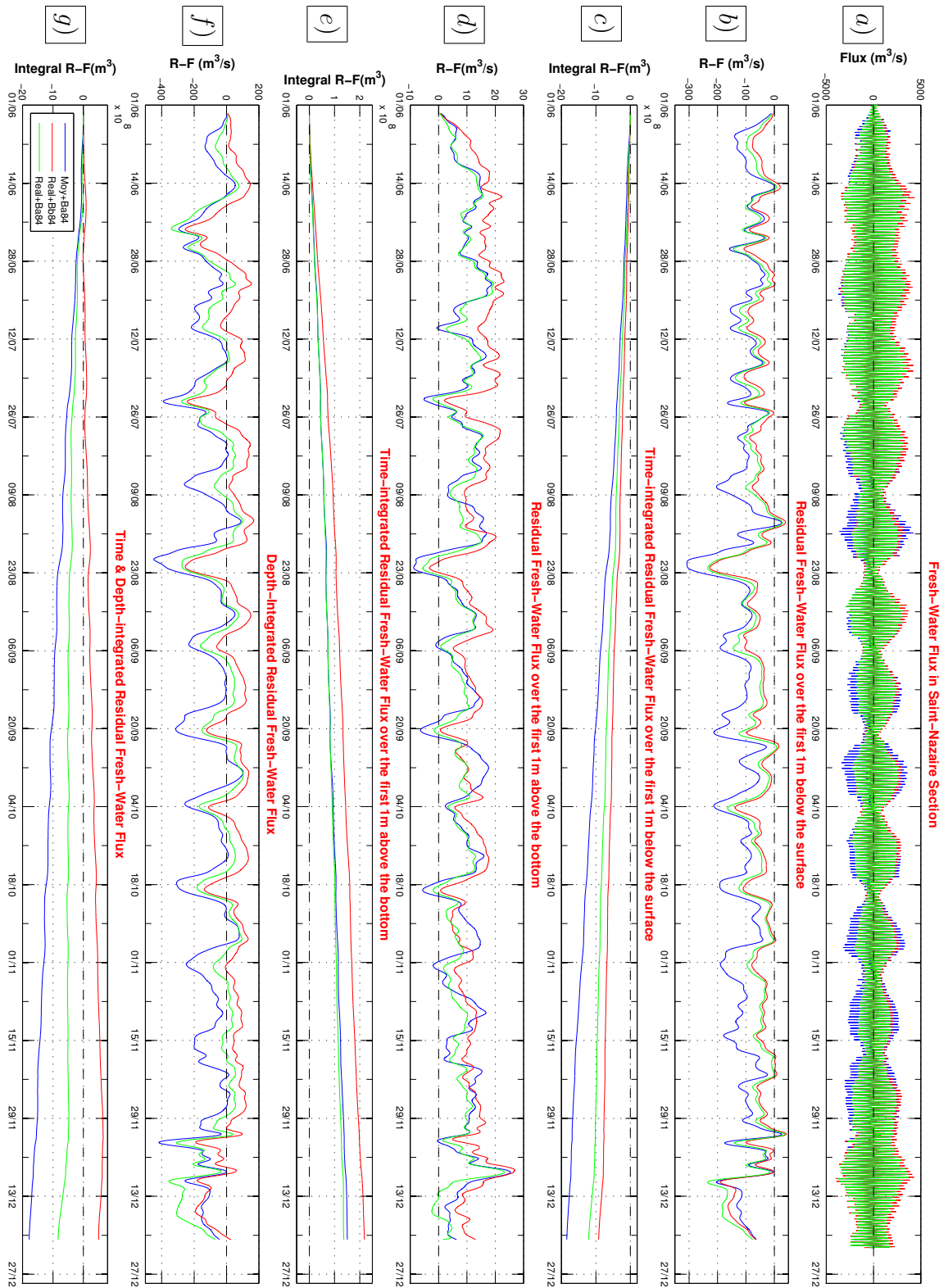


Figure 4.34: Fresh water exchange in the shallow sub-section in St-Nazaire. The color coding is as follows:
 -Blue: mean outflow of Loire (900 m³/s) and Vilaine (70 m³/s), wind, and present day bathymetry are taken into account.
 -Red: real outflow of both rivers, wind; bathymetry in principal channel which is 3 meter higher than nowadays and represents the depth before channel dredging. Here, maximum depth of main channel is 9m.
 -Green: a semi-realistic situations such as real meteorological conditions, river discharges, and present day bathymetry are the elements taken into account here.

4.5 Water fluxes entering the bay of Bourgneuf

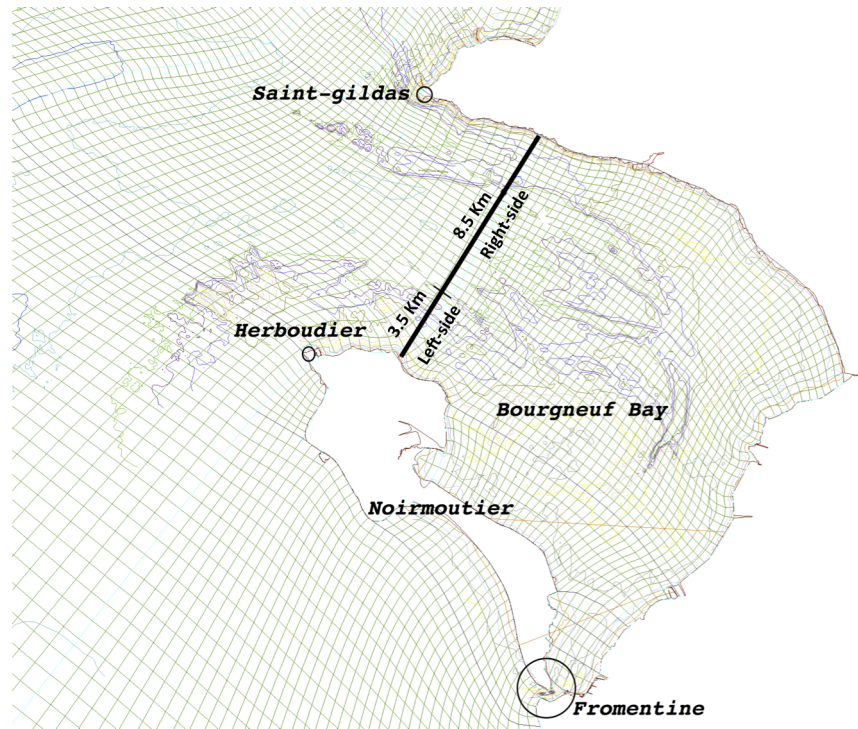


Figure 4.35: Bourgneuf section divided into the left (3.2 Km) and right (8 Km) subsections.

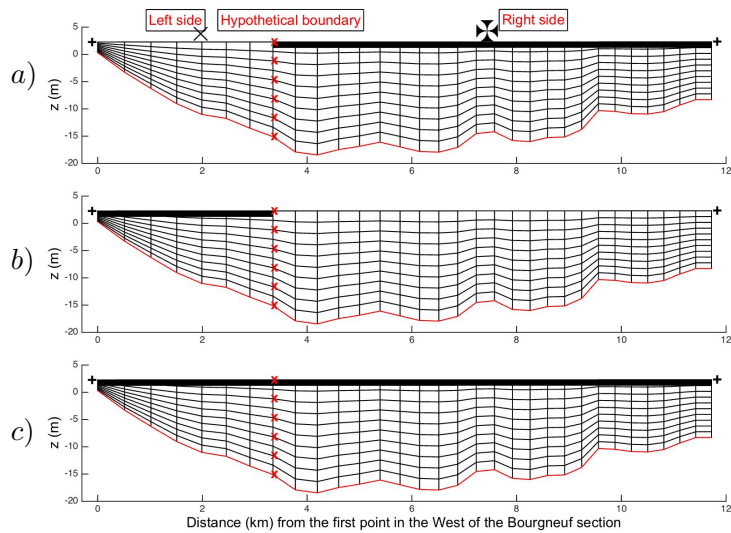


Figure 4.36: Schematic view of the cross-section in which (Fresh) Water Flux is calculated over the first 1m below the surface in Bourgneuf section (two point indicated by \times and \boxtimes are chosen for the vertical profiles of hydrological characteristics):

- a) Flux computed over the surface of right sub-section
- b) Flux computed over the surface of left sub-section
- c) Flux computed over the surface of overall section.

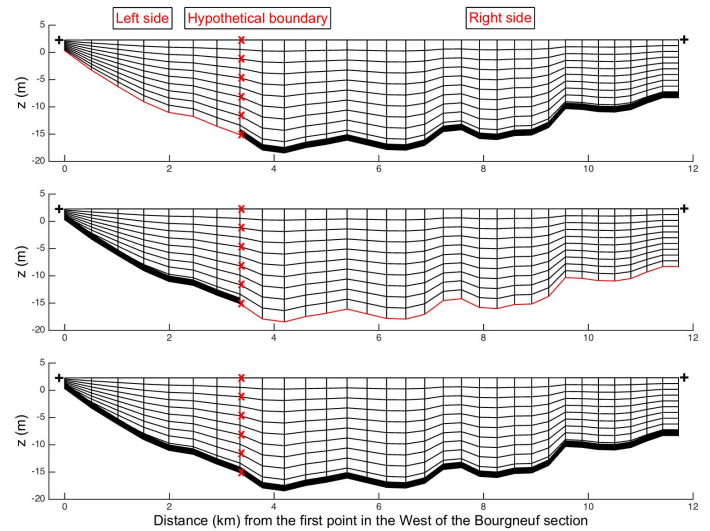


Figure 4.37: Schematic view of the cross-section in which (Fresh) Water Flux calculated over the first 1m above the bottom in Bourgneuf section:

- a) Flux computed over the bottom of right sub-section
- b) Flux computed over the bottom of left sub-section
- c) Flux computed over the bottom of overall section.

The Bourgneuf section, provides insights on the impact of estuarine waters in the Bay of Bourgneuf (*e.g.* nutrients, contaminants, fine particles). Defined between St-Gildas and L'Herbaudière point with a length of 11.2 km, this section is used to address the principal exchange between the Loire Estuary and Bourgneuf Bay. It is important to notice that there is a strait between Noirmoutier Island and the coast, near Fromentine in the south of this bay which has been taken into account for the model but not considered in this discussion.

The cross-section is represented in Fig. 4.35, 4.36 and 4.37. Regarding the residual circulation scheme at a regional scale (Fig. 1.15 issues from Lazure et Salomon, (1991)), we choose to split the section into two subsections, the South-West ("left" side) one, and the North-East ("right" side) one. The NE part is about 2.5 times larger and also deeper.

Vertical profiles analysis in Bourgneuf section

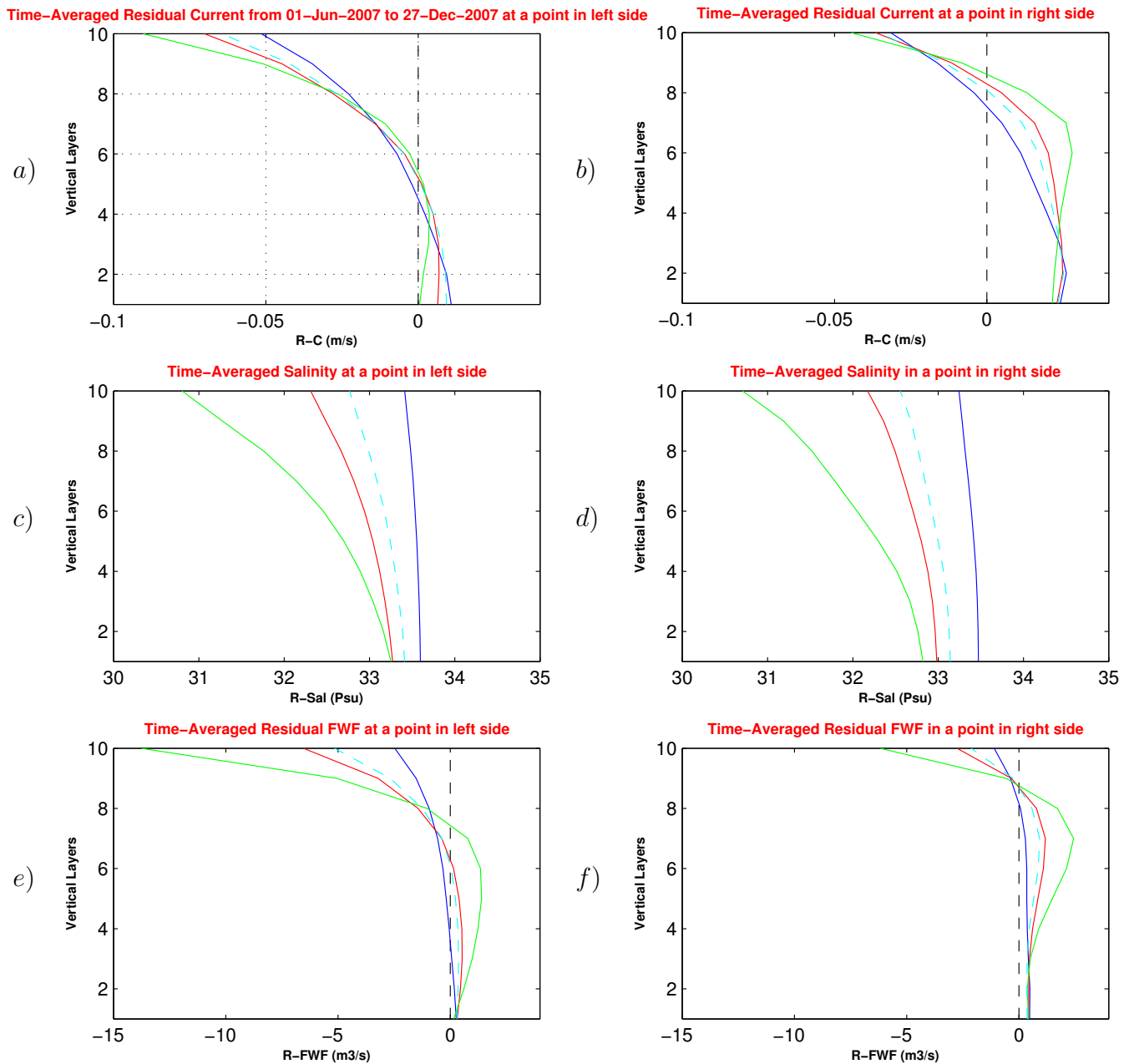


Figure 4.38: Representative vertical profiles of hydrological characteristics across the Bourgneuf section, averaged over seven months. Left hand side; Right hand side. a) and b) Residual current; c) and d) Time-averaged salinity; e) and f) Time-averaged residual Fresh water Fluxes. Colors correspond to the different river discharges (blue: low, red: mean, green: high and cyan/dashed: real). Positive fluxes or currents are oriented off the bay.

Residual currents, time-averaged salinity and FWF profiles in the middle of each subsection (locations are indicated by symbols in Fig. 4.36) are presented in Fig. 4.38. Salinity profiles are moderately stratified on both locations, but residual flow profiles show a water entrance near the surface and an opposite mean current in bottom layers, more developed in the NE subsection.

As a consequence, FWF is clearly oriented towards the bay near the surface (especially near Noirmoutier Island) and off the bay in bottom or intermediate layers, especially in the middle of the NE subsection. The fresh water exchanges are nearly linearly dependent on the Loire River discharge.

4.5.1 Water Flux in bourgneuf section (overall)

Water flux variations can be analyzed through Fig. 4.39 for the whole section and Fig. 4.40 and 4.41 for the SW and NE subsections respectively. A net inflow of water through the section appears clearly in Fig. 4.39g, which implies a similar net outflow towards the open sea through the straight between Noirmoutier Island and the continent, south of the bay. These fluxes seem independent of the Loire river regime, but are related to the tidal amplitude and can vary with meteorological events (Fig. 4.39f). In average, they amount to $\sim 400 \text{ m}^3/\text{s}$.

The comparison between time-integrated residual fluxes near surface and near bottom show a clear opposition between them, in agreement with flux profiles previously commented: the entrance near the bay is somehow related to the Loire river regime, but not as much as the outflow through the bottom layers, indicating that stratifications are not clearly or not only induced by the river regime. Looking at the variations of these tidal residual fluxes, one notices that the Loire River's discharge seems to amplify the effects of the wind. Looking at the flux variations according to time (Fig. 4.39b), it can be said that the winds which blow from the North, West and specially North-West (26/06) intensifies water mass getting into the area through this section, and the winds from South, East and Particularly South-East (19/12) tend to reduce or even inverse the water entrance (see the interval 29/11 till 27/12 in Fig. 4.39b). The rate of residual water flux (RWF) in the first meter above the bottom level is strongly influenced by the tidal regime in a way that during neap tide the RWF can enter the bay (*e.g.* neap tides from mid-August up to mid-November) while it is clearly oriented off the bay on spring tides (Fig. 4.39d).

Fig. 4.39e shows that the RWF over the lower layer in the long period (during 7 months) is outward in opposite to the upper layer. An interesting point is the influence of Loire discharge: when it is high, simultaneously the entering flux in surface layer is increased and the outflow in bottom layers is attenuated, inducing a likely larger flow from the north to the bay, which is not confirmed by depth-integrated fluxes (4.39 f & g). This means that opposite trends occur in intermediate layers, where a residual flux to the North should be reinforced by high Loire river discharge, as shown in Fig 4.38a & b.

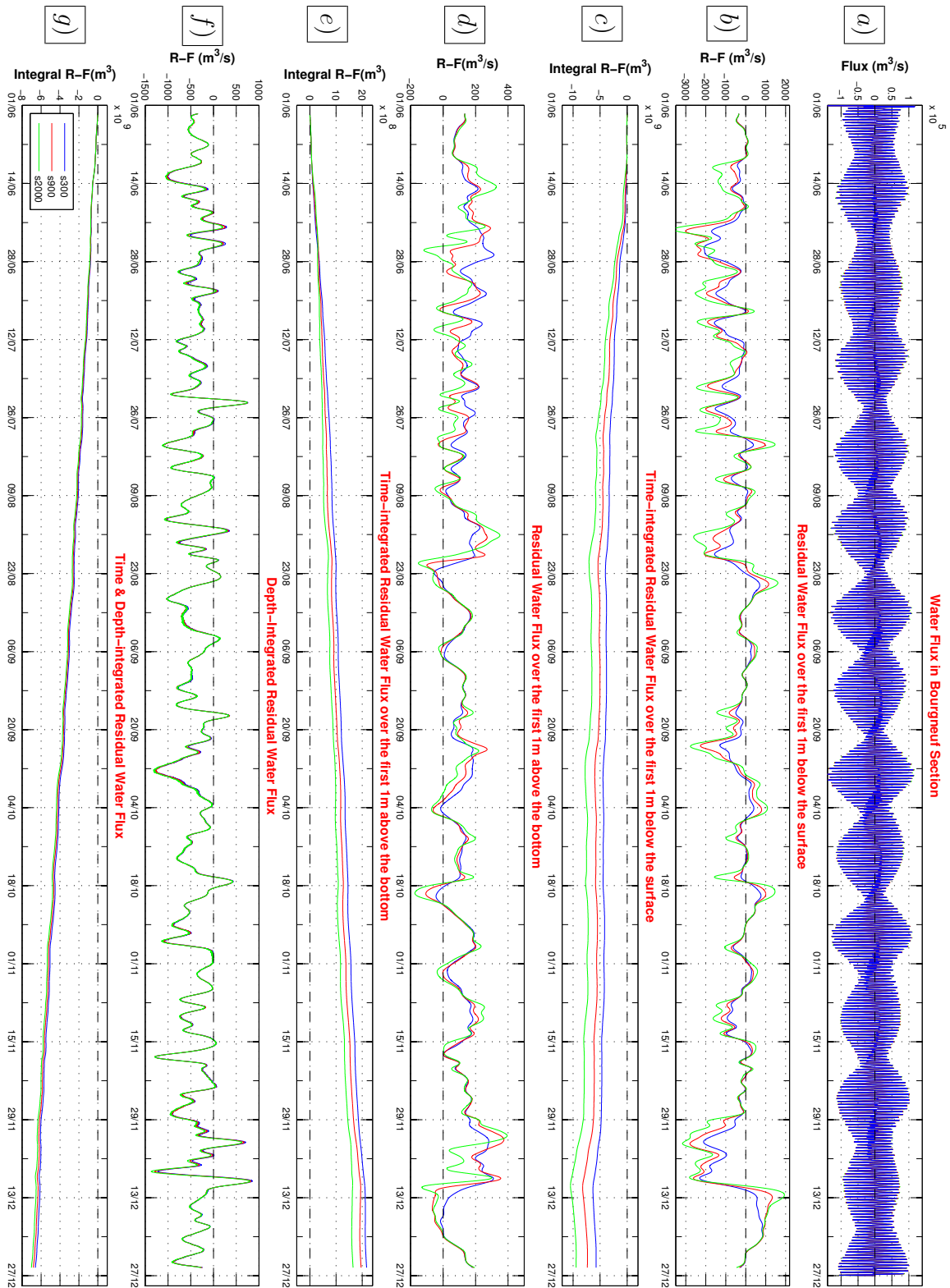


Figure 4.39: Water exchange in the Bourgneuf cross-section, three simulations are shown. The positive value means outward and the negative indicates inward current flux. The color coding is as follows:

- Blue: a semi-realistic situations with real meteorological conditions (wind, salinity, temperature), actual bathymetry and low flow (300, 20 m^3/s as constant discharges of Loire and Vilaine rivers).
- Red: a semi-realistic situations with real meteorological conditions (wind, salinity, temperature), actual bathymetry and average flow (900, 70 m^3/s as constant discharges of Loire and Vilaine rivers).
- Green: a semi-realistic situations with real meteorological conditions (wind, salinity, temperature), actual bathymetry and flood flow (2000, 180 m^3/s as constant discharges of Loire and Vilaine rivers).

4.5.2 Water Flux in SW (left) and NE (right) subsections of Bourgneuf Bay

According to Fig. 4.40a and 4.41a, water fluxes are about five times larger in the NE subsection than in the SW one. As a consequence the global circulation in this NE subsection looks like the circulation across the whole section (Fig. 4.41 & 4.39). But results in the SW subsection reveal different trends. Near surface (Fig. 4.40b & c), the variation according to the Loire river regime is much larger, and for low river discharge, the residual flux is even oriented outward the bay, contrary to the one on high river flow.

The effect of wind is also more obvious, with a south-eastward flux during the first period of westerly winds until August 20th (Fig. 4.7) and then an outward flux until end of November, in relation with NE winds (Fig. 4.40c). Near bottom in this subsection close to Noirmoutier Island, it is striking that neither the wind nor the Loire River regime influence water fluxes, while a strong influence of tides is observed: the residual flux is nearly zero on neap, and clearly northward on spring. Despite the small width of this subsection, the residual bottom water flux has nearly the same intensity as in the NE subsection, but in a different direction, revealing a tide-induced clockwise eddy at the scale of the Bourgneuf Bay.

These bottom residual circulations may have important consequences on the fine sediment budget in the bay of Bourgneuf: even if fine particles are brought from the Loire by surficial waters, they are likely expelled northward when reaching bottom layers, which would prevent or slow the infilling of the bay.

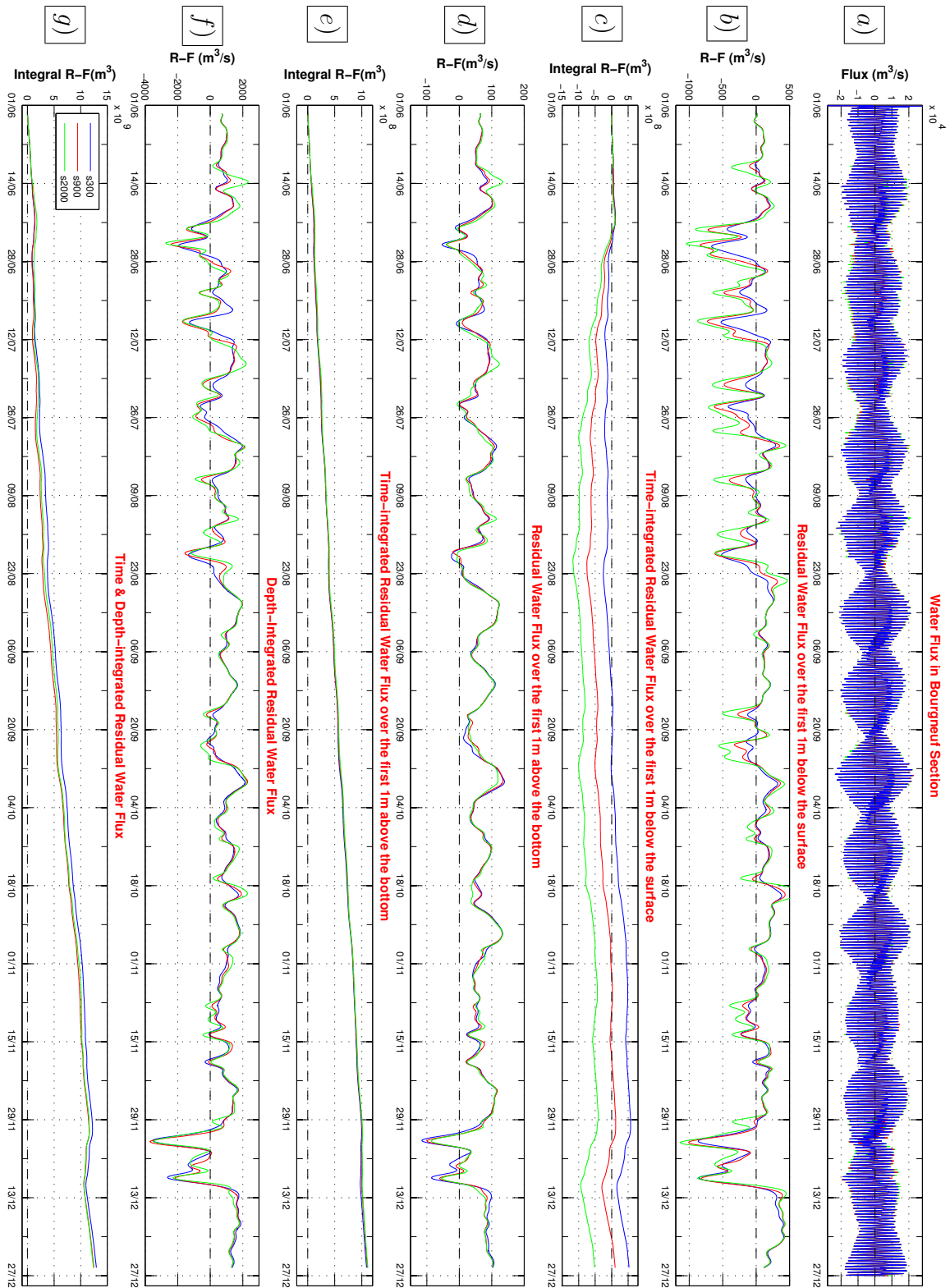


Figure 4.40: Water exchange in the Bourgneuf SW sub-section, three simulations are shown. The positive value means outward and the negative indicates inward current flux. The color coding is as follows:

- Blue: a semi-realistic situations with real meteorological conditions (wind, salinity, temperature), actual bathymetry and low flow (300, 20 m³/s as constant discharges of Loire and Vilaine rivers).
- Red: a semi-realistic situations with real meteorological conditions (wind, salinity, temperature), actual bathymetry and average flow (900, 70 m³/s as constant discharges of Loire and Vilaine rivers).
- Green: a semi-realistic situations with real meteorological conditions (wind, salinity, temperature), actual bathymetry and flood flow (2000, 180 m³/s as constant discharges of Loire and Vilaine rivers).

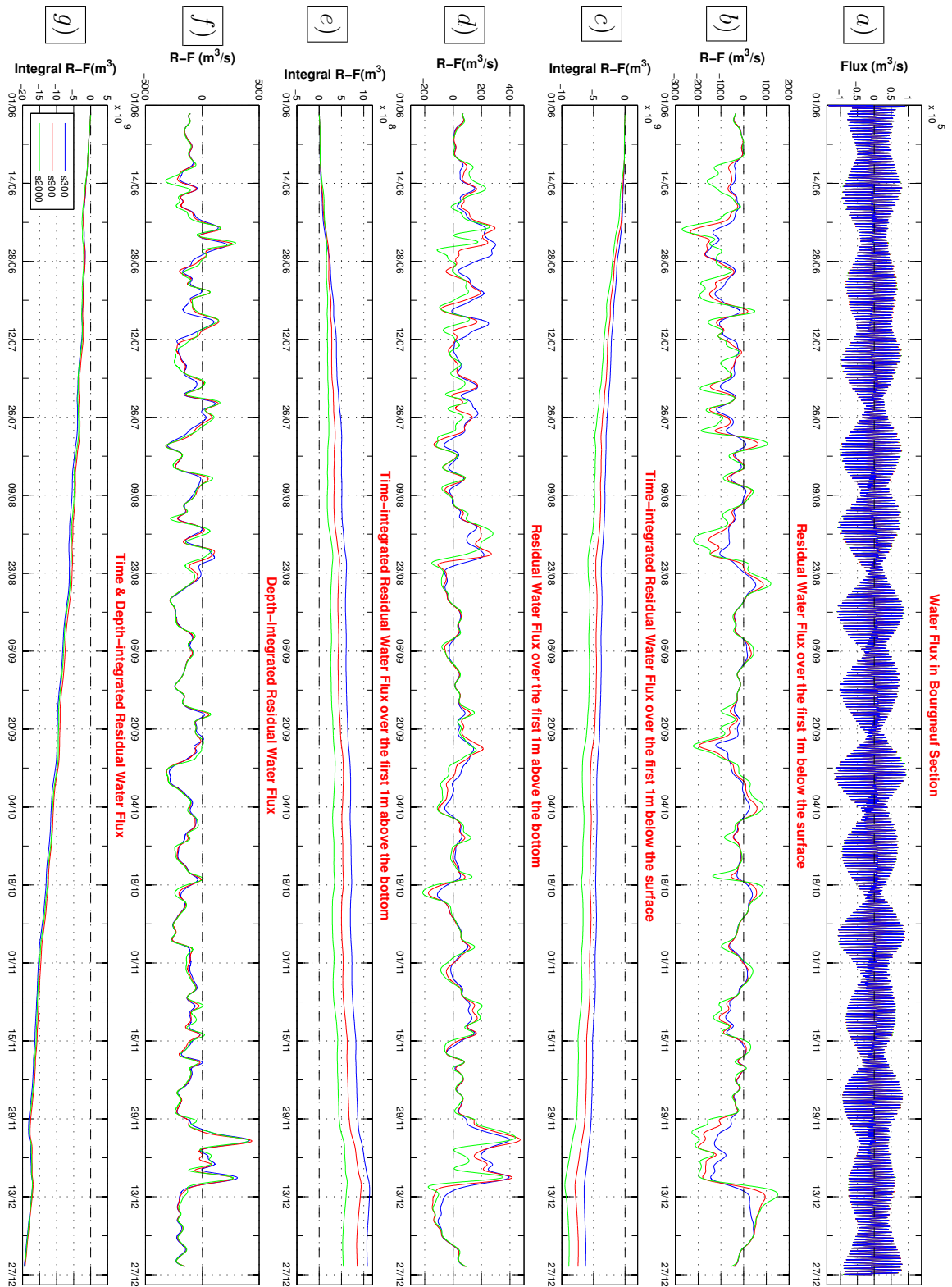


Figure 4.41: Water exchange in the Bourgneuf NE sub-section, three simulations are shown. The positive value means outward and the negative indicates inward current flux. The color coding is as follows:

- Blue: a semi-realistic situations with real meteorological conditions (wind, salinity, temperature), actual bathymetry and low flow (300, 20 m^3/s as constant discharges of Loire and Vilaine rivers).
- Red: a semi-realistic situations with real meteorological conditions (wind, salinity, temperature), actual bathymetry and average flow (900, 70 m^3/s as constant discharges of Loire and Vilaine rivers).
- Green: a semi-realistic situations with real meteorological conditions (wind, salinity, temperature), actual bathymetry and flood flow (2000, 180 m^3/s as constant discharges of Loire and Vilaine rivers).

4.5.3 Fresh-Water Flux in Bourgneuf section

In this section, in order to clarify the influence of the Loire outflow on the 3d circulation in the Bay of Bourgneuf, we consider fresh water fluxes. In Fig. 4.42a, sharp increases of freshwater volumes exchanged through the cross-section at the entrance of Bourgneuf Bay can be noticed, nearly independently of the tide amplitude (*e.g.* from 28/06 to 12/07, 26/07 to 02/08, 27/09 and 06/12 to 13/12).

These fresh water exchanges logically vary with the Loire river flow. According to Fig. 4.1, the periods in which freshwater exchanges are intensified occur mainly when the wind direction is from the SW (*e.g.* before 28/06, around 26/07). The magnitude of exchange even seems intensified when the wind rotates from the SW to the NW or N, as it can be noticed on 05/07 and more specifically on 06/12 (Fig. 4.42a).

Referring to Fig. 4.42b, it is clear that the major factor of FWRP variations near surface in this section is the rate of Loire outflow, while the wind force plays as a resonator of exchange: for instance, on 25/06, the difference of RFPF in the surface layer (1m) between low and high flow reaches 1200 m³/s. Part 'c' of the same figure, which represents the time-integrated RFPF over 1 meter below surface, confirms that in superficial layer, the Loire discharge has crucial influence (quasi linear) on the rate of freshwater exchanges, while near bottom its effect is negligible.

As previously mentioned, a major factor in determining the rate and direction of RFPF exchanges is the wind forces while the variations of Loire discharge have also an amplifying effect on the exchanges. It can be seen in Fig. 4.42 that in the predominant cases where FWF through the surface layer are inward (with negative value on the graph) very often residual fluxes are in the opposite direction through bottom layers. It should be noted that salinities of surface and bottom waters are not the same (see Fig. 4.38).

Thus the inward waters over the surface layers, connected to the Loire plume, have generally lower salinity than the outward ones closer to the bottom, which amplifies the contrast between residual fluxes in surface and bottom layers when considering the fresh water content. When superimposing the wind forcing (Fig. 4.1-4) and the residual fresh water flux (Fig. 4.42b), it appears clearly that westerly winds are responsible for the input of fresh water through the upper meter, whatever the North-South component.

For identifying the influence of Loire discharge on RFPF and RFPF respectively, we computed an indicator R_v (Eq. 4.1) defined as the ratio between the time-integrated value of RFPF

after 7 months through the surface first meter¹ and the through the first meter above bottom².

$$R_v = \frac{\text{Time integrated RWF or RFWF over the first 1m below the surface}}{\text{Time integrated RWF or RFWF over the first 1m above the bottom}} \quad (4.1)$$

R_v values are computed for both water exchanges and fresh water exchanges, considering the three Loire river regimes. Results are given in the following table:

| Loire discharge | 300 m3/s | 900 m3/s | 2000 m3/s |
|-----------------|----------|----------|-----------|
| Rv total water | 2.8 | 3.7 | 5.8 |
| Rv fresh water | 3.7 | 8.8 | 20.3 |

Table 4.1: (Fresh) Water Flux in Bourgneuf during 01/Jun-28/Dec.

Comparing R_v values in RWF and RFWF shows that during the low discharge of Loire River the exchange of total water and FW have the same order of magnitude. On the other hand, RFWF are remarkably higher than RWF during mean and high flow of Loire. The results obtained in this section can give us a better understanding of how potential pollutants disperse in the area.

The lighter contaminants that remain in superficial layers disperse mostly toward the center of the Bay and may go out through the Fromentine strait (see Fig. 4.35) while pollutants which density is higher than the water density are likely to get out of the bay through its northern entrance mainly through bottom layers and close to L'Herbaudière point (see Fig. 4.35).

In order to summarize results on exchanges through the Bourgneuf section, water and fresh water exchanges are given for typical scenarios in two locations, one close to Noirmoutier island (Fig. 4.40), the other one in the middle of the NE subsection (Fig. 4.36 & 4.37). In the same way it has been presented for the Saint-Nazaire section, the results are shown in Fig. 4.43.

¹Current velocity over the 1th meter below surface is assumed the same as the value computed in the first Sigma layer (vertical discretization).

²Current velocity over the 1th meter above bottom is achieved by computed from the velocity in the lower Sigma layer (vertical discretization) by integrating over the last meter.

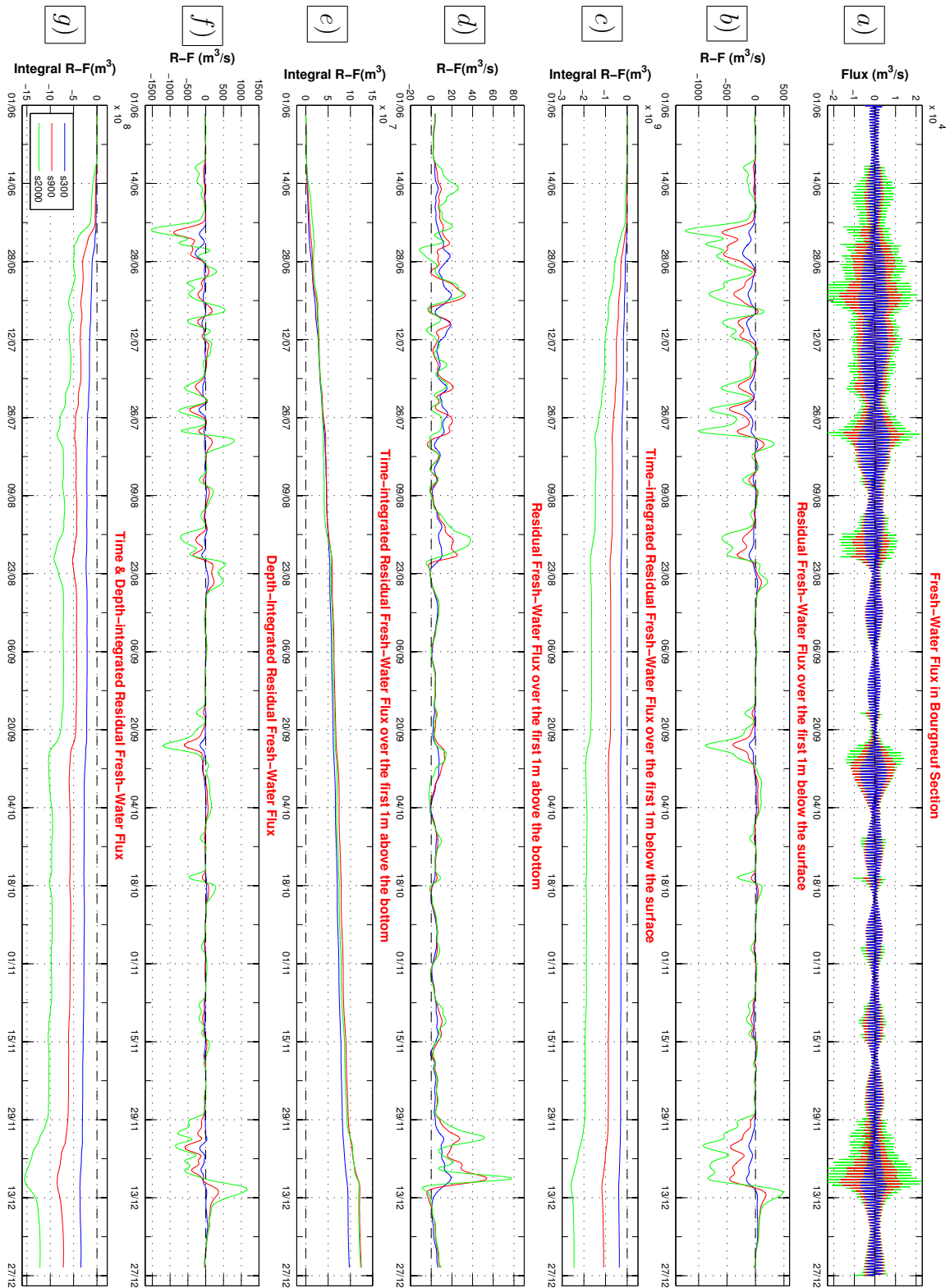


Figure 4.42: Fresh-Water exchange in the Bourgneuf cross-section, three simulations are shown. The positive value means outward and the negative indicates inward current flux. The color coding is as follows:

- Blue: a semi-realistic situations with real meteorological conditions (wind, salinity, temperature), actual bathymetry and low flow (300, 20 m^3/s as constant discharges of Loire and Vilaine rivers).
- Red: a semi-realistic situations with real meteorological conditions (wind, salinity, temperature), actual bathymetry and average flow (900, 70 m^3/s as constant discharges of Loire and Vilaine rivers).
- Green: a semi-realistic situations with real meteorological conditions (wind, salinity, temperature), actual bathymetry and flood flow (2000, 180 m^3/s as constant discharges of Loire and Vilaine rivers).

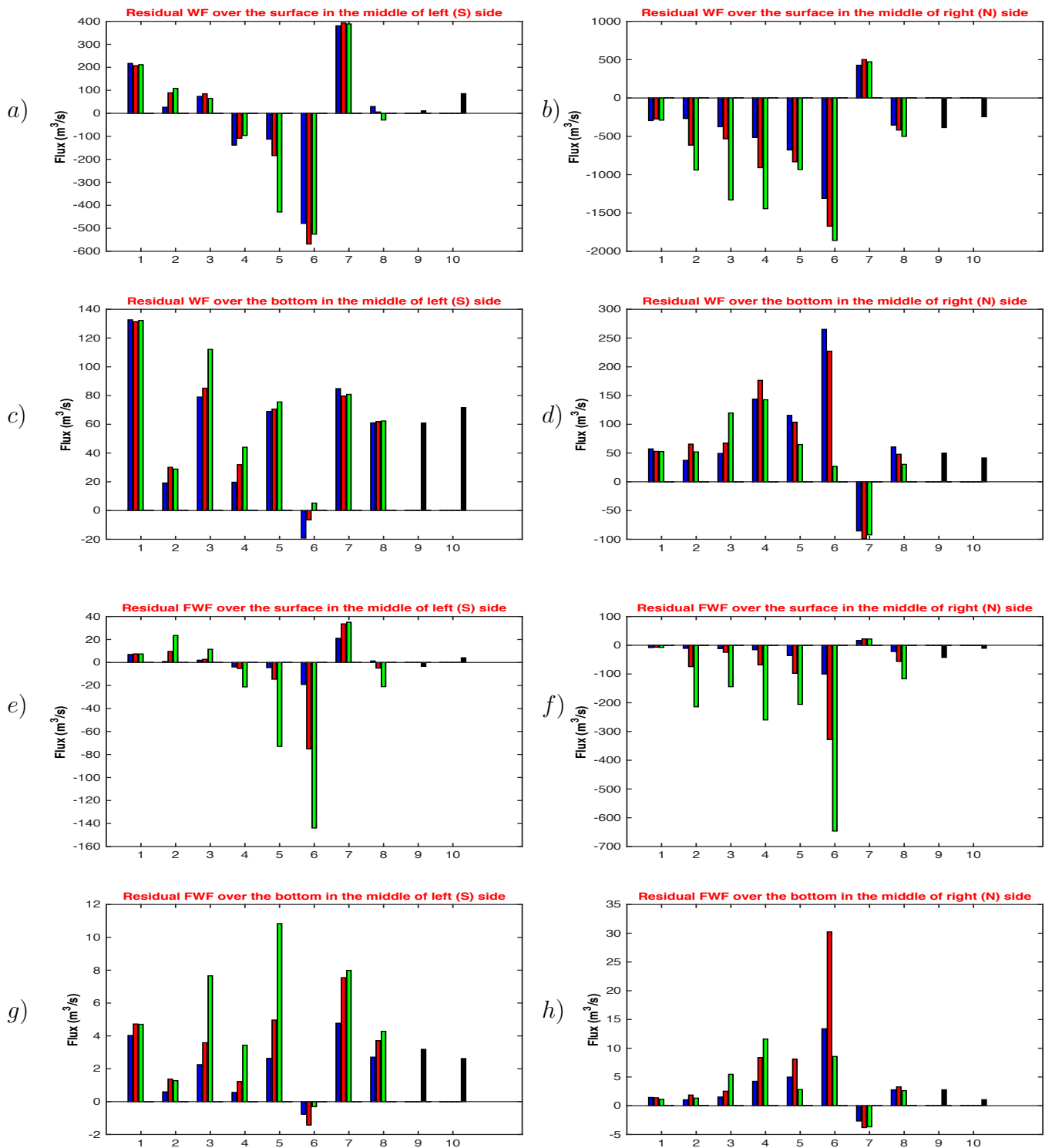


Figure 4.43: Water and Fresh Water exchange in the Bourgneuf section for 10 scenarios:

| | |
|--|--|
| 1) Spring tide without wind forcing (~Oct 26); | 6) West wind (July 7, ~mean tide); |
| 2) Neap tide without wind forcing (~Sep 20); | 7) East wind (Dec 17, ~mean tide); |
| 3) South wind (Jun 13, ~spring tide); | 8) Averaged over 7 months with real wind forcing; |
| 4) S-W wind (Jun 21, ~neap tide); | 9) Averaged over 7 months with real river regime and wind forcing; |
| 5) North wind (Sept 25, ~spring tide); | 10) Averaged over 7 months with real river regime but no wind forcing. |

The Fig. 4.43 synthesize the residual fluxes of water and fresh water for different tide or wind scenarios and typical river regimes, in 4 different locations in the Bourgneuf cross-section: in the middle of NE subsection (right) and in the middle of SW subsection (left), either near the surface or near the bottom. Scenarios are numbered from one to ten. The first two scenarios describe the tidal residual flux, scenarios 3 to 7 show the effect of typical wind. Scenarios 1 to 8 consider 3 steady river regimes (low: $300 \text{ m}^3/\text{s}$, mean: $900 \text{ m}^3/\text{s}$ and high river discharge $2000 \text{ m}^3/\text{s}$ respectively, in blue, red and green). The 8th scenario averages the effect of tide and real wind over 7 months, while the last two scenarios consider the real river discharge in 2007, either without wind (scenario 10) or with actual wind forcing (scenario 9). Each value is computed as the average of Water Flux (WF) or Fresh Water Flux (FWF) passing through one mesh in a given period of time over which the wind forcing is approximatively steady (scenarios 1 to 7) or not (scenarios 8 to 10). Values are negative when fluxes are inwards.

It appears that residual fluxes are very small over the long term, especially near surface (scenarios 8, 9 and 10), and that tidal effects are significant on the SW subsection and particularly on the exchanges near bottom (scenarios 1, 2 in Fig. 4.43c & g). The river regime changes the (fresh) water fluxes significantly during a neap tide, without or in presence of S and SW wind forces (scenarios 2, 3 and 4 in Fig. 4.43b & f). The contrast between scenario 6 (West wind) and 7 (East wind) simultaneously near surface and bottom in both subsections is surprising. Stronger effects are related to the NE subsection, in which the direction of flow is opposite near surface and bottom for both scenarios (scenarios 6, 7 in Fig. 4.43b & d). A westerly wind (scenario 6) generates a strong inflow near surface through both subsections, while for the NE subsection it is compensated by a strong outflow near bottom. Fresh water fluxes (FWF) are even more contrasted. To summarize, it should be reminded that water fluxes towards or out of the Bourgneuf Bay are essentially controlled by wind episodes, but gets to some equilibrium in average (scenarios 8 and 9).

4.6 Water fluxes passing through the Mor-Braz region

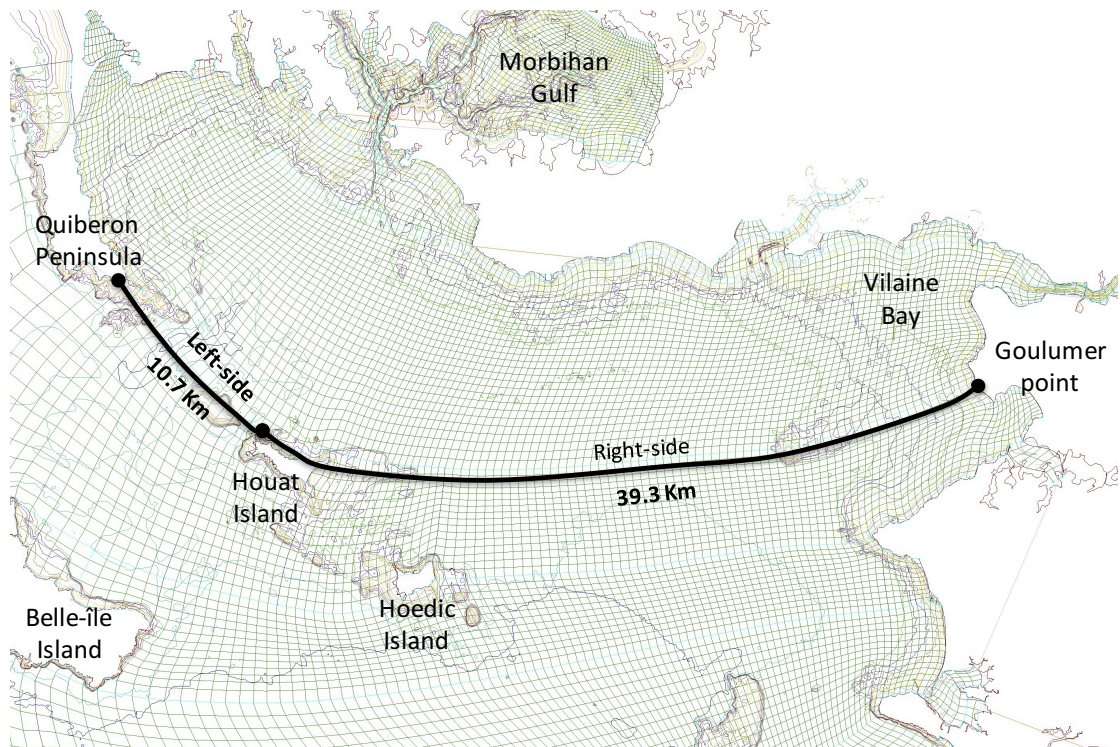


Figure 4.44: Mor-Braz section divided into the left (10.7 Km) and right (39.3 Km) subsections.

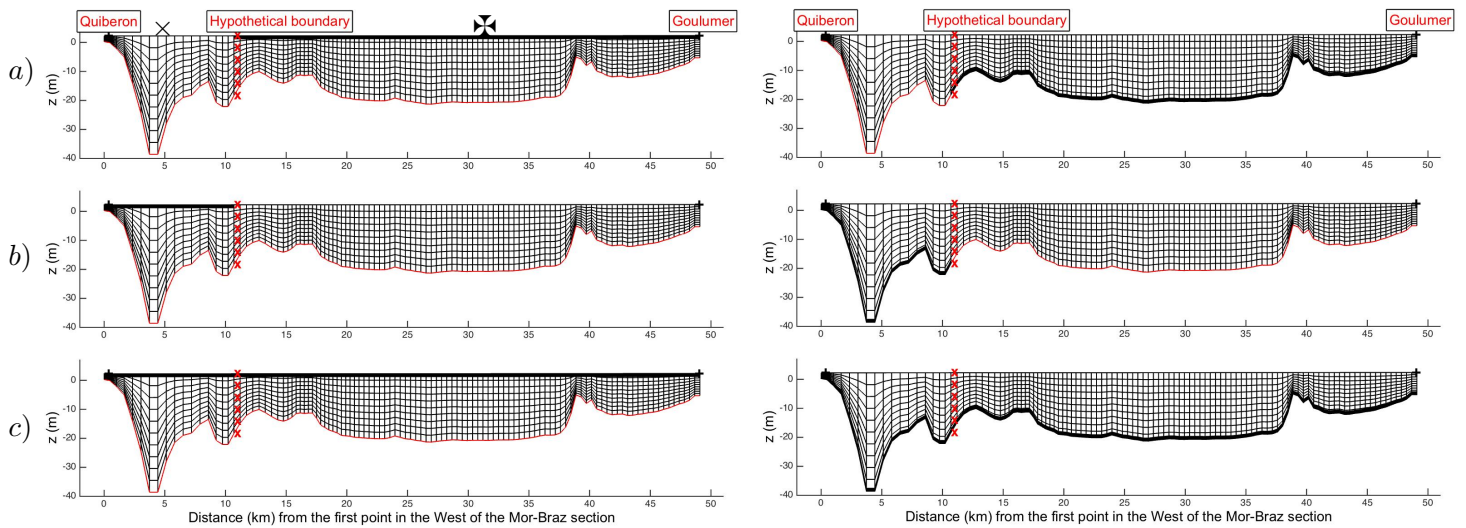


Figure 4.45: Schematic view of the cross-section in which (Fresh) Water Flux is calculated over the first 1m below the surface in Mor-Braz section (two point indicated by \times and \times are chosen for the vertical profiles of hydrological characteristics):

- a) Flux computed over the surface of right sub-section
- b) Flux computed over the surface of left sub-section
- c) Flux computed over the surface of overall section.

Figure 4.46: Schematic view of the cross-section in which (Fresh) Water Flux is calculated over the first 1m above the bottom in Mor-Braz section:

- a) Flux computed over the bottom of right sub-section
- b) Flux computed over the bottom of left sub-section
- c) Flux computed over the bottom of overall section.

The third section of our study zone encloses the "Mor-Braz" area, composed of the Vilaine Bay, the Morbihan Gulf and the Quiberon Bay. The section joins the Quiberon peninsula to the south of the Vilaine bay through the island of Houat. As shown in Fig. 4.44, the cross-section follows a "j=cte" line of the curvilinear grid, and then, starting from Quiberon at its west end, reaches the continent at the Goulumer (Bile) point. The reason for selecting such a section and the Mor Braz area is twofold: the area is exploited for shellfish farming, is submitted to discharges in the Morbihan gulf and to the outflow of the Vilaine River. It is known for hypoxia periods during summer (*e.g.* Chapelle (1990)). One main question is the influence of fresh water coming from the Loire River and its weight versus fresh water coming from the Vilaine river. Another reason for selecting this section is the willing to evaluate one result from Tessier work (Tessier, 2006) who obtained a net input of sediment from offshore in the western subsection, between Quiberon and Houat Island, and an output towards the South in the eastern part of the section. One important goal of our work is a better description and understanding of circulations in the area, including their variations according to various forcing. Then the division of the cross-section into two subsections shown in Fig. 4.44 became natural. Their respective bathymetry are shown in Fig. 4.45 and 4.46. The eastern segment is about 3.7 times wider than the western one. But due to a deep channel (La Teignouse) in the latter, the ratio between cross-section areas is only 3 (Fig. 4.45).

Vertical profiles analysis in Mor-Braz section

As for the other sections, residual currents, time-averaged salinity and FWF profiles in the middle of each subsection (locations are indicated by symbols in Fig. 4.45) are presented in Fig. 4.47. Water depth are about 35 m (west) and 30 m (east) for these locations.

A strong stratification of residual flow is observed on the western subsection, the flow getting into the bay of Quiberon near bottom and getting out near surface, whatever the river flow (with a slightly lower intensity for the low river regime). Through the eastern subsection, the residual flow is entering the bay near the surface, also near bottom, and presents a minimum intensity at around 30% of water depth. It should be reminded that residual current is not necessarily representative of residual depth integrated flow, as the water height variations may be not phased with the current. The salinity profile is more or less mixed on the western side (strong tidal currents in the Teignouse Strait), and still stratified on the eastern one, under the influence of the Loire river regime. A clear circulation scheme characterizes the fresh water circulation, which enters the Mor-Braz region through the eastern subsection and gets out through the western one, except near bottom where the residual current entrains a small quantity of fresh water to the North-East.

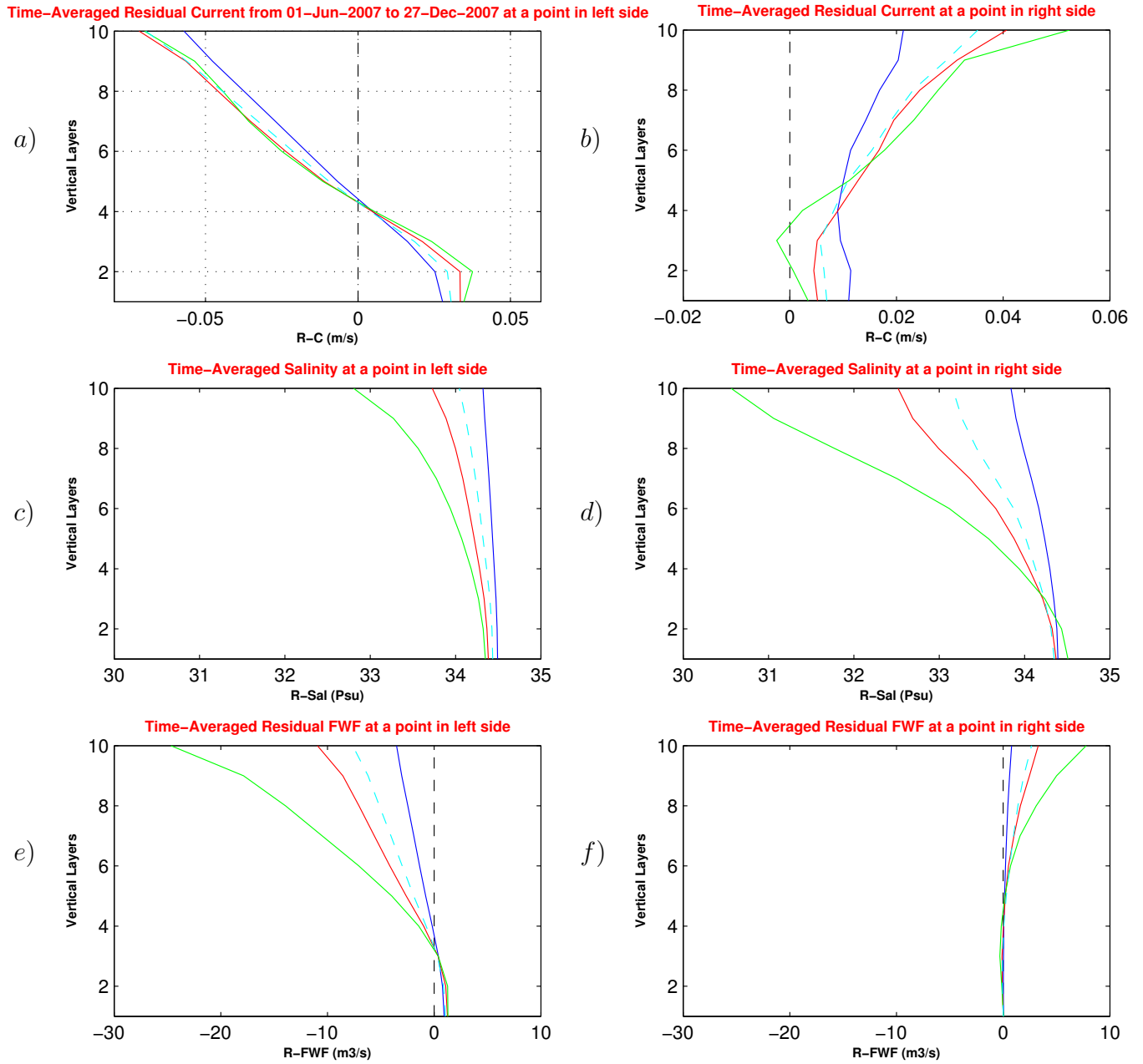


Figure 4.47: Representative vertical profiles of hydrological characteristics across the Mor-Braz section, averaged over seven months. Left hand side (west); Right hand side (east). a) and b) Residual current; c) and d) Time-averaged salinity; e) and f) Time-averaged residual Fresh water Fluxes. Colors correspond to the different river discharges (blue: low, red: mean, green: high and cyan/dashed: real). Positive fluxes or currents are entering the Mor-Braz area.

4.6.1 Water Flux in Mor-Braz section (overall)

The volume of water passing through the overall section reaches $0.25 \text{ Mm}^3/\text{s}$ (Fig. 4.48a). Despite a much smaller cross-section, the western subsection accounts for more than 60% of the total flux at each tide (Fig. 4.49a and 4.50a). Residual depth-integrated fluxes show variations of rather short period, probably related to wind forcing, and apparently neither correlated to the tide amplitude nor to the rivers regime (all curves are superimposed in Fig. 4.48f). However, the general trends along the seven months simulation is quite different according to the rivers regime, with a slight increase of water mass for low river discharges and a clearer decrease for large river discharges (Fig. 4.48g). It should be reminded that the cross section enclose the region constituted by the Mor-Braz and Morbihan (respectively "large and small seas", in Breton language), so that the actual residual flux of water through the section should match the river inputs (mainly the Vilaine outflow) in the long term.

The small residual water input in the Mor-Braz for low river flow indicates a non equilibrium regime over the simulated period, assuming the model is perfectly conservative (the input after 7 months, *i.e.* $18.4 \text{ e}^6 \text{ s}$, is $0.6 \text{ e}^9 \text{ m}^3$, that is approximately 6% of the total volume of Mor-Braz ($50 \text{ km} \times 10 \text{ km} \times 20 \text{ m} = \text{e}^{10} \text{ m}^3$).

The shift in residual water exchange is approximately $0.9 \text{ e}^9 \text{ m}^3$ (resp. $2.5 \text{ e}^9 \text{ m}^3$) when the Vilaine river increases from 20 to $70 \text{ m}^3/\text{s}$ (resp. $180 \text{ m}^3/\text{s}$), corresponding to an additional fresh water input of $50 \text{ m}^3/\text{s} \times 18.4 \text{ e}^6 \text{ s} = .92 \text{ e}^9 \text{ m}^3$ (resp. $2.9 \text{ e}^9 \text{ m}^3$): then the shifts in fluxes averaged over the whole simulated period are equivalent to the additional Vilaine input, which confirms the conservativity of the model. However, changes in residual fluxes do not distribute uniformly, neither on the vertical nor between west and east subsections.

On the vertical, residual fluxes in the first meter below the surface or above bottom are in average in the same direction, towards the south, with a clear increase with river flow near bottom (Fig. 4.48e). These fluxes are much larger than depth-averaged ones, which means that there should be opposite residual fluxes in intermediate layers, as partly suspected in Fig. 4.47, but probably with a larger intensity, for instance within the eastern subsection. Also the trend along the eastern subsection can be non uniform near bottom or near surface. The trend of outflow near surface (Fig. 4.48c) seems dominant during the north-easterly winds (dark blue points in Fig.4.1-4). The global outflow near bottom is larger when river regimes are lower, and is strongly attenuated for high river discharge, which could be related to estuarine near bottom circulation induced by the Vilaine plume.

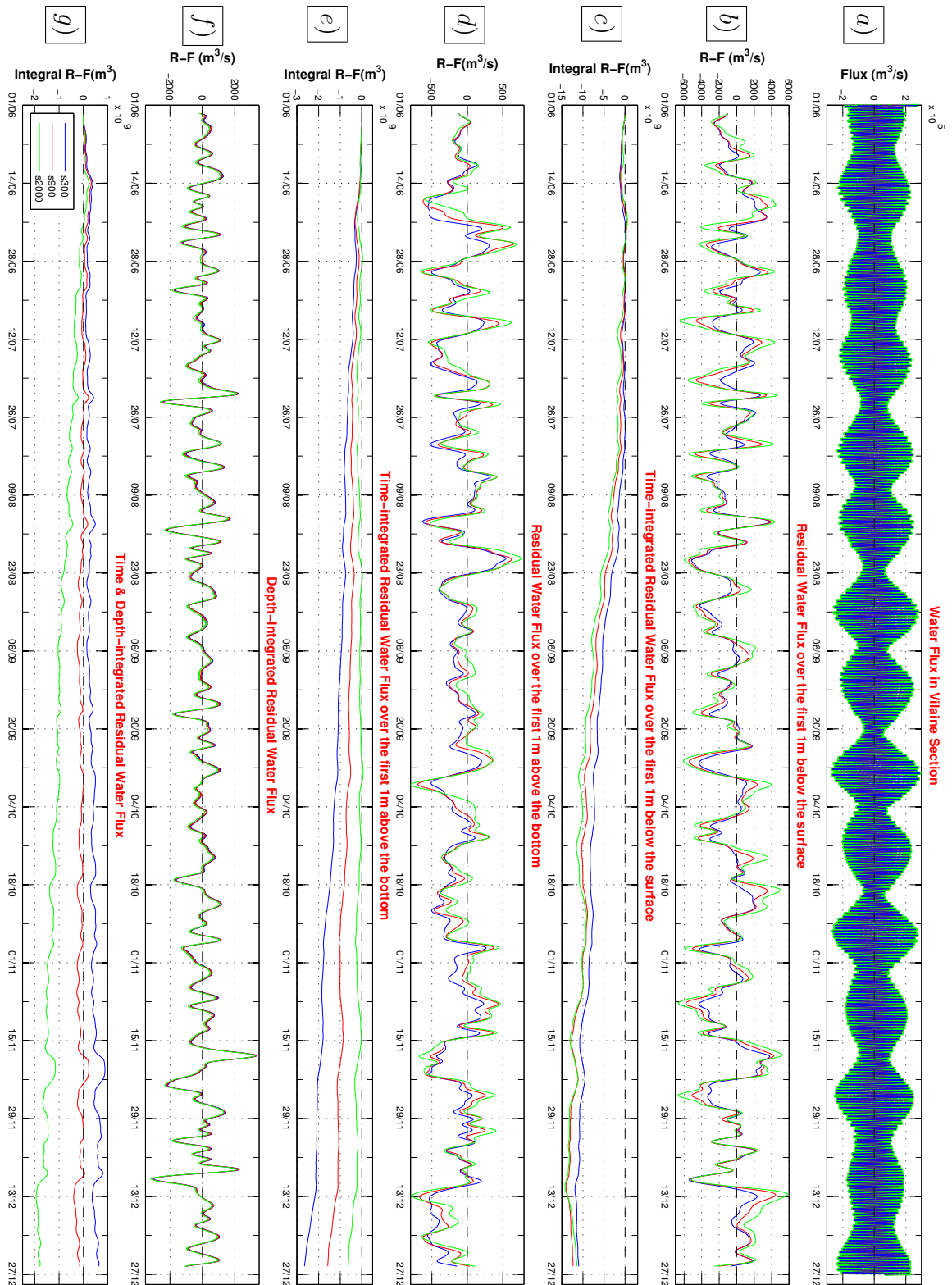


Figure 4.48: Water exchange in the Vilaine cross-section (overall), three simulations are shown. The positive value means inward and the negative indicates the outward current flux. The color coding is as follows:

- Blue: a semi-realistic situations with real meteorological conditions (wind, salinity, temperature), actual bathymetry and low flow (300, 20 m^3/s as constant discharges of Loire and Vilaine rivers).
- Red: a semi-realistic situations with real meteorological conditions (wind, salinity, temperature), actual bathymetry and average flow (900, 70 m^3/s as constant discharges of Loire and Vilaine rivers).
- Green: a semi-realistic situations with real meteorological conditions (wind, salinity, temperature), actual bathymetry and flood flow (2000, 180 m^3/s as constant discharges of Loire and Vilaine rivers).

The flux distribution along the section is marked by an opposition between the western and eastern subsections: Fig. 4.49g and 4.50g show exact opposite mean term variations of depth-averaged fluxes, in a range 10 times the order of magnitude of total flux (Fig. 4.48g). When referring to the wind forcing (Fig. 4.1-3 & 4), it appears that water is getting in through the west subsection and getting out through the east one when the wind is blowing from western directions (for instance, in June/July, and especially during the storms of beginning of December, while the opposite occurs from 23rd of August until 20th of November, or after mid-December, when the wind is blowing from the East. These wind-induced depth-integrated fluctuations are likely to concern the whole water depth, because trends are similar but smoothed both near surface and bottom in the west subsection (Fig. 4.49c & e). In addition, the effect of river regime is not visible near bottom, and indicates an increase of outflow near surface.

On the other hand, residual fluxes are much more vertically contrasted through the eastern subsection, with clear southward flow near surface for westerly winds and a northward one when wind is blowing from South and East. A large river flow reinforces these near-surface fluxes, probably enhanced by stratification. Near bottom, the flux is more or less entering Mor-Braz, except during the storms of December. The influence of river flow is larger, similar to a density-induced current related to the Vilaine plume (*i.e.* entering Mor-Braz near bottom).

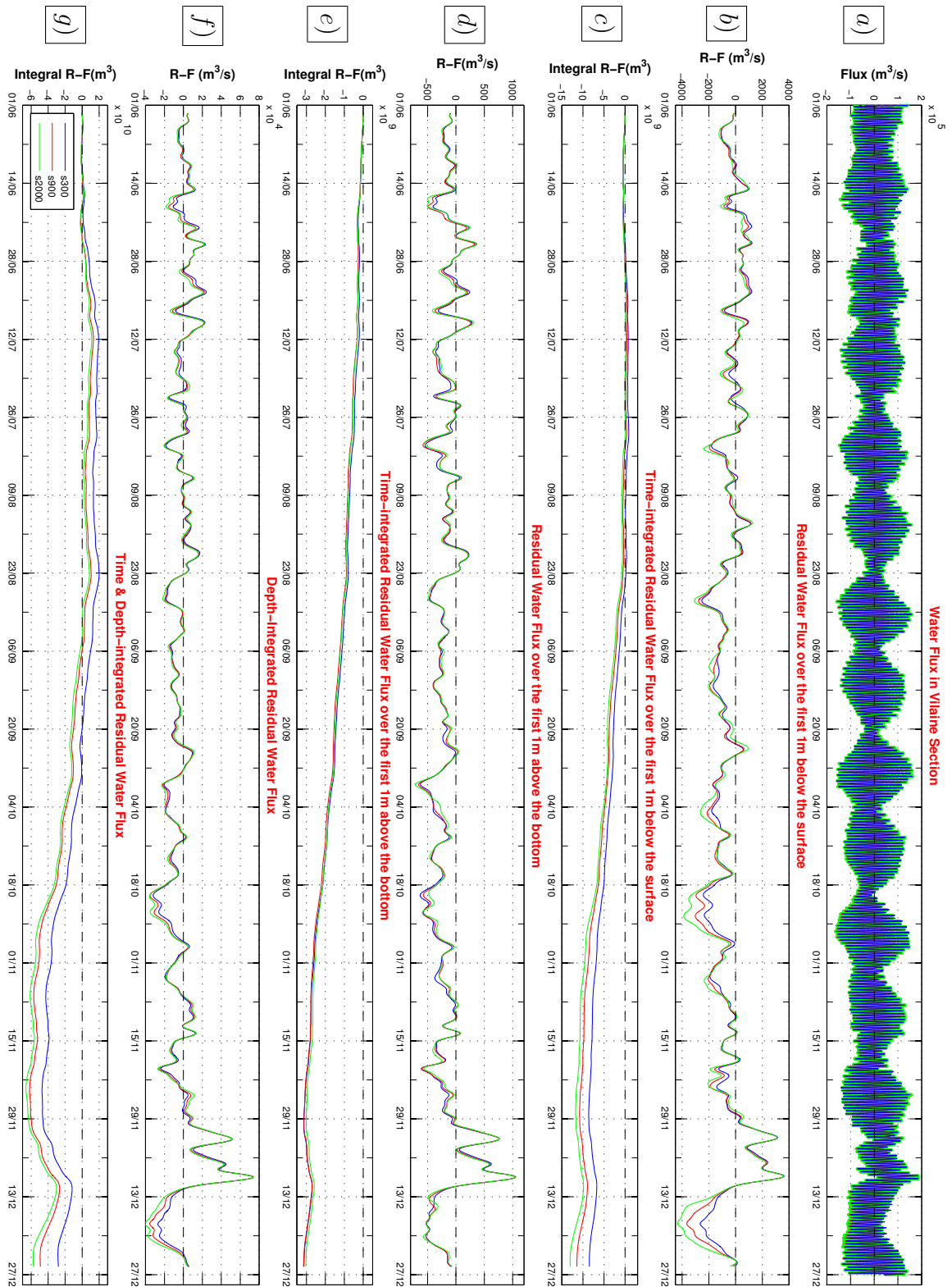


Figure 4.49: Water exchange in the Vilaine western sub-section, three simulations are shown. The positive value means inward and the negative indicates the outward current flux. The color coding is as follows:

- Blue: a semi-realistic situations with real meteorological conditions (wind, salinity, temperature), actual bathymetry and low flow (300, 20 m^3/s as constant discharges of Loire and Vilaine rivers).
- Red: a semi-realistic situations with real meteorological conditions (wind, salinity, temperature), actual bathymetry and average flow (900, 70 m^3/s as constant discharges of Loire and Vilaine rivers).
- Green: a semi-realistic situations with real meteorological conditions (wind, salinity, temperature), actual bathymetry and flood flow (2000, 180 m^3/s as constant discharges of Loire and Vilaine rivers).

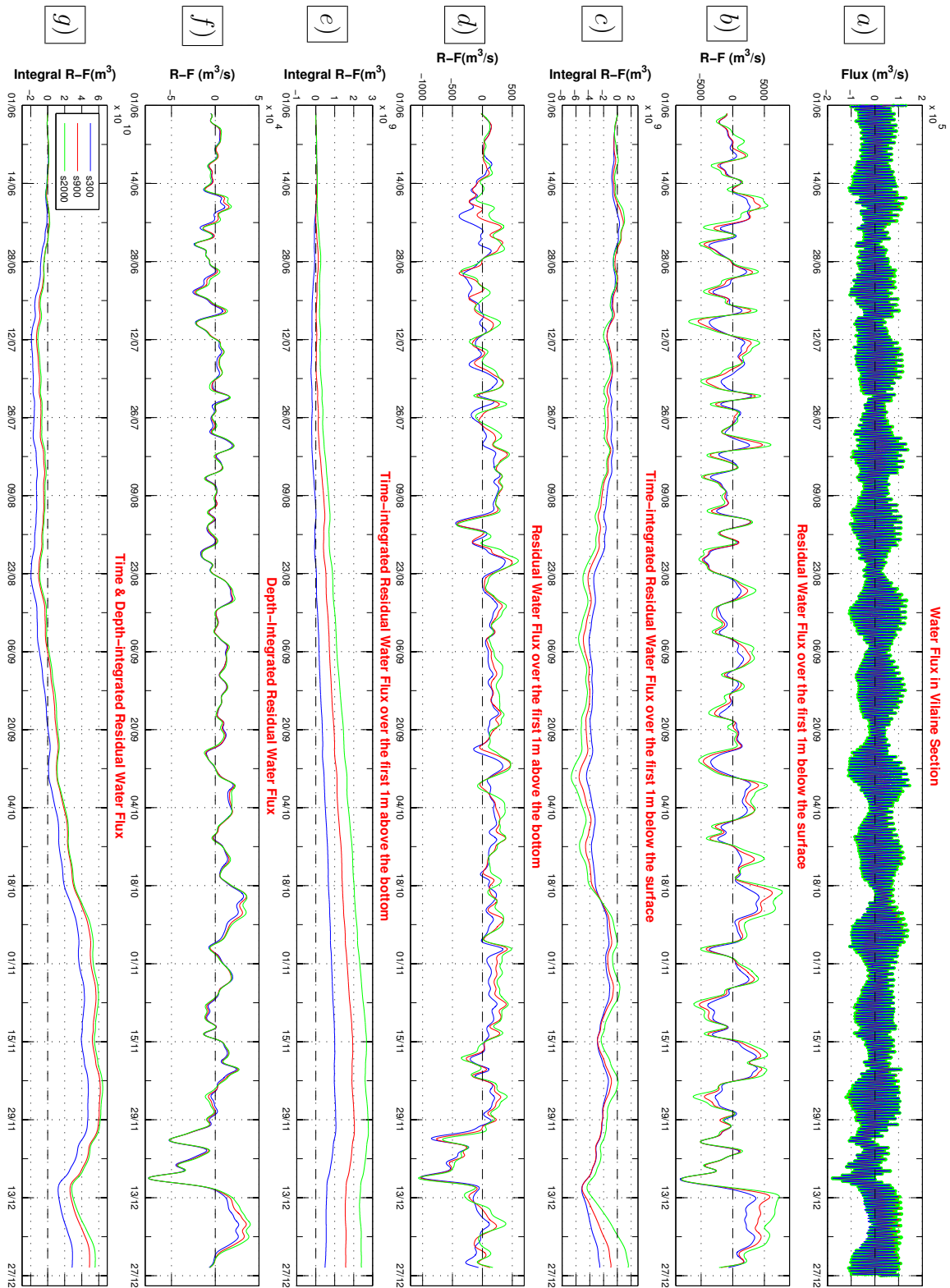


Figure 4.50: Water exchange in the Vilaine eastern subsection (right), three simulations are shown. The positive value means inward and the negative indicates the outward current flux. The color coding is as follows:

- Blue: a semi-realistic situations with real meteorological conditions (wind, salinity, temperature), actual bathymetry and low flow (300, 20 m³/s as constant discharges of Loire and Vilaine rivers).
- Red: a semi-realistic situations with real meteorological conditions (wind, salinity, temperature), actual bathymetry and average flow (900, 70 m³/s as constant discharges of Loire and Vilaine rivers).
- Green: a semi-realistic situations with real meteorological conditions (wind, salinity, temperature), actual bathymetry and flood flow (2000, 180 m³/s as constant discharges of Loire and Vilaine rivers).

The Fig. 4.51 synthesizes the residual fluxes of water and fresh water for different tide or wind scenarios and typical river regimes, in 4 different locations in the Mor-Braz cross-section: in the middle of eastern subsection (right) and in the middle of western subsection (left), either near the surface or near the bottom. Scenarios are numbered from one to ten. The first two scenarios describe the tidal residual flux, scenarios 3 to 7 show the effect of typical wind. Scenarios 1 to 8 consider 3 steady river regimes (low: $300 \text{ m}^3/\text{s}$, mean: $900 \text{ m}^3/\text{s}$ and high river discharge $2000 \text{ m}^3/\text{s}$ respectively, in blue, red and green). The 8th scenario averages the effect of tide and real wind over 7 months, while the last two scenarios consider the real river discharge in 2007, either without wind (scenario 10) or with actual wind forcing (scenario 9). Each value is computed as the average of Water Flux (WF) or Fresh Water Flux (FWF) passing through one mesh in a given period of time over which the wind forcing is approximately steady (scenarios 1 to 7) or not (scenarios 8 to 10). Values are negative when fluxes are inwards.

It appears that residual fluxes are very small over the long term (scenarios 8, 9 and 10), and that tidal effects are significant on the western subsection only (left hand side of Fig. 4.51). The river regime does not change the water fluxes so much, except for scenario 4 (S-W wind) on the eastern subsection. The contrast between scenario 8 (constant river discharges) and 9 (actual river regimes) near the bottom of the west subsection is surprising. Stronger effects are related to the wind direction, with entrance in the Mor-Braz area from the west and outflow through the east side for westerly winds, and the opposite for easterly winds, simultaneously near surface and bottom.

A northerly wind (scenario 5) generates a small southward flow through the western subsection, and a stronger southward flow near surface in the eastern subsection, compensated by a northward flux near bottom. Fresh water fluxes (FWF) are even more contrasted. Through the western subsection, they are oriented outward under spring tide and also under easterly winds. Through the eastern subsection, they follow similar trends as total water fluxes near surface, but may vary a lot near bottom according to the river regime, which could be more deeply analyzed by considering river plumes location and stratification occurrences simultaneously.

To summarize, it should be reminded that water fluxes towards or out of the Mor-Braz are essentially controlled by wind episodes, but get to some equilibrium in average (scenarios 8 and 9).

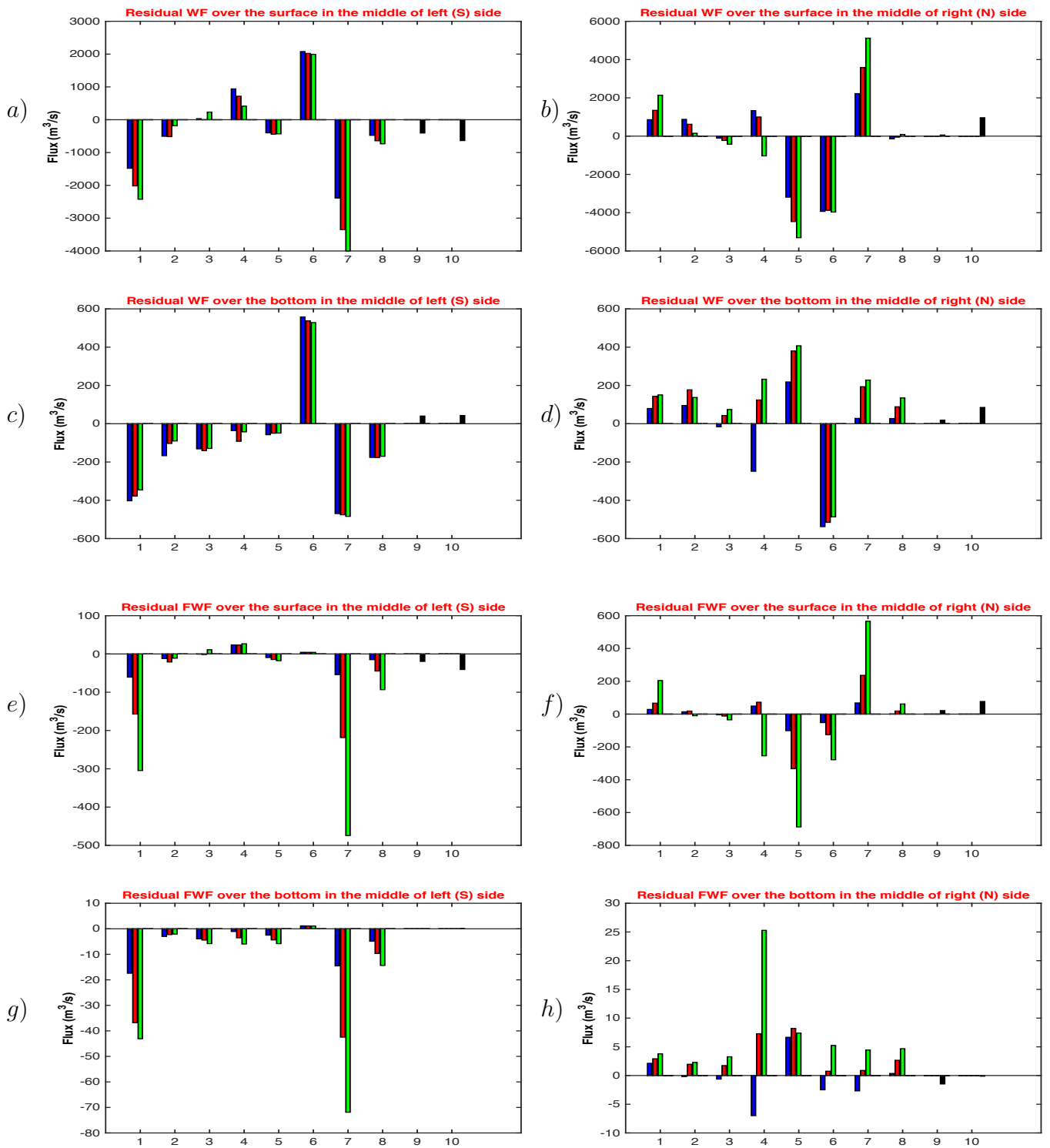


Figure 4.51: Water and Fresh Water exchanges in the Mor-Braz subsection for 10 scenarios:
 1) Spring tide without wind forcing (~Oct 26);
 2) Neap tide without wind forcing (~Sep 20);
 3) South wind (Jun 13, ~spring tide);
 4) S-W wind (Jun 21, ~neap tide);
 5) North wind (Sept 25, ~spring tide);
 6) West wind (July 7, ~mean tide);
 7) East wind (Dec 17, ~mean tide);
 8) Averaged over 7 months with real wind forcing;
 9) Averaged over 7 months with real river regime and wind forcing;
 10) Averaged over 7 months with real river regime but no wind forcing.

Chapter 5

Time scales analysis (Mean Age, Flushing Time)

Introduction

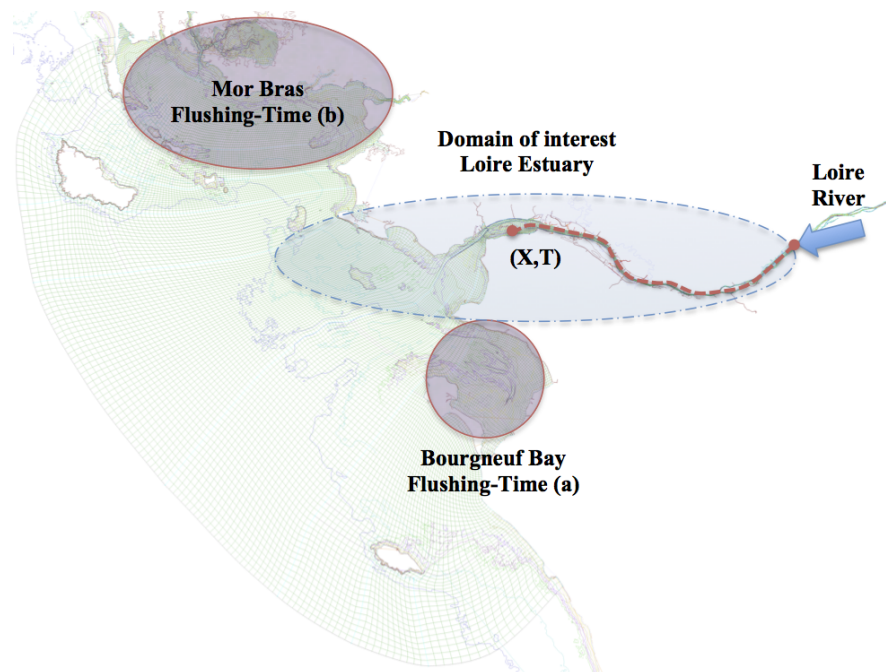


Figure 5.1: Areas of interest for water age (blue) and Flushing-time (purple)

Water quality of a semi-enclosed system may be described by water age and flushing time (Andrejev et al., 2004). Two indicators for characterizing the temporal scale of water exchanges in the study area have been computed: mean age, and time for renewing water in a given areas (Deleersnijder et al., 2007).

First, the age of water from a given source, at a specific location X, refers to the time "T" that takes for a water parcel starting from the source to reach this location (Fig. 5.1).

This time can vary according to hydrodynamics in the area, either dependent on tidal, runoff or meteorological forcing. When the source is steady, its mean age is the averaged value of the transit time. The concept has been developed by Delhez (Delhez et al., 1999) and provides methods to quantify transport characteristics of dissolved substances within an eulerian coordinate framework. Using this method, the estimation time of transport presents spatial variations, and its distribution may inform on differences in water storage capacity or renewal. In the present work, it has been chosen to trace freshwater from the Loire River, and to identify the distribution and variations of mean age of this fraction of water in the whole area, distinguishing surface and bottom layers. Similar computations have been run in the Seine estuary and applied either to the river input, or to a steady water release from Honfleur, at the mouth of the estuary (Le Hir and Jacinto, 2007).

The second indicator, the "flushing time", is the time required to renew the water at a given location; it has been analyzed following the method described in Koutitonsky et al. (2004). Such a computation is always tricky. Actually, the time required to replace water is strongly dependent on the size-scale of the water mass which is considered. If this water mass is infinitely small, the renewal time (or flushing time) will be close to zero. It can become very long if the water body is large. Here, we are interested in describing the variability or contrasts in the water renewal time scale. Two areas have been considered (see Fig. 5.1): (a) the Bay of Bourgneuf and (b) the Mor-Braz region, including the Morbihan gulf. The selected time scale is the required time to have the concentration of water initially inside the area divided by "e" ($= 2.718$). In other word, the time required for the tracer concentration to drop below 37% of the initial concentration. Then computations consist in considering a specific conservative tracer of water, submitted to physical processes (advection and diffusion), introduced only in the selected area with a uniform concentration of $1 \text{ (m}^{-3}\text{)}$. Then in any cell of the 3D computation grid, the time necessary to get a vertically averaged concentration below e^{-1} is saved, and kept as a local descriptor of the time required for renewing local water by water coming from outside the considered area.

5.1 Age of water masses

As explained in the introduction of this chapter, the age of the fresh water introduced by the river upstream of the estuary is likely to vary at different time scales, even at the tidal scale. These large variabilities are exemplified in Fig. 5.2. The mean age is progressively increasing from the inner estuary to the mouth (~ 2 days at Nantes, 6 days at St-Nazaire) and more strongly to the adjacent bays.

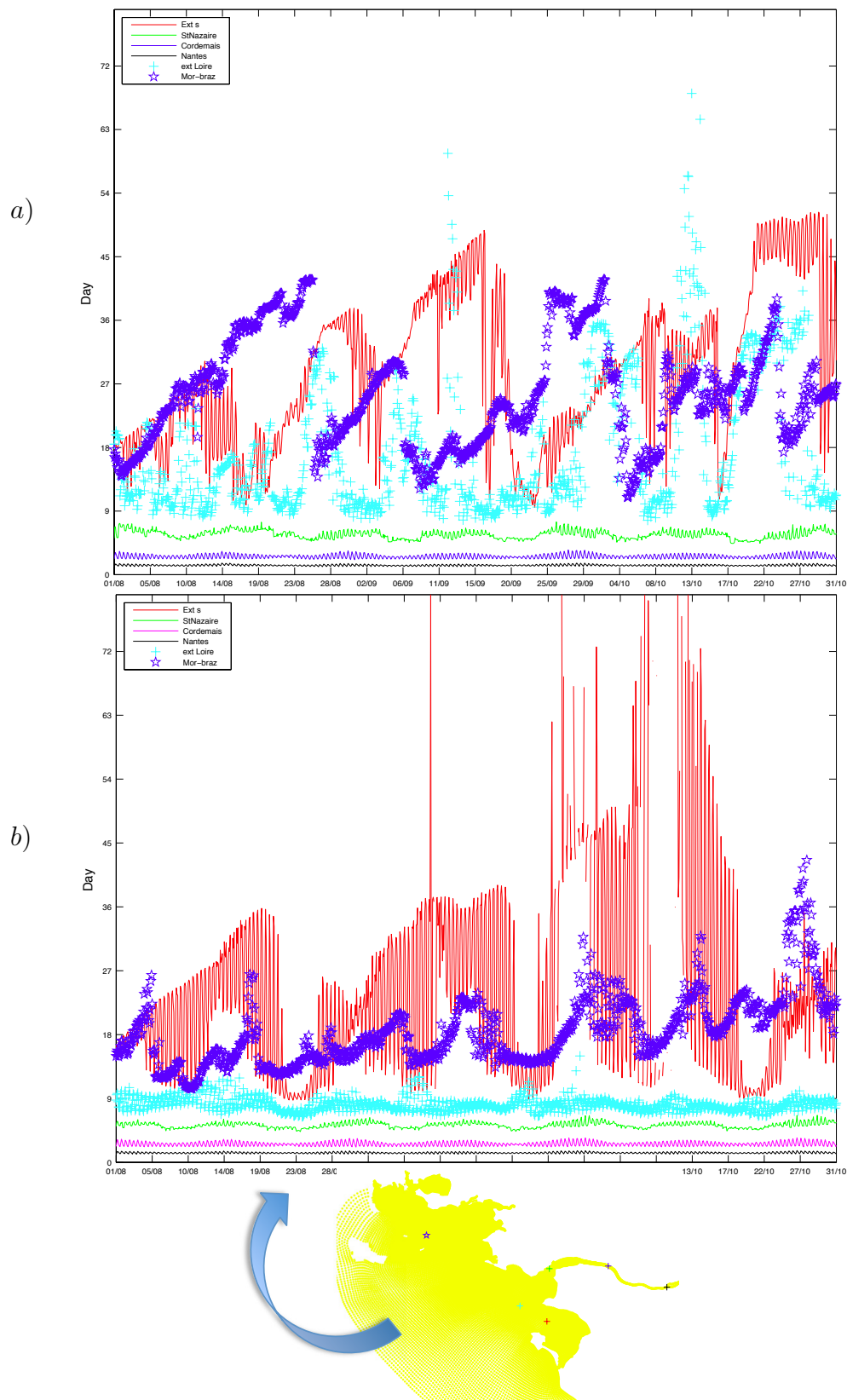


Figure 5.2: Time evolution of mean age of fresh water provided by the Loire River at the upstream end of the estuary, at different locations of the study area, always in surface layers. Locations are indicated on the joined map. a) simulation with realistic wind and steady mean river flow ; b) simulation without wind and with steady mean river flow (900 m³/s)

At St-Nazaire, mean age is more variable when wind is accounted for (see Fig. 5.2a), and is a bit larger in average (6 days with wind, instead of ~ 5.5 days without wind), although wind is blowing from NE most of the time during the 3 months, as represented in Fig. 4.1 (August, September, October 2007). Mean age varies considerably out of the estuary, even without wind (see Fig. 5.2, b): it is the case within the semi-diurnal tide at the entrance of the bay of Bourgneuf (red line), or within the fortnightly tidal cycle at the entrance of the Mor-Braz (dark blue stars in Fig. 5.2), where the age is increasing with tidal amplitude, with some delay (~ 1 day). All results presented in Fig. 5.2 are related to surficial waters : may be because of stratification, the mean age in surface layers (at the Mor-Braz southern limit) is lower on neap (about 15 days) than on a spring tide (about 20-25 days), as freshwaters are more quickly affected outside the mouth when the estuarine circulation is more intense. If the wind is accounted for, variations are even larger, still in the Mor-Braz area: between 10 and 40 days at the same location. The significance of such large variations of mean age at a fixed location is difficult to catch, and such variations should be associated with strong gradients either vertical (especially during neap tide) or horizontal, as water bodies are advected in the neighborhood of this fixed location. For this reason, it can be easier to analyze the spatial distribution of mean age in the area.

Because tidal oscillations are negligible on neap tide, we selected a snapshot on October the 19th, in order to represent the spatial distribution of mean age, both in surface and bottom layers (Fig. 5.3 and 5.4). Fig. 5.3 c and d represent the plume of the Loire River, through its tracer, and naturally look like the salinity results. A strong stratification is noticeable, mean age being less than 20 days in the surface layer of most of the study area, and undefined in bottom layers. When the bottom computation is possible, mean age differences are not so large: this is true for instance in the so-called "Courreau de Belle-île", between the Belle-île Island and Quiberon/Houat (around 25 days), in the bay of Quiberon (30 days in bottom layers, but 40 days in surface layer), or in the bay of Vilaine (about 25 days). Generally speaking, the age of Ligerian (*i.e.* from the Loire) waters is larger in the middle of the Mor-Braz area and in the inner bay of Quiberon. Surprisingly, the age of water from the Loire is very large in the Morbihan Gulf (~ 60 days), signifying a lack of mixing, especially in the eastern part of the Gulf. Another striking feature is the very large age of Ligerian waters in the bay of Bourgneuf, and south-west of Noirmoutier Island, showing a sharp gradient (from 60 days to 20 days within few kilometers) with waters along the axis of the Loire paleovalley (south west of St-Nazaire). This contrast is coherent with the tidal variation denoted at the entrance of the bay of Bourgneuf in Fig. 5.2, meaning that this station is likely to be located on each side of the frontal zone, depending on the tidal phase. However the concentration gradients of the

tracer are not so sharp, and the reason for such a difference of mean age is not very clear. A beginning of explanation could be the lack of mixing in the NW-SE direction, and a strong mixing in the SW-NE one, "old" water from the Loire re-circulating along this direction.

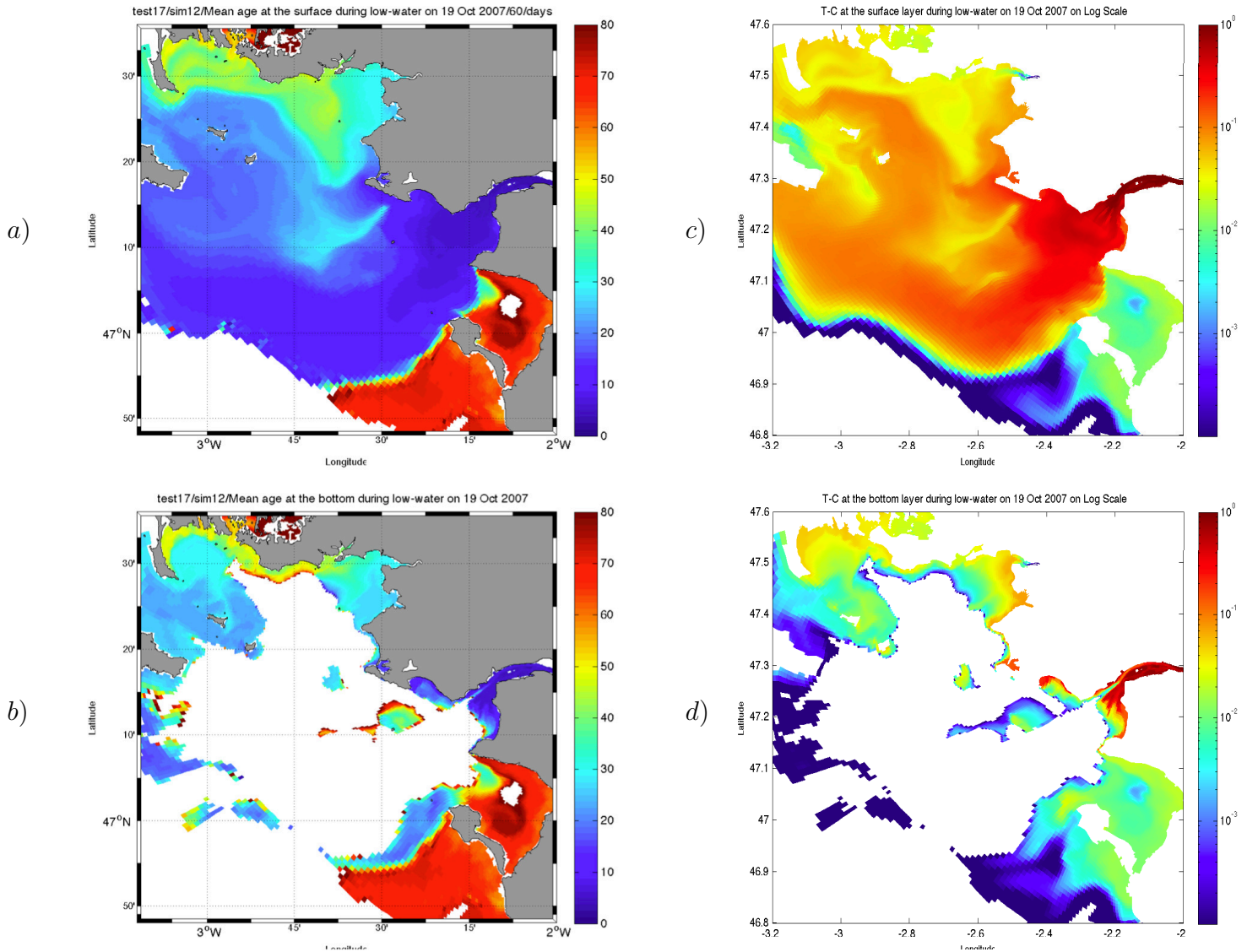


Figure 5.3: Spatial distribution of mean age of freshwater from the Loire River on neap tide (LW) , a) in surface layers b) in bottom layers. c) & d): concentration of the tracer of freshwater (the continuous release is $1 s^{-1}$ at the upstream end), at the same time, respectively in surface and bottom layers; Simulation without wind. Mean age computations are not represented (= white on figure) either when concentration of tracer $\leq 10^{-6} m^{-3}$, or when mean age ≤ 0.1 day or ≥ 80 days

Mean age results are completely different when wind forcing is accounted for (Fig. 5.4). The plume is oriented N-W along the coast (wind is moderate, and blowing from east at this time), and Ligerian waters inside this plume are about 20 days old in front of Le Croisic. In the middle of the study area, stratification remains high, and the mean age of bottom layers is in the range 40-60 days. In the bay of Vilaine, the age of freshwater from the Loire is about 20 days, both in surface and bottom layers. In the bay of Quiberon, the age is around 40 days, in

the same range as in the case without wind, and does not present any vertical difference (due to mixing with tidal currents). Horizontal gradients are strongly attenuated (when comparing with the case without wind), because of recirculation by winds. In the Morbihan gulf, results are very similar to the ones without wind, with the same contrast between the western and eastern parts.

In the bay of Bourgneuf, the mean age of Ligerian waters is in the continuity of the age at the estuary mouth, denoting a better exchange in the NW-SE direction than without wind (see Fig. 5.3), and increases towards the inner bay, varying from 30 days at the entrance to 40 days in the far east of the bay. As in the case without wind, the age remains similar on the other side of Noirmoutier Island.

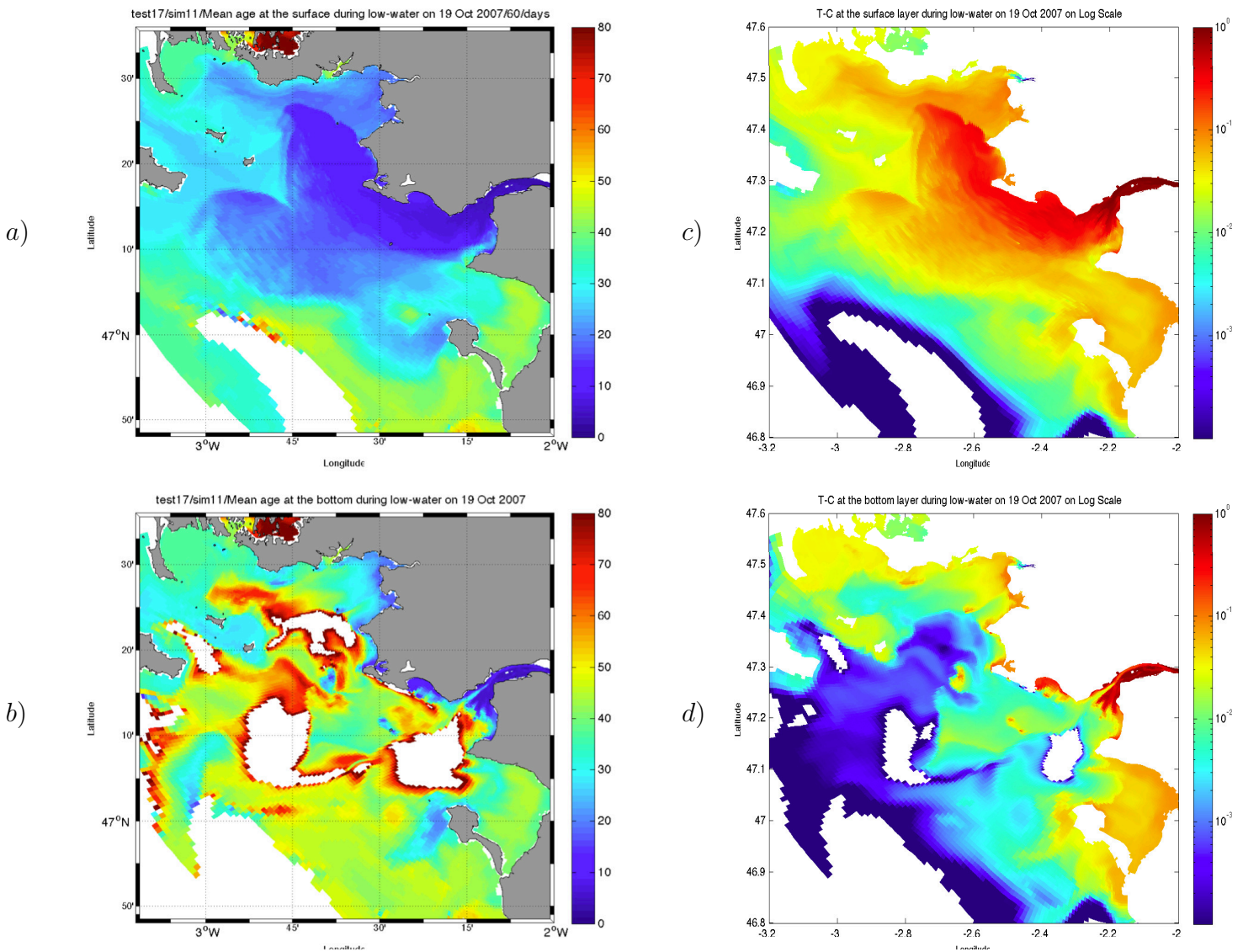


Figure 5.4: Spatial distribution of mean age of freshwater from the Loire River on neap tide (LW), a) in surface layers b) in bottom layers. c) & d): concentration of the tracer of freshwater (the continuous release is 1 s^{-1} at the upstream end), at the same time, respectively in surface and bottom layers; Simulation with realistic wind. Mean age computations are not represented (= white on figure) either when concentration of tracer $\leq 10^{-6} \text{ m}^{-3}$, or when mean age ≤ 0.1 day or ≥ 80 days

5.2 Flushing time

The flushing or turnover time is here considered, defined as the time necessary for a significant portion of a water body to be replaced by water coming from outside the chosen areas, *i.e.* from the ocean or the rivers.

The flushing time is governed by the barotropic and baroclinic tidal exchanges between the system and the adjacent water. In this section, a general method to compute the flushing time of a stratified water body in two key regions is presented via a numerical tracer experiment (see Fig. 5.1).

5.2.1 Flushing time in the bay of Bourgneuf

Flushing time shows a simple scheme in the bay of Bourgneuf. The range of variation is large : between 20 days near the N-W entrance and 80 days at the eastern end (see Fig. 5.5b), and an east-west asymmetry is noticeable. Several features can be noted :

The comparison of flushing time for two regimes of the Loire River shows that the influence of the Loire discharge on water quality over the Bourgneuf Bay is considerable, the renewing time of water mass in some parts (S-E) being multiplied by 1.5 while the Loire flow rate changes from low ($300^3 \cdot s^{-1}$) to mean ($900^3 \cdot s^{-1}$) values.

At the S-W connection with the ocean (Fromentine Strait), the flushing time is rather large, revealing a lack of water renewal from this sea connection of the bay and can vary from 40 to 60 days depending on the Loire discharge.

The iso-contours of flushing time follow the horizontal anti-cyclonic tidal eddy already mentioned in Chap. 1 (see Fig. 1.25), entraining a quasi uniform flushing time of 60 days (quite a lot) in the south of the bay. Flushing time is much longer (about 80 days) along the NE coast of the bay, denoting a lack of water exchange in the cross-shore direction, which could have incidence in case of accidental pollution (provisional protection from any pollution coming from the Loire, but concentration of a possible local pollution).

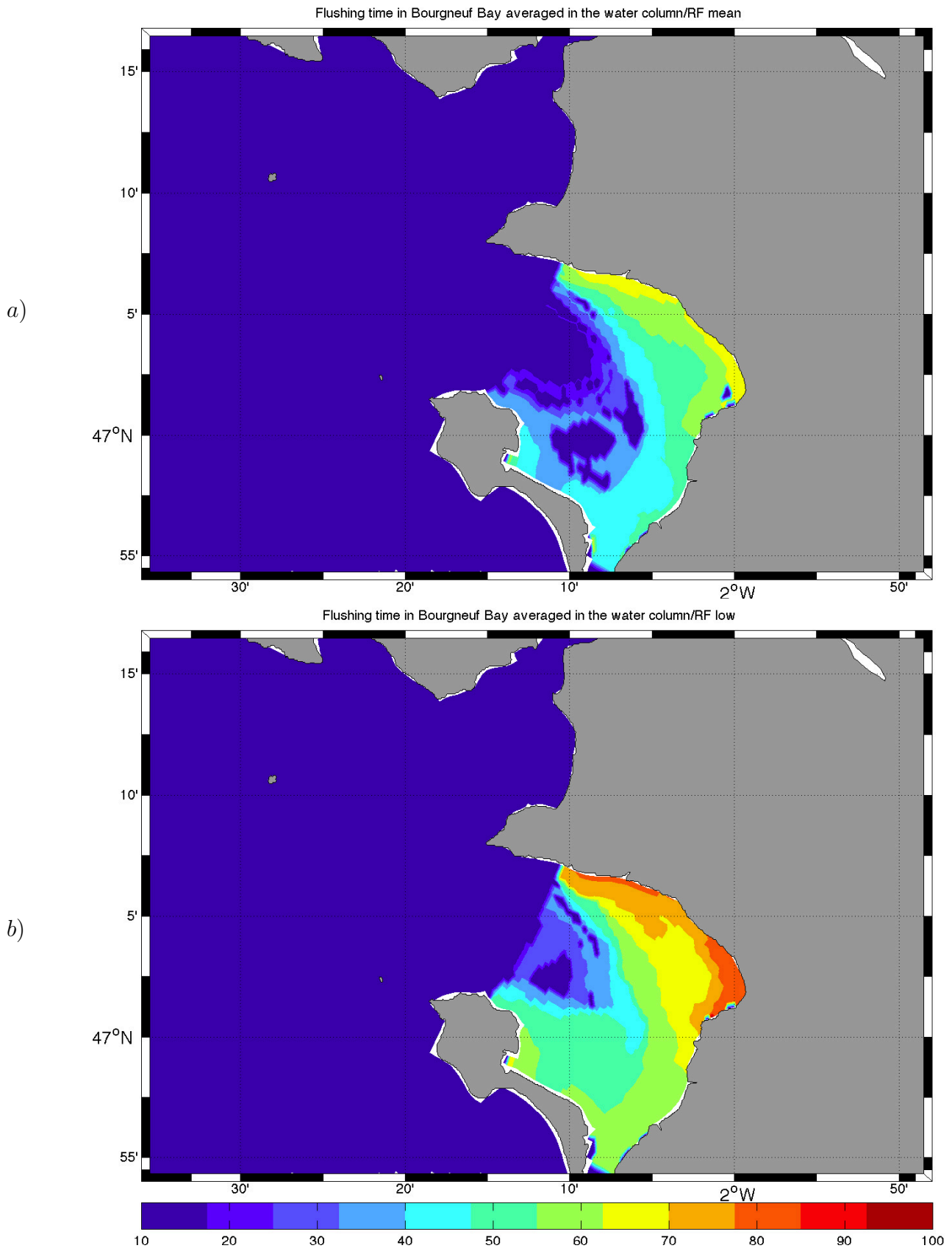


Figure 5.5: Spatial distribution of vertically averaged flushing time of the bay of Bourgneuf, simulated without wind. a) Mean river discharges (900 and 70 m^3/s for the Loire and Vilaine rivers respectively); b) Low river discharges (300, 20 m^3/s).

5.2.2 Flushing time in the Mor-Braz region

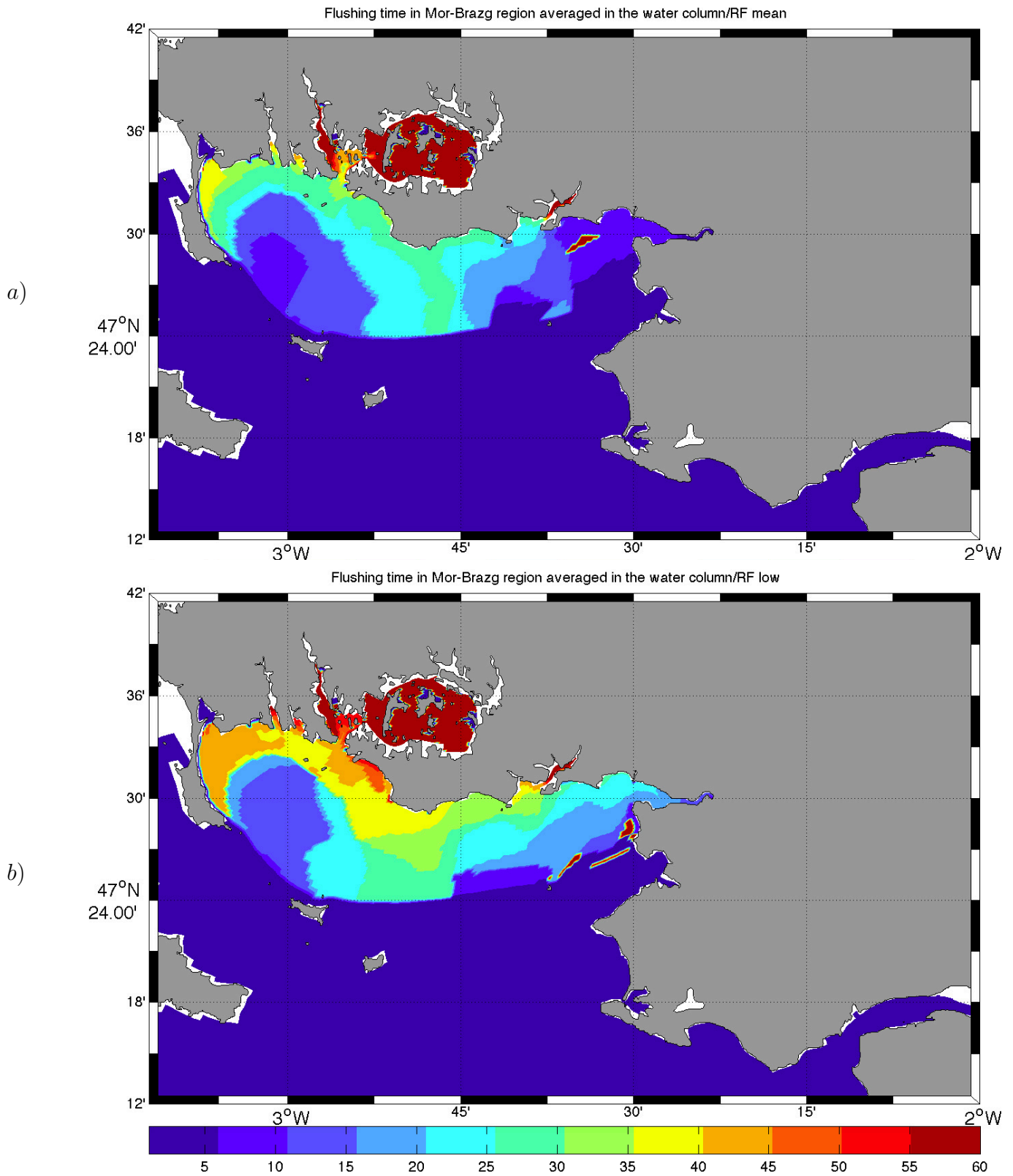


Figure 5.6: Spatial distribution of vertically averaged flushing time of the Mor-Braz, simulated without wind. a) Mean river discharges (900 and 70 m^3/s for the Loire and Vilaine rivers respectively); b) Low river discharges (300, 20 m^3/s).

According to Fig. 5.6, except in the Morbihan gulf where it goes beyond 60 days, the flushing time of the Mor-Braz area is lower in average than in the bay of Bourgneuf, even in a period of low discharge (see in Fig. 5.6, b). Half of the area is renewed within 15 to 25 days, in relation with the Vilaine and Loire discharges (the renewal time reduces with the river flow). The dependence on the Loire river regime is effective even in the bay and the estuary of Vilaine : actually, the renewal of the water volume located East of the meridian $2^{\circ} 40' W$ (approximately 10km x 10 km x 15 m) by Vilaine water would only be 4% after 10 days (the renewal time under mean river discharge condition and specifically 70 m³/s for the Vilaine) or 2.3% after 20 days (the renewal time under low river discharge condition and specifically 20 m³/s for the Vilaine), which represent small contributions to the 63% renewal.

On the opposite, the flushing time is rather high in the bay of Quiberon (between 35 and 45 days), and around the entrance of the Morbihan gulf, denoting a lack of horizontal mixing in the cross shore direction (4 km off Port Navalo strait, a strong gradient is observed : from 15 days to 40 days within 1 km). Like in the eastern part of the bay of Bourgneuf, the north-west coast of the Mor-Braz area is slowly renewed, and could constitute a provisional trap for local pollutions.

Conclusion générale de la thèse

Pour étudier l'effet de l'utilisation d'un modèle de haute résolution avec un temps de calcul raisonnable et une précision élevée en zone côtière, un développement considérable dans un code de calcul existant (MARS-3D) a été effectué pour qu'il puisse fonctionner avec un maillage non-orthogonal curviligne.

L'application au secteur de l'estuaire de la Loire et des baies adjacentes, et en particulier l'étude de la variabilité spatio-temporelle des échanges des particules en suspension dans cette zone ont été entreprises en privilégiant l'exploitation de la modélisation numérique 3D.

Cette thèse exploite un développement du code de calcul MARS-3D, compatible avec les maillages non-orthogonaux curvilinéaires. Ce dernier nous a obligé à consacrer une grande partie du temps de travail à modifier et optimiser les formulations équations de continuités et de conservation de la quantité de mouvement (système d'équations primitives).

Les simulations quasi-réalistes réalisées sur la période de juin 2007 à décembre 2007 ont permis de reproduire la variabilité des échanges entre l'estuaire de la Loire et les baies adjacentes, en prenant en compte les forçages par la marée, les fleuves et le vent ainsi que les conditions variables de salinité et de température au large. La propagation des panaches de la Loire et de la Vilaine a été prise en compte à partir des simulations du modèle MARS-3D curviligne avec une résolution qui varie de 2 km (au large) à 30 mètres (dans l'estuaire).

En l'absence de vent, l'influence dominante de la Loire dans la zone de travail est bien détaillée au niveau des différents secteurs jusqu'à la baie de Vilaine. En revanche, en présence des forçages du vent, selon le régime, la durée, la direction et l'amplitude, la dynamique du panache peut être modifiée et parfois même complètement renversée.

Les circulations résiduelles sur le domaine ont été étudiées à partir de données de simulations numériques en filtrant la marée. Les schémas de circulation ainsi que l'influence liés au

vent sur l'échange des eaux douces et salées ont été mis en évidence pour différentes conditions du vent, d'hydrologie et de marée.

Le modèle permet d'intégrer tous les processus et de reconstituer leur enchaînement dans la génération de la circulation en trois dimensions en zone côtière. Dans le chapitre 3, nous avons montré que le modèle est capable de générer des profils de vitesses le long de la verticale tout à fait réalistes et conformes aux observations . Ces profils nous ont permis de détecter une circulation inversée à l'entrée de l'embouchure de la Loire entre la surface et le fond (la circulation inversée) ayant le débit en période d'étiage et moyenne pour la partie peu profond (sud), ainsi que pour tous les régimes sur la partie profonde (nord).

Cette circulation tridimensionnelle a été illustrée aussi en baie de Bourgneuf ; elle nous permet de définir un seuil de débit de Loire pour lequel les circulations résiduelles en surface et au fond peuvent s'inverser dans la partie Est de la section d'entrée de la baie de Bourgneuf (entre la pointe St-Gildas et celle de l'Herbaudière).

Enfin, la circulation moyenne tridimensionnelle, a été reproduite aux abords du Mor-Bras, en illustrant l'effet des débits des deux fleuves et l'influence du vent sur la distribution verticale des courants dans cette zone extra-côtière. La variabilité de ces forçages fait fortement varier les circulations résiduelles mais des schémas type de circulation peuvent être dégagés de cette variabilité; ils ont pu être confirmés au moins localement par les mesures ADCP acquises au point fixe à proximité du Croisic. Ces circulations sont potentiellement responsables des transits des pollutions et des particules en suspension dans la zone.

L'évolution des échanges dans la zone Loire-Vilaine a été décrite pour un événement de tempête (10-13 décembre). On a observé une augmentation du débit de la Loire et de la vilaine, créant un gradient salinité fort à l'entrée de l'embouchure de la Loire et une advection par les courants résiduels liés au vent. La dynamique est forte en baie de Vilaine, du fait de la complexité des circulations, alors qu'en baie de Bourgneuf les structures sont bien plus stables, maintenues par des courants de marée plus forts.

Les perspectives sont une utilisation du modèle pour étudier les flux de différents éléments dissous, mais c'est surtout l'application au transport de sédiment qui apportera une information aujourd'hui manquante et précieuse pour le bilan sédimentaire à l'échelle régionale (de la baie de Bourgneuf au Mor-Bras en incluant l'estuaire de la Loire). Une modélisation sédi-

mentaire de ce type a été réalisée et validée pour le système Seine, son application à la Loire pourrait donc être assez rapide.

Publication

1. KERVELLA, Y., KHOJASTEH POUR FARD, I., LE HIR, P., RENAULT, E., LEMOINE, J. *Modélisation hydrodynamique tridimensionnelle en coordonnées curvilignes non-orthogonales de l'estuaire de la Seine. Ed. PARALIA, DOI:10.5150/jngcgc.2012.010-K. 2012, XII^e journées Génie Côtier Génie Civil, Cherbourg, 12-14 juin, 89-100*

Bibliography

- [Agrawal, 2002] Agrawal, M. (2002). Abstract mathematics. pages 75–76. [74](#)
- [Allen and Castaing, 1977] Allen, G. and Castaing, P. (1977). Carte de répartition des sédiments superficiels sur le plateau continental du golfe de gascogne. *Bulletin de l’Institut de Géologie du Bassin d’Aquitaine*, pages 255–260. [24](#)
- [Andre et al., 2005] Andre, G., P.garreau, V.garnier, and Fraunie, P. (2005). Modelled variability of the sea surface circulation in the north-western mediterranean sea and in the gulf of lions. *Artificial Intelligence and Law*, (55):294–308. [54](#)
- [Andrejev et al., 2004] Andrejev, O., Myrberg, K., and Lundberg, P. A. (2004). Age and renewal time of water masses in a semi-enclosed basin—application to the gulf of finland. *Tellus A*, 56(5):548–558. [228](#)
- [Arakawa and Lamb, 1977] Arakawa, A. and Lamb, V. (1977). Computational design of the basic dynamical processes of the ucla general circulation model. volume 17, pages 173–265. http://www-pcmdi.llnl.gov/projects/modeldoc/amip/33ucla_fn.html. [64](#)
- [Ascensio et al., 1987] Ascensio, N., Darchen, D., and D, D. (1987). Eléments climatologiques concernant les cotes de la france métropolitaine. *Boulogne: Direction de la Météorologie nationale*, IV:135. [167](#)
- [Auby et al., 1994] Auby, I., Manaud, F., Maurer, D., and Trut, G. (1994). Etude de la prolifération des algues vertes dans le bassin d’arcachon. *Rapport Ifremer-Cemagref-Ssa-Sabarc*. [166](#)
- [Bailly Du Bois et al., 2012] Bailly Du Bois, P., Dumas, F., Solier, L., and Voiseux, C. (2012). In-situ database toolbox for short-term dispersion model validation in macro-tidal seas, application for 2d-model. *Continental Shelf Research*. [54](#)
- [Blumberg et al., 1987] Blumberg, A., Herring, H., et al. (1987). Circulation modelling using orthogonal curvilinear coordinates. *Three-dimensional models of marine and estuarine dynamics*, 45:55–88. [67](#)

- [Blumberg and Mellor, 1987] Blumberg, A. F. and Mellor, G. L. (1987). A description of a three-dimensional coastal ocean circulation model. *Three-dimensional coastal ocean models*, pages 1–16. [55](#)
- [Brand et al., 1991] Brand, C., Heinemann, J., and Aziz, K. (1991). The grid orientation effect in reservoir simulation. In *SPE Symposium on Reservoir Simulation*. [66](#)
- [Britannica, 2011] Britannica (2011). *Bay of Biscay*. Encyclopaedia Britannica. [22](#)
- [Castaing et al., 1999] Castaing, P., Froidefond, J., Lazure, P., Weber, O., Prud’Homme, R., and Jouanneau, J. (1999). Relationship between hydrology and seasonal distribution of suspended sediments on the continental shelf of the bay of biscay. *Deep Sea Research Part II: Topical Studies in Oceanography*, 46(10):1979–2001. [30](#)
- [Castaing and Jouanneau, 1987] Castaing, P. and Jouanneau, J. (1987). Les apports sédimentaires actuels d’origine continentale aux océans. *Bulletin de l’Institut de Géologie du Bassin d’Aquitaine*, 41:53–65. [25](#)
- [Chapelle, 1990] Chapelle, A. (1990). Phytoplankton and eutrophication modelling in the vi-laine bay. *Coastal and Estuarine Studies*, 36:369–376. [51](#)
- [Charria et al., 2013] Charria, G., Lazure, P., Le Cann, B., Serpette, A., Reverdin, G., Louazel, S., Batifoulier, F., Dumas, F., Pichon, A., and Morel, Y. (2013). Surface layer circulation derived from lagrangian drifters in the bay of biscay. *Journal of Marine Systems*, 109:60–76. [25](#), [31](#), [32](#), [33](#), [35](#)
- [Chesshire and Henshaw, 1990] Chesshire, G. and Henshaw, W. (1990). Composite overlapping meshes for the solution of partial differential equations. *Journal of Computational Physics*, 90(1):1–64. [67](#)
- [Costanza et al., 1997] Costanza, R., Arge, R., Groot, R., Farber, S., Grasso, M., Hannon, B., Limburg, K., Naeem, S., O’Neill, R. V., Paruelo, J., et al. (1997). La valeur des services de l’écosystème mondial et du capital naturel. *Nature*, 387:253–260. [16](#)
- [CSEEL, 1984] CSEEL (1984). rapport final cnexo. Number 55, page 25. <http://archimer.ifremer.fr/doc/00000/4939/>. [16](#), [41](#), [42](#), [44](#), [45](#), [46](#)
- [Cugier and Le Hir, 2002] Cugier, P. and Le Hir, P. (2002). Development of a 3d hydrodynamic model for coastal ecosystem modelling. application to the plume of the seine river (france). *Estuarine, Coastal and Shelf Science*, 55(5):673–695. [67](#)

- [Date, 2005] Date, A. (2005). *Introduction to computational fluid dynamics*. Cambridge University Press. 112
- [Deleersnijder et al., 2007] Deleersnijder, E., Delhez, E. J., et al. (2007). Timescale-and tracer-based methods for understanding the results of complex marine models. *Estuarine, Coastal and Shelf Science*, 74(4). 228
- [Delhez et al., 1999] Delhez, E. J., Campin, J.-M., Hirst, A. C., and Deleersnijder, E. (1999). Toward a general theory of the age in ocean modelling. *Ocean Modelling*, 1(1):17–27. 229
- [Demerliac, 1974] Demerliac, M. (1974). Calcul du niveau moyen journalier. *Annales hydrographiques du SHOM*, 5:49–57. 176, 179, 182, 183
- [Denis-Papin and Kaufman, 1966] Denis-Papin, M. and Kaufman, A. (1966). Cours de calcul tensoriel appliqué. pages 43,55–57,107–108,113,118. Albin Michel. 68, 78, 80, 86
- [Dorel et al., 1991] Dorel, D., Koutsikopoulos, C., Desaunay, Y., and Marchand, J. (1991). Seasonal distribution of young sole in the nursery ground of the bay of vilaine (northern bay of biscay). *Netherlands Journal of Sea Research*, 27(3):297–306. 51
- [Douglas Downing, 2009] Douglas Downing, P. (2009). Covariant and contravariant vectors. In *Dictionary of Mathematics Terms*, pages 66–68, School of Business and Economics Seattle Pacific University. Barron’s Educational Series, Inc. 70
- [Douillet et al., 2001] Douillet, P., Ouillon, S., and Cordier, E. (2001). A numerical model for fine suspended sediment transport in the south-west lagoon of new caledonia. *Coral Reefs*, (20):361–372. 54
- [Dufois et al., 2014] Dufois, F., Verney, R., Le Hir, P., Dumas, F., and Charmasson, S. (2014). Impact of winter storms on sediment erosion in the rhone river prodelta and fate of sediment in the gulf of lions (north western mediterranean sea). *Continental Shelf Research*, 72:57–72. 54
- [Duhaut et al., 2008] Duhaut, T., Honnorat, M., and Debreu, L. (2008). Développements numériques pour le modèle mars. *PREVIMER report-Ref: 06/2 210*, 290. 63, 111
- [Dussauze et al., 2009] Dussauze, M., Sanchez, M., Barillé, L., Hitier, B., Oger-Jeanneret, H., Robin, M., et al. (2009). Modélisation de la turbidité en baie de bourgneuf (france). <http://www.paralia.fr>. 48
- [eaufrance, 2007] eaufrance (2007). Annual mean runoff of major rivers. <http://www.hydro.eaufrance.fr/>. 27

- [Erturk and Dursun, 2007] Erturk, E. and Dursun, B. (2007). Numerical solutions of 2-d steady incompressible flow in a driven skewed cavity. *ZAMM-Journal of Applied Mathematics and Mechanics*, 87(5):377–392. 105, 122
- [ESRI, 2002] ESRI, I. (2002). Bathymetrie du golfe de gascogne. http://envlit.ifremer.fr/index.php/surveillance/pollutions_accidentelles/prestige/fr/hydrodynamique/bathymetrie_du_golfe_de_gascogne. 21
- [Ferrer et al., 2009] Ferrer, L., Fontán, A., Mader, J., Chust, G., González, M., Valencia, V., Uriarte, A., and Collins, M. (2009). Low-salinity plumes in the oceanic region of the basque country. *Continental Shelf Research*, 29(8):970–984. 25
- [Figueres et al., 1985] Figueres, G., Martin, J., Meybeck, M., and Seyler, P. (1985). A comparative study of mercury contamination in the tagus estuary (portugal) and major french estuaries (gironde, loire, rhône). *Estuarine, Coastal and Shelf Science*, 20(2):183–203. 40, 43
- [Fletcher, 1988] Fletcher, C. (1988). Computational techniques for fluid dynamics. volume 2-specific techniques for different flow categories. In *Berlin and New York, Springer-Verlag*, volume 2, pages 50–51. 72
- [Froidefond et al., 1996] Froidefond, J.-M., Castaing, P., and Jouanneau, J.-M. (1996). Distribution of suspended matter in a coastal upwelling area. satellite data and in situ measurements. *Journal of Marine systems*, 8(1):91–105. 35
- [Gaspar et al., 1990] Gaspar, P., Grégoris, Y., and Lefevre, J. (1990). A simple eddy kinetic energy model for simulations of the oceanic vertical mixing: Tests at station papa and long-term upper ocean study site. *Journal of Geophysical Research*, 95(C9):16179–16. 62, 63
- [Gouleau et al., 1981] Gouleau, D., Maillocheau, F., and Ottmann, F. (1981). L’envasement du bas estuaire de la vilaine résultant de la construction du barrage d’arzal. *Séminaire National du Ministère de l’Environnement et du Service Géologique National*, La gestion régionale des sédiments:187. 51
- [Haure and Baud, 1995] Haure, J. and Baud, J.-P. (1995). Approche de la capacité trophique dans le bassin ostréicole (baie de bourgneuf). 47, 48, 50
- [Haure et al., 1996] Haure, J., Sauriau, P., and Baud, J. (1996). Effets du vent sur la remise en suspension particulaire en baie de bourgneuf: conséquences sur la croissance de crassostrea gigas. *J. Rech. Océanogr*, 11:21–30. 49

- [Hir, 1980] Hir, P. L. (1980). *Calcul par modélisation numérique de la structure verticale des courants et application à la baie de Seine*. PhD thesis. 199
- [Ifremer, 2010a] Ifremer, P. (2010a). Centre de production previmer. http://www.previmer.org/content/download/8973/47438/file/S1.4_production_et_centre_donnees.pdf. 162
- [Ifremer, 2010b] Ifremer, U. d. N. (2010b). Gestion globale des ressources marines et des risques dans les espaces côtiers. <http://archimer.ifremer.fr/doc/00136/24733/22795.pdf>. 48
- [Jegou and Lazure, 1995] Jegou, A. and Lazure, P. (1995). Quelques aspects de la circulation sur le plateau atlantique. *Actas del IV Coloquio Internacional sobre Oceanografía del Golfo de Vizcaya. Instituto Español de Oceanografía, Santander*, pages 99–106. 35
- [Jézéquel et al., 1998] Jézéquel, N., Maze, R., Pichon, A., et al. (1998). Effects of stratification and vertical velocity on tidal dynamics over a continental slope. In *The Eighth International Offshore and Polar Engineering Conference*. International Society of Offshore and Polar Engineers. 35
- [Khojasteh et al., 2011] Khojasteh, I., Le Hir, P., Dumas, F., and Pages, A. (2011). Mesh generation. *Curvilinear Grid Generation report, IFREMER*. 126
- [Koutsikopoulos and Le Cann, 1996] Koutsikopoulos, C. and Le Cann, B. (1996). Physical processes and hydrological structures related to the bay of biscay anchovy. *Scientia Marina*, 60:9–19. 30, 31
- [Large and Yeager, 2004] Large, W. G. and Yeager, S. G. (2004). *Diurnal to decadal global forcing for ocean and sea-ice models: the data sets and flux climatologies*. National Center for Atmospheric Research. 25
- [Lazure, 1992] Lazure, P. (1992). Etude de l’hydrodynamique de la baie de bourgneuf. *IFREMER/DEL*. 47, 49
- [Lazure and Dumas, 2008] Lazure, P. and Dumas, F. (2008). An external-internal mode coupling for a 3d hydrodynamical model for applications at regional scale (mars). *Advances in Water Resources*, 31(2):233–250. 34, 54, 55, 57, 62, 92, 95, 99, 104, 131
- [Lazure et al., 2008] Lazure, P., Dumas, F., and Vrignaud, C. (2008). Circulation on the armorican shelf (bay of biscay) in autumn. *Journal of Marine Systems*, 72(1):218–237. 23, 25, 36

- [Lazure et al., 2009] Lazure, P., Garnier, V., Dumas, F., Herry, C., and Chifflet, M. (2009). Development of a hydrodynamic model of the bay of biscay. validation of hydrology. *Continental Shelf Research*, 29(8):985–997. [27](#), [54](#)
- [Lazure and Jégou, 1998] Lazure, P. and Jégou, A.-M. (1998). 3d modelling of seasonal evolution of loire and gironde plumes on biscay bay continental shelf. *Oceanologica acta*, 21(2):165–177. [25](#), [27](#), [35](#), [36](#), [39](#)
- [Lazure et al., 2006] Lazure, P., Jegou, A.-M., and Kerdreux, M. (2006). Analysis of salinity measurements near islands on the french continental shelf of the bay of biscay. *Scientia Marina*, 70(1):7–14. [35](#)
- [Lazure and Salomon, 1991a] Lazure, P. and Salomon, J. (1991a). Coupled 2-d and 3-d modeling of coastal hydrodynamics. pages 173–180. *Oceanologica Acta*, 14(2). <http://archimer.ifremer.fr/doc/00101/21248/18862.pdf>. [38](#), [39](#)
- [Lazure and Salomon, 1991b] Lazure, P. and Salomon, J.-C. (1991b). Coupled 2-d and 3-d modeling of coastal hydrodynamics. *Oceanologica Acta*, 14(2):173–180. [103](#)
- [Le Boyer et al., 2009] Le Boyer, A., Cambon, G., Daniault, N., Herbette, S., Le Cann, B., Marie, L., and Morin, P. (2009). Observations of the ushant tidal front in september 2007. *Continental Shelf Research*, 29(8):1026–1037. [35](#)
- [Le Cann, 1990] Le Cann, B. (1990). Barotropic tidal dynamics of the bay of biscay shelf: observations, numerical modelling and physical interpretation. *Continental Shelf Research*, 10(8):723–758. [33](#), [35](#), [39](#)
- [Le Cann and Pingree, 1995] Le Cann, B. and Pingree, R. (1995). Circulation dans le golfe de gascogne: une revue de travaux récents. *Actas del IV Coloquio Internacional sobre Oceanografía del Golfo de Vizcaya*, pages 217–234. [25](#)
- [Le Hir et al., 1986] Le Hir, P., Duchene, C., Merel, A., De Nadaillac, G., and Merceron, M. (1986). Impact du régime du barrage d’arzal sur la stratification a l’embouchure de la vilaine: étude par modélisation numérique. [51](#)
- [Le Hir and Jacinto, 2007] Le Hir, P. and Jacinto, S. (2007). water movements in the seine estuary. *Booklet N 2 of the Seine-Aval scientific program*, page 27. [229](#)
- [Le Hir and Thouvenin, 1992] Le Hir, P. and Thouvenin, B. (1992). Modélisation mathématique simplifiée de la masse turbide dans l’estuaire de la loire. *Journées Génie Civil—Génie Côtier*, pages 141–158. [133](#)

- [Le Pape et al., 2003] Le Pape, O., Chauvet, F., Désaunay, Y., and Guérault, D. (2003). Relationship between interannual variations of the river plume and the extent of nursery grounds for the common sole (*solea solea*, l.) in vilaine bay. effects on recruitment variability. *Journal of Sea Research*, 50(2):177–185. 52
- [Le Roy and Simon, 2003] Le Roy, R. and Simon, B. (2003). Réalisation et validation d’un modèle de marée en manche et dans le golfe de gascogne(application à la réalisation d’un nouveau programme de réduction des sondages bathymétriques). 129
- [Leendertse and Gritton, 1971] Leendertse, J. and Gritton, E. (1971). A water-quality simulation model for well-mixed estuaries and coastal seas: Vol. iii, jamaica bay simulation. Rand. 63, 65
- [Lemoine, 1989] Lemoine, G. (1989). Etude sédimentaire de la baie de quiberon: La zone ostréicole en eau profonde et ses abords. 51, 52, 53
- [Leonard, 1996] Leonard, B. (1996). Convection-diffusion algorithms. *Advances in numerical heat transfer*, 1:1. 63
- [Leonard et al., 1995] Leonard, B., MacVean, M., and Lock, A. (1995). The flux integral method for multidimensional convection and diffusion. *Applied mathematical modelling*, 19(6):333–342. 63
- [LeVeque and Calhoun, 2001] LeVeque, R. and Calhoun, D. (2001). Cartesian grid methods for fluid flow in complex geometries. *Computational Modeling in Biological Fluid Dynamics*, pages 117–143. 66
- [Luyten et al., 1996] Luyten, P., Deleersnijder, E., Ozer, J., and Ruddick, K. (1996). Presentation of a family of turbulence closure models for stratified shallow water flows and preliminary application to the rhine outflow region. *Continental Shelf Research*, 16(1):101–130. 62
- [Lyard et al., 2006] Lyard, F., Lefevre, F., Letellier, T., and Francis, O. (2006). Modelling the global ocean tides: modern insights from fes2004. *Ocean Dynamics*, 56(5-6):394–415. 130
- [Maliska and Raimundo, 1981] Maliska, C. and Raimundo, C. (1981). *A Solution Method for Three-dimensional Parabolic Fluid Flow Problems in Nonorthogonal Coordinates*. University of Waterloo. 152
- [Maliska and Raithby, 1983] Maliska, C. and Raithby, G. (1983). Calculating three-dimensional fluid flows using nonorthogonal grids. In *Numerical Methods in Laminar and Turbulent Flow*, volume 1, pages 656–666. 152

- [Marchand, 1993] Marchand, J. (1993). The influence of seasonal salinity and turbidity maximum variations on the nursery function of the loire estuary (france). *Netherland Journal of Aquatic Ecology*, 27:427–436. [40](#)
- [Méléder et al., 2007] Méléder, V., Rincé, Y., Barillé, L., Gaudin, P., and Rosa, P. (2007). Spatiotemporal changes in microphytobenthos assemblages in a macrotidal flat (bourgneuf bay, france) 1. *Journal of phycology*, 43(6):1177–1190. [48](#)
- [Mellor and Blumberg, 1985] Mellor, G. and Blumberg, A. (1985). Modeling vertical and horizontal diffusivities with the sigma coordinate system. *Monthly Weather Review*, 113(8):1379–1383. [56](#)
- [Mellor and Yamada, 1982] Mellor, G. and Yamada, T. (1982). Development of a turbulence closure model for geophysical fluid problems. *Reviews of geophysics and space physics*, 20(4):851–875. [62](#)
- [Michel et al., 2009a] Michel, S., Treguier, A.-M., and Vandermeirsch, F. (2009a). Temperature variability in the bay of biscay during the past 40 years, from an in situ analysis and a 3d global simulation. *Continental Shelf Research*, 29(8):1070–1087. [26](#)
- [Michel et al., 2009b] Michel, S., Vandermeirsch, F., and Lorance, P. (2009b). Evolution of upper layer temperature in the bay of biscay during the last 40 years. *Aquatic living resources*, 22(4):447–461. [26](#)
- [Migniot and Le Hir, 1997] Migniot, C. and Le Hir, P. (1997). Estuaire de la loire–hydrosédimentaire. *Rapports de synthèse de l’APEEL*, (1). [16](#), [40](#), [45](#)
- [OSPAR, 2010] OSPAR (2010). *Quality Status Report 2000: Region II: Greater North Sea*. OSPAR Commission for the Protection of the Marine Environment of the North-East Atlantic. [23](#), [24](#), [30](#), [33](#), [40](#)
- [Ouillon et al., 2010] Ouillon, S., Douillet, P., Lefebvre, J., Le Gendre, R., Jouon, A., Bonneton, P., Fernandez, J., Chevillon, C., Magand, O., Lefèvre, J., et al. (2010). Circulation and suspended sediment transport in a coral reef lagoon: The south-west lagoon of new caledonia. *Marine pollution bulletin*, 61(7):269–296. [54](#)
- [Pairaud et al., 2010] Pairaud, I. L., Auclair, F., Marsaleix, P., Lyard, F., and Pichon, A. (2010). Dynamics of the semi-diurnal and quarter-diurnal internal tides in the bay of biscay. part 2: Baroclinic tides. *Continental Shelf Research*, 30(3):253–269. [33](#)

- [Pairaud et al., 2008a] Pairaud, I. L., Lyard, F., Auclair, F., Letellier, T., and Marsaleix, P. (2008a). Dynamics of the semi-diurnal and quarter-diurnal internal tides in the bay of biscay. part 1: Barotropic tides. *Continental Shelf Research*, 28(10):1294–1315. [33](#)
- [Pairaud et al., 2008b] Pairaud, I. L., Lyard, F., Auclair, F., Letellier, T., and Marsaleix, P. (2008b). Dynamics of the semi-diurnal and quarter-diurnal internal tides in the bay of biscay. part 1: Barotropic tides. *Continental Shelf Research*, 28(10):1294–1315. [33](#), [34](#)
- [Palma and Matano, 1998] Palma, E. D. and Matano, R. P. (1998). On the implementation of passive open boundary conditions for a general circulation model: The barotropic mode. [60](#)
- [Pingree and Le Cann, 1989] Pingree, R. and Le Cann, B. (1989). Celtic and armorican slope and shelf residual currents. *Progress in Oceanography*, 23(4):303–338. [31](#), [33](#), [35](#), [36](#)
- [Pingree and Le Cann, 1990] Pingree, R. and Le Cann, B. (1990). Structure, strength and seasonality of the slope currents in the bay of biscay region. *Journal of the Marine Biological Association of the United Kingdom*, 70(04):857–885. [166](#)
- [Pollard and Pu, 1985] Pollard, R. and Pu, S. (1985). Structure and circulation of the upper atlantic ocean northeast of the azores. *Progress in Oceanography*, 14:443–462. [22](#)
- [Pous, 2005] Pous, S. (2005). *Dynamique océanique dans les golfes Persiques et d’Oman*. PhD thesis, Brest. [54](#)
- [Puillat et al., 2004] Puillat, I., Lazure, P., Jegou, A.-M., Lampert, L., and Miller, P. (2004). Hydrographical variability on the french continental shelf in the bay of biscay, during the 1990s. *Continental shelf research*, 24(10):1143–1163. [28](#), [30](#), [35](#), [36](#)
- [Puillat et al., 2006] Puillat, I., Lazure, P., Jegou, A.-M., Lampert, L., and Miller, P. (2006). Mesoscale hydrological variability induced by northwesterly wind on the french continental shelf of the bay of biscay. *Scientia Marina*, 70(S1):15–26. [25](#), [35](#), [36](#)
- [Reverdin et al., 2013] Reverdin, G., Marié, L., Lazure, P., d’Ovidio, F., Boutin, J., Testor, P., Martin, N., Lourenço, A., Gaillard, F., Lavin, A., et al. (2013). Freshwater from the bay of biscay shelves in 2009. *Journal of Marine Systems*, 109:134–143. [30](#)
- [Rincé et al., 1985] Rincé, Y., Guillaud, J.-F., and Gallenne, B. (1985). Qualité des eaux en milieu estuarien: suivi annuel de critères physiques et chimiques dans les eaux de l’estuaire de la loire. *Hydrobiologia*, 124(3):199–210. [41](#), [42](#), [45](#)
- [Robin, 2011] Robin, M. (2011). Concepts et outils pour l’analyse spatiale des conflits d’usages. [46](#), [47](#)

- [Sadarjoen et al., 1994] Sadarjoen, A., Van Walsum, T., Hin, A., and Post, F. (1994). *Particle tracing algorithms for 3D curvilinear grids*. Delft University of Technology, Faculty of Technical Mathematics and Informatics. 72
- [Saha et al., 2010] Saha, S., Moorthi, S., Pan, H.-L., Wu, X., Wang, J., Nadiga, S., Tripp, P., Kistler, R., Woollen, J., Behringer, D., et al. (2010). The ncep climate forecast system reanalysis. *Bulletin of the American Meteorological Society*, 91(8):1015–1057. 130
- [Salomon and Breton, 1993] Salomon, J.-C. and Breton, M. (1993). An atlas of long-term currents in the channel. *Oceanologica Acta*, 16(5–6):439–448. 35
- [Sanchez et al., 2008] Sanchez, M. et al. (2008). Dynamique des sédiments fins dans une zone côtière à forte turbidité à proximité de l’embouchure de la loire. *Xèmes Journées nationales Génie Côtier-Génie Civil*. 50
- [Sanchez et al., 2000] Sanchez, M., Grovel, A., and Hosseini, K. (2000). Impact sédimentaire des travaux d’aménagement de l’estuaire de la loire. *Bulletin of Engineering Geology and the Environment*, 59(3):239–246. 133
- [Sharman et al., 1988] Sharman, R., Keller, T., and Wurtele, M. (1988). Incompressible and anelastic flow simulations on numerically generated grids. *Monthly weather review*, 116(5):1124–1136. 80, 81
- [Sheng and Hirsh, 1984] Sheng, Y. and Hirsh, J. (1984). Numerical solution of shallow water equations in boundary fitted grid. Technical report, Tech. Memo 84-15. Aeronautical Research Associates of Princeton, Princeton, NJ. 72, 80
- [Sheng, 1990] Sheng, Y. P. (1990). Evolution of a three-dimensional curvilinear-grid hydrodynamic model for estuaries, lakes and coastal waters: Ch3d. In *Estuarine and Coastal Modeling (1989)*, pages 40–49. ASCE. 67, 80
- [Sheng et al., 2010] Sheng, Y. P., Alymov, V., and Paramygin, V. A. (2010). Simulation of storm surge, wave, currents, and inundation in the outer banks and chesapeake bay during hurricane isabel in 2003: The importance of waves. *Journal of Geophysical Research: Oceans (1978–2012)*, 115(C4). 67, 72, 80
- [S.H.O.M., 1997] S.H.O.M. (1997). Service hydrographique et océanographique de la marine (s.h.o.m.). Instructions nautiques pour la plaisance, France, Bretagne Sud de la Pointe de Penmarch a la Vilaine. 51

- [Shyy and Vu, 1991] Shyy, W. and Vu, T. (1991). On the adoption of velocity variable and grid system for fluid flow computation in curvilinear coordinates. *Journal of Computational Physics*, 92(1):82–105. [80](#), [82](#)
- [Smagorinsky, 1963] Smagorinsky, J. (1963). General circulation experiments with the primitive equations. *Monthly weather review*, 91(3):99–164. [62](#)
- [Smirnov, 2004] Smirnov, A. (2004). Introduction to tensor calculus. [76](#), [77](#), [79](#)
- [Sorrel et al., 2010] Sorrel, P., Tessier, B., Demory, F., Baltzer, A., Bouaouina, F., Proust, J.-N., Menier, D., and Traini, C. (2010). Sedimentary archives of the french atlantic coast (inner bay of vilaine, south brittany): Depositional history and late holocene climatic and environmental signals. *Continental Shelf Research*, 30(10):1250–1266. [51](#)
- [Spain, 2003] Spain, B. (2003). Tensor calculus: A concise course. Dover Publications. [71](#)
- [Sturman and Zawar-Reza, 2002] Sturman, A. and Zawar-Reza, P. (2002). Application of back-trajectory techniques to the delimitation of urban clean air zones. *Atmospheric environment*, 36(20):3339–3350. [67](#)
- [Suits et al., 1978] Suits, D. B., Mason, A., and Chan, L. (1978). Spline functions fitted by standard regression methods. *The Review of Economics and Statistics*, pages 132–139. [126](#)
- [Taylor, 2001] Taylor, K. E. (2001). Summarizing multiple aspects of model performance in a single diagram. *Journal of Geophysical Research*, 106:7183–7192. [135](#), [136](#)
- [Tessier, 2006] Tessier, C. (2006). *Caractérisation et dynamique des turbidités en zone côtière: L'exemple de la région marine Bretagne Sud*. PhD thesis, Université de Bordeaux 1. [33](#), [38](#), [51](#), [54](#), [134](#), [219](#)
- [Thomas and Lombard, 2012] Thomas, P. and Lombard, C. (2012). Geometric conservation law and its application to flow computations on moving grids. *AIAA journal*, 17(10). [81](#)
- [Thompson, 1982] Thompson, J. (1982). General curvilinear coordinate system in numerical grid generation. *Elsevier Science Publishing Company, Inc*, pages 1–30,70–71. [72](#)
- [Thompson et al., 1985] Thompson, J. F., Warsi, Z. U., and Mastin, C. W. (1985). *Numerical grid generation: foundations and applications*, volume 45. North-holland Amsterdam. [68](#), [71](#)
- [Traini et al., 2013] Traini, C., Menier, D., Proust, J.-N., and Sorrel, P. (2013). Transgressive systems tract of a ria-type estuary: The late holocene vilaine river drowned valley (france). *Marine Geology*. [52](#)

- [van Aken, 2002] van Aken, H. M. (2002). Surface currents in the bay of biscay as observed with drifters between 1995 and 1999. *Deep Sea Research Part I: Oceanographic Research Papers*, 49(6):1071–1086. 31
- [Vandermeirsch et al., 2010] Vandermeirsch, F., Charraudeau, M., Bonnat, A., Fichaut, M., Maillard, C., Gaillard, F., and Autret, E. (2010). Bay of biscay’s temperature and salinity climatology. pages 4–6. XII International Symposium on Oceanography of the Bay of Biscay. <http://www.ifremer.fr/climatologie-gascogne/climatologie/index.php>. 28, 29
- [Vanney, 1977] Vanney, J.-R. (1977). *Géomorphologie de la marge continentale sud-armoricaine*, volume 21. Société d’édition d’enseignement supérieur. 25, 48
- [Vested et al., 2013] Vested, H. J., Tessier, C., Christensen, B. B., and Goubert, E. (2013). Numerical modelling of morphodynamics—vilaine estuary. *Ocean Dynamics*, 63(4):423–446. 52
- [Vreugdenhil, 2013] Vreugdenhil, C. B. (2013). *Numerical methods for shallow-water flow*, volume 13. Springer Science & Business Media. 82, 108
- [Walther et al., 2009] Walther, R., Rivier, A., Rieu, J., David, E., and Hamm, L. (2009). Modeling three-dimensional hydrosedimentary of the estuary of the loire evaluation of vertical turbulence model). *Morphodynamics and sediment management in estuaries, bays and deltas*. 134, 143
- [Willmott et al., 1985] Willmott, C. J., Ackleson, S. G., Davis, R. E., Feddema, J. J., Klink, K. M., Legates, D. R., O’donnell, J., and Rowe, C. M. (1985). Statistics for the evaluation and comparison of models. *Journal of Geophysical Research*, 90:8995–9005. 113
- [Wiseman and Garvine, 1995] Wiseman, W. and Garvine, R. (1995). Plumes and coastal currents near large river mouths. *Estuaries*, 18(3):509–517. 35
- [You et al., 2006] You, D., Mittal, R., Wang, M., and Moin, P. (2006). Analysis of stability and accuracy of finite-difference schemes on a skewed mesh. *Journal of Computational Physics*, 213(1):184–204. 122

Résumé

Les estuaires sont des zones à l'interface terre-mer au cœur de la question du devenir des apports continentaux drainés par les grands bassins versants. L'objet de cette étude est focalisé sur l'estuaire de la Loire et ses zones adjacentes (*i.e.* baie de Bourgneuf et le Mor-Bras) situés dans le nord-est du Golfe de Gascogne. C'est un environnement soumis à l'influence significative de la marée qui se propage en amont de l'embouchure à plus de 100km, de forçages météorologiques de moyennes latitudes donc hautement variables qui induisent en particulier des débits fluviaux pouvant varier d'un facteur dix. Cette variabilité est étudiée à l'aide d'un modèle numérique et des outils de description de la circulation qui permettent de mieux cerner les temps de séjours et de transits des eaux continentales dans l'estuaire et vers les baies riveraines. L'approche s'appuie sur un modèle en grille structurée mais dont la malléabilité pour décrire la complexité du domaine à simuler est donnée par le caractère non-orthogonal des mailles employées pour la discrétisation. Le choix d'un système de coordonnées optimale (covariantes ou contravariantes) est discuté puis implémenté dans le code MARS-3D. Ce nouvel outil est qualifié et validé sur des cas-test puis implémenté en conditions réelles sur un domaine à la géométrie particulièrement accidentée. Les simulations reproduisent très finement la dynamique du grand panache de la Loire et confirment sa très grande variabilité spatiale et temporelle que décrivent partiellement des observations à haute fréquence et ponctuelles; elles permettent de décrire les chemins privilégiés des masses d'eau à travers les sections de références choisies.

Mots clés : Golfe de Gascogne, Simulations Numériques, Estuaire de la Loire, MARS-3D, Non-Orthogonal, Maillage Curviligne.

Abstract

Estuaries are key areas in between land and ocean which play a major role in the spreading of continental runoff drained by large watershed. This study focused on the Loire Estuary and its adjacent bays (*i.e.* Bourgneuf bay and Mor-Braz sea) all located in the north-east side of the bay of Biscay. It is influenced by the large tidal wave that propagates upstream the mouth on more than a 100 km, by highly mid-latitude meteorological forcing that may not only induced High variability in the circulation drivers but also on the river runoffs that may vary from 1 to 10 from early spring to late summer. This High variability is studied thanks to numerical simulation and tools dedicated to describe the circulation with synthetic index such as transit time and mean age of water. The approach lies on a numerical model discretized on a structure grid which constraints have been relaxed to better fit the fractal coastal line using non orthogonal grid cells. The optimal coordinate framework (covariant or contravariant) have been discussed, and implemented within a pre-existing code (*i.e.* MARS-3D). This tool was validated with test cases and implemented on a domain with a particular complex geometry. The numerical simulations catch very accurately the dynamic of this large plume at least as it is described by available in situ observations. This numerical solution allowed to exhibit the main path of water masses through the area and from place to place and their variability according to the main forcing.

Key-words : Coastal Hydrodynamics, River Plume, Loire Estuary (France), Flushing Time, MARS-3D, Non-Orthogonal, Curvilinear grid.